



**HAL**  
open science

# Modeling of the sEMG / Force relationship by data analysis of high resolution sensor network

Mariam Al Harrach

► **To cite this version:**

Mariam Al Harrach. Modeling of the sEMG / Force relationship by data analysis of high resolution sensor network. Bioengineering. Université de Technologie de Compiègne, 2016. English. NNT : 2016COMP2298 . tel-01470368

**HAL Id: tel-01470368**

**<https://theses.hal.science/tel-01470368v1>**

Submitted on 17 Feb 2017

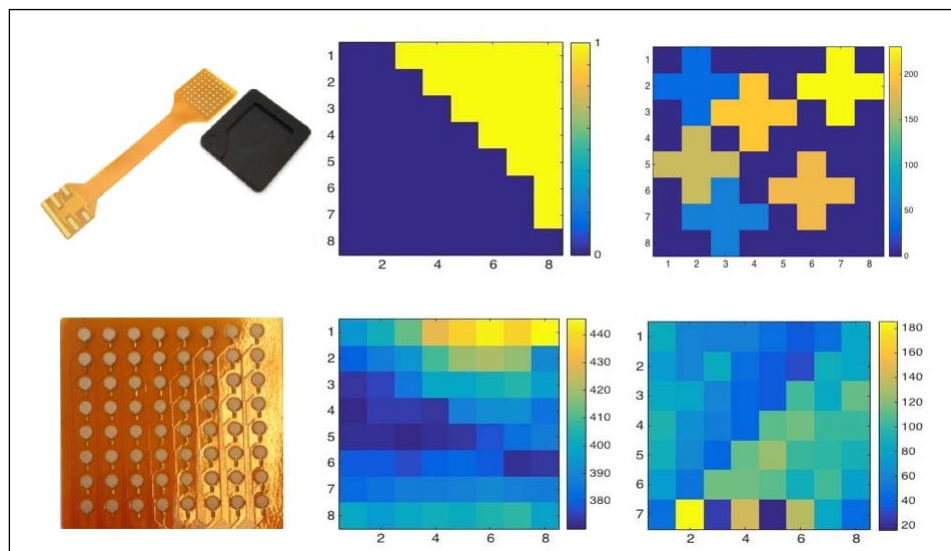
**HAL** is a multi-disciplinary open access archive for the deposit and dissemination of scientific research documents, whether they are published or not. The documents may come from teaching and research institutions in France or abroad, or from public or private research centers.

L'archive ouverte pluridisciplinaire **HAL**, est destinée au dépôt et à la diffusion de documents scientifiques de niveau recherche, publiés ou non, émanant des établissements d'enseignement et de recherche français ou étrangers, des laboratoires publics ou privés.

Par **Mariam AL HARRACH**

*Modeling of the sEMG / Force relationship by data analysis of high resolution sensor network*

Thèse présentée  
pour l'obtention du grade  
de Docteur de l'UTC



Soutenue le 27 septembre 2016  
**Spécialité** : Biomedical Engineering

D2298



**THESIS** presented to:

Sorbonne University, Université de Technologie de Compiègne (UTC)

Doctoral school « Sciences pour l'ingénieur »

for the Degree of

**Doctor**

in

**Biomedical Engineering**

Titled:

Modeling of the sEMG/Force relationship by data  
analysis of high resolution sensor network

Presented and publicly defended by:

**MARIAM AL HARRACH**

27/09/2016

**Jury members:**

David Guiraud	DR INRIA, LIRMM, Université de Montpellier	Reviewer
Christine Serviere	CR CNRS, GIPSA Lab, Institut National Polytechnique de Grenoble	Reviewer
Roberto Merletti	Prof., LISiN, Politecnico di Torino	Examiner
Amine Nait Ali	Prof., LiSSi, Université Paris-Est-Créteil	Examiner
Catherine Marque	Prof., BMBI, Université de Technologie de Compiègne	Examiner
Sofiane Boudaoud	Associate Prof., BMBI, Université de Technologie de Compiègne	Supervisor
Frédéric Marin	Prof., BMBI, Université de Technologie de Compiègne	Supervisor

“The noblest pleasure is the joy of understanding.”

— Leonardo da Vinci

# Acknowledgements

This work was carried out and funded in the framework of the Labex MS2T. It was supported by the French Government, through the program “Investments for the future” managed by the National Agency for Research (Reference ANR-11-IDEX-0004-02).

Firstly, I want to thank Dr. *Sofiane Boudaoud* and Prof. *Frédéric Marin* for their teaching, guidance and help throughout the three years of P.hD. I also want to express my sincere gratitude for Dr. *Sofiane Boudaoud* for his excellent ideas, his rigorous work manner, his advises and attention regarding my professional life and most importantly his great investment in my thesis work in general.

Besides my advisors, I would like to thank the rest of my thesis committee: Prof. *Catherine marque*, Prof. *Amine Nait Ali*, Dr. *Christine Serviere* and Prof, *David Guiraud* for being a part of my thesis defense jury.

A more particular thanks goes to Prof. *Roberto Merletti* who provided me with the opportunity of temporarily join his team, and gave me access to the laboratory and research facilities. I also would like to thank him for his insightful comments, advices and encouragement which inspired me to widen my research from various perspectives.

Further, I want thank the members of the NSE team: *Jérémy Laforet*, *Noujoude Nader*, *Adrien Létocart* and *Firas Farhat* with whom I had the pleasure to share memorable moments and scientific collaborations.

Many thank goes to my colleague *Vincent Carriou*, without whom my thesis would have been much harder and a lot more boring. Thus, I thank him for his scientific help as well as moral support.

Finally, a special thanks to my mother *Ikkal* and sister *Amina* for their continuous support and unconditional love and to all my family members for their best wishes and prayers especially my brother Brother *Abdul Rahman*.

# Acronyms

<b>ANN</b>	Artificial neural network	<b>HD-sEMG</b>	High density surface EMG
<b>ANOVA</b>	Analysis of variance	<b>HOS</b>	High order statistics
<b>AP</b>	Action potential	<b>HRS</b>	High recruitment strategy
<b>ARV</b>	Averaged rectified value	<b>ICA</b>	Independent component analysis
<b>BB</b>	Biceps Brachii	<b>ICC</b>	Intra-class correlation
<b>BMI</b>	Body mass index	<b>iEMG</b>	Integrated EMG
<b>BR</b>	Brachialis	<b>IRNA</b>	Interior-reflective Newton algorithm
<b>BRD</b>	Brachioradialis	<b>ISI</b>	Inter spike interval
<b>BSS</b>	Blind source separation	<b>LM</b>	Levenberg-Marquardt
<b>CCA</b>	Canonical correlation analysis	<b>LRS</b>	Low recruitment strategy
<b>CE</b>	Contractil element	<b>LSD</b>	Left shape distance
<b>CNS</b>	Central Nervous System	<b>MA</b>	Motion artifacts
<b>CSD</b>	Center shape distance	<b>MMG</b>	Mechanomyogram
<b>CSM</b>	Core shape model	<b>MRI</b>	Magnetic resonance imaging
<b>EEG</b>	Electroencephalograms	<b>MoCap</b>	Motion capture
<b>EEMD</b>	Ensemble EMD	<b>MU</b>	Motor unit
<b>EMD</b>	Empirical mode decomposition	<b>MUAP</b>	Motor Unit Action Potential
<b>EMG</b>	Electromyogram	<b>MVC</b>	Maximum voluntary contraction
<b>EV</b>	Eigen value	<b>NMJ</b>	Neuromuscular Junction
<b>FAP</b>	Fiber action potential	<b>NRMSE</b>	Normalized root mean squared error
<b>FFMU</b>	Fast fatiguable motor unit	<b>PCA</b>	Principal component analysis
<b>FIntMU</b>	Fast intermediate motor unit	<b>PCI</b>	Parallel cascade identification
<b>FOS</b>	Fast orthogonal search	<b>PDF</b>	Probability density function
<b>FRMU</b>	Fast resistant motor unit	<b>PE</b>	Parallel spring element

<b>PLI</b>	Power line interference	<b>sEMG</b>	Surface electromyogram
<b>PSD</b>	Power Spectral Density	<b>SMG</b>	Sonomyography
<b>PSO</b>	Particle swarm optimization	<b>SMU</b>	Slow motor unit
<b>RMS</b>	Root mean square	<b>SNR</b>	Signal to noise ratio
<b>RMSE</b>	Root mean squared error	<b>SoS</b>	Systems of systems
<b>RSD</b>	Right shape distance	<b>SVD</b>	Singular value decomposition
<b>sCCA</b>	Selective CCA	<b>WGN</b>	White Gaussian noise
<b>SD</b>	Shape distances	<b>WS</b>	Watershed
<b>SE</b>	Serial spring element	<b>WVT</b>	Wavelet

# Résumé

## Titre

**Modélisation de la relation entre le signal EMG de surface et la force musculaire par analyse de données d'un réseau de capteurs à haute résolution**

## Contenu

Les systèmes neuro-musculaire et musculo-squelettique sont considérés comme un système de systèmes complexe. En effet, le mouvement du corps humain est contrôlé par le système nerveux central par l'activation des cellules musculaires squelettiques [1]. L'activation du muscle produit deux phénomènes différents : mécanique et électrique [2]. Ces deux activités possèdent des propriétés différentes, mais l'activité mécanique ne peut avoir lieu sans l'activité électrique et réciproquement. L'activité mécanique de la contraction du muscle squelettique est responsable du mouvement [3]. Le mouvement étant primordial pour la vie humaine, il est crucial de comprendre son fonctionnement et sa génération qui pourront aider à détecter des déficiences dans les systèmes neuro-musculaire et musculo-squelettique [3]. Ce mouvement est décrit par les forces musculaires et les moments agissant sur une articulation particulière. En conséquence, les systèmes neuro-musculaire et musculo-squelettique peuvent être évalués avec le diagnostic et le management des maladies neurologiques et orthopédiques à travers l'estimation de la force [4]. Néanmoins, la force produite par un seul muscle ne peut être mesurée que par une technique très invasive. C'est pour cela, que l'estimation de cette force reste l'un des grands challenges de la biomécanique. De plus, comme dit précédemment, l'activation musculaire possède aussi une réponse électrique qui est corrélée à la réponse mécanique. Cette résultante électrique est appelée l'électromyogramme (EMG) et peut être mesurée d'une façon non invasive à l'aide d'électrodes de surface [5].

L'EMG est la somme des trains de potentiel d'action d'unité motrice qui sont responsable de la contraction musculaire et de la génération du mouvement [5, 2]. Ce signal électrique peut être mesuré par des électrodes à la surface de la peau et est appelé l'EMG de surface (sEMG). Pour un muscle unique, en

supposant que la relation entre l'amplitude du sEMG et la force est monotone [6], plusieurs études ont essayé d'estimer cette force en développant des modèles actionnés par ce signal [7, 8]. Toutefois, ces modèles contiennent plusieurs limites à cause des hypothèses irréalistes par rapport à l'activation neurale.

Dans cette thèse, nous proposons un nouveau modèle de relation sEMG/force en intégrant ce qu'on appelle le sEMG haute définition (HD-sEMG), qui est une nouvelle technique d'enregistrement des signaux sEMG ayant démontré une meilleure estimation de la force [9] en surmontant le problème de la position de l'électrode sur le muscle [10]. Ce modèle de relation sEMG/force sera développé dans un contexte sans fatigue pour des contractions isométriques, isotoniques et anisotoniques du Biceps Brachii (BB) lors une flexion isométrique de l'articulation du coude à 90°.

Pour cela, nous sommes passés par plusieurs étapes de traitement et de préparation des signaux sEMG afin de pouvoir mettre en place ce modèle. La première étape de ce travail a été le traitement des signaux HD-sEMG afin de les préparer pour l'étape de la fusion des données. Ce traitement se fait d'abord par un débruitage de ces signaux. Dans la littérature, il n'existe pas d'algorithme de débruitage multi-voies prenant en compte l'hétérogénéité du bruit propagé sur la grille HD-sEMG. Ainsi, la première contribution de cette thèse est le développement d'un algorithme de débruitage basé sur une méthode de séparation aveugle de source (BSS) du second ordre appelée l'analyse par composante canonique (CCA). Cette méthode est appelée le CCA sélectif (sCCA) combinant une procédure de sélection suivie de l'élimination de certaines sources puis d'un seuillage afin de débruiter de façon optimale les signaux HD-sEMG. Cet algorithme a aussi été comparé à d'autres méthodes de débruitage et a démontré son efficacité et sa robustesse. La seconde étape du traitement des signaux avait pour but de séparer l'activité électrique du BB de celle du Brachialis (BR). En effet, le BR étant un muscle profond proche du BB, le sEMG du BR n'est pas facilement mesurable en utilisant des électrodes bipolaires classiques, ainsi des superpositions des signaux électriques des deux muscles peuvent être enregistrées. C'est pour cela qu'il est important d'extraire l'activité électrique du BR et du BB. La seconde contribution de cette thèse est la proposition d'une procédure de séparation des activités électriques musculaires aussi basée sur le CCA ainsi que sur un algorithme de segmentation d'images. Cette méthode nous permet de retirer l'activité du BR présente lors de la mesure des signaux sEMG sur le BB.

Après le traitement des signaux, la prochaine étape du travail s'est intéressée à la fusion des données et la sélection du vecteur de paramètres d'entrée du modèle de relation HD-sEMG/force. Pour la fusion des données, nous avons utilisé un algorithme de segmentation d'image qui traite la matrice de paramètres des signaux sEMG comme une image. Cela a réduit le nombre de voies utilisées en localisant une région d'intérêt. Ensuite, la troisième contribution de ce travail est l'étude de la variation des statistiques d'ordres supérieures (HOS) pendant des contractions isométriques anisotoniques en proposant une méthode de fusion des données basée sur le l'analyse par composante principales (PCA) donnant la sélection optimale de la position des filtres Laplaciens. Ce travail nous a permis de trouver les mêmes profils pour les

deux paramètres des HOS pour tous les sujets malgré la grande variabilité anatomique, neuronale et morphologique entre eux. La dernière contribution de cette partie de travail est l'étude global en simulation et en expérimentation de la variation des HOS ainsi que des paramètres de distances de forme (SD) avec le niveau de contraction musculaire selon les valeurs des paramètres morphologiques, anatomiques et de contrôle nerveux. Cette tâche a été réalisé grâce à un modèle cylindrique multi-couches de simulation des signaux HD-sEMG personnalisé par des paramètres physiologiques obtenus par échographie.

La dernière étape de cette thèse a été consacré à la modélisation de la relation sEMG/force. Pour cela nous avons utilisé le modèle cylindrique multi-couches pour la simulation des signaux HD-sEMG et un modèle Twitch pour la simulation de la force musculaire correspondante. Tout d'abord, nous avons réalisé une étude de sensibilité de cette relation par rapport aux paramètres morphologiques, anatomiques et neuraux. Cette étude nous a permis d'établir les paramètres essentiels qui influent sur la forme de la relation sEMG/force et qui doivent être pris en compte dans la modélisation. Ensuite nous avons comparé les différentes équations proposées dans la littérature décrivant cette relation. Ce qui nous a permis de trouver la meilleure équation; un polynôme d'ordre 3. En se basant sur cette équation, nous avons étudié plus profondément l'effet des paramètres sur les coefficients de l'équation. Finalement, la dernière contribution de cette thèse est de proposer une méthode d'estimation de force basée sur un réseau de neurones artificiels entraîné sur une base de données suffisamment large et une alternative analytique par optimisation sou contraintes. Partant de ce qui a été présenté ci-dessus, cette thèse est organisée comme suit :

- **Chapitre 1** : il présente une revue bibliographique décrivant des informations indispensables sur les mécanismes de génération de la force musculaire et du signal sEMG ainsi que leurs caractéristiques. De plus, il expose un état de l'art sur la relation sEMG/force ainsi que les modèles d'estimation de la force musculaire à partir du signal sEMG. Ensuite, il introduit l'HD-sEMG comme une technique innovante d'enregistrement du sEMG et il expose ses applications et ses avantages. Finalement, il finit par définir notre position vis à vis de la problématique principale de la thèse : la modélisation de la relation sEMG/force.
- **Chapitre 2** : le travail de ce chapitre vise à préparer les données pour l'étape de fusion. Il comprend deux parties principales : le débruitage des signaux HD-sEMG et la séparation des activités électriques du BB et du BR. En effet, les signaux sEMG sont souvent contaminés par différents types de bruit notamment le bruit blanc et le bruit du réseau (50 Hz). Ainsi, on a développé une méthode de débruitage basée sur le CCA avec une méthode de sélection des sources basée sur un nouveau critère de seuillage qui est explicité dans la première section de ce chapitre. Pour la deuxième section, nous avons expliqué en détails la méthode de séparation de sources qui combine le CCA avec une méthode de segmentation d'images afin de séparer les sources électriques du BB

et du BR.

- **Chapitre 3** : ce chapitre présente une étude sur les paramètres d'entrée du modèle sEMG/force obtenu par fusion de données du réseau de capteurs HD-sEMG. Le chapitre commence par l'introduction d'une méthode de fusion basée sur la segmentation des matrices de paramètres calculées sur la matrice HD-sEMG de 64 signaux. Ensuite, deux différentes études sont faites afin d'étudier la variation des paramètres HOS en fonction de la force musculaire. La première étude est une étude expérimentale qui traite des contractions isométriques anisotoniques. La deuxième étude présente une étude globale en simulation et en expérimentation sur les HOS ainsi que les SD. Ce chapitre se termine par une étude sur la déformation de la surface du BB afin de d'explorer la relation activation/déformation musculaire.
- **Chapitre 4** : ce dernier chapitre a pour but de modéliser la relation sEMG/force. Pour cela, il présente une étude de sensibilité de la forme de cette relation par rapport aux différents paramètres. Ensuite, une étude sur l'équation qui décrit au mieux cette relation est réalisée. par la suite, cette équation sera utilisée pour quantifier l'effet des paramètres étudiés dans la partie précédente sur les coefficients de l'équation. Pour finir, un modèle d'estimation de force basée sur un réseau de neurones à apprentissage est détaillé. Une alternative analytique est aussi présentée qui prête mieux au contexte multi-muscle

## Mots clés

Système de systèmes, électromyogramme de surface, force musculaire, analyse par composantes canoniques, modélisation, analyse de forme, biceps brachii, réseau de capteurs à haute résolution.

# Abstract

The neuromuscular and musculoskeletal systems are complex System of Systems (SoS) that perfectly interact to provide motion. This interaction is illustrated by the muscular force, generated by muscle activation driven by the Central Nervous System (CNS) which pilots joint motion. The knowledge of the force level is highly important in biomechanical and clinical applications. However, the recording of the force produced by a unique muscle is impossible using noninvasive procedures. Therefore, it is necessary to develop a way to estimate it. The muscle activation also generates another electric phenomenon, measured at the skin using electrodes, namely the surface electromyogram (sEMG). In the biomechanics literature, several models of the sEMG/force relationship are provided. They are principally used to command musculoskeletal models. However, these models suffer from several important limitations such as lacks of physiological realism, personalization, and representability when using single sEMG channel input. In this work, we propose to construct a model of the sEMG/force relationship for the Biceps Brachii (BB) based on the data analysis of a High Density sEMG (HD-sEMG) sensor network. For this purpose, we first have to prepare the data for the processing stage by denoising the sEMG signals and removing the parasite signals. Therefore, we propose a HD-sEMG denoising procedure based on Canonical Correlation Analysis (CCA) that removes two types of noise that degrade the sEMG signals and a source separation method that combines CCA and image segmentation in order to separate the electrical activities of the BB and the Brachialis (BR). Second, we have to extract the information from an  $8 \times 8$  HD-sEMG electrode grid in order to form the input of the sEMG/force model. Thusly, we investigated different parameters that describe muscle activation and can affect the relationship shape then we applied data fusion through an image segmentation algorithm. Finally, we proposed a new HD-sEMG/force relationship, using simulated data from a realistic HD-sEMG generation model of the BB and a Twitch based model to estimate a specific force profile corresponding to a specific sEMG sensor network and muscle configuration. Then, we tested this new relationship in force estimation using both machine learning and analytical approaches. This study is motivated by the impossibility of obtaining the intrinsic force from one muscle in experimentation.

**Keywords:** System of systems, surface electromyogram, muscle force, canonical correlation analysis, machine learning, biceps brachii, high resolution sensor network.

# Publications

## International conference papers

- **M. Al Harrach**, F. S. Ayachi, S. Boudaoud, J. Laforet, and F. Marin, “Sensitivity evaluation of HOS parameters by data fusion from HD-sEMG grid”, 2nd IEEE International Conference on Advances in Biomedical Engineering (ICABME), 2013, , Tripoli, Lebanon, pp. 97–100.
- S. Allouch, **M. Al Harrach**, S. Boudaoud, J. Laforet, F. S Ayachi, and R. Younes, “Muscle Force Estimation Using Data Fusion from “High-Density SEMG Grid ”, 2nd IEEE International Conference on Advances in Biomedical Engineering (ICABME), 2013, Tripoli, Lebanon, pp. 195–198.
- **M. Al Harrach**, S. Boudaoud, D. Gamet, J.F. Grosset, and F. Marin, “Evaluation of High Order Statistic Trends from HD-sEMG recordings during Ramp Exercise”, 36th Annual International Conference of the IEEE Engineering in Medicine and Biology Society (EMBS), Chicago, U.S.A, 2014, pp. 2209-2212.
- S. Boudaoud, H. Rix, **M. Al Harrach**, and F. Marin, “Robust Functional Statistics applied to Probability Density Function Shape screening of sEMG data”, 36th Annual International Conference of the IEEE Engineering in Medicine and Biology Society (EMBS), Chicago, U.S.A, 2014, pp. 2213–2216.
- A. Zaylaa, A. Diab, **M. Al Harrach** and S. Boudaoud, “Evaluation of HD- sEMG grid misalignment with muscle fibers using nonlinear correlation”, 3rd International Conference on Advances in Biomedical Engineering (ICABME), 2015, pp. 289 - 292.
- S. Boudaoud, S. Allouch, **M. Al Harrach** and F. Marin, “On the benefits of using HD-sEMG technique for estimating muscle force”, 40th conference of the biomechanics society, Paris, October 2015.
- **M. Al Harrach**, S. Boudaoud, K. Ben Mansour, J. F Grosset and F. Marin, “Estimation of the relationship between external Biceps Brachii deformation and isometric contraction level using

Motion Capture technique”, XIV Mediterranean Conference on Medical and Biological Engineering and Computing (MEDICON), Paphos, , Cyprus, 2016, pp 37-41.

- V. Carriou, **M. Al Harrach**, J. Laforet and S. Boudaoud, “Sensitivity analysis of HD-sEMG amplitude descriptors relative to grid parameter variation”, XIV Mediterranean Conference on Medical and Biological Engineering and Computing (MEDICON), Paphos, Cyprus, 2016, pp 119-123.
- **M. Al Harrach**, B. Afsharipour, S. Boudaoud, V. Carriou, F. Marin and R. Merletti, “Extraction of the Brachialis muscle activity using HD-sEMG technique and Canonical Correlation Analysis”, 38th Annual International Conference of the IEEE Engineering in Medicine and Biology Society (EMBS), Orlando, U.S.A, 2016.
- V. Carriou, J. laforet, S. Boudaoud and **M. Al Harrach**, “Realistic motor units placement in a cylindrical HD-sEMG generation Model”, 38th Annual International Conference of the IEEE Engineering in Medicine and Biology Society (EMBS), Orlando, U.S.A, 2016.

## International Journal papers

- **M. Al Harrach**, S. Boudaoud, M. Hassan, F. S. Ayachi, D. Gamet, J.F. Grosset and F. Marin, “Denoising of HD-EMG Signals Using Canonical Correlation Analysis”, Journal Medical & Biological Engineering & Computer, 2016, pp 1-14.
- **M. Al Harrach**, S. Boudaoud, V. Carriou, A. Letocart, J. Laforet and F. Marin, “Monitoring of the HD-sEMG Probability Density Function Shapes With Varying Muscle Force”, Journal of Biomedical Signal Processing and Control (under submission).
- **M. Al Harrach**, V. Carriou, J. Laforet, S. Boudaoud, and F. Marin, “Analysis of the sEMG/ Force Relationship using HD-sEMG Technique and Data Fusion: A Simulation Study”, Journal of Computers in Biology and Medecine (under submission).
- V. Carriou, J. Laforet , S. Boudaoud and **M. Al Harrach**, “Sensitivity analysis of HD-sEMG amplitude descriptors relative to parameter variations of a cylindrical multilayered muscle model”, Journal of Biomedical Physics & Engineering Express (submitted)

“To the strongest person I know, my mother

*Ikbal*, who made me who I am”

# Contents

<b>General introduction</b>	<b>29</b>
<b>1 General context</b>	<b>32</b>
1.1 Introduction . . . . .	33
1.2 Skeletal muscles and motion genesis . . . . .	34
1.2.1 Mechanism of muscle contraction . . . . .	42
1.2.1.1 Generation and propagation of fiber action potential (FAP) . . . . .	45
1.2.1.2 Different types of muscle contraction . . . . .	46
1.2.2 Surface Electromyogram (sEMG) . . . . .	46
1.2.2.1 Motor Unit Action Potential (MUAP) . . . . .	47
1.2.2.2 Motor Unit recruitment and firing (Rate coding) . . . . .	47
1.2.2.3 Discharge frequency and generated force . . . . .	49
1.2.2.4 Electrode configurations and spatial filtering . . . . .	49
1.2.2.5 sEMG signal Processing . . . . .	50
1.2.2.6 Basic signal processing of the sEMG signal . . . . .	51
1.2.2.7 Elements affecting the sEMG signal . . . . .	52
1.2.3 Muscle force generation . . . . .	54
1.2.3.1 Twitch generation and summation of twitches . . . . .	54
1.3 EMG driven force estimation models . . . . .	56
1.3.1 sEMG/force relationship . . . . .	57
1.3.2 Phenomenological models . . . . .	59

1.3.3	Physiological models . . . . .	65
1.3.4	Regressive type models . . . . .	68
1.4	High Density sEMG (HD-sEMG) technique . . . . .	73
1.5	Position of the problem and objectives of the thesis . . . . .	74
<b>2</b>	<b>Preprocessing of HD-sEMG signals</b>	<b>77</b>
2.1	Introduction . . . . .	78
2.2	Denoising of HD-sEMG signals using Canonical Correlation Analysis . . . . .	78
2.2.1	Canonical Correlation Analysis (CCA) . . . . .	80
2.2.2	CCA component thresholding . . . . .	82
2.2.3	Selective CCA method . . . . .	83
2.2.4	HD-sEMG simulation model . . . . .	85
2.2.5	Denoising simulated HD-sEMG signals . . . . .	86
2.2.6	Experimental protocol . . . . .	88
2.2.6.1	Subjects . . . . .	88
2.2.6.2	Mechanical and electrophysiological recordings . . . . .	88
2.2.6.3	Procedure . . . . .	89
2.2.7	Denoising experimental HD-sEMG signals . . . . .	89
2.2.8	Comparative study . . . . .	94
2.2.8.1	CCA-EMD . . . . .	95
2.2.8.2	CCA-WVT . . . . .	96
2.2.8.3	ICA . . . . .	97
2.2.9	Discussion and conclusion . . . . .	98
2.3	Extraction of the Brachialis's muscle activity from the HD-sEMG recorded at the surface of the Biceps Brachii . . . . .	101
2.3.1	Experimental protocol . . . . .	102
2.3.1.1	Subjects . . . . .	102
2.3.1.2	Procedure . . . . .	102

2.3.1.3	Mechanical and electrophysiological recordings . . . . .	103
2.3.2	Data Processing . . . . .	104
2.3.3	Otsu thresholding method . . . . .	106
2.3.4	Application of the separation method on the experimental signals . . . . .	106
2.3.5	Analysis of the results and discussion . . . . .	110
2.4	Conclusion . . . . .	111
<b>3</b>	<b>HD-sEMG map fusion and input parameter design</b>	<b>112</b>
3.1	Introduction . . . . .	113
3.2	HD-sEMG map fusion . . . . .	113
3.2.1	RMS map generation . . . . .	114
3.2.2	RMS map segmentation . . . . .	114
3.3	Shape analysis of the probability density function of HD-sEMG signals . . . . .	117
3.3.1	Evaluation of High Order Statistic Trends from HD-sEMG recordings during Ramp Exercise . . . . .	118
3.3.1.1	High Order Statistics (HOS) . . . . .	119
3.3.1.2	Principal Component Analysis (PCA) . . . . .	119
3.3.1.3	Experimental protocol . . . . .	120
3.3.1.4	Laplacian selection procedure . . . . .	120
3.3.1.5	Results and discussion . . . . .	121
3.3.2	Monitoring of the HD-sEMG PDF shapes with varying muscle force . . . . .	124
3.3.2.1	Experimental protocol . . . . .	125
3.3.2.2	HD-sEMG signal processing . . . . .	126
3.3.2.3	HD-sEMG simulation . . . . .	132
3.3.2.4	HOS and SD variations with force level increase for the simulated signals	134
3.3.2.5	HOS and SDs variations with force level increase for the experimental signals . . . . .	141
3.3.2.6	Discussion and conclusion . . . . .	144
3.4	Muscle surface deformation . . . . .	147

3.4.1	Experimental protocol . . . . .	148
3.4.2	Data processing . . . . .	149
3.4.3	Results and discussion . . . . .	150
3.5	Conclusion . . . . .	154
<b>4</b>	<b>HD-sEMG/Force relationship modeling</b>	<b>156</b>
4.1	Introduction . . . . .	157
4.2	HD-sEMG/Force relationship modeling . . . . .	158
4.2.1	Muscle force generation model . . . . .	159
4.2.2	HD-sEMG simulation . . . . .	160
4.2.3	Study of the parameters influencing the shape of the HD-sEMG/Force relationship	162
4.2.3.1	Morphological parameters . . . . .	162
4.2.3.2	Anatomical and neural parameters . . . . .	164
4.2.4	HD-sEMG/force relationship fitting . . . . .	166
4.2.5	Improving polynomial fitting using optimization . . . . .	169
4.2.6	Sensitivity analysis of the polynomial fitting . . . . .	170
4.2.7	Discussion and conclusion . . . . .	176
4.3	HD-sEMG driven muscle force estimation model . . . . .	177
4.3.1	Supervised regression approach . . . . .	177
4.3.1.1	Artificial Neural Network (ANN) . . . . .	177
4.3.1.2	Levenberg-Marquardt algorithm . . . . .	180
4.3.1.3	Force estimation . . . . .	180
4.3.1.4	Improving force estimation using HOS . . . . .	183
4.3.2	Analytical approach . . . . .	185
4.4	Conclusion . . . . .	188
	<b>General conclusion</b>	<b>189</b>
	<b>Bibliography</b>	<b>193</b>

<b>A Image segmentation study</b>	<b>210</b>
A.1 Implementation and accuracy computing . . . . .	210
A.2 Results and Discussion . . . . .	211
<b>B The anatomies and force combinations used in chapter 4</b>	<b>215</b>
B.1 An example of the MU positions for LRS and HRS for one muscle anatomy . . . . .	215
B.2 The different force level combinations tested for force estimation by ANN . . . . .	218

# List of Figures

1.1	The neuromuscular and musculoskeletal system interaction (figure adapted from © Pearson Education Inc 2012 and 2013).	33
1.2	The elbow joint muscles responsible for elbow flexion (image from McGraw-Hill companies, Inc).	35
1.3	Muscle architecture (photo created by © Benjamin Cummings, Addison Wesley Longman, Inc 2001).	36
1.4	Skeletal muscle structure (photo created by © Encyclopedia Britannica 2015).	37
1.5	Muscle fiber structure (photo created by © Pearson Education Inc 2013).	38
1.6	Muscle fiber structure (photo created by © Benjamin Cummings, Addison Wesley Longman Inc 2001).	39
1.7	Motor Unit (MU) illustration from © Pearson Education Inc 2013.	40
1.8	Four cross sections of the deltoid muscle showing different myofibrillar ATPase reactions, illustrating the morphological typing of muscle fibers [11].	40
1.9	Illustration of the muscle fibers characteristics according to their types [12].	41
1.10	The block diagram describing the muscle fiber contraction mechanism.	43
1.11	The mechanism of muscle contraction (image from © Pearson Education, Inc, 2013).	44
1.12	The steps of the sliding filaments phenomenon during muscle contraction (image from © McGraw Hill, Inc).	45
1.13	Action potential (image from © Pearson prentice Hall, Inc 2005).	45
1.14	EMG generation during voluntary contraction.	48
1.15	EMG generation during voluntary contraction.	48
1.16	Different electrode configurations and the corresponding recorded MUAP.	50

1.17	The factors affecting the sEMG signal [6]. . . . .	52
1.18	Twitch force shape and parameters and twitch shape variation according to the MU type.	54
1.19	Tetanic force generation during voluntary contraction (figure from © Pearson Education, Inc 2013). . . . .	55
1.20	Muscle force generation from the superposition of MU twitches. . . . .	56
1.21	Mind mapping of the techniques used for muscle force estimation. . . . .	56
1.22	Normalized EMG/force amplitude relations using different simulations [13]. A, C, and E: simulated EMG/force amplitude relation when MUAP amplitude is proportional to square root of twitch force. A: simulated force-EMG amplitude relation derived from motor unit firing rate strategy FR1. C: simulated force-EMG amplitude relation derived from MU firing rate strategy FR2. E: simulated force-EMG amplitude relation derived from motor unit firing rate strategy FR3. B, D, and F: simulated force-EMG amplitude relation when MUAP amplitude is linearly proportional to twitch force. B: simulated force-EMG amplitude relation derived from motor unit firing rate strategy FR1. D: simulated force-EMG amplitude relation derived from MU firing rate strategy FR2. F: simulated force-EMG amplitude relation derived from MU firing rate strategy FR3. FR1, FR2 and FR3 are defined in [13]. . . . .	59
1.23	A general model that relates the sEMG of each muscle to its force [14]. . . . .	60
1.24	The transformation of neural excitation $u(t)$ to muscle force $F(t)$ by means of activation dynamics and muscle contraction dynamics. . . . .	60
1.25	Transformation from sEMG signal into muscle activation $a(t)$ . . . . .	61
1.26	The relationship between $a(t)$ and $u(t)$ for muscle-specific values of A as presented by [15]. Each plot has a reference line $u = a$ . The node point for each piecewise curve is specified by $(u_0, a_0)$ as described in [15]. . . . .	62
1.27	Schematic representation of the Hill muscle model. . . . .	63
1.28	Schematic representation of the musculotendinous actuator. . . . .	64
1.29	Normalized force-length relationship for different activation levels [16]. . . . .	66
1.30	The block diagram of the force estimation model combining the Hill type model with the multi-scale physiological model. . . . .	67
1.31	Huxley filament model [17]. . . . .	68
1.32	Schematic of the regressive type models. . . . .	69

1.33	Architectural graph of a multilayered Artificial Neural Network (ANN) model. . . . .	70
1.34	The structure of the Parallel Cascade Identification (PCI) model. . . . .	71
1.35	Block diagram of the biomechanical based estimation model [18]. . . . .	73
1.36	The block diagram representing the methodology of the thesis work. . . . .	75
2.1	Block diagram of the CCA component thresholding procedure. . . . .	83
2.2	The block diagram of the CCA and the sCCA denoising techniques. . . . .	84
2.3	Obtained denoising results for the simulated HD-sEMG signals at 20 %MVC (Simulation 5). . . . .	87
2.4	The experimental setup used for the recording of the HD-sEMG signals for isometric isotonic contractions of 20 %MVC. . . . .	89
2.5	The HD-sEMG grid placement on the BB. . . . .	90
2.6	The first 32 canonical components (a.u) in descending order from top to bottom according to the value of the autocorrelation coefficient for subject 1 which we found representative of the subjects. . . . .	91
2.7	The CCA thresholding procedure for subject 1. . . . .	92
2.8	The SNR dispersion of the 64 channels before (blue) and after (red) denoising with CCA and selective CCA (green) for the five subjects. . . . .	93
2.9	The sEMG signals and the corresponding PSDs for channel 62 before and after denoising with CCA for subject 1. . . . .	94
2.10	The wavelet decomposition tree. . . . .	96
2.11	Obtained results of the comparative study for the five subjects. . . . .	98
2.12	A) Serial Cross Sections Through the upper limb. Each section (I, II, and III) is taken at the corresponding labeled level in the figure at panel "B". C) Side view of the right arm showing the BB and BR muscles, which are synergists in elbow flexion. The Triceps Brachii is an antagonist of those two muscles and is the prime mover in elbow extension. Panels "A", "B" and "C" are a courtesy of Dr. Afsharipour. . . . .	102
2.13	The position of the dominant arm during the isometric elbow flexion contraction (left) and the Placement of the HD-sEMG grids on the upper arm during the protocol (right). Note that the elbow was always aligned with the load cells in order to obtain a precise contraction level recording. . . . .	103
2.14	The experimental settings: A 64-channel WEMG system, a notebook PC, Isometric brace are used to record from the Brachialis and Biceps Brachii. . . . .	104

2.15	The block diagram of the CCA based muscular activity separation algorithm. . . . .	105
2.16	The SNR of the 64 EMG signals for one of the subjects before (blue) and after denoising with CCA (red) and sCCA (green). . . . .	107
2.17	The electrode numbering of the $8 \times 8$ kapton grid system, and the placement with respect to the geometry of the subject's arm. . . . .	108
2.18	Two sources weight maps (in a.u, absolute value), one corresponding to the BB and the other for the BR according to the contraction levels: 5, 10, 30 and 50 %MVC and their corresponding filter after segmentation. . . . .	108
2.19	The bipolar APs corresponding to the BB for each columns of the HD-sEMG grid obtained after reconstruction for 5, 10, 30 and 50 %MVC observed for one of the subjects. . . . .	109
2.20	The bipolar APs corresponding to the BR for each columns of the HD-sEMG grid obtained after reconstruction for 30 and 50 %MVC observed for one of the subjects. . . . .	110
3.1	The grayscale image (bottom panel) created with the RMS values computed for an experimental EMG recorded from the BB during isometric flexion at 30 %MVC and the corresponding EMG signals for the first column (upper panel). . . . .	114
3.2	Schematic of the WS segmentation (bottom) applied to the grayscale image (Top) obtained from the RMS map of simulated EMG signals with its topographical representation (middle). . . . .	115
3.3	Schematic of the WS segmentation results (e) and (f) applied to: (a) the gradient (G) of the image and (b) the smoothed gradient obtained by opening and closing techniques respectively. With their corresponding topographical representation (c) and (d). . . . .	117
3.4	Block diagram representing the steps of the WS based segmentation method. . . . .	118
3.5	Laplacian channel positions according to higher muscle activation areas for subject 1. . . . .	121
3.6	Schematic of the steps employed in order to obtain the final HOS parameters. . . . .	121
3.7	The kurtosis and skewness variations for the six Laplacian signals obtained for subject 1 (see Figure 3.5) and the corresponding PCA modes according to force level increase from 0% to 50%MVC. . . . .	122
3.8	Trends of the Skewness (up) and the Kurtosis (bottom) for the six subjects with force intensity increase from 0% to 50% MVC. . . . .	123
3.9	The three ultrasound images: a: Longitudinal, b: Panoramic and c: Cross section, taken for the extraction of morphological parameters for one of the subjects. . . . .	125

3.10	The steps of the monopolar channels selection procedure for subject 1. Starting from the RMS maps (top), then the equalized RMS maps (middle) the segmentation filter is computed by WS segmentation (bottom) for the three contraction levels (30, 50 and 70% MVC) and the final filter is the intersection of all three filters. . . . .	128
3.11	The steps of the bipolar channels selection procedure for subject 1. Starting from the RMS maps (top), then the equalized RMS maps (middle) the segmentation filter is computed by WS segmentation (bottom) for the three contraction levels (30, 50 and 70% MVC) and the final filter is the intersection of all three filters. . . . .	129
3.12	The obtained Laplacian filter after Laplacian selection for the same subject presented in Figure 3.10 . . . . .	130
3.13	Schematic of the cylindrical simulation model. . . . .	133
3.14	The two recruitment strategies LRS (green) and HRS (blue) used in the simulation model.	134
3.15	The muscle anatomy, the corresponding kurtosis, skewness and the three SDs (LSD, RSD and CSD) maps of the 64 HD-sEMG signals according to contraction level (30, 50 and 70% MVC) for the LRS strategy. . . . .	135
3.16	The muscle anatomy, the corresponding kurtosis, skewness and the three SDs (LSD, RSD and CSD) maps of the 64 HD-sEMG signals according to contraction level (30, 50 and 70% MVC) for the HRS strategy. . . . .	136
3.17	The profile variation for the kurtosis, skewness for the monopolar (left), bipolar (middle) and Laplacian (right) signals according to the contraction level (30, 50 and 70 %MVC) for the maximum and the minimum skin tissue thickness. . . . .	137
3.18	The profile variation for the kurtosis, skewness for the monopolar (left), bipolar (middle) and Laplacian (right) signals according to the contraction level (30, 50 and 70 %MVC) for the maximum and the minimum muscle length. . . . .	137
3.19	The obtained profile variation for kurtosis, the skewness, RSD-LSD and CSD according to contraction level (30, 50 and 70 %MVC) for the LRS for monopolar, bipolar and Laplacian arrangements. . . . .	139
3.20	The obtained profile variation for kurtosis, the skewness, RSD-LSD and CSD according to contraction level (30, 50 and 70 %MVC) for the HRS for monopolar, bipolar and Laplacian arrangements.. . . .	140
3.21	The PDF corresponding to the dominant profiles according to force intensity (30, 50 and 70 %MVC) for anatomy 1 with high recruitment strategy. . . . .	141

3.22	The RMS, kurtosis, skewness, LSD and CSD variations for the $8 \times 8$ HD-sEMG grid according to force intensity (30, 50 and 70% MVC) for subject 1. . . . .	142
3.23	The variation of the kurtosis, skewness and LSD and CSD) for the monopolar, bipolar and Laplacian arrangements according to force intensity (30, 50 and 70 %MVC) for subjects 1, 2 and 3. . . . .	143
3.24	The PDF corresponding to the dominant profiles according to force intensity (30, 50 and 70 %MVC) for subjects 1. . . . .	144
3.25	Setup for the simultaneous collection of the muscle force and the motion data. . . . .	149
3.26	The experimental protocol setup with the force sensor. . . . .	150
3.27	The LabVIEW force monitoring interface used as feedback for the subjects. . . . .	151
3.28	The placement of the 41 markers in a lozenge shape on the BB . . . . .	151
3.29	Elbow angle computing from the positions of the 5 markers placed on the acromion, the medial and lateral epicondyle, the radius and the ulna. . . . .	152
3.30	The ellipsoid fitting of the 3D marker positions for two contraction levels: 20 and 80%MVC for one studied subject. . . . .	152
3.31	3D surface fitting of the surface of the BB . . . . .	153
3.32	Ellipsoid fitting for the 9 markers at the center of the diamond. . . . .	153
3.33	The corresponding parameters (a and b) for all subjects. . . . .	154
4.1	Schematic of the HD-sEMG and Force simulation models used in the modeling of the sEMG/Force relationship. . . . .	157
4.2	The two rate coding strategies used in simulation. . . . .	161
4.3	Schematic diagram presenting the different configurations used for the simulation. . . . .	161
4.4	The HD-sEMG/force relations for the five anatomies relative to different morphological parameters and values (see Table 4.2). . . . .	163
4.5	The HD-sEMG/force relations for the five anatomies relative to different MU type distributions, recruitment strategies and firing rates (see Table 3.3). . . . .	165
4.6	The variation of the fitting parameters with respect to the fitting type. . . . .	167
4.7	The RMS/Force relationships for the simulated data and the polynomial fitting using different skin and adipose tissue thickness for each one of the five anatomies. . . . .	171

4.8	The three coefficients of the polynomial fitting using different adipose tissue thickness for the five anatomies. . . . .	172
4.9	The three coefficients of the polynomial fitting using different adipose tissue thickness for the five anatomies. . . . .	172
4.10	The RMS/Force relationships for the simulated data and the polynomial fitting using different MU type distributions for each one of the five anatomies. . . . .	173
4.11	The three coefficients of the polynomial fitting using different MU type distributions for the five anatomies. . . . .	174
4.12	The RMS/Force relationships for the simulated data and the polynomial fitting using different spatial recruitment strategies and firing rates for the five anatomies. . . . .	175
4.13	The three coefficients of the polynomial fitting using different spatial recruitment strategies (LRS vs HRS) and firing rates ( linear vs nonlinear) for the five anatomies. . . . .	176
4.14	The feedforward neural network basic architecture. . . . .	178
4.15	A simple artificial neuron. . . . .	179
4.16	Schematic of the input/output system. . . . .	181
4.17	The NRMSE between the target and the estimated coefficients using ANN approach for the 35 different contraction level combinations. . . . .	182
4.18	The block diagram of the polynom coefficients estimation after classification into three groups according to the MU type distribution. . . . .	184
4.19	The mean and std variation of the HOS parameters the kurtosis and the skewness according to the force levels 30, 50 and 70 %MVC. . . . .	184
4.20	The NRMSE between the target and the estimated coefficients using optimization approach for the 35 different contraction level combinations. . . . .	186
4.21	The NRMSE values obtained for all the different HD-sEMG/force simulations. . . . .	186
4.22	The NRMSE values obtained for all the different HD-sEMG/force simulations. . . . .	187
A.1	The repartition of the MUs in the muscle for the five anatomies relative to three contraction level: 30, 50 and 80 %MVC. The red MUs are the active (recruited) MUs and the blue MUs are the inactive (non recruited) MUs. . . . .	211
A.2	An example that shows the ability of watershed and Otsu algorithms in detecting the active portion of a simulated RMS map (a), after equalization (b) using the watershed (c) and the Otsu (d) algorithms. . . . .	212

- A.3 Percentage accuracy values of EMG segmentation for 20 threshold levels (from 5% to 100% of the maximum of the simulated RMS) and three adipose tissue thickness values using both watershed and Otsu algorithms and three contraction levels: 30, 50 and 70 %MVC. The SNR values were obtained from realistic experimental signals. . . . . 213
- B.1 The MU placement in the muscle for anatomy 1, D1, HRS for the ten force levels 10, 20, 30, 40, 50, 60, 70, 80, 90 and 100 %MVC. With the recruited MUs are illustrated in red and the non recruited MUs in blue. . . . . 216
- B.2 The MU placement in the muscle for anatomy 1, D1, LRS for the ten force levels 10, 20, 30, 40, 50, 60, 70, 80, 90 and 100 %MVC. With the recruited MUs are illustrated in red and the non recruited MUs in blue. . . . . 217

# List of Tables

1.1	Summary of the differences in skeletal muscle fiber types (Table adapted from [19]) . . . .	42
2.1	MU and fiber parameters (mean $\pm$ SD) used in the simulation model. . . . .	85
2.2	HD-sEMG generation model parameters. . . . .	86
2.3	The SNR of the noisy simulated HD-sEMG signals before and after denoising in dB and the corresponding SNR improvement, intensity ratio threshold and NRMSE. . . . .	87
2.4	The SNR of the selected HD-sEMG signals before and after denoising in dB and the corresponding SNR improvement, denoised channels number, and intensity ratio threshold	94
2.5	The SNR of the selected HD-sEMG signals before and after denoising in dB and the corresponding SNR improvement, denoised channels number, and intensity ratio threshold	95
3.1	Morphological parameters obtained from ultrasound measurements for six subjects. . . . .	126
3.2	Description of the parameters used to simulate the HD-sEMG signals. . . . .	133
3.3	MUs percentage for each distribution . . . . .	133
3.4	The morphological parameters values corresponding to the different simulations. . . . .	135
4.1	The twitch parameters corresponding to the four MU types [20]. . . . .	159
4.2	The physiological parameters used in the simulations. . . . .	160
4.3	The error computed for the $3^{rd}$ degree polynom fitting for all the parameter types discussed above. . . . .	169
4.4	The error computed for the $3^{rd}$ degree polynom fitting by optimization for the different morphological, anatomical and neural parameter values. . . . .	170
4.5	Commonly used activation functions and their corresponding equations. . . . .	179
4.6	ANN training parameters. . . . .	181

4.7	The mean $\pm$ std values of NRMSE computed for the force levels 10, 20, 40, 60, 80, 90 and 100 %MVC for the signals that were not used in the training phase for different configurations of ANN parameters. . . . .	182
4.8	The mean $\pm$ std values of NRMSE computed for the force levels 10, 20, 40, 60, 80, 90 and 100 %MVC for the signals that were not used in the training phase and the NRMSE for the polynom coefficient estimation for different input parameters. . . . .	183
4.9	The mean $\pm$ std values of NRMSE computed for the force levels 10, 20, 40, 60, 80, 90 and 100 %MVC (not used in the training phase) and the NRMSE for the polynom coefficient estimation for different input parameters. . . . .	185
A.1	Percentage accuracy values of EMG segmentation for three adipose tissue thickness values using both watershed and Otsu algorithms and three contraction levels: 30, 50 and 70 %MVC. The threshold was fixed at 70%. . . . .	214
B.1	Different combinations of contraction levels tested for the polynomial coefficients estimation.	218

# General introduction

The neuromuscular and musculoskeletal systems are complex System of Systems (SoS) that mutually interact during motion genesis. In fact, the human motion is managed by the Central Nervous System (CNS) through activation of skeletal muscle cells [1]. The muscle activation produces two types of contractile responses; mechanical and electrical [2]. These two activities have different properties, nevertheless one cannot occur without the other. The mechanical outcome of skeletal muscle contraction manifests by motion production [3]. And since movement is crucial for survival and human life, it is imperative to understand all its aspects that can determine the functions and detect anomalies of the musculoskeletal and neuromuscular systems [3]. This movement is portrayed by muscle forces and moments that act on a certain joint. Accordingly, the neuromuscular, musculoskeletal, biomechanics, and robotic systems can be evaluated along with the diagnosis and management of both neurological and orthopedic diseases through estimation and qualification of this mechanical response which is the force [4]. Nevertheless, the force produced by an individual muscle can only be measured through very invasive procedures. For these reasons, the estimation of individual muscle force remains one of the leading challenges in biomechanics and motor control. However, as mentioned earlier the muscle activation have another contractile response that is correlated to the mechanical one; the electrical activity. This electrical response is called the Electromyogram (EMG) and can be measured in a non invasive manner using surface electrodes [5].

The EMG signal is the summation of Action Potential (AP) trains produced by Motor Units (MUs) which are responsible for muscle contraction and motion genesis [2, 5]. This electrical signal can be measured from the surface of the skin above the muscle using surface electrodes. The signal measured by the surface electrodes is called surface EMG (sEMG). Considering that the relationship between the sEMG amplitude of a particular muscle and the corresponding force is monotonic [6] many studies attempted to estimate the individual muscle force or moment by proposing sEMG driven force estimation models [7, 8]. However, these models suffer from many physiological and non-physiological limitations due to unrealistic assumptions about muscle activation and neural command.

In this thesis, we will propose a new sEMG/force relationship model using a novel multichannel sEMG recording technique; the High density sEMG (HD-sEMG) which has proven to improve force estimation

[9] by overcoming the electrode positioning dilemma [10]. This HD-sEMG/force relationship model will be defined in an isometric isotonic and anisotonic non-fatiguing context for the Biceps Brachii (BB) muscle during isometric flexion of the elbow joint at 90° degree of elbow angle.

Based on all of the above, this manuscript is organized as follow:

- Chapter 1: In this chapter, we start the first section by introducing the main notions concerning the skeletal muscles and motion genesis, essentially the skeletal muscle properties and architecture, the MU and the fiber types. Wherein we describe also the mechanisms of muscle contraction and sEMG signal generations by detailing the generation and propagation of Fiber AP (FAP), MUAP, MU recruitment and firing and enumerating the different types of contractions and the relations between the discharge frequency and the generated force. In addition we define the different electrode configurations and spatial filtering as well as some of the basic sEMG signal processing tools. In the second section, we propose a state of the art of the sEMG driven force estimation models that exist in the literature after exploring the sEMG/force relationship. Afterwards, in the next section, we introduce the HD-sEMG technique as a innovative recording procedure that have many applications and advantages and can improve sEMG based force estimation. Finally, we finish this chapter by positioning the proposed thesis work in the face of the current force estimation paradigm and indicating the objectives of the thesis.
- Chapter 2: This chapter is dedicated to the data preprocessing. Therefore, it is divided into two steps: denoising and separation of the Brachialis's sEMG from that of the Biceps Brachii. In fact, the HD-sEMG channels are usually contaminated by noise in a heterogeneous manner. These noises are mainly power line interference, white Gaussian noise and motion artifacts. Thus, we propose in this first part, a denoising algorithm based on a the Canonical Correlation Analysis (CCA). We proposed a specific and automatic canonical component selection, using noise ratio thresholding. We also proposed amelioration based on a channel selection procedure that we called selective CCA. These methods showed better abilities in the denoising of our HD-sEMG signals for low contraction levels in comparison with other commonly used denoising techniques (ICA, bipolar, etc..). The second part of the preprocessing was oriented toward the separation of the two electrical activities of the Brachialis (BR) and the BB in order to minimize the error of the force estimation due to the crosstalk from the Brachialis in collaboration with the LISiN Laboratory (Prof. R. Merletti).
- Chapter 3: The purpose of this step was the combination of the information collected from the 64 sensors of a grid in order to construct the input vector of the sEMG/Force Model after feature selection based on a focused study of the parameters sensitivity. Therefore, we studied the variation of the probability density function shape with force level increase by using High Order Statistics (HOS) and principal component analysis for the data fusion step. This study was applied on iso-

metric anisotonic experimental signals. Afterwards, both experimental and personalized simulation studies were conducted for isometric isotonic contractions at different contraction levels. Wherein, we used ultrasound imaging in order to measure physiological parameters from the subjects. Then, an image segmentation algorithm was employed for the data fusion of the HOS and the Shape Distance (SD) parameters. We also simulated different electrode configurations, recruitment threshold and motor unit type distributions in the muscle to assess the sensitivity of PDF shape descriptors with force level toward several physiological and anatomical parameters. A final exploratory work concerns the use of the Motion Capture (MoCap) technique to estimate in a non-invasive manner the muscle activation based on the surface deformation of the BB muscle.

- Chapter 4: This block represents the sEMG/force relationship modeling and prediction step for one muscle, the BB, after the preprocessing and the data fusion phases. Before the actual force estimation, we studied the shape variation of HD-sEMG/Force relationship using a multilayered cylindrical model for the simulation of the HD-sEMG signals and a twitch model for the simulation of the corresponding force during isometric plateaus of several intensities. This study is achieved by a focused sensitivity analysis of the relationship shape variation according to neural, anatomical and physiological parameters. Finally, we will test a machine learning system that will be trained using a selection of parameters (amplitude and statistics) obtained from the HD-sEMG grid after data fusion, as well as physiological parameters (skin and adipose tissue thickness) in order to estimate the muscle force. In addition, we will also propose an analytical resolution for muscle force estimation using an optimization approach. Then, a validation phase will be conducted, in simulation, to assess the model prediction accuracy and generalization ability following several configurations (input). Finally, the obtained results and main contributions of the thesis are discussed and benefits and limitations are pointed out for future applications mainly in a multi-muscle configuration.

# Chapter 1

## General context

### Contents

---

<b>1.1</b>	<b>Introduction</b>	<b>33</b>
<b>1.2</b>	<b>Skeletal muscles and motion genesis</b>	<b>34</b>
1.2.1	Mechanism of muscle contraction	42
1.2.2	Surface Electromyogram (sEMG)	46
1.2.3	Muscle force generation	54
<b>1.3</b>	<b>EMG driven force estimation models</b>	<b>56</b>
1.3.1	sEMG/force relationship	57
1.3.2	Phenomenological models	59
1.3.3	Physiological models	65
1.3.4	Regressive type models	68
<b>1.4</b>	<b>High Density sEMG (HD-sEMG) technique</b>	<b>73</b>
<b>1.5</b>	<b>Position of the problem and objectives of the thesis</b>	<b>74</b>

---

## 1.1 Introduction

Since the early human life, man has shown unceasing interest in the organs responsible for mobility in his own body first and those of animals after. This extreme curiosity is due to the fact that movement is considered the capital sign of animal life; to move is to survive. Actually, part of the first ever scientific experiments were conducted on muscles to study its functions. A lot of philosophers and scientists from Leonardo da Vinci, Andreas Vesalius to Galvani, whose findings constructed the beginning of neurophysiology and muscle contraction dynamics studies, showed immense interest in neuromuscular and musculoskeletal systems. However, the most important contribution in this domain was that of Duchenne, with his immortal work "Physiologie des mouvements" [21]. Where he introduced the use of electricity for understanding the conductivity of neural pathways and the dynamics of muscle contractions.

Modestly, this thesis will continue this investigation by the focus on the interaction between the neuromuscular and musculoskeletal systems (see Figure 1.1) illustrated by muscular force generation. Actually,

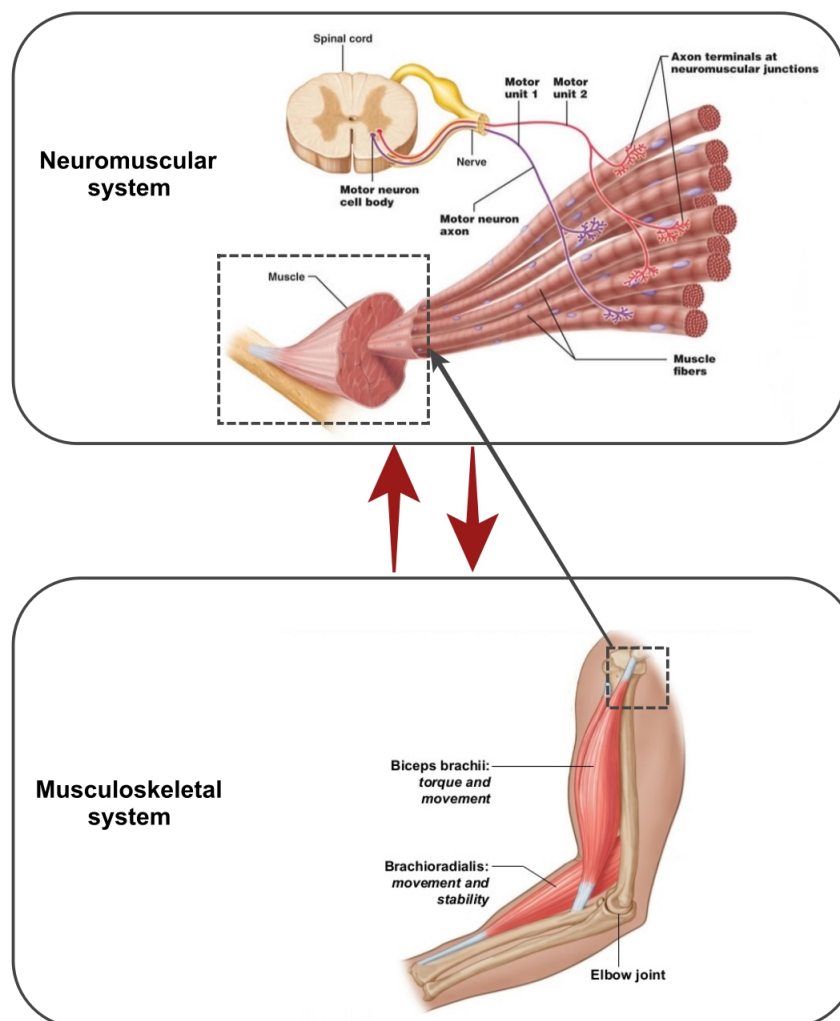


Figure 1.1: The neuromuscular and musculoskeletal system interaction (figure adapted from © Pearson Education Inc 2012 and 2013).

these systems are complex systems that perfectly interact in order to provide motion. The muscle force produced following this interaction is generated by muscle activation driven by the CNS which pilots the joint motion. In fact, the understanding of the force generation mechanism is fundamental in many areas such as the study of muscle activation and coordination forces since it is the main determinant of joint loading. But more importantly, this understanding allows the evaluation of the two systems, the neuromuscular and the musculoskeletal systems, interaction and the ability of this system of systems to produce mechanical work.

This study is motivated by the fact that individual muscle force modeling is still an open field of research due to the lack of consensus and limited validation; direct measures on muscle need very invasive procedures [22, 8]. Consequently, it is essential to find pertinent ways to model it. At the current stage, we know for a certainty that muscle activation, in addition to the mechanical response, produces an electrical response which is the EMG signal. Experimentally, this signal can be measured non-invasively using simple surface electrodes placed on the surface of the skin. As a matter of fact the EMG signal and the generated force following muscle activation are associated. Accordingly, the majority of the force estimation models are based on sEMG recordings [8]. However, these approaches for muscle modeling or estimation present several problems [8, 7]. Thus, in this work we propose to use a novel sEMG recording technique called High Density sEMG (HD-sEMG). This innovative sEMG measurement approach presents many advantages relative to the classical technique and surpasses its limitations.

In this chapter we will introduce the notions of skeletal muscle and motion genesis, EMG and muscle force generation (section 1.2). Then, we will detail the relationship between the sEMG and the muscle force and present the EMG based muscle force estimation models that exist in the literature as segmental motions generator (section 1.3). Finally, after introducing the HD-sEMG technique (section 1.4) we will conclude this chapter by presenting the problem and the objectives of this thesis (section 1.5).

## 1.2 Skeletal muscles and motion genesis

The human body contains more than 700 muscles attached to the bones of the skeletal system that make up roughly half of a person's body weight [23]. These muscles can generate force, accomplish movements of the skeletal units, conform to a wide variety of needs, assist to temperature regulation of the body, and repair themselves when needed. There are three types of muscle tissue in vertebrates [23]:

- Visceral or smooth muscles are involuntary muscles found within the walls of organs like the stomach, intestines, blood vessels and uterus;
- Cardiac muscle is found only in the heart and is responsible for pumping blood throughout the body. It is also an involuntary muscle that stimulates itself in order to contract;

- Skeletal muscles are the only voluntary muscles in the human body. All physical movements that a person consciously achieve require skeletal muscles.

## Muscle properties

The skeletal muscles possess four essential characteristics:

- **Excitability:** is the capability of the muscle tissue to contract when stimulated by a voluntary or involuntary neural command;
- **Contractility:** is the ability of the muscle tissue to respond to a stimulus by developing a tension;
- **Elasticity:** refers to the ability of the tissue to return to its resting state after being stretched;
- **Extensibility:** refers to the ability of the muscle tissue to be stretched or increased in length.

Except for facial muscles, all skeletal muscles are attached to two bones by tendons. Tendons are tough band of fibrous connective tissues whose strong collagen fibers firmly attach muscles to bones. Tendons are able to withstand tension. They are put under extreme stress when muscles pull on them, so they are strong and are interlaced into the covering of both muscles and bones.

In this thesis, our interest will be focused on the skeletal muscles and more precisely the elbow flexors. A muscle is called a flexor when it acts to bend a joint in the body. Figure 1.2 illustrates the elbow joint and the three flexors: the BB, the Brachialis (BR) and the Brachioradialis (BRD).

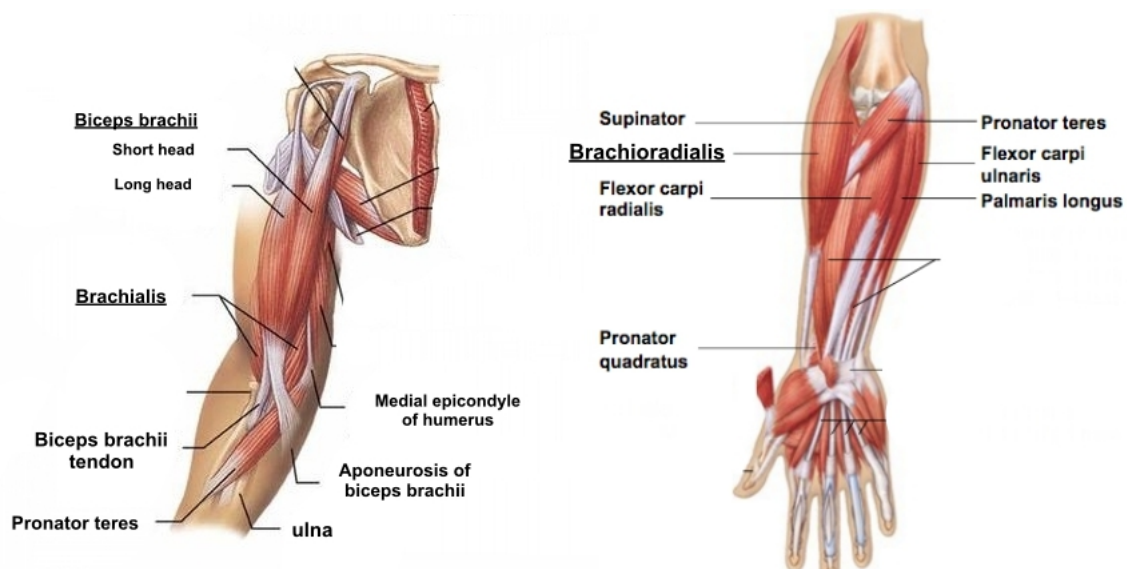


Figure 1.2: The elbow joint muscles responsible for elbow flexion (image from McGraw-Hill companies, Inc).

The BB is located between the shoulder and the elbow joint. It has two heads, the long and the short head, that starts from the scapula in the shoulder and then are merged to form the muscle belly near the

deltoid insertion [24]. The BB ends also in two tendons, the stronger is attached to the radial tuberosity on the radius and the other on the ulnar part of the antebrachial fascia. The main functions of the BB are elbow flexion and forearm supination [24]. As for the BR, it is a deeper muscle that is located between the lower half of the front of the humerus and extends 2.5 cm below the margin of the articular surface of the humerus at the elbow joint [25]. Further, the BR emerges from the intermuscular septa of the arm more frequently from the medial. It is separated from the lateral below by the BRD and extensor carpi radialis longus muscles. Its fibers gather to form a thick tendon at the tuberosity of the ulna [25]. Its main function is the elbow flexion. This muscle works as a synergist to the BB in elbow flexing. The last elbow flexor is the BRD. Unlike the BR, the BRD is a superficial muscle attached to the lateral supracondylar ridge of the humerus and to the radius. Near the elbow, this muscle constitutes the lateral limit of the cubital fossa [25].

### Muscle architecture

The skeletal muscles in the human body have a variety of shapes depending on the fiber orientation whether it is in the direction of the tendon (fusiform) or at a certain angle from the tendon (pennate). In the case of a pennate muscle, the fibers are connected to the aponeurosis of the muscle [26]. Thus, the muscle fiber types vary between: fusiform, parallel, unipennate, bipennate, multipennate, circular and convergent as illustrated in Figure 1.3 where every shape has its own conveniences. In this thesis as

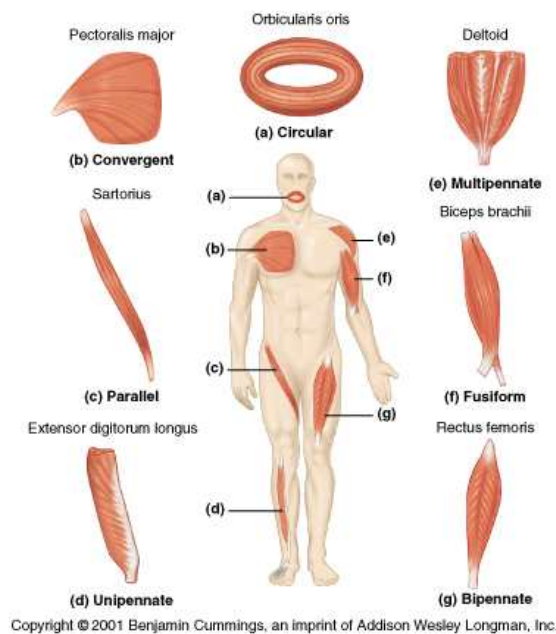


Figure 1.3: Muscle architecture (photo created by © Benjamin Cummings, Addison Wesley Longman, Inc 2001).

mentioned before, we will focus on the elbow joint flexors (BB, BR and BRD) especially the BB. The BB is generally active during flexion of spine forearm but not during the flexion of the prone forearm [5]. It

was also, reported that the long head of the BB provides more activity than the short head [5]. The BR is considered to be a “flexor with excellence” since it contributes to the flexion of supine, semi-prone and prone forearm [27, 28]. As for the BRD, it assists the BB in the flexion. It is described by Duchenne [21] as a supinator of the prone forearm and a pronator of the supine forearm. All three muscles are fusiform muscles. The BB and the BRD are superficial muscles. Otherwise, the BR is a deeper muscle that have a superficial part between the BB and the Triceps.

The skeletal muscles are covered by a firm coat of connective tissue called the epimysium. The epimysium covers the entire muscle and separates it from other muscles [29]. It contains packages of collagen fibers connected to the perimysium (see Figure 1.4). The perimysium itself is also strong. It partitions the muscle into fascicles and supplies the pathway for the blood vessels and nerves to pass through the muscle belly [29].

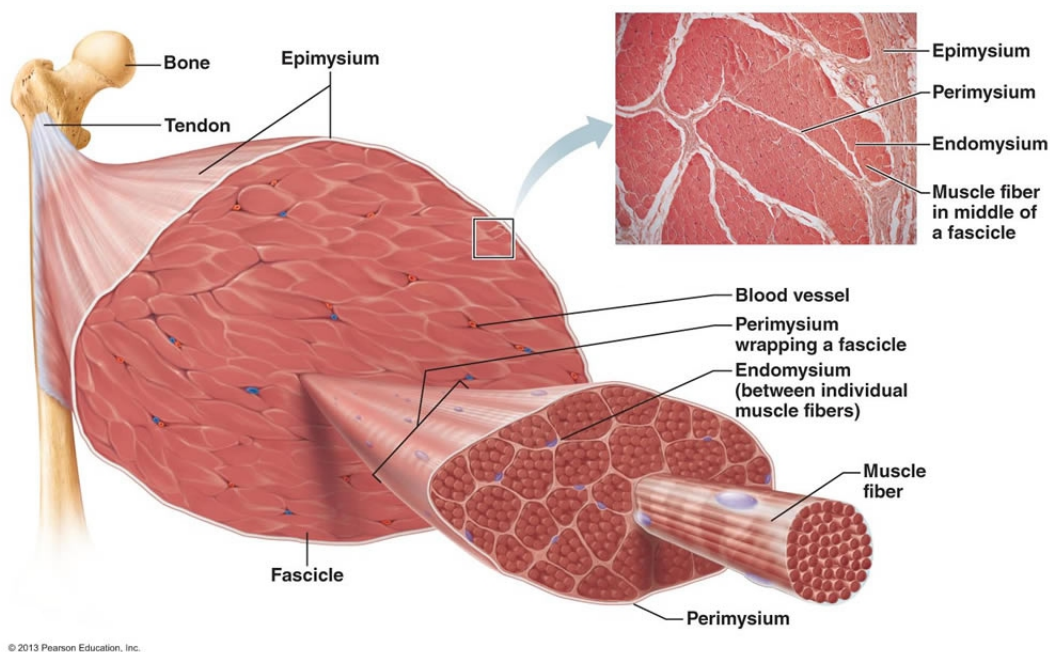


Figure 1.4: Skeletal muscle structure (photo created by © Encyclopedia Britannica 2015).

The foundation of the skeletal muscle tissue is the muscle fiber, also called muscle cell. The muscle fibers are wrapped into fascicles, which are themselves bundled together to form the muscle (see Figure 1.4). The collagenous membranes, at each level of bundling, support the muscle functions including a resistance to passive stretching of the tissue and the distribution of forces applied to the muscle. The fiber cells are threadlike shaped, where each one of them contains nuclei, myofibril, mitochondrion, endoplasmic reticulum and is sheathed with its own endomysium of collagen fibers [30] (see figure 1.4 and 1.5).

They are arranged in parallel with each other with a diameter between 10 and 100  $\mu m$  [31] and a length that can reach 30  $cm$  for some muscles. Most of the muscle fiber volume ( $\sim 80\%$ ) is occupied by the myofibrils which are a cylindrical elements with a diameter between 1 and 2  $\mu m$  [29, 31]. The myofibril

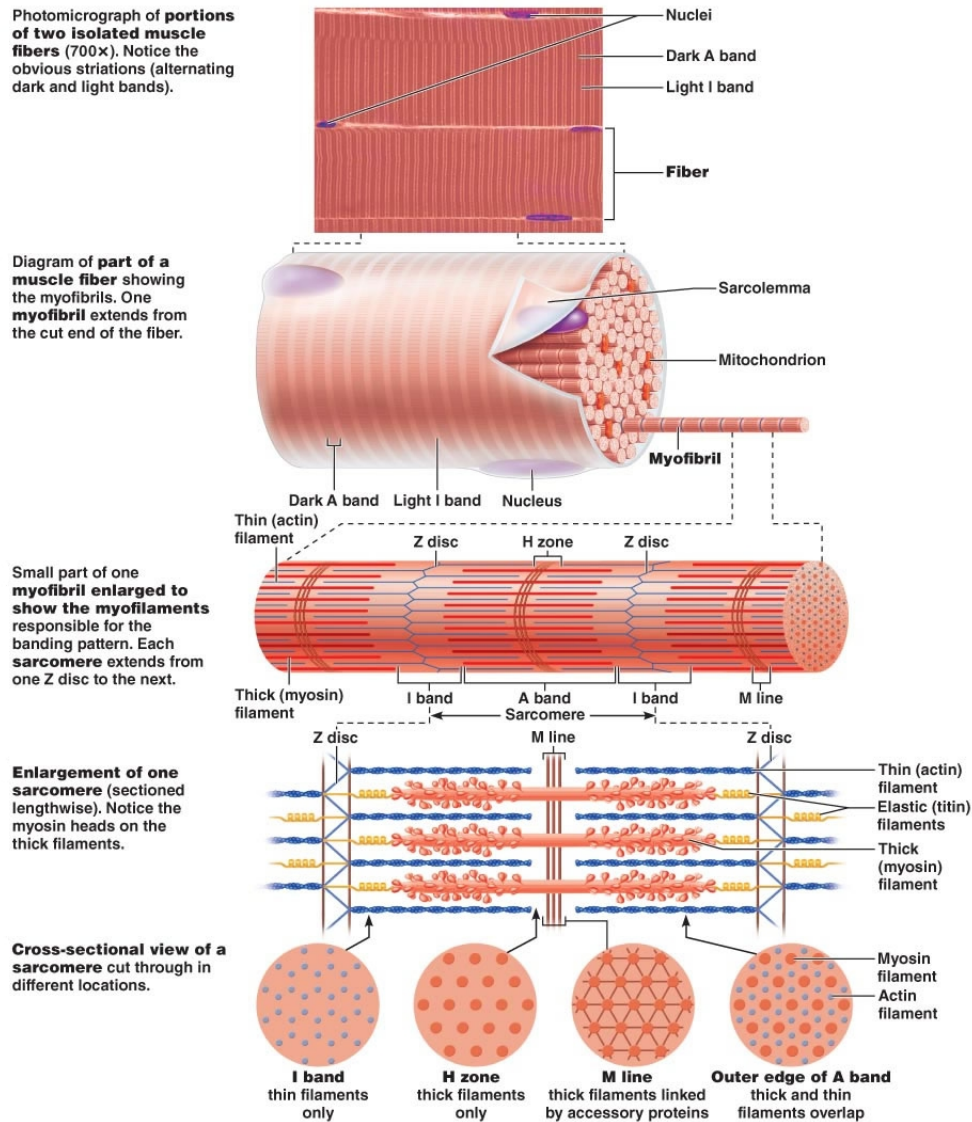


Figure 1.5: Muscle fiber structure (photo created by © Pearson Education Inc 2013).

are the units responsible for contraction and relaxation of the fiber [29]. Each myofibril contains two types of protein filament: actin (thin filament) and myosin (thick filament). In fact, the alternation of the dark, anisotropic, A-bands corresponding to the presence of myosin filaments and the light, isotropic, I-bands that contain actin filament along the myofibril gives the myofibril and the muscle fiber its striated appearance.

In rest position, actin and myosin filaments overlap to a certain extent as shown in Figure 1.5. The region of myosin without overlapping in the A-band is called the H-zone as illustrated in Figures 1.5 and 1.6. In the middle of the H-zone there is a dark region which is the M-region that contains filamentous structures that cross-connect the myosin filaments [29]. Similarly, in the center of the I-Band we have a dark line called the Z-disk where actin filaments are bounded together (see Figures 1.5 and 1.6). The cylindrical space bounded by two consecutive Z-disks is called a sarcomere. It is the basic unit of striated

Copyright © The McGraw-Hill Companies, Inc. .

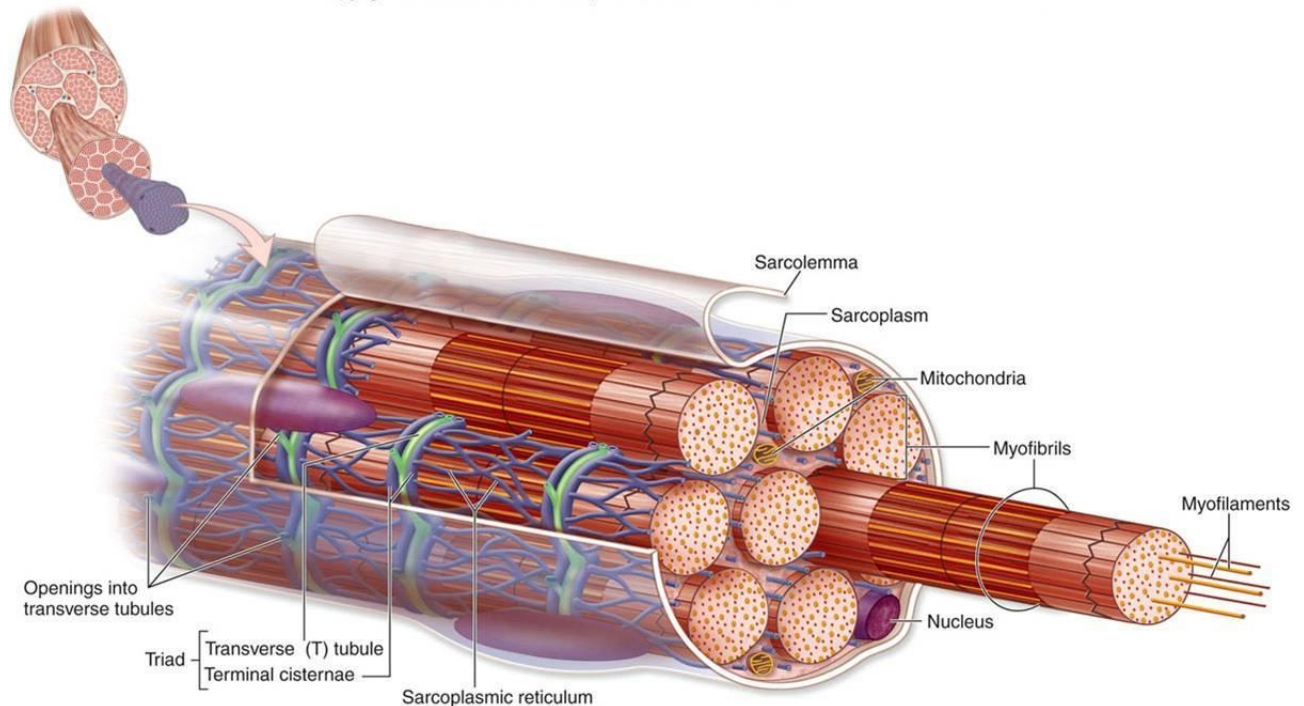


Figure 1.6: Muscle fiber structure (photo created by © Benjamin Cummings, Addison Wesley Longman Inc 2001).

muscle tissue. At the resting position, a sarcomere has a length of about  $2.2 \mu\text{m}$ . The length of the muscle fiber depends on the number of sarcomeres in series that comprise it [29]. For example, a muscle fiber from the BB can contain up to 100000 sarcomeres. Each muscle fiber is surrounded by a plasma membrane called sarcolemma. The extension of the sarcolemma between the muscle cells is a transverse tubules called T tubules. These extensions are perpendicular to the fiber length as shown in Figure 1.6 and have the role of conducting electrical impulses deep into the muscle fiber.

### Motor Unit (MU)

In the skeletal muscle, the muscle cells (fibers) contract in troops never as an independent entity. These groups of muscle fibers contracting at the same moment are innervated by the same motoneuron [5]. Accordingly, this motoneuron along with its axon, terminal branches and all the muscle cells innervated by these branches compose the Motor Unit (MU) (see Figure 1.7).

The motoneuron called  $\alpha$ -motoneuron is the point of summation for the voluntary and the reflex inputs [2]. In fact, the final membrane current brought by the synaptic innervation sites at this  $\alpha$ -motoneuron decides the activity of the MU [2]. The MU is considered to be the functional unit in a striated muscle as all the corresponding fibers contract almost as one, following an impulse in the associated nerve. The number of MUs in the muscle has always been an ambiguous issue for the anatomists, therefore they estimated this number using various methods. This number can vary between 100 MUs for the smaller hand muscles

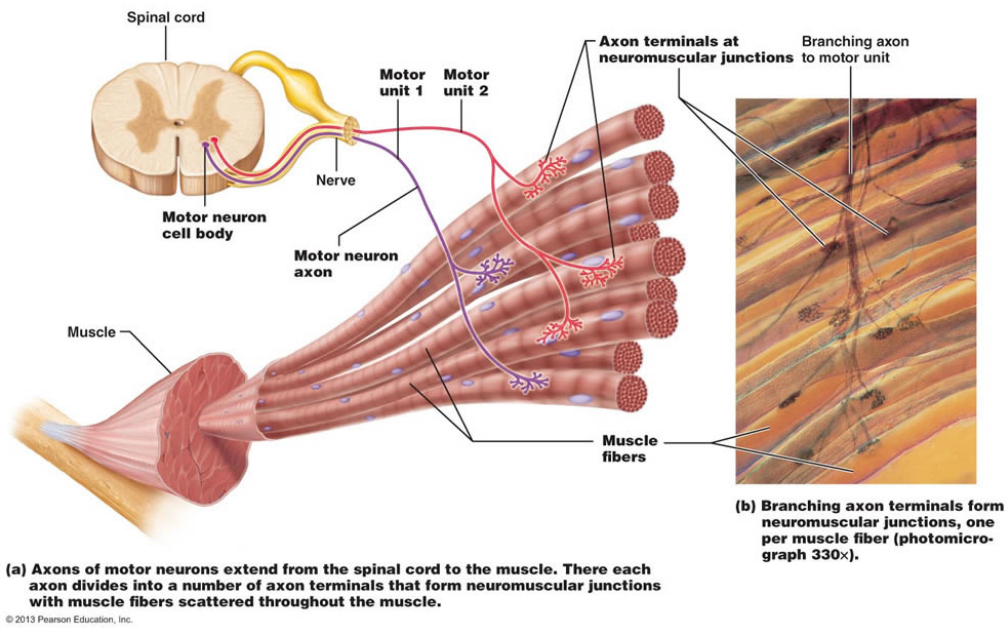


Figure 1.7: Motor Unit (MU) illustration from © Pearson Education Inc 2013.

and 1000 MUs for bigger leg muscles [29]. For example, the number of MUs in the BB muscle has been approximated to 770 MUs in [32]. The MUs in the skeletal muscles have a wide range of physiological properties similar to the vast morphological and electrophysiological properties of the corresponding motoneurons. Therefore, a distinct motoneuron and the corresponding MU that it innervates have similar biochemical, histochemical and contractile properties [2]. However, the classification of the MUs following their physiological properties is a laborious task [29]. As a result, all studies try to identify the muscle fiber populations in the muscle's cross section by studying their histochemical criteria. Figure 1.8 shows the histochemical typing in a human deltoid muscle. Hence, MUs are classified based on the properties

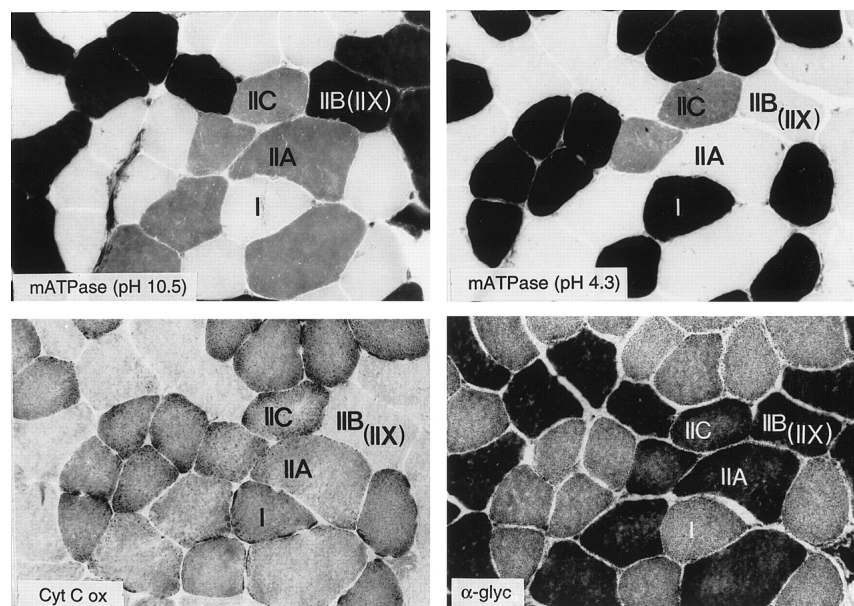


Figure 1.8: Four cross sections of the deltoid muscle showing different myofibrillar ATPase reactions, illustrating the morphological typing of muscle fibers [11].

of their muscle fibers [33]. These properties and fiber types are presented in the following paragraph.

### Types of fibers

As described in the previous paragraph, the skeletal muscles are heterogeneous structures that possess great adaptation abilities. These muscles contain several types of muscle fibers which are classified into two main categories, type I or slow twitch fibers and type II or fast twitch fibers that are presented in Figure 1.9. Where all fibers innervated by the same  $\alpha$ -motoneuron are of the same type.

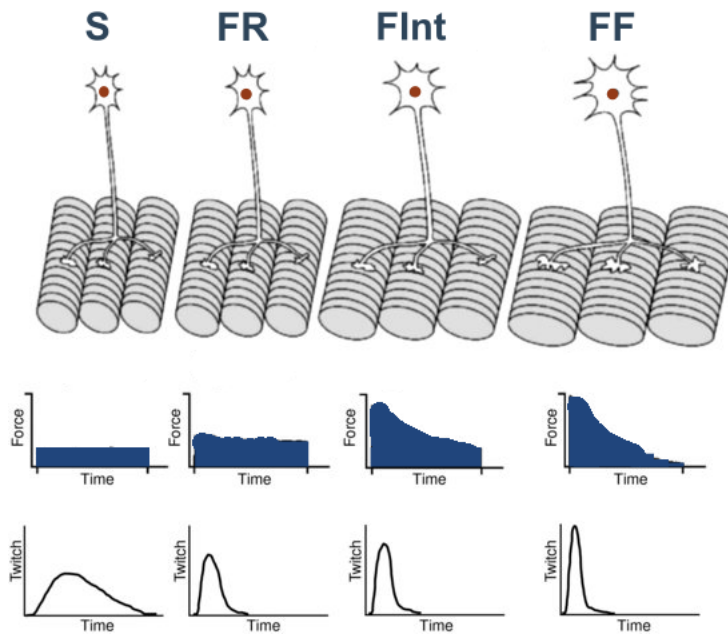


Figure 1.9: Illustration of the muscle fibers characteristics according to their types [12].

- Type I fibers are characterized by a low force, power and speed production but an important endurance. They have smaller diameter but a higher mitochondrial and capillary density, and a higher myoglobin content. That's why they have darker coloration (red). These fibers have slow twitch response (slow contraction) and a slow fatiguability. They contain enzymes involved in the oxidative pathways (Krebs cycle, electron transport chain). From the activity point of view, these fibers are used in low force level requiring activities like maintaining posture, walking and daily activities. The MUs that contains these types of fibers are called Slow MUs (SMUs) [2, 5].
- Type II fibers are described by having a high force production but low resistance to fatigue. They have bigger diameter than the type I fibers but less myoglobin content. Therefore, they are lighter in color. They also have higher rates of calcium release by the sarcoplasmic reticulum and by myosin-ATPase enzyme activity that breaks down Adenosine Triphosphate (ATP) inside the myosin head of the contractile proteins [2, 5]. This type of fibers can be further sub-classified into three classes:

1. Type IIA: These fibers have similarities with the type I fibers, from the fact that they are relatively more resistant to fatigue than other type II fibers. They also have more mitochondrial, capillary and myoglobin numbers. The associated MUs are called Fast Resistant MUs (FRMUs);
2. Type IIB: These fibers resembles mostly the type II description, having high force production, fast contraction velocity and very low resistance to fatigue. The corresponding MUs are called Fast Fatigable MUs (FFMUs);
3. Type IIX: The MUs consisting of this fiber type are called Fast Intermediate (FIntMUs). This means that they are intermediate between the FF and the FR type.

All these fiber types are presented in Figure 1.9 with a summary of their characteristics presented in Table 1.1.

Table 1.1: Summary of the differences in skeletal muscle fiber types (Table adapted from [19]) .

	S	FR	FInt	FF
Contraction speed	Slow	Moderate fast	Fast	Very fast
Resistance to fatigue	High	Fairly high	Moderate	Low
Activity	Aerobic	Long-term anaerobic	Short-term anaerobic	Short term anaerobic
Maximum contraction duration	Hours	Less than 30 minutes	Less than 5 minutes	Less than one minute
Power produced	Low	Medium	High	Very High
Mitochondrial density	Very high	High	Medium	Low
Capillary density	High	Intermediate	Low	Low
Oxidative capacity	High	High	Moderate	Low
Major storage fuel	Triglycerides	Creatine phosphate, glycogen	ATP, creatine phosphate, glycogen	ATP, creatine phosphate
Properties	Consumes lactic acid	Produce lactic acid and creatine phosphate	Consume creatine phosphate	Consume creatine phosphate

### 1.2.1 Mechanism of muscle contraction

In this part, we will introduce the mechanisms of muscle contraction starting from the sliding filament theory and the cross-bridge theory to the generation and propagation of AP in the fibers.

The leading contribution to the understanding of muscle contraction mechanism was brought by Huxley in the early 50's [34, 35]. He introduced what we call the sliding filament theory of muscle contraction. In reality, a muscle fiber contracts following two phases: muscle fiber stimulation phase and excitation-contraction phase. The block diagram of the contraction mechanism is presented in Figure 1.10. Accordingly, a muscle fiber excitation starts by a stimulation with an AP at the terminal of a

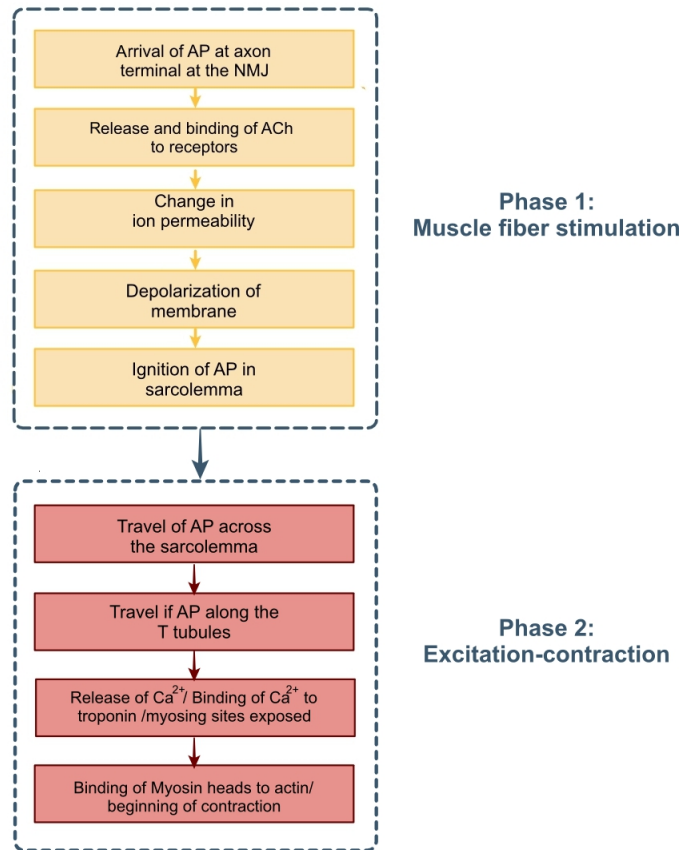
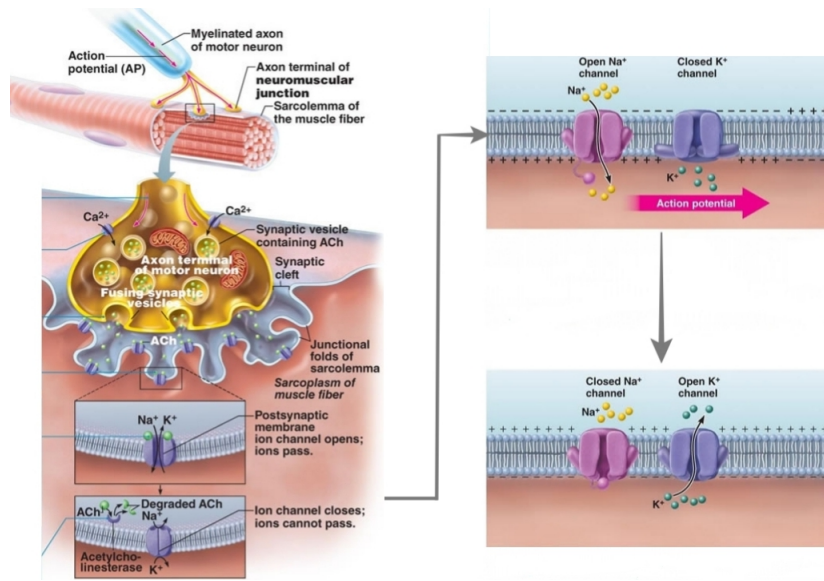


Figure 1.10: The block diagram describing the muscle fiber contraction mechanism.

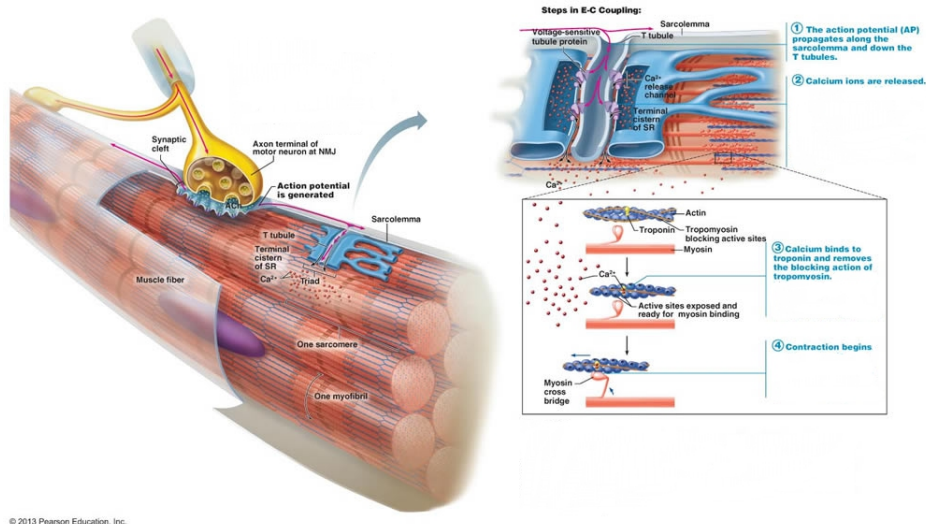
motoneuron's axon. This phenomenon is presented in Figure 1.11a where the Calcium ( $Ca^{2+}$ ) dynamics are exhibited.

Wherefore, the muscle fiber excitation phase starts by the arrival of AP at the axon's terminal which causes the release of Acetylcholine (ACh) following the penetration of  $Ca^{2+}$  ions in the axon's terminal. Then, the ACh binds to the sarcolemma receptors which induces the opening of ion channels. In consequence, Sodium ( $Na^{2+}$ ) ions enters and Potassium ( $K^+$ ) ions exits the muscle fiber. This variation in the ions concentrations changes the membrane potential (end plate potential) which causes the depolarization of the membrane and the propagation of the AP at the sarcolemma. The second phase of muscle contraction, the excitation-contraction phase, is illustrated in Figure 1.11b.

Following the propagation of the AP along the sarcolemma, the AP travels down the T tubule where the voltage sensitive proteins lead to the opening of  $Ca^{2+}$  channels and the releasing of  $Ca^{2+}$  in the sarcoplasmic reticulum. Thus, the  $Ca^{2+}$  ions concentration in the sarcoplasmic reticulum increases and the  $Ca^{2+}$  ions start to bind to the troponin of the actin filaments (see Figure 1.11b). When the  $Ca^{2+}$  binds to the troponin, it causes it to change shape exposing binding sites for myosin and the sliding filaments phenomenon responsible for muscle contraction begins [36, 37].



(a) The calcium dynamics at the terminal-sarcolemma border.



(b) The dynamic of AP propagation in the fiber.

Figure 1.11: The mechanism of muscle contraction (image from © Pearson Education, Inc, 2013).

As mentioned before the sliding filament theory introduced by Huxley [38] is the essence of muscle contraction where the shortening of muscle fibers is induced by the sliding of actin filaments changing the fiber length. It also describes in details the formation of cross bridges from the binding of energized myosin heads to actin filaments. The binding of myosin head to the actin filament induces the release of adenosine diphosphate (ADP) and phosphate. Sequently, the myosin head pulls the actin filament towards the M line. Then, the myosin head detaches from the actin filament when an adenosine triphosphate (ATP) is attached to the myosin. Ultimately, the ATP is hydrolyzed into ADP and phosphate and the myosin head retakes its original position. This cycle is presented in Figure 1.12.

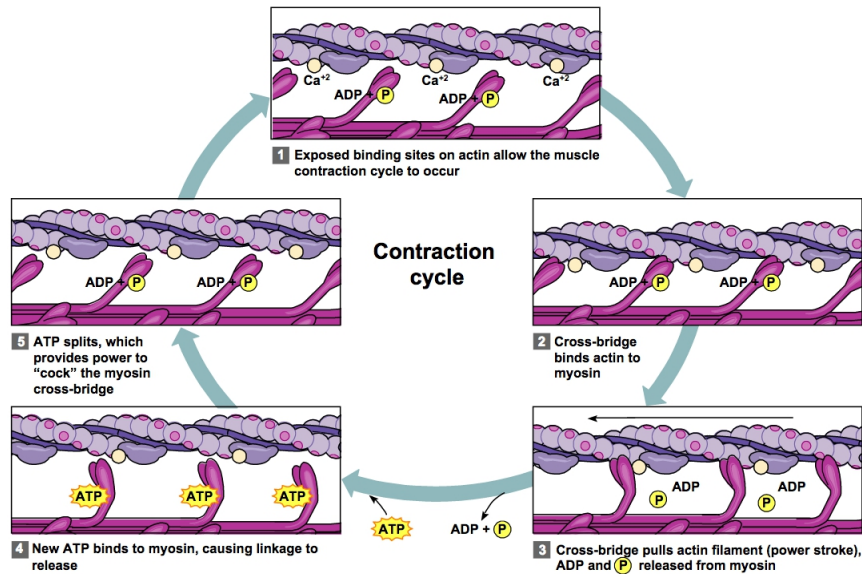


Figure 1.12: The steps of the sliding filaments phenomenon during muscle contraction (image from © McGraw Hill, Inc).

### 1.2.1.1 Generation and propagation of fiber action potential (FAP)

The generation of the AP starts at the axon terminal and sarcolemma interface called the Neuromuscular Junction (NMJ). As described in the previous paragraph, when a neural AP arrives at the NMJ, it causes the change of ion concentrations at the membrane of the fiber (sarcolemma). In the case where this AP exceeds a certain threshold, it results in the depolarization of the fiber’s membrane causing the generation of an AP at the sarcolemma. This AP changes quickly from  $-70\text{ mV}$  to  $+30\text{ mV}$  (see Figure 1.13).

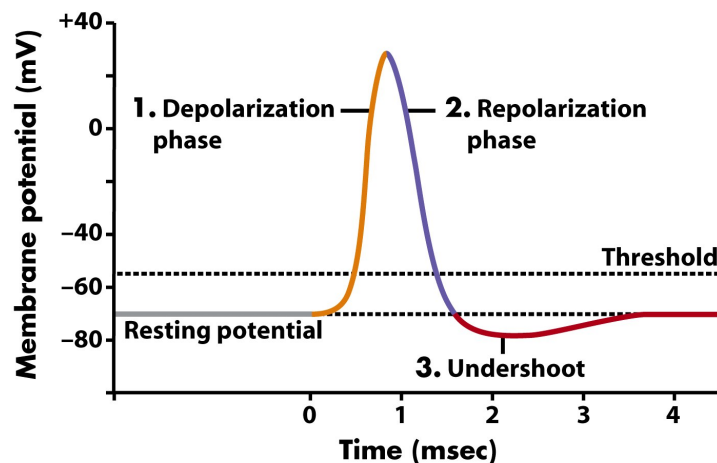


Figure 45-5 Biological Science, 2/e © 2005 Pearson Prentice Hall, Inc.

Figure 1.13: Action potential (image from © Pearson prentice Hall, Inc 2005).

This depolarization is expressed by an outburst of monopolar electric tension that induces the muscle contraction. This is followed by a repolarization state where the membrane’s potential regains its original

potential of  $-70\text{ mV}$  and the muscle contraction ends. This repolarization is caused either by cessation of signals from the motoneuron or a lack of ATP caused by fatigue. Eventually, the potential is stable after an undershoot state due to the recovery of the ion concentrations in the membrane by the active pumping mechanism [31]. This FAP propagates along the fiber length in the two directions with a velocity that lies between 2 and 6  $m/s$  and an intensity of  $\sim 100\text{ mV}$  [31, 37].

### 1.2.1.2 Different types of muscle contraction

The muscle contraction type is usually divided into two main classes based on muscle length variation [39]:

- Isometric contraction, during which the muscle length does not change when the muscle generates tension. However, we can also observe changes in the muscle shape due to the shortening of the contractile element.
- Anisometric contraction also called dynamic contraction, implies that the muscle length changes during the contraction causing also a deformation of the muscle shape due to both length variation of the contractile element and the tendons. This type can be further broken down into two subtypes:
  - Anisometric eccentric contraction which is described by a lengthening of the muscle during contraction.
  - Anisometric concentric contraction which is distinguished by a shortening of the muscle during contraction.

From the point of view of the produced force we can differentiate between:

- Isotonic contraction: which is the type of contraction obtained when the generated force does not change along the contraction time.
- Anisotonic contraction: which is attained when the generated force changes all along the contraction.

In this thesis work, the proposed studies in both simulation and experimentation will concern isometric isotonic and anisotonic contractions.

## 1.2.2 Surface Electromyogram (sEMG)

The first study of EMG was achieved in 1912 in Germany by H. Piper, where he used a string galvanometer to measure the EMG [5]. Afterwards, during the 20's similar studies appeared by different researchers among which the concentric electrode technique was introduced [40]. This impressive tool

employed by Adrian and Bronk [40] is still used until nowadays. Then, through the 50's and 70's major contributions were achieved including the quantitative analysis of the Motor Unit AP (MUAP) which will be explained in the following paragraph, EMG decomposition techniques and EMG amplitude analysis. Thereupon, the sEMG was introduced as a non invasive technique that has the advantage of detecting the MUAP activity in a large volume as opposed to the needle EMG technique that detects the MUs activity in a small volume near the needle's tip. The first team to use the sEMG technique was Hardyck and his researchers in 1966 [41]. Subsequently, in the following years the use of sEMG technique was radiated by many hundreds of papers. And nowadays, Basmajian's book, "Muscles alive", remains the ultimate reference on sEMG technique [5]. Despite the fact that the sEMG signal is a stochastic and often non stationary signal, many applications have been rising since the last decade [26, 42, 16, 43] indicating its ability to asses the functional behaviors of skeletal muscles. However, this technique suffers from limitations that have to be carefully taken into account such as spatial filtering of living tissues and electrodes. In addition to the auto-cancellation phenomenon that can lead to a misestimation of the muscle activation [7, 44].

### 1.2.2.1 Motor Unit Action Potential (MUAP)

As explained in section 1.2, the MU consists of a  $\alpha$ -motoneuron and the group of fibers by which they are innervated. Therefore, when this MU is recruited all the fibers are activated almost instantly. The electrical result of this recruitment is an electrical discharge with an amplitude that can be evaluated in  $\mu V$  (using needle electrodes) and a duration of about 9 msec [5]. Indeed, the potential resulting from corresponding fiber responses of a MU is called MUAP. The shape and the amplitude of this MUAP depends on several parameters that will be discussed later on. Beyond recall, the summation of these MUAP generates the EMG signal as portrayed in Figure 1.14.

The sEMG is a noninvasive technique to measure the electrical activity of a muscle on the surface of the skin. The obtained sEMG signal is the summation of MUAP corresponding to the activated MUs detected by an electrode placed on the surface of the skin (see Figure 1.15). Thus, in this thesis we will focus on sEMG signal analysis since it contains information about the MU recruitment process, AP characteristics, that are influenced by anatomical and physiological parameters [45], and is also correlated to the mechanical response of muscle activation, i.e the muscle force.

### 1.2.2.2 Motor Unit recruitment and firing (Rate coding)

When a muscle is voluntarily activated, the sEMG signal and the produced force are modulated by two major mechanisms: the spatial MU recruitment (number and localization) and the MU rate coding (firing rate variation) [2]. Actually, the force and the sEMG amplitude increase when the number of

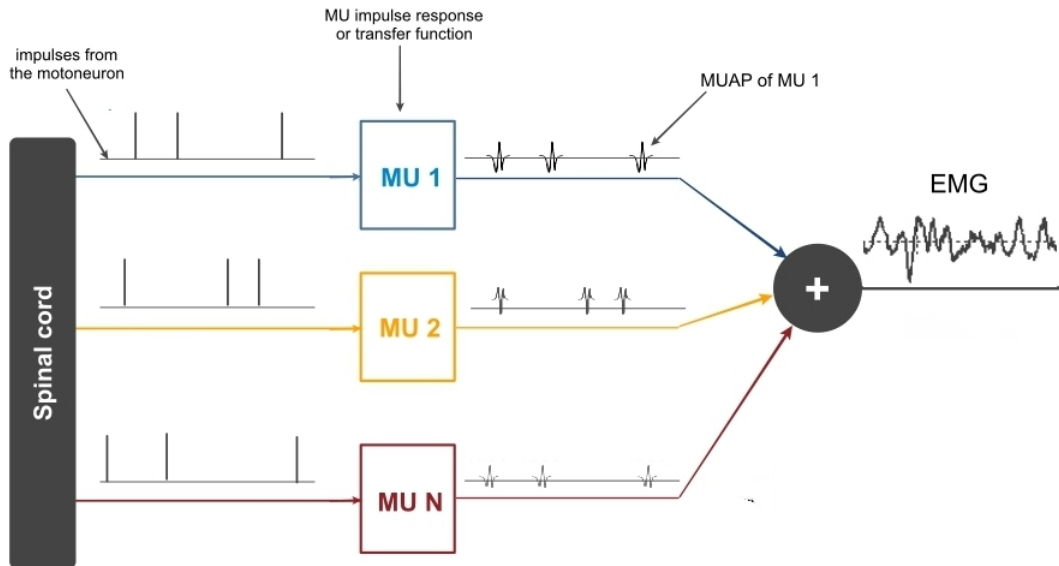


Figure 1.14: EMG generation during voluntary contraction.

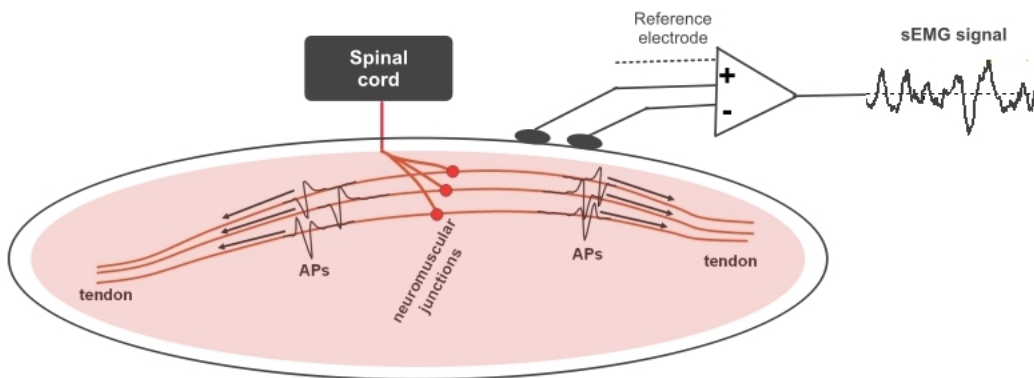


Figure 1.15: EMG generation during voluntary contraction.

recruited MU and their firing rate increase [2]. Clearly, these two mechanisms depend mainly on the contraction level and speed (in the dynamic case). A low contraction level implies a low recruitment threshold for the MUs. These MUs are typified as low force generation MUs (SMU) that are resistant to fatigue. However, a high contraction level suggests that additional MUs are recruited. These MUs are much more fatigable and have a higher force response (FFMU).

The MU recruitment depends on the level of contraction and is based on the “size principle” defined by Henneman in [46], which evidenced that the recruitment of MUs is done through increasing motoneuron and MU size [46, 47]. This size based recruitment is often referred to as the “orderly recruitment” [48, 2]. It was evidenced that the MU recruitment law, which described the evolution of the recruitment threshold with contraction level, is exponential [49]. At a certain contraction level that varies between 60 and 85 % of the maximum voluntary contraction (MVC) depending on the muscle characteristics [45, 49], all MUs are recruited. Beyond this contraction level only increasing MU firing rate can influence the resulting

force and sEMG signals.

When recruited, a MU's motoneuron discharges, following random point processes, at a minimal frequency that increases with force level increase following a certain strategy [49]. In the literature, recent studies defined different types of firing rate strategies [13, 49]. These strategies vary between linear and nonlinear with similar or different minimal and maximal discharge frequencies [50, 45, 49, 51]. The MU firing regularity can be assessed by analysis of the Coefficient of Variation (CoV) of the Inter Spike Intervals (ISIs), corresponding to elapsed time between two successive firings, that is supposed to respect a Gaussian distribution.

### 1.2.2.3 Discharge frequency and generated force

The force frequency relationship has different characteristics [29] that depends on the MU type and other circumstantial properties like the muscle's prior activity and temperature. These characteristics are:

- Fusion frequency which is the lowest frequency at which there is no oscillations in the force
- Peak force which is the maximal obtained force
- Tetanic force ratio which is the ratio of the developed force of a twitch to the peak force

### 1.2.2.4 Electrode configurations and spatial filtering

The electrodes usually used in surface electromyography are simple silver chloride discs of different sizes. Their main advantages are being noninvasive and convenient for use without giving discomfort to the subjects. One thing that should be verified is a correct electrical conduction between the skin and the electrode. This should be thoroughly prepared by removing first the dead cell layer and the oils of the skin in order to have reduced skin-electrode interface impedance of  $\sim 3 K\Omega$  [5]. This can be achieved by providing sufficient quantity of conductive gel between the electrode and the skin.

A sEMG signal is called monopolar when it is recorded using differential amplifier by measuring the difference between two signals; a first signal recovered by a surface electrode placed on the surface of the skin above a certain muscle (active electrode) and the signal recorded by an electrode placed in a neutral position (reference electrode). This arrangement has the largest detection volume compared to the others [5]. In the case where two electrodes connected to the differential amplifier are placed on the skin over the muscle, the sEMG signal is called bipolar (see Figure 1.16). The bipolar installation of the acquisition system has a filtering effect on the obtained sEMG signals [52]. This filtering effect causes a reduction of the detection volume by altering the spatial selectivity of the electrode system [53, 10].

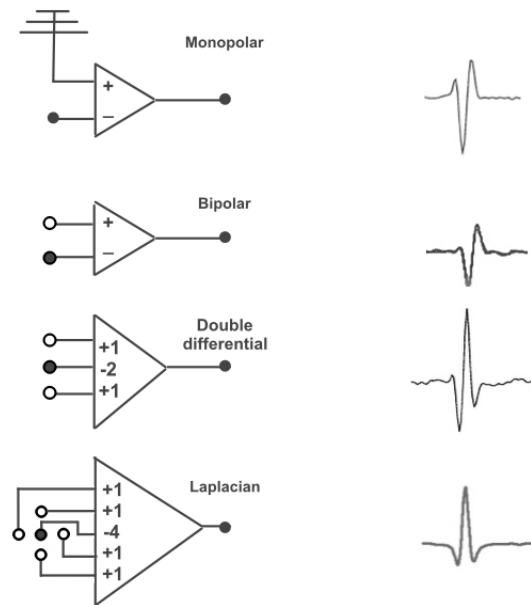


Figure 1.16: Different electrode configurations and the corresponding recorded MUAP.

Other electrode setups are used such as the double differential and the Laplacian configurations (Figure 1.16). The Laplacian configuration presents the advantage of filtering the non propagating component in the sEMG signal. This non propagating component is due to the extinction of the transmembrane currents at the tendon. It is important to note that the detection volume depends largely on the electrode configuration since when the filtering order increases the volume detection becomes smaller and the signal amplitude decreases. Finally, in order to record an sEMG with an excellent quality there is a number of factors to consider like the electrode configuration, the electrode placement on the surface of the skin and electrodes alignment with respect to the direction of fibers [54, 55].

#### 1.2.2.5 sEMG signal Processing

As previously described, muscle contraction is a consequence of physical and chemical sequence of events that the signal processing of sEMG is expected to qualify and quantify. Among the many information contained in the sEMG signal, we can register anatomical facts like the location and the shift of the NMJ [56, 57], mechanical information [26, 42, 16] and fatigue evaluation [58, 59]. Moreover, a direct relationship exists between the sEMG and the exerted force [2, 60]. This technique has been also extensively used in a variety of applications; in kinesiology, sEMG is often used in the control of prosthetic devices for individuals with amputations or congenitally deficient limbs [61, 43, 62], in rehabilitation and in biofeedback experiments [63]; in biomechanics, for the estimation of muscle activation, neural command [64], muscle force and moments [65, 59]; in clinical neurophysiology, for the estimation of nerve conduction variables [66], anatomical properties of the muscular tissue [65] and the study of motor unit behavior [59, 67].

### 1.2.2.6 Basic signal processing of the sEMG signal

Usually the sEMG signal is processed either in the time or the frequency domain before it is exploited. Some of the most popular parameters are:

In the time domain, the parameters allowing quantification of the activation level are:

- The integrated EMG (iEMG) which is the integral of a rectified digitized signal  $x_i$  during a period of time corresponding to  $N_{tot}$  samples:

$$iEMG = \sum_{i=1}^{N_{tot}} |x_i| \quad (1.1)$$

- The Averaged Rectified Value (ARV) that corresponds as its name indicates to the average of the rectified values of a sEMG signal  $x_i$  during a segment of time corresponding to  $N_{tot}$  samples. It is expressed by the following equation:

$$ARV = \frac{1}{N_{tot}} \sum_{i=1}^{N_{tot}} |x_i| \quad (1.2)$$

- The Root Mean Squared (RMS) value that correlates with the signal power. It is computed using the equation below:

$$RMS = \sqrt{\frac{1}{N_{tot}} \sum_{i=1}^{N_{tot}} x_i^2} \quad (1.3)$$

In the frequency domain, the spectral parameters are based on the Power Spectral Density (PSD) of the sEMG signal expressed by [2]:

$$S(e^{k\omega}) = \sum_{\tau=-\infty}^{+\infty} r(\tau) \cdot e^{-jk\omega} \quad (1.4)$$

Where  $e^{-jk\omega}$  ( $\omega = 2\pi f$ ) is the  $k^{th}$  sinusoidal harmonic and  $r(k)$  is the autocorrelation function expressed as:  $r(\tau) = E[x(k+\tau)x(k)]$ .

The power of the sEMG signal is generally comprised between 5 and 500  $Hz$  with the primary energy contained in 50-150  $Hz$  portion [58]. The change in the spectral content of the EMG signal is usually tested using frequency parameters such as:

- The modal frequency  $f_{mod}$  presenting the frequency corresponding to the maximum PSD in the signal defined by:

$$Max(S) = S(f_{mod}), f_{mod} > 0 \quad (1.5)$$

- The median frequency  $f_{med}$  presenting the frequency that breaks the PSD in two parts with equal power. It is expressed by [68]:

$$\sum_{k=1}^{f_{med}} S_k = \sum_{k=f_{med}}^{F_{tot}} S_k \quad (1.6)$$

With  $F_{tot}$  is the total number of samples in the frequency domain.

- The mean frequency  $f_{mean}$  presenting the ratio of the first spectral moment with respect to the signal power. It is computed using the following equation [68]:

$$f_{mean} = \frac{\sum_{k=1}^{F_{tot}} f_k S_k}{\sum_{k=1}^{F_{tot}} S_k} \quad (1.7)$$

With  $f_i$  is the frequency value at the  $i^{th}$  sample.

### 1.2.2.7 Elements affecting the sEMG signal

As described earlier, the sEMG signal reflects the process of MU recruitment in addition to the MUs characteristics. Nevertheless, the amplitude and spectral content of the sEMG signal depend on different factors that can lead to misinterpretation of the measured signals. These factors were targeted in details by De Luca [6]. They are illustrated with a schematic diagram in Figure 1.17 and are grouped by De

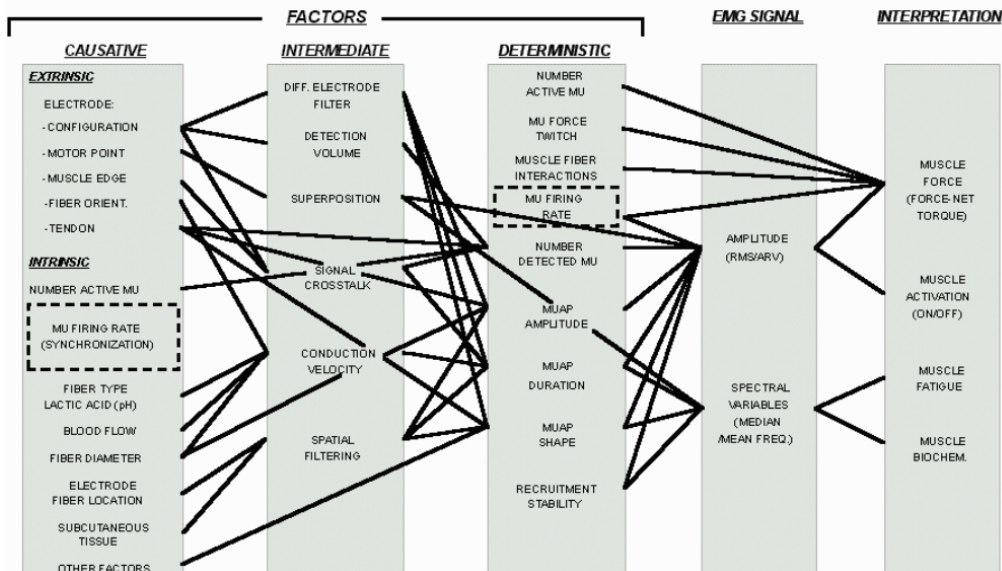


Figure 1.17: The factors affecting the sEMG signal [6].

Luca into three categories:

- Causative factors that elementary influences the signal and are further branched into two classes:

- Extrinsic causative aspects are related to the electrode structures and their positions on the skin. A few of these factors are:
  - \* The electrodes configuration (size and arrangement);
  - \* The electrodes positions with respect to the NMJ and other muscles;
- Intrinsic causative aspects are connected to the physiological, anatomical and biochemical properties of the muscle like:
  - \* The type distribution of fibers composing the muscle;
  - \* The depth and the diameters of the fibers in the muscle;
  - \* The conjunctive tissue that separates the muscle and the electrode (skin and adipose tissues thickness);
  - \* The blood flow in the muscle;
- Intermediate factors which represent physical and physiological phenomena influenced by causative factors and influencing in their turn the deterministic factors. Some of these factors are:
  - FAP conduction velocity;
  - Spatial filtering effect due to the electrode position;
  - MUAP superposition and auto-cancellation phenomenon;
  - Electrode detection volume;
- Deterministic facts that have direct impact on the information present in the sEMG signal and the obtained muscular force. Among these factors:
  - The active MU number;
  - MU force or twitch;
  - Mechanical interaction between fibers;
  - MU discharge frequency;
  - The number of detected MUs;
  - MUAP amplitude and duration;

All these parameters have to be taken into account when designing any experimental protocol and analyzing the obtained results to avoid possible misinterpretation.

### 1.2.3 Muscle force generation

In this section, we will introduce the generation of the other consequences to muscle activation, in complement to the electrical response (EMG signal), which is the muscle force. First, we will explain the contractile response of a MU then we will discuss the genesis of the global force and the parameters influencing this force.

#### 1.2.3.1 Twitch generation and summation of twitches

The twitch is the elementary contractile event. It is the mechanical response i.e. contractile force (in Newton) of a single MU to a neural stimulus from the corresponding motoneuron (in the voluntary case). The shape of the twitch is presented in Figure 1.18a. By looking at Figure 1.18a, we can note different stages of this contractile response: stimulus is sent, start of contraction (time delay to the stimulus), contraction phase and relaxation phase.

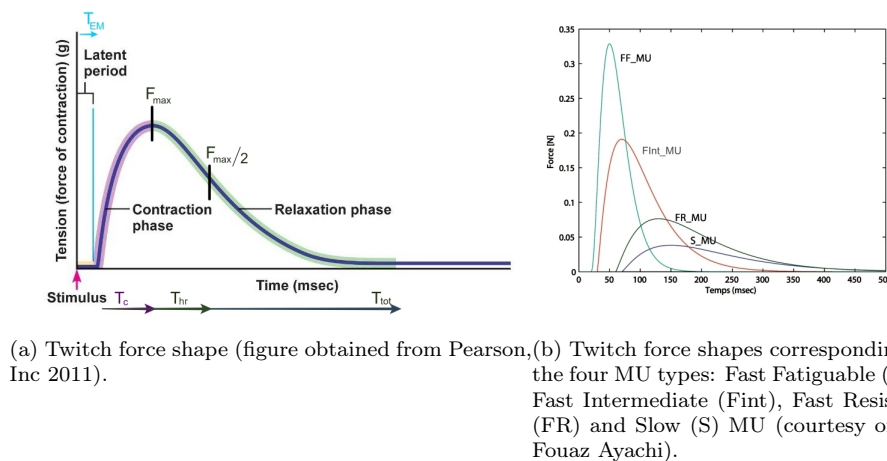


Figure 1.18: Twitch force shape and parameters and twitch shape variation according to the MU type.

The delay between the detection of the AP and the start of the contraction or force development is called the electromechanical delay [29]. It is due to the time needed to conduct the AP into the T tubule and release  $Ca^{2+}$  ions into the cytoplasm in order to initiate the cross-bridge cycle after the binding of  $Ca^{2+}$  ions on the troponin (see section 1.2.1). Furthermore, we have to note that the contraction and the relaxation durations depend on the MU type [20, 69, 70] (see Section 1.2). Thus, the shape of the twitch as well as its parameters changes with respect to the MU type as illustrated in Figure 1.18b. Where  $T_{EM}$  is the electromechanical delay between the time the stimulus is sent and the start of the contraction,  $T_c$  is the contraction time between the start of the contraction and when it reaches its maximum value  $F_{max}$ ,  $T_{hr}$  is the duration between the start of the contractile response and the moment the force decreases to half of the maximum value and  $T_{tot}$  is the total duration of the contraction.

Whenever another stimulation is exercised before the end of relaxation of the previous twitch response, we obtain a twitch summation. This results in an unfused tetanic force as shown in figure 1.19. The

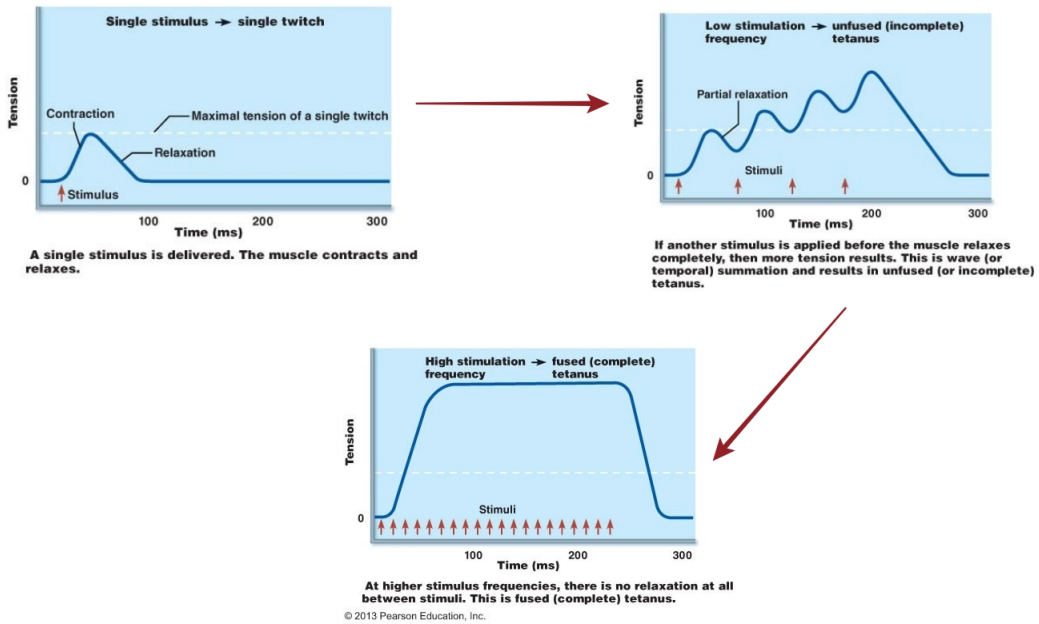


Figure 1.19: Tetanic force generation during voluntary contraction (figure from © Pearson Education, Inc 2013).

obtained peak force depends on the MU type and firing rate. When the firing rate is sufficiently high in order to obtain a force plateau, we have what we call a fused or a complete tetanic force (figure 1.19). Thus, the total force produced by a muscle is the summation of the contractile response of all the activated MUs as presented in Figure 1.20. As mentioned before the contraction level depends on two major factors: the spatial recruitment and the firing rate of MUs. The spatial recruitment of MUs based on the size principle has been discussed earlier (Section 1.2.2.2). Thus, we will focus on the relation between the discharge frequency and the generated force.

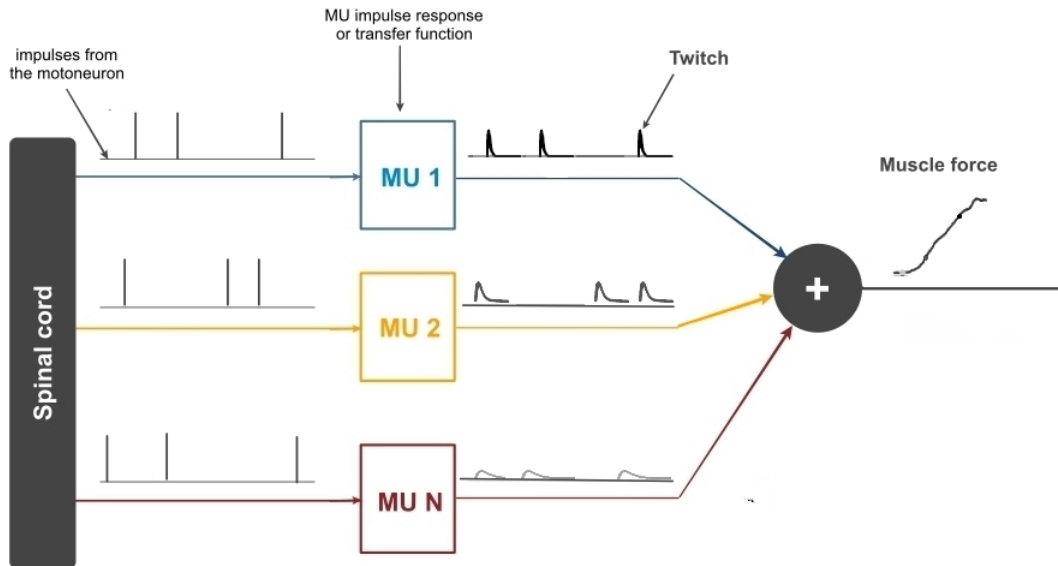


Figure 1.20: Muscle force generation from the superposition of MU twitches.

### 1.3 EMG driven force estimation models

The estimation of the force generated by an individual muscle is of high importance in many fields such as clinical applications for diagnosis and treatment purposes, biomechanical studies for prosthesis control and kinesiology applications for rehabilitation purposes [43, 71, 72, 73]. Several force estimation techniques exist in the literature. Figure 1.21 presents a mind mapping of these different techniques.

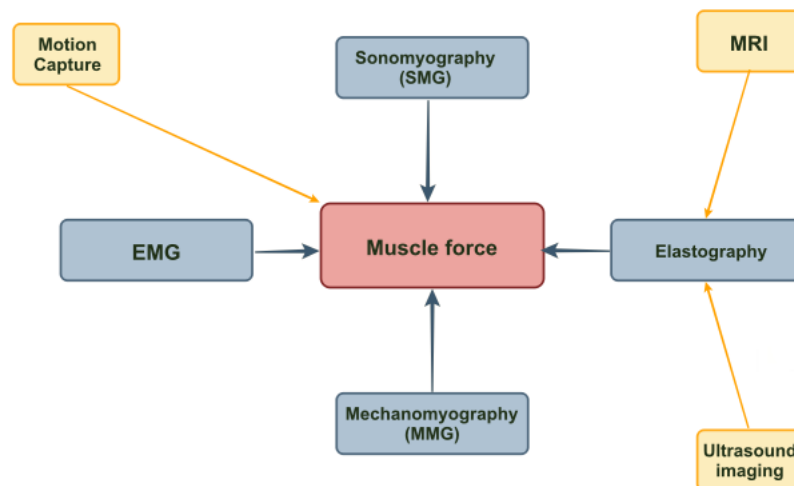


Figure 1.21: Mind mapping of the techniques used for muscle force estimation.

Among these methods, we have the Mechanomyogram (MMG) which is a signal that represents the muscle oscillations on the surface of the skin caused by the change in the muscle shape during con-

traction [74]. This techniques has been used in muscle force estimation [75, 74, 76] but its validation is questionable. Another force estimation method would be based on the Sonomyography (SMG) technique, which represents the continuous capturing of ultrasound images of the muscle. It aims at tracking the morphological variation of the muscle with muscle force variation [77, 78, 79]. This technique is similar to the elastography technique which measures the elasticity variation of the muscle using various techniques like MRI or ultrasound based elastography [80, 81] and supersonic shear imaging [4]. One of these elastography based force estimation models that is worth mentioning is that of Bouillard et al. [4]. It is the only study where they successfully measured the individual muscle force of two muscle fingers, the abductor digiti minimi and the first dorsal interosseous, during abduction by using both supersonic shear imaging and sEMG. But although this study was really innovative, it supposes a linear relationship between the RMS and the muscle force which is not true in many conditions (see section 1.3.1). Also, it only applies to specific muscle architecture (intrinsic hand muscles). Lastly, a new motion tracking technique that is popular mainly in the entertainment industry, the Motion Capture (MoCap) technique, was also proven to be an efficient tool to track the muscle force variation through measuring the surface deformation of the muscle [82]. However, the sEMG based estimation models remain the most popular and effective force estimation models out there since it was evidenced that, under isometric static contractions, it can give a viable measurement of the force output [7]. This can be justified by the strong link between the sEMG and the force produced by a singular muscle since they are driven by the same recruitment pattern. Thus, in this section, we will carry out the state of the art for the sEMG based force estimation models present in the literature. All these models can be classified into three main types: phenomenological, physiological and regressive type models.

### 1.3.1 sEMG/force relationship

The sEMG/force relationship has been the focal point of inspection for researchers since the early 70s [83, 5]. The reason behind this grown interest in this relationship is motivated by the fact that understanding this relationship can contribute to a great extent in the force estimation and modeling paradigms. Thus, a number of studies attempted to discover the shape of this relationship. Some of these studies found it to be linear for small muscles, such as the first dorsal interosseous, and nonlinear for larger muscle, such as the BB and the deltoid [84]. However, these results were obtained using bipolar electrodes, which suffer from experimental issues, especially electrodes placement problems. They also consider the relationship between a certain muscle, the BB for example, and the global force measured at the elbow which is not the individual BB force but rather the summation of all muscle forces acting on this joint [85]. Despite all the later work, the relationship between the sEMG and the force of a single muscle is not well understood. Aside from these experimental studies, more recent work by Zhou and Rymer [13] used simulation in order to study the factors affecting the shape of the relationship between

the EMG of the first dorsal interosseus and the corresponding muscle force. Figure 1.22 illustrates the different relationship patterns they obtained for different linear firing rate strategies FR1 (the slope of the excitatory drive-firing rate relation was set to be the same for all motoneurons. Peak firing rate of a motoneuron was inversely proportional to its recruitment threshold), FR2 (the slope of the excitatory drive-firing rate relation of a motoneuron increased with increasing recruitment threshold. All motor units finally reached the same peak firing rate at maximum excitation) and FR3 (the slope of the excitatory drive-firing rate relation was set to be the same for all motoneurons. Peak firing rates were linked to mechanical properties of motor units) and for linear twitch-MUAP relation and square root twitch-MUAP relation [13]. They found that the nonlinear relationship is mainly affected by the relation between electrical and mechanical characteristics of MUs [13] and by the recruitment threshold range [49]. Based on these linear and nonlinear relationship hypothesis, an Botter et al. [42] tried to solve this relationship by classifying the sEMG/force relationship into three patterns (see Figure 1.23): linear, nonlinear with downward concavity and nonlinear with upward concavity. This study defines the EMG/force relationship for each muscle  $m$  by [42]:

$$F_m = x_m sEMG^{y_m} \quad (1.8)$$

with  $x_m$  and  $y_m$  are constant coefficients.

A simulation study of the sEMG/force relationship form will be presented in chapter 4, where we will study in details the effect of different neural (recruitment strategy and firing rate), anatomical (MUs type percentages in the muscle) and physiological parameters (subcutaneous tissue thickness, skin tissue thickness and muscle length) on the shape of the sEMG/force relationship, in the purpose of a more realistic modeling and estimation since there are different factors that can influence the sEMG/force relationship shape. These factors are [7]:

- The MU activation law;
- The anatomical, mechanical and electrical properties of the muscle;
- The placement of the sEMG electrodes on the surface of the skin above the considered muscle;
- The characteristics of contraction filaments;
- The morphological properties of the muscle (skin tissue thickness and adipose tissue thickness);
- The recruitment strategy and firing rate.

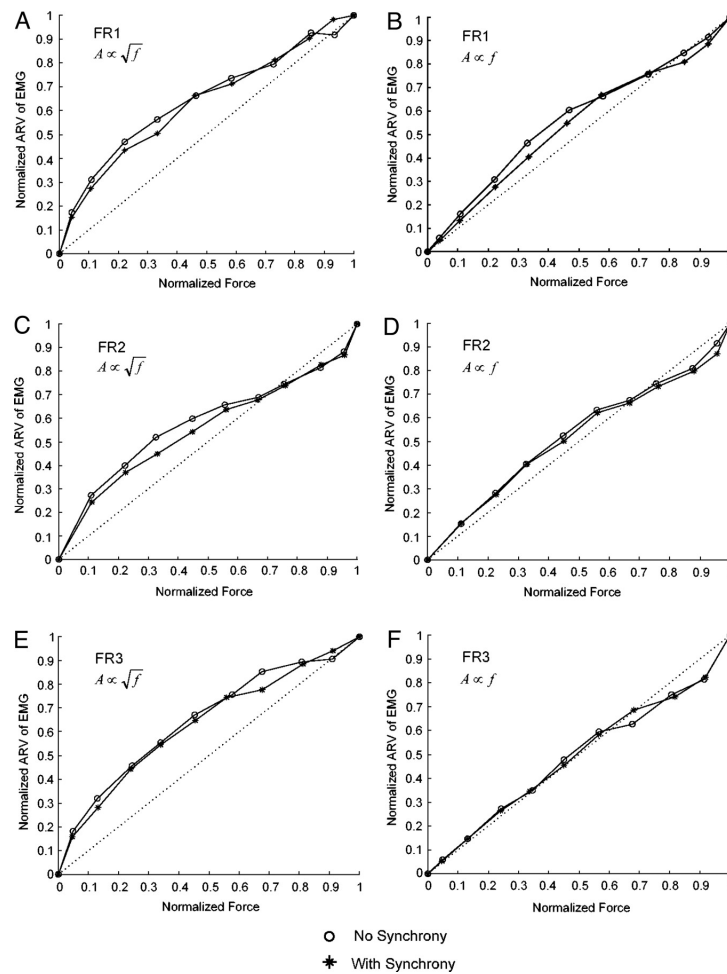


Figure 1.22: Normalized EMG/force amplitude relations using different simulations [13]. A, C, and E: simulated EMG/force amplitude relation when MUAP amplitude is proportional to square root of twitch force. A: simulated force-EMG amplitude relation derived from motor unit firing rate strategy FR1. C: simulated force-EMG amplitude relation derived from MU firing rate strategy FR2. E: simulated force-EMG amplitude relation derived from motor unit firing rate strategy FR3. B, D, and F: simulated force-EMG amplitude relation when MUAP amplitude is linearly proportional to twitch force. B: simulated force-EMG amplitude relation derived from motor unit firing rate strategy FR1. D: simulated force-EMG amplitude relation derived from MU firing rate strategy FR2. F: simulated force-EMG amplitude relation derived from MU firing rate strategy FR3. FR1, FR2 and FR3 are defined in [13].

### 1.3.2 Phenomenological models

During the past centuries, a large number of papers attempted to quantify the muscle force based on the sEMG signal. The majority of these studies are phenomenological models derived from Hill's study [86] and resumed by Zajac [26]. These studies started to appear after the first observation of the changes in the sEMG amplitude with muscle force by Inman et al. [87] and then the study of the sEMG/force relation by Bigland and Lippold [88]. Usually in these type of models, we have two major blocks [26, 89, 16, 90]:

1. Neural excitation to muscle activation;
2. Muscle activation to muscle force.

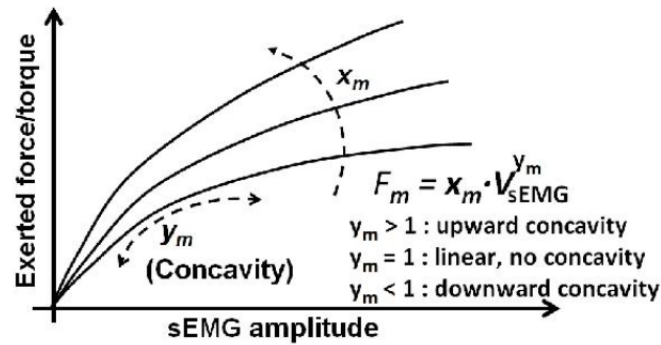


Figure 1.23: A general model that relates the sEMG of each muscle to its force [14].

These stages outline the muscle tissue dynamics and are presented in Figure 1.24.

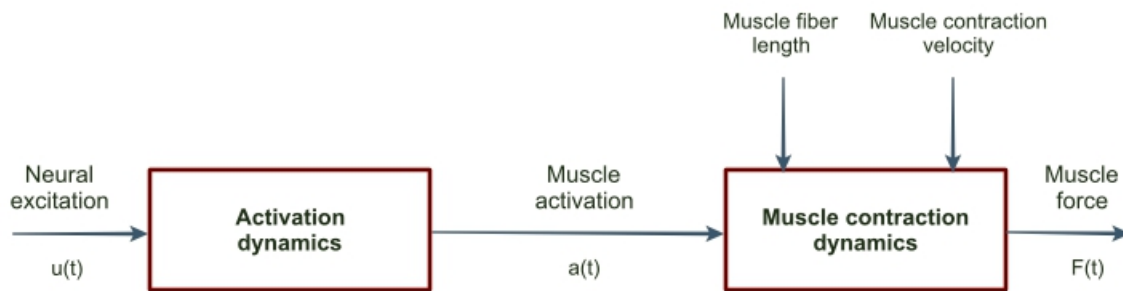


Figure 1.24: The transformation of neural excitation  $u(t)$  to muscle force  $F(t)$  by means of activation dynamics and muscle contraction dynamics.

As we can see, the first step is to transform the neural excitation  $u(t)$ , namely the neural intent to contract at a specific level, into muscle activation  $a(t)$ , namely the normalized intensity of muscle contraction, which is not a trivial task. On the contrary, it consists on several steps. Starting from the raw input sEMG signal, the muscle activation can be obtained by the steps presented in Figure 1.25. Initially, the neural excitation is obtained after removal of DC component by rectification, low-pass filtering and normalization of the raw sEMG input signal [16, 91]. The low pass filtering aims at extracting the envelope of the rectified sEMG signal. A strong hypothesis behind this approach is that the sEMG signal intensity should be correlated (hopefully, in a linear manner) with the neural intent from the CNS. The cutoff frequency is usually somewhere between 3 and 10 Hz [16]. Some studies in the literature consider this envelope, after normalization, as the muscle activation  $a(t)$  [89]. Still, even if this hypothesis could be practical under certain conditions, it is not always acceptable and pertinent. Thus, Zajac presented a detailed model of muscle activation dynamics that allows to obtain the neural activation  $u(t)$  from the processed sEMG signal  $e(t)$  [26]. He proposed a first order differential equation to model the activation dynamics. This equation is presented below [26]:

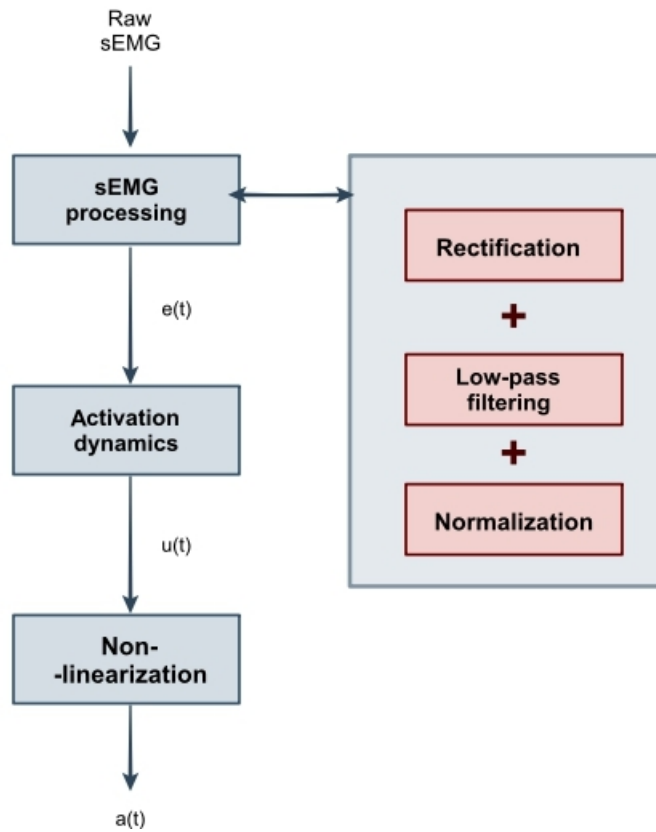


Figure 1.25: Transformation from sEMG signal into muscle activation  $a(t)$ .

$$\frac{du(t)}{dt} + \left[ \frac{1}{\tau_a} (\beta + (1 - \beta) e(t)) \right] \cdot u(t) = \frac{1}{\tau_a} e(t) \quad (1.9)$$

where  $\beta$  is a constant ( $0 < \beta < 1$ ) and  $\tau_a$  is the muscle activation delay. Additional to this first order differential equation, a second order differential equation proposed by Milner et al. [92] was found to be more convenient [16]. This equation is elaborated as follow:

$$u(t) = A \frac{d^2 e(t)}{dt^2} + B \frac{de(t)}{dt} + C e(t) \quad (1.10)$$

where  $A$ ,  $B$  and  $C$  are constants. The discrete approximation of equation 1.10 would be the recursive filter given by:

$$u(t) = \alpha e(t - d) - \beta u(t - 1) - \gamma u(t - 2) \quad (1.11)$$

with  $d$  being the electromechanical delay and  $\alpha$ ,  $\beta$  and  $\gamma$  are constants. A lot of studies considers  $u(t)$  to be an acceptable representative of muscle activation  $a(t)$ . However, studies showed that in isometric condition the sEMG signal is nonlinearly related to the muscle force, especially for low contraction levels [91, 16]. Therefore, some studies used a nonlinear power function [91], others used logarithmic function

for low level contractions and linear for the higher contraction levels [15] such as:

$$\begin{aligned} a(t) &= d.\ln(cu(t) + 1) & \text{if } 0 \leq u(t) < 0.3 \\ a(t) &= m.u(t) + b & \text{if } 0.3 \leq u(t) \leq 1 \end{aligned} \quad (1.12)$$

where  $c$ ,  $d$ ,  $m$  and  $b$  can be transformed into one parameter  $A$  ( $0.00 \leq A \leq 0.12$ ) [15]. This parameter is thusly used for the tuning of the nonlinearity of this relationship as presented in Figure 1.26.

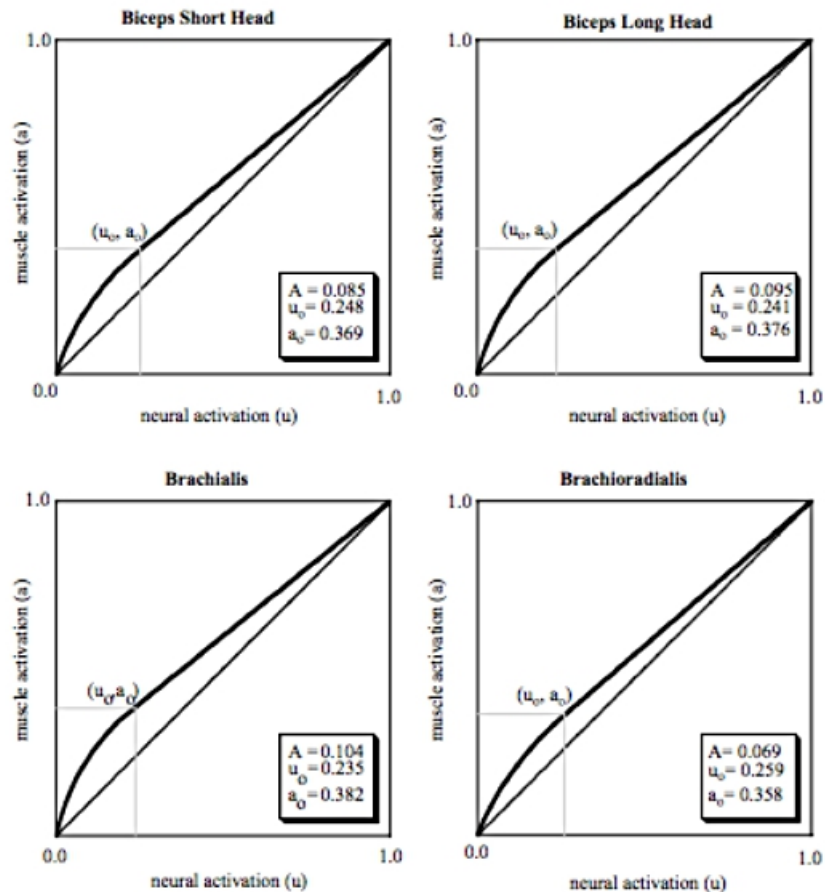


Figure 1.26: The relationship between  $a(t)$  and  $u(t)$  for muscle-specific values of  $A$  as presented by [15]. Each plot has a reference line  $u = a$ . The node point for each piecewise curve is specified by  $(u_0, a_0)$  as described in [15].

Further formulations have been used that are easier to use. One of these formulations is presented by the following equation [93]:

$$a(t) = \frac{e^{Au(t)} - 1}{e^A - 1} \quad (1.13)$$

Where  $A$  is the nonlinear parameter ( $-3 \leq A < 0$ ).

The second step to force estimation, as previously discussed and illustrated in Figure 1.24, is the muscle contraction dynamics which estimate the relationship between the activation  $a(t)$  and the generated

muscle force  $F(t)$ . For this step, the Hill-type model is mostly used since it is simple and fast to compute [86]. The general Hill model is composed of three elements [86, 16] as shown in Figure 1.27:

- The Contractile Element (CE) which models the fiber contraction at the sarcomere level and is responsible for force production;
- The Serial spring Element (SE) which models the mechanical attitude of the tendon and represents the elasticity of the myofilaments;
- The Parallel spring Element (PE) which models the mechanical behavior of the connective tissues and presents their passive force surrounding the muscle fiber.

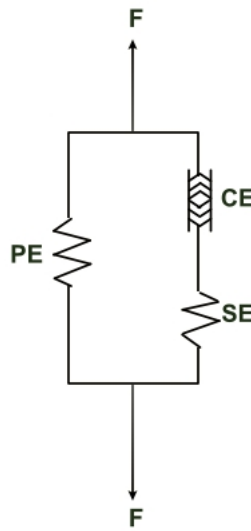


Figure 1.27: Schematic representation of the Hill muscle model.

According to this model, the total force  $F$  produced by the muscle is computed by:

$$F = F^{PE} + F^{SE}, F^{CE} = F^{SE} \quad (1.14)$$

with  $F^{CE}$ ,  $F^{SE}$  and  $F^{PE}$  the forces produced by the CE, the SE and the PE respectively.

Similarly, the total muscle length  $L$  is represented by:

$$L = L^{CE} + L^{SE}, L = L^{PE} \quad (1.15)$$

with  $L^{CE}$ ,  $L^{SE}$  and  $L^{PE}$  the lengths of the CE, SE and the PE respectively.

The muscle-tendon complex is modeled as displayed in Figure 1.28 [26]. As indicated in Figure 1.28, this model takes into account the muscle pennation angle  $\theta$  (for the BB case  $\theta = 0$ ).

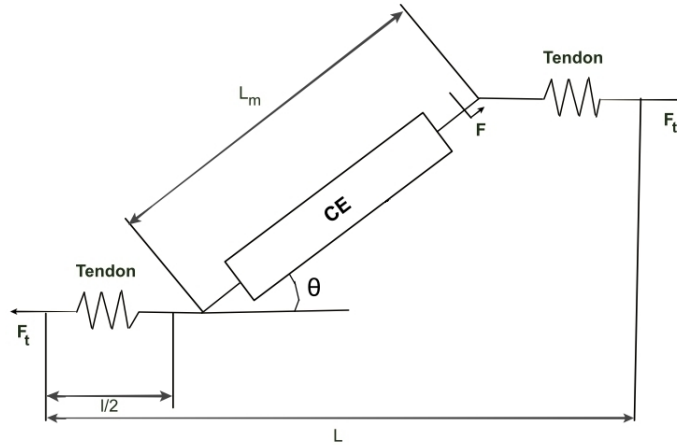


Figure 1.28: Schematic representation of the musculotendinous actuator.

Usually, the muscle and tendon properties previously discussed, are normalized with respect to a set of parameters specifically to a certain muscle. From these parameters, we note:

- Maximum isometric active fiber force  $F_0$ ;
- Muscle fiber length  $L_0$  corresponding to the maximum force;
- Muscle fiber pennation angle  $\theta_0$  corresponding to the maximum force;
- Maximal velocity  $V_m$  corresponding to the muscle shortening;
- Activation time  $\tau_a$ ;
- Deactivation time  $\tau_d$ ;
- Time parameter for time scaling  $\tau_s$  ( $\tau_s = \frac{L_0}{V_m}$ ).

Then, based on the Hill-type muscle model, the muscle force  $F(t)$  is obtained from the muscle activation  $a(t)$  (see Figure 1.24) by the following equation [86, 16]:

$$F(t) = a(t) \cdot f(v) \cdot f(l) \cdot F_0 \quad (1.16)$$

Where  $f(v)$  and  $f(l)$  are the normalized velocity and length dependent fiber force respectively. Thus, in order to characterize the muscle force, in anisometric conditions, we need to consider two relationships [94]: the force-length and the force-velocity functions. Starting by the muscle length and force relationship,

Figure 1.29 illustrates a normalized muscle force-length relationship in dimensionless units. As we can see we have two parts: active and passive ones. The active part is caused by the CE. It produces maximal force when the length is equal to  $L_0$ . As for the passive force it is produced by the PE that produces a force when it is stretched beyond its limits.

Thus, the total force produced by a muscle during contraction is the summation of both active and passive components:

$$F = F_A + F_P \quad (1.17)$$

with  $F_A$  and  $F_P$  are the active and the passive forces respectively. The active force is defined by [95] using the equation below:

$$F_A = f_A(l) \cdot F_0 \cdot a(t) \quad (1.18)$$

with  $f_A(l)$  is the normalized length dependent fiber active force.

And the passive force  $F_P$  is given by [26] as:

$$F_P = f_P(l) F_0 \quad (1.19)$$

with  $f_P(l) = \frac{e^{10(l-1)}}{e^5}$  [16].

Although this model is widely used by researchers because of its simplicity, computational efficiency and somewhat accuracy, it is only valid in a limited number of scenarios. A recent work evaluated the accuracy of the Hill-type muscle models during movement [96]. They found the errors at low firing rates to be consequential and even obtained errors that exceeds 50% for large muscles during normal locomotion [96]. They explained these results by the independently treated relationships: force-length, force-velocity and muscle activation properties in the Hill-type based models. We also have to note that these models are obtained from studies on isolated fibers. Hence, in the next part we will present microscopic sEMG driven force estimation models, that present the advantages of having a more physiological realism in comparison with the macroscopic models (Hill-type models).

### 1.3.3 Physiological models

The first physiological and biophysical model was outlined by Huxley [38]. It explained the force generation by specifying the cross-bridge interaction at the sarcomere level. Then, Zahalak introduced

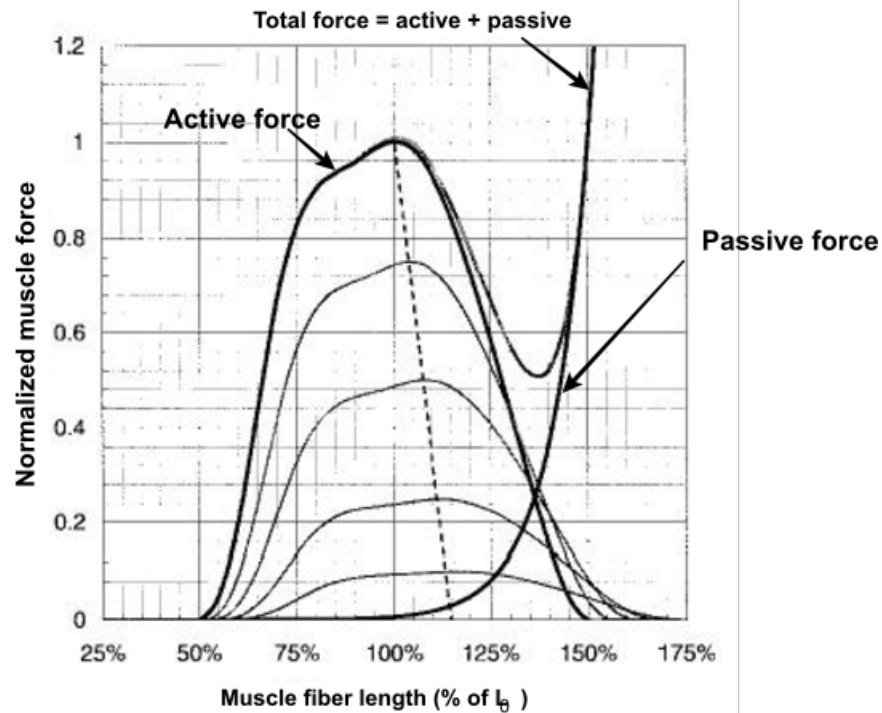


Figure 1.29: Normalized force-length relationship for different activation levels [16].

the distribution-moment approach for sarcomeres [97]. This approach approximates the Huxley cross-bridge model for the sarcomere or the whole muscle. It is important to note, that the Huxley model is complex and computationally pricy. Besides Huxley and Hill-type models, a more recent study presented a settlement between complexity and physiology [98]. This study proposed a model of the calcium dynamics that triggers the contraction. It was then used in a multi-scale physiological muscle model [17]. This work presents a novel physiological approach that integrates a microscopic cross-bridge and recruitment activation dynamics for the CE as well as the Hill approach for the PE. The block diagram of this model is presented in Figure 1.30. As illustrated in this Figure, the physiological model has two inputs: the first is the neural activation obtained by processing of the raw sEMG signal as previously explained in Figure 1.25 for the Hill-type muscle models in the previous section, and the second is the chemical signal named  $u(t)$  here. This input represents the underlying physiological process of the contraction and the relaxation states [17]. In order to obtain this signal the authors first processed the sEMG signal through rectification, low-pass filtering with a cut-off frequency of  $30\text{ Hz}$ . Then the obtained signal is transformed into chemical input  $u(t)$  by thresholding. The obtained signal  $u(t)$  defines the contraction-relaxation durations.

Afterwards, the force is computed through a series of steps inspired by Huxley's sliding filament model illustrated in Figure 1.31. At the sarcomere scale, and by assuming all sarcomere identical and in series, they computed the strain of the contractile element by [17]:

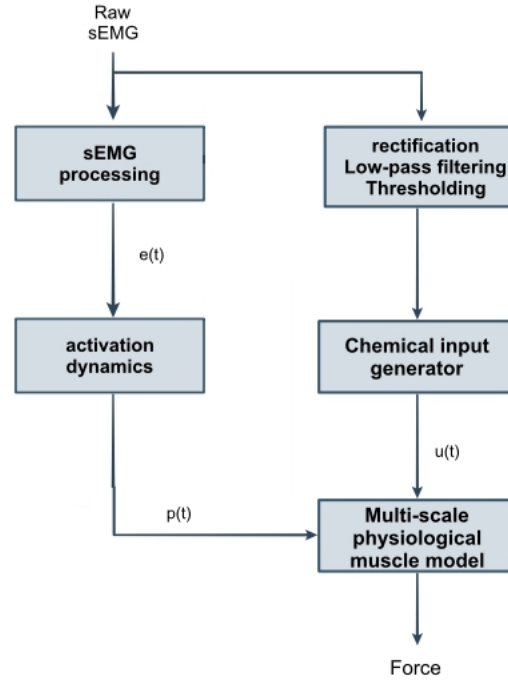


Figure 1.30: The block diagram of the force estimation model combining the Hill type model with the multi-scale physiological model.

$$\varepsilon_c = \frac{(S - S_0)}{S_0} = \frac{(L_c - L_{c0})}{L_{c0}} \quad (1.20)$$

With  $S$ ,  $S_0$  being the sarcomere length at a random position and at rest position respectively and  $L_c$ ,  $L_{c0}$  the length of the contractile element at a random position and at rest position respectively.

According to the Huxley study, there are two states for the actin-myosin filaments: attached and detached as presented in Figure 1.31. Afterwards, based on the Bestel-Sorine and Zahalak studies [98, 97], they expressed the force and the stiffness of each sarcomere by:

$$F_s(t) = k_0 h \int_{-\infty}^{+\infty} \xi(y, t) \eta(\xi(y, t), t) dy \quad (1.21)$$

$$k_s(t) = k_0 \int_{-\infty}^{+\infty} \eta(\xi(y, t), t) dy \quad (1.22)$$

where  $y$  is the normalized position,  $\eta$  is a distribution function representing the fraction of the attached cross-bridges relative to the position  $y$ ,  $\xi$  is the elongation of a cross-bridge due to sarcomere extension and  $k_0$  is the maximal stiffness corresponding to the attachment of all cross-bridges.

Lastly, these equations are transformed to represent all the muscle fibers. The obtained equations incorporate the force-length relationship at the microscopic level since it is directly linked to the actin-myosin sites [17]. And then the recruitment rate is introduced in the contraction-relaxation dynamics.

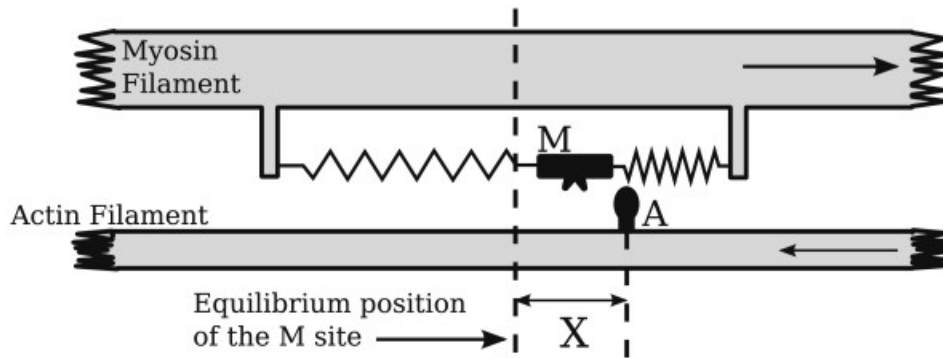


Figure 1.31: Huxley filament model [17].

The comparison between this physiological model and the Hill type model demonstrated the limitations of the Hill-type models even after modifications. This was proven by the large error obtained in comparison with the physiological based model.

Although this type of model seem realistic from the outside, we have to consider its complexity brought by the integrated phenomenological and physiological models. Not to mention that it has not been validated yet and is difficult to apply in clinical environment due to its complexity. But the major problem in these types of models is the fact that they use the sEMG signal as an input to physiological force modeling which is not the case. The input of these somewhat called physiological models should be the neural command expressed by the MU recruitment pattern not the approximation of this later by sEMG signal processing. The physiological way would be to use the sEMG in order to extract the MU recruitment pattern and thereon the neural command that would be the input of the chemical system.

In the next section, we will present the third and final type of sEMG-driven models, the regressive type that has less physiological realism but is, by far, easier to compute comparing to physiological and phenomenological models.

### 1.3.4 Regressive type models

We decided to class all the alternative methods used in sEMG based force estimation in this group that we defined as regressive type models. This class includes all the optimization, machine learning and regressive methods used to solve this estimation problem. The global structure of these types of models are represented in Figure 1.32.

Before we begin to list these methods, we have to recall and insist on the fact that the main problem is that the individual force produced by a muscle cannot be measured experimentally or at least not without invasive procedures. The force we measure experimentally is the force produced by all the muscles that are acting on the same joint. Therefore and since the majority of these studies are experimental, they

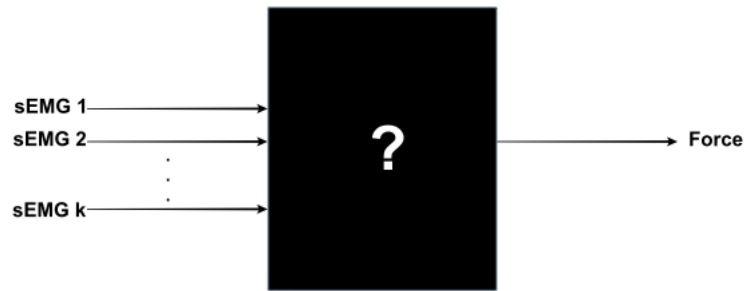


Figure 1.32: Schematic of the regressive type models.

are mostly multi-muscle studies that aims at estimating the individual force of muscle by recording simultaneously the sEMG signals and the corresponding global joint force. Also, if we look closely at this group of methods, we can observe two subclasses: the total black box type models that does not consider at all the shape of the relationship between the input and the output signals. Thus, converting this problem into a blind regression problem that is solved by machine learning or regression algorithms [99, 100, 71, 101, 102]. The second subclass bears on optimization and identification methods that rely on a predefined relationship type between the sEMG signals and the corresponding force [42].

We need to note here that the muscle force  $F$  and moment  $M$  at the joint center are related in 2D by the following equation:

$$M(k) = F(k).d \quad (1.23)$$

with  $d$  being the effective moment arm of the considered muscle. Thus, the sEMG/force or moment relationships are equivalent by a scaling factor.

Starting by the first subclass of regressive models, the most used method in these models is the Artificial Neural Network (ANN). Over the years, a lot of researchers attempted to estimate the muscle force using ANN. An ANN is composed of groups of processing entities called “neurons” [100]. These “neurons” are hooked all together and scattered into layers as illustrated in Figure 1.33.

Where the circles and the solid lines represent the neurons and the weight factors respectively. In this case we have one input layer, two hidden layers and an output layer. This shape of ANN model is capable of solving any kind of problem with any complexity degree. The advantage of the ANN approach to solve the sEMG/force relationship is the fact that it is a machine learning method that comprises two stages: A training stage and a validation or testing stage. The most recent work of this type is presented by de Vries et al. [102]. In this work, they attempted to estimate the shoulder joint forces using ANN. They also used 3D kinematics as input along with the sEMG signals from 13 elbow muscles [102]. The obtained results were somewhat promising. However, their data base consisted on only one subject which is not sufficient to draw conclusive results especially when we know that a lot of physiological, anatomical and

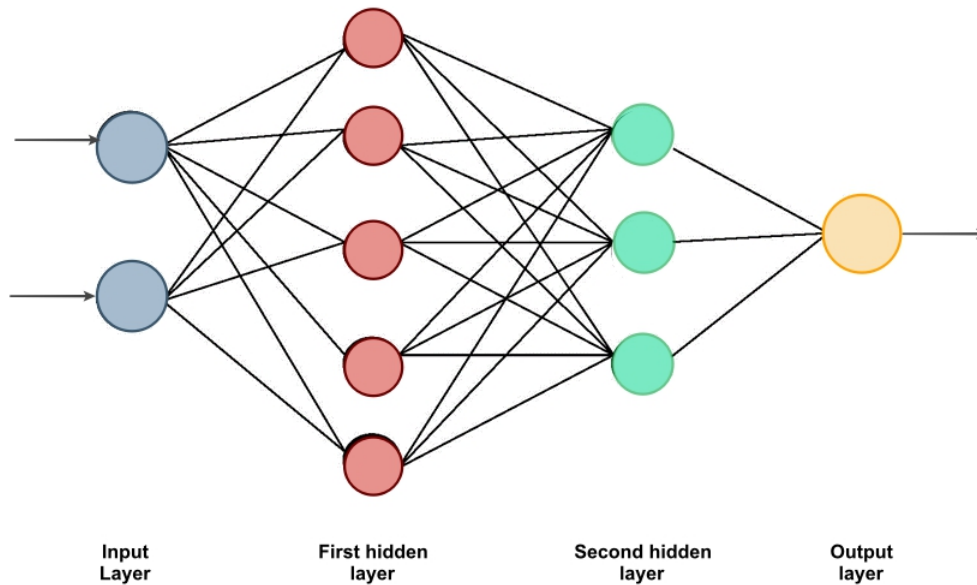


Figure 1.33: Architectural graph of a multilayered Artificial Neural Network (ANN) model.

neural parameters influence the shape of the sEMG/force relationship (this will be presented in chapter 4 with a detailed sensitivity analysis of the parameters that affect the sEMG/force relationship form).

Another nonlinear procedure used in force estimation is the Fast Orthogonal Search (FOS) method [103, 104] and the Ensemble FOS [105]. It consists on a summation of a linear and nonlinear functions that are defined in order to minimize the Root Mean Squared Error (RMSE). This method have the advantage of being very fast but not very accurate.

Other than the ANN and FOS, Parallel Cascade Identification (PCI) has been also used in sEMG/force modeling [106]. The PCI is usually used in order to model dynamic systems. Its global structure is presented in Figure 1.34.

As we can see in Figure 1.34 the PCI consists on a cascade of linear and nonlinear elements in parallel. This type of structure was used by Hashemi et al. [106] in order to model the sEMG/force relationship during isometric elbow flexion extension in experimental conditions. They compared the results to the FOS method and found a 44% improvement by using the PCI [106]. The main problem of this method is the inter-session variability obtained which can be attributed to instrumental or even physiological reasons [106]. A more recent PCI based sEMG/force estimation presented an enhanced study of the previous one by introducing angle based EMG calibration with PCI [107]. The calibration enhanced the RMSE especially for concentric contractions ( $RMSE < 10\%$ ) but did not overcome the variability problem.

The second type of regressive sEMG/force estimation models is based on solving a predefined relation-

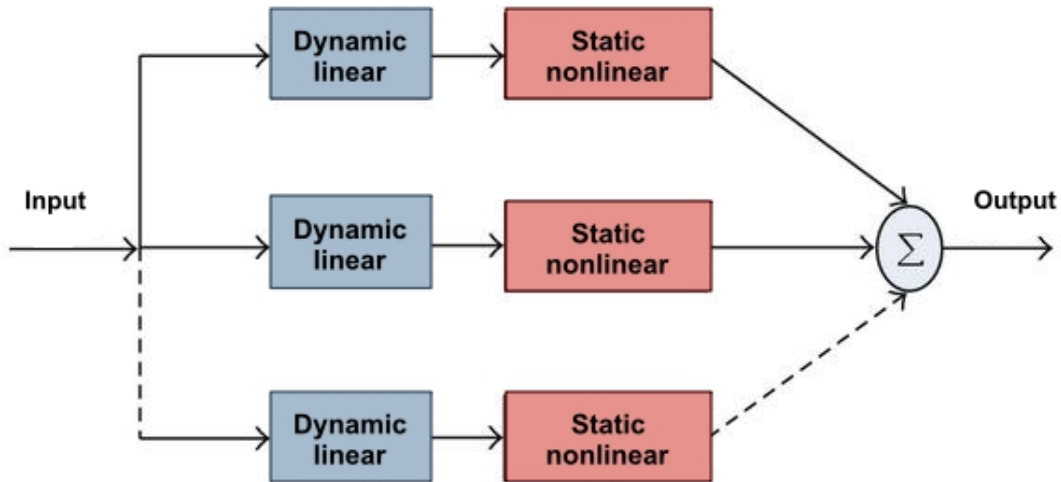


Figure 1.34: The structure of the Parallel Cascade Identification (PCI) model.

ship between the sEMG signal and the corresponding force using an optimization method. A recent work proposed a nonlinear EMG/moment relationship by taking inspiration from the literature [108]. They defined this relationship by:

$$M_i(k) = \alpha_i sEMG(k)^{\beta_i} \quad (1.24)$$

Where  $M_i$  and  $sEMG_i$  are the moment and the sEMG of muscle  $i$  at sample  $k$  respectively,  $\alpha_i$  and  $\beta_i$  are constant coefficients to be identified by minimizing the RMSE between the experimentally obtained and the estimated torque  $T = \sum_{i=1}^N T_i$  (with  $N$  being the number of muscles involved in force production). The relative error is presented by [42]:

$$e = \frac{\sum_{k=1}^K \left( T(k) - \sum_{i=1}^N \alpha_i sEMG_i(k)^{\beta_i} \right)^2}{\sum_{k=1}^K (T(k))^2} \quad (1.25)$$

The optimization method used in this study is the Particle Swarm Optimization (PSO) and is compared to the Interior-Reflective Newton Algorithm (IRNA). Results showed similar error values for both optimization methods [42]. However, the PSO algorithm is computationally demanding in comparison with the IRNA algorithm but cancels the initialization problems. The advantage of this technique is the fact that it proposes to solve the “load sharing problem”, which is one of the main challenges in Biomechanics. This problem is engendered by the synergist muscles acting on the same joint and activated at the same time. Thus, the force of each individual muscle cannot be measured, as previously mentioned, but the global force produced by this group of muscle can be recorded experimentally using non invasive

procedure. The problem of determining the distinctive contribution of each muscle in this global measured force is what we call the “load sharing problem. Nevertheless, this model has several limitations that are worth mentioning:

- It presents the same relationship for both extension and flexion contractions which is not necessary the case;
- It considers the envelope of the sEMG as input which is highly dependent on various parameters (cut-off frequency...);
- It does not consider the BR in the estimation which can induce major errors since it contributes quite strongly in elbow flexion.

Lastly, this method needs validation with a simulation model, because nothing can guaranty that the obtained solution is the exact one. We also have to mention the problem of finding wrong solutions or sticking with a local minima and thereby not finding solutions. Adding that the solutions are highly dependent on the starting conditions [42].

Alternative to these estimation methods, some researcher proposed to estimate the force by using an EMG coefficient method [109]. Where they defined the total wrist moment as:

$$M_i^e = \sum_{j=1}^m sEMG_{ij} \rho_j r_j \quad (1.26)$$

Where  $M_i^e$  is an applied external moment at configuration  $i$ ,  $EMG_{ij}$  is the EMG of the muscle  $j$  at configuration  $i$ ,  $\rho_j$  is the force-EMG coefficient for muscle  $j$  and  $r_j$  is the muscle moment arm vector.

This method, that adopts a linear relationship between the EMG and the joint moment, was successful in estimating the individual forces of the wrist but it cannot be used in redundant systems due to the limited mechanical redundancy of the wrist. Other researchers used linear regression in order to estimate the individual force by minimizing the error between the total measured and estimated force [99].

A recently published approach, estimates the joint force using sEMG peaks and a biomechanical muscle model [18]. This study targets the force produced by the joint of the index finger when abducted. To our knowledge, the abductor digiti minimi and the first dorsal interosseus are the only muscles where researchers succeeded to non-invasively measure the individual force [4]. Thus, this study uses the force produced by the abductor digiti minimi in order to test their biomechanical based force estimation model [18]. The corresponding block diagram is presented in Figure 1.35.

The peak detection block aims at quantifying the number of recruited MUs, then the muscle model presents the summation of the twitch responses corresponding to the number of activated MUs at a certain instance. This force can be expressed by:



Figure 1.35: Block diagram of the biomechanical based estimation model [18].

$$F(t) = y(t) * m(t) \quad (1.27)$$

Where  $y(t)$  and  $m(t)$  are the sEMG peaks and the muscle model function respectively and  $*$  is the convolution operator. The transfer function associated to  $m(t)$  is written as:

$$M(s) = \frac{K\omega_n^2}{s^2 + 2\zeta\omega_n s + \omega_n^2} \quad (1.28)$$

With  $K$  the gain,  $\omega_n$  the natural frequency,  $\zeta$  the damping ratio and  $s$  the Laplace variable. The major problem of this technique that seems to be promising is that it does not have any realism since it does not take into consideration the MU types. Also, it seems that it can only be applied for low contraction levels (in the study between 0 and 20 %MVC) since the sEMG peaks detection would be much harder with higher contraction level. We should also note that the auto-cancellation phenomenon can be a major limitation to be considered in the sEMG peaks detection algorithm.

To conclude, this paragraph demonstrates various method and calculation strategy for muscle force estimation, however none of these approaches are validated for an individual muscle.

## 1.4 High Density sEMG (HD-sEMG) technique

In this section, we will present a novel sEMG recording technique, the HD-sEMG technique which has many advantages comparing to the classical sEMG recording methods previously described.

The conventional sEMG recording techniques suffer from many limitations. One of the main limitations of the classic sEMG techniques is the deficient spatial resolution [2]. Which can be explained by the difficulty of extracting the sources of activity from the sEMG signal. Therefore, it gives information about the activity of a group of MUs but not a single MU. Notting that obtaining information about the activity of a single MU is substantially beneficial in many domains such as therapy and neuromuscular disorder diagnosis and evaluation [2]. In addition, the sEMG signal collected from a certain location with respect to muscle using a monopolar or a bipolar configuration is not necessarily representative of the activity of the whole muscle [8]. Other limitation and a major problem of the conventional sEMG recording would be the electrode placement problem [8]. This parameter has direct influence on

the precision of the latter applications like force estimation [7] for example. Thus, the placement of the electrodes with respect to the active MUs should be as constant as possible between subjects and recordings [8]. The recommendations for sensor placement for sEMG recordings are reported by Hermens et al. [110]. Finally, we have the problem of destructive superposition of the APs from different MUs due to their biphasic and triphasic nature which is known as auto-cancellation phenomenon [9]. These limitations of sEMG recordings can be overcome by using the HD-sEMG technique.

This novel sEMG recording technique is based on a multi-channel electrode recording system. It is composed of a two dimensional array of electrodes called a HD-sEMG grid that is characterized by being a spatiotemporal variant of the usual single channel sEMG techniques [111, 66]. The HD-sEMG technique overtops the classical singular and bipolar recordings by taking into account aspects of spatial distribution of electrical potentials [112] and by overcoming their basic limitations such as the electrode placement problem, the representativity of the recorded signal, the auto-cancellation phenomenon and the spatial resolution. It was also demonstrated through some researchers that it can improve force estimation [9, 112, 105] and thereby prosthesis control [113, 114].

The HD-sEMG recording technique has become widespread in the last few years, which is due to multiple reasons. Therefore, the HD-sEMG found its way into many applications due to the fact that it provides rich information about the muscle physiology and anatomy such as the MUs number [115] and properties [64, 116, 117] and the neural command by HD-sEMG decomposition [59, 66, 118]. In addition, the HD-sEMG found its way into clinical applications such as fatigue studies, neurogenic changes, myopathies and positive muscle phenomena [119]. Thus, becoming a valuable clinical diagnostic tool. Not to mention, the improvement that this novel technique has provided in force estimation [9, 42, 120].

## 1.5 Position of the problem and objectives of the thesis

As mentioned previously, the main problem is the fact that the force developed by an individual skeletal muscle cannot be measured non-invasively. In addition, the external force measured by ergometer or force sensors is the total contribution of the active muscles acting on the studied joint. Thus, this thesis's work is dedicated to improve the modeling the relationship between the sEMG signal of the BB muscle and the corresponding force by using HD-sEMG technique during isometric non fatiguing context. To achieve this goal, we will propose an original work based on several steps: (i) preprocessing the HD-sEMG signals which includes denoising and elimination of parasite signals, (ii) determining the input parameters by testing new parameters and data fusion approaches and (iii) modeling of the sEMG/force relationship.

Based on the literature and what have been previously discussed concerning the EMG driven force estimation models (see section 1.3), the sEMG/force models that exists lack a lot of important factors

like realism, mono-muscle validation (for multi-muscle studies) and reproducibility. Thus, in order to appropriately model this relationship we need to resolve several obstacles that can affect the quality of the force estimation. The first obstacle, is the heterogeneous noise contaminating the HD-sEMG signal during experimental recordings. We also have the problem of cross-talk from the BR muscle which is located near the BB. Second, we have the data fusion problem that consists on extracting the model's input parameters from the 64 sEMG signals. Third and last, the sEMG/force relationship will be modeled through a regressive model after a focused sensitivity analysis of the different parameters influencing the form of this relationship. We will also be using morphological and other High Order Statistics (HOS) as inputs in order to personalize our model and make it subject specific. This model will be finally validated by computing the Normalized Root Mean Squared Error (NRMSE) between the estimated and the simulated muscle force.

Thus, the following chapters of this thesis as described in the general introduction will address all these problems in order to model the sEMG/force relationship in a realistic manner. The block diagram illustrating the methodology of the thesis work is presented in Figure 1.36.

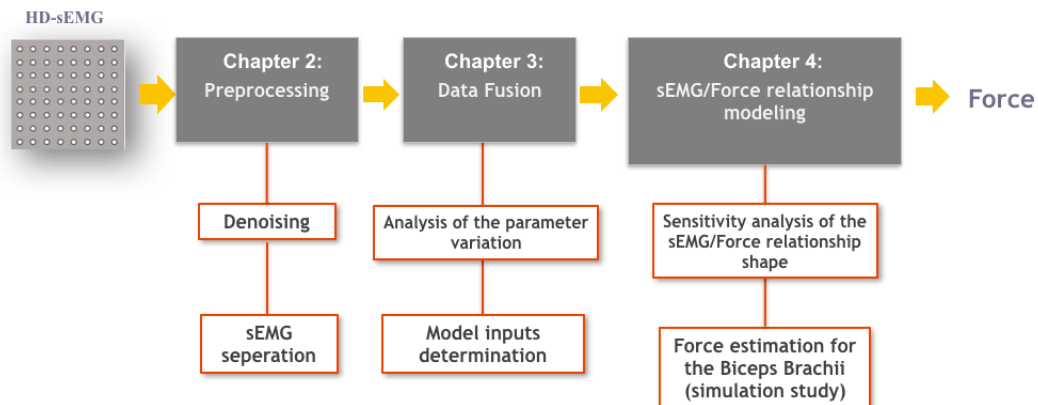


Figure 1.36: The block diagram representing the methodology of the thesis work.

Finally, the objectives of this work can be summarized by:

- Denoising of a HD-sEMG grid in order to minimize the estimation error;
- Elimination of the BR's activity from the BB's signal thus reducing the obtained signal's contamination;
- The study of the variation of the sEMG amplitude with force level increase in order to characterize the parameters influencing this signal;
- Selection of the sEMG descriptor and data fusion of the parameter in order to obtain a representation of the HD-sEMG grid in one signal;

- Study of different physiological, neural and anatomical parameters influence on the shape of the sEMG/force relationship;
- Modeling of the sEMG/force relationship using a realistic simulation model, optimization and machine learning algorithms.

## Chapter 2

# Preprocessing of HD-sEMG signals

### Contents

---

<b>2.1</b>	<b>Introduction</b>	<b>78</b>
<b>2.2</b>	<b>Denoising of HD-sEMG signals using Canonical Correlation Analysis</b>	<b>78</b>
2.2.1	Canonical Correlation Analysis (CCA)	80
2.2.2	CCA component thresholding	82
2.2.3	Selective CCA method	83
2.2.4	HD-sEMG simulation model	85
2.2.5	Denoising simulated HD-sEMG signals	86
2.2.6	Experimental protocol	88
2.2.7	Denoising experimental HD-sEMG signals	89
2.2.8	Comparative study	94
2.2.9	Discussion and conclusion	98
<b>2.3</b>	<b>Extraction of the Brachialis's muscle activity from the HD-sEMG recorded at the surface of the Biceps Brachii</b>	<b>101</b>
2.3.1	Experimental protocol	102
2.3.2	Data Processing	104
2.3.3	Otsu thresholding method	106
2.3.4	Application of the separation method on the experimental signals	106
2.3.5	Analysis of the results and discussion	110
<b>2.4</b>	<b>Conclusion</b>	<b>111</b>

---

## 2.1 Introduction

This chapter is dedicated to the preprocessing of the HD-sEMG signals. In fact, the raw sEMG signals suffer from two major issues. Firstly, since the intensity of the sEMG signal is very low (between  $\mu V$  and  $mV$ ) [5], the acquired signals are usually very noisy due to the contamination by different types of noise especially at low contraction levels. Secondly, activity of neighboring muscles can interfere with the recorded signals, consequently the identification of a single muscle source of EMG became hazardous. Thus, one may record at the same time the activity from neighboring and underlying muscles. For these reasons, this chapter is divided into two parts: the denoising of the HD-sEMG signals (section 2.2) and the extraction of the BR's muscle activity from the total sEMG recorded from the upper limb (section 2.3).

The first part (section 2.2) includes a simulation and an experimental study. Where the proposed denoising technique is solely based on CCA. It suggests the denoising of the HD-sEMG signals by targeting two types of noise that are commonly present in these high density signals. This denoising is based on a multithresholding technique applied on the canonical components. The second part is a separation technique also using the CCA algorithm. It intends to separate the two muscle activities of the BB and the BR in order to minimize the crosstalk problem induced by the deep position of the BR in the upper arm. Therefore, it attempts to classify each source of activity between the BB and the BR to reconstruct the BB's EMG with minimal influence from the BR.

## 2.2 Denoising of HD-sEMG signals using Canonical Correlation Analysis

As previously showed in the state of the art section 1.2.2.5, the sEMG is widely used in different fields. In such applications, it was demonstrated that for low level muscle contraction with consequently a low sEMG magnitude, the sEMG signal quality is mainly corrupted by three types of noise [59]: the power line interference (PLI), the white Gaussian noise (WGN) and the motion artifacts (MA).

In the case of HD-sEMG signals recorded during low voluntary contraction levels, i.e. 20 % of the Maximum Voluntary Contraction (MVC), noise contamination could occur on some channels and could become critical. Consequently, an important dispersion of the Signal to Noise Ratio (SNR) throughout the HD-sEMG signals can be observed due to the noise that accompanies certain channels more than others. Indeed, this level of contraction is commonly used in signal decomposition and identification of MUs activities [67], neural drive estimation for prosthesis control [121], force classification [50], and the evaluation of probability density function shape deformation with force intensity variation [122].

Furthermore, the amplitude descriptors used for these studies are very sensitive to noise especially the HOS [122]. Nonetheless, denoising these signals from such multichannel grid appears to be a challenge considering the fact that not all channels are equally noisy.

Several sEMG signal denoising methods have been proposed in the literature including baseline noise spectrum subtraction [123] and power line noise subtraction techniques [123]. However, these methods make unrealistic assumptions regarding the line noise i.e constant phase and amplitude of the power line noise over the duration of the sEMG recording session which is only true under restricted conditions and no differentiation between the different sources of noise [59, 123]. Conventional digital filters have been also proposed to reduce noise during reduced muscle activity by delimiting the frequency band of the sEMG and removing some noise and their harmonics [124]. But they often alter the signal waveform resulting in the loss of some EMG information due to spectral overlapping of the noise and the sEMG [59, 124]. Recently, the Empirical Mode Decomposition (EMD) has been employed as an effective denoising procedure that can decompose any time-series into a set of functions labeled intrinsic mode functions [125]. This was followed by Ensemble EMD (EEMD) [126] which overcomes the limitation of mode mixing brought by standard EMD algorithm. The advantage of the EEMD is in the fact that it targets all three types of noise. However, Zhang and Zhou applied two types of intrinsic mode functions filtering and various thresholding techniques and they only apply the denoising on simulated noise [126]. Additionally, wavelet and adaptive wavelet thresholding methods are also used [127, 128] but they target only the WGN component thanks to the time-frequency representation. Furthermore, a nonlinear filtering method has been proposed to specifically identify the electromagnetic noise by a sharp spectral lines method [129]. However, despite the fact that it provides a gain in the precision of the later applications it tampers with the sEMG signals because it only considers the sEMG signals from the point of view of nonlinearity and chaos [129].

To denoise biomedical multichannel recordings such as Electroencephalograms (EEG) and sEMG, Blind Source Separation (BSS) techniques are often used, as Independent Component Analysis (ICA) [130, 131]. Recently, a new method has emerged and has been used for biomedical multichannel signal denoising, the CCA [130, 132]. This method has the main advantage of ranking the estimated sources according to a correlation coefficient and allowing the construction of a pertinent thresholding paradigm. It has been successfully used in removing artifacts from EEG signals without altering the underlying ictal activity [133, 134, 135]. A recent comparative study between deterministic (EMD and wavelet) and stochastic approaches (ICA and CCA) for EEG artifact denoising, showed that the performance of either method depends on the level of noise corruption [131]. Latterly, a combination of CCA and EMD approaches, has proven to be successful in denoising multichannel monopolar uterine sEMG signals using a suited correlation coefficient thresholding [130]. Other combinations with CCA have been tested such as CCA-EEMD [132] that showed better performance in artifact removal but was much more time consuming.

Based on this previous review of denoising technique, we have chosen to use the CCA in order to eliminate two types of noise (PLI, WGN), and possibly isolate the MA components, on HD-sEMG signals recorded from the BB at voluntary low contraction levels (20 %MVC). For this purpose, a specific methodology is proposed using a dedicated thresholding rule based on intensity ratio computed on the estimated canonical components selection (section 2.2.2). Afterwards, these approaches will be evaluated in simulation using an HD-sEMG generation model supposing planar multilayered conductor volume and realistic noise spreading on the grid (sections 4.2.2 and 2.2.5). Finally, they will be used to denoise a dataset from five healthy subjects during isometric isotonic contractions of the BB at 20 %MVC, following a specific protocol, and are compared to ICA and previous CCA combinations (CCA-EMD and CCA-wavelet) using statistical tests (section 2.2.8).

### 2.2.1 Canonical Correlation Analysis (CCA)

CCA is a statistical multivariate method that correlates linear relationships between two multidimensional variables. The CCA algorithm attempts to extract the original sources, in a BSS paradigm, having maximum autocorrelation values (at a specific time delay) and minimum intercorrelation values with each other [133]. For this purpose, we assume that a multidimensional random variable  $X = [X_1, X_2, \dots, X_n]$  (with  $n$  being the number of sensors) is the result of an unknown mixture of unknown source signals  $S = [s_1, s_2, \dots, s_n]$ . The mixing is assumed to be linear, reducing the mixing to a matrix multiplication and allowing to write [134]:

$$X = A \cdot S \quad (2.1)$$

Where  $S$  and  $X$  are the source and the grid signals matrices respectively of dimension  $n \times m$  with  $n$  being the number of sensors,  $m$  the number of samples ( $n = 64$  and  $m = 11000$  in this study), and  $A$  is the mixing matrix of dimension  $n \times n$ . The goal here is to retrieve the original source matrix  $S$  by estimating the mixing matrix  $A$ . This can be achieved by introducing the demixing matrix  $W$  such that:

$$Z = W \cdot X \quad (2.2)$$

Where the matrix  $Z$  approximates the source matrix  $S$  by a scaling factor. Let  $Y$  be the delayed version of the source matrix  $X$  such that  $Y(k) = X(k - 1)$  where  $k$  represents the sample number. The one sampling period delay was chosen after multiple denoising trials using different time delay values between  $X$  and  $Y$ . The CCA algorithm obtains two sets of basis vectors, canonical vectors, for  $X$  and  $Y$  respectively, such that the correlation between the projections of these matrices onto these basis vectors is mutually maximized. First, the mean value of each row from the data matrices  $X$  and  $Y$  is removed. Then by considering  $u = w_x^T \cdot X$  and  $v = w_y^T \cdot Y$  the linear combinations of the elements in  $X$  and  $Y$

respectively, the correlation between  $u$  and  $v$ , called the variates or the canonical components, [133] can be represented by:

$$\rho = \frac{E[uv]}{\sqrt{E[u^2]E[v^2]}} = \frac{E[(w_x^T X)(w_y^T Y)]}{\sqrt{E[(w_x^T X)(w_x^T X)]E[(w_y^T Y)(w_y^T Y)]}} = \frac{w_x^T C_{xy} w_y}{\sqrt{(w_x^T C_{xx} w_x)(w_y^T C_{yy} w_y)}} \quad (2.3)$$

Where  $C_{xx}$  and  $C_{yy}$  represent the auto-covariance matrices of  $X$  and  $Y$  respectively,  $C_{xy}$  represents the crosscovariance matrix of  $X$  and  $Y$ , and  $w_x$  and  $w_y$  are the corresponding weight vectors. Then, the maximization problem will be solved by setting the derivative of  $\rho$ , with respect to  $w_x$  and  $w_y$ , equal to zero which leads to the equation 2.4.

$$\left\{ \begin{array}{l} C_{xx}^{-1} C_{xy} C_{yy} w_x = \rho^2 w_x \\ C_{yy}^{-1} C_{yx} C_{xx} w_y = \rho^2 w_y \end{array} \right\} \quad (2.4)$$

With  $\rho$  as the square root of the eigenvalue,  $w_x$  and  $w_y$  as eigenvectors of  $C_{xx}^{-1} C_{xy} C_{yy}$  and  $C_{yy}^{-1} C_{yx} C_{xx}$  respectively. Since the two solution are related by equation 2.5 only the first part of the equation is used to construct the weight vector  $w_x$ .

$$\left\{ \begin{array}{l} C_{xy} w_x = \rho \lambda_x C_{xx} w_x \\ C_{yx} w_y = \rho \lambda_y C_{yy} w_y \end{array} \right\} \quad (2.5)$$

Where  $\lambda_x = \lambda_y^{-1} = \sqrt{\frac{w_y^T C_{yy} w_y}{w_x^T C_{xx} w_x}}$

The first variates obtained by CCA are, thus, maximally correlated with each other. The next pair of weight vectors is obtained likewise by finding variates which are maximally correlated with each other and uncorrelated with the variates of the first pair and so on all the variates are found in an iterative manner [133]. As a consequence, these variates are considered as the sources having maximal autocorrelation and are uncorrelated with each other. Thus, when CCA algorithm is applied on the raw HD-sEMG signal matrix, we obtain the sources (estimated canonical components) ranked from the higher to the lower delayed autocorrelation value as depicted on Figure 2.6. Then, the noise sources can be identified (by specific thresholding) and removed by setting the corresponding rows in the source matrix equal to zero, and then  $X_{denoised}$  is obtained by:

$$X_{denoised} = \hat{A} \cdot Z_{denoised} \quad (2.6)$$

Where the matrix  $Z_{denoised}$  represents the approximated source matrix obtained by CCA after removing the noise sources, and  $\hat{A}$  is the estimated mixing matrix equal to the inverse of the estimated demixing matrix  $\hat{W}(\hat{A} = \hat{W}^{-1})$ .

At this stage, we need to establish the best way to detect the sources of noise without removing any of the sEMG sources. Thus, the next step will be to propose a thresholding algorithm that can remove the sources of noise based on a valid criteria.

### 2.2.2 CCA component thresholding

The denoising process consists of eliminating, by thresholding operation, the sources of noise estimated by the CCA method. This was accomplished, based on the intensity ratio (ranked intensity component ratio  $r_j(i)$  depicted on Figure 2.7a) between both cumulated, normalized and rectified source and corresponding noise. We define this intensity ratio as follows:

$$r_j = \frac{\sum_{i=1}^N |S_j(i)|}{N} \times \frac{P}{\sum_{i=1}^P |b_{s_j}(i)|} \quad (2.7)$$

Where  $S_j(i)$  represents the  $i^{th}$  sample of the  $j^{th}$  estimated source containing muscle activity during contraction,  $b_{s_j}(i)$  the corresponding noise obtained from the first 0.5 s period of  $S_j(i)$  without muscle contraction ( $N = 10000$ ,  $P = 1000$ , sampling frequency  $F_e = 2\text{kHz}$ ). All the sources with a ratio below a specific threshold are removed. This threshold was defined according to two criteria:

- the first one is linked to the noise intensity, represented by the ranked intensity ratio present in the estimated source, as depicted on Figure 2.7a;
- the second is the mean correlation value obtained between the 32 bipolar signals (see Figure 2.7b), with and without a pre-step of CCA denoising over the grid and subjects.

On one hand, the first criterion sorts the components from the most (sEMG component) to the least significant (noise component). On the other hand, the second evaluates the conservation of muscle activity in the denoised recordings with CCA algorithm. In this study, our intention was to maximize the threshold to remove the maximum of the noise sources but without removing any component linked to muscle activity. Thus, after computing the correlation coefficient between the bipolar signals before and after denoising with CCA by changing the threshold between 1 and 4 with a step of 0.1, the correlation coefficient was fixed to 0.8, and the corresponding threshold was chosen as the most adequate for each subject. The block diagram of the thresholding method is presented in Figure 2.1 where the correlation coefficient corresponding to the optimal threshold was fixed at 0.8.

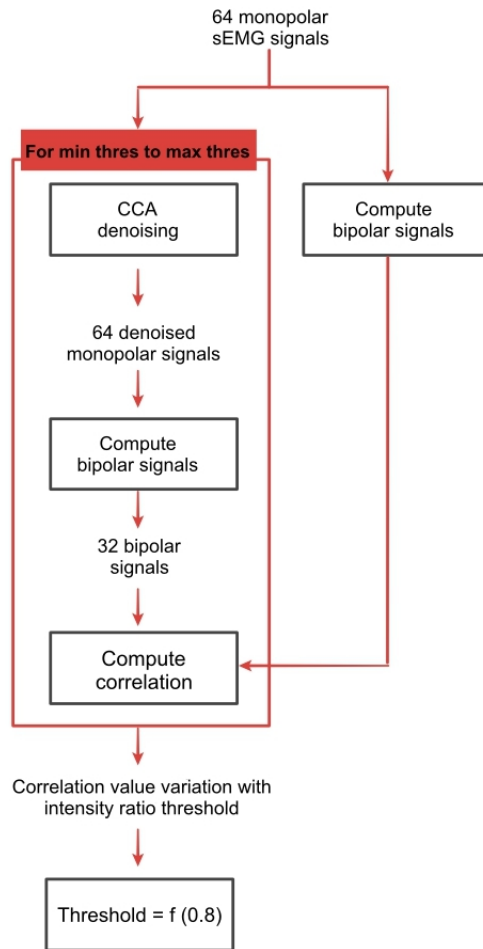


Figure 2.1: Block diagram of the CCA component thresholding procedure.

### 2.2.3 Selective CCA method

As described before, the CCA method is employed in this study for denoising the channels of the grid that have low SNR, then reducing the SNR variance and enhancing the mean SNR among channels of the grid. The SNR of each channel was computed using the following equation similar to that of the intensity ratio (Eq 2.7):

$$SNR_j = 20 \log_{10} \left( \frac{\sum_{i=1}^N |EMG_j(i)|}{N} \times \frac{P}{\sum_{i=1}^P |b_j(i)|} \right) \quad (2.8)$$

Where  $EMG_j(i)$  represents the  $i^{th}$  sample of the  $j^{th}$  sEMG channel,  $b_j(i)$  the corresponding noise obtained from the first 0.5 s period without muscle contraction. The block diagram of the complete CCA denoising procedure is illustrated in Figure 2.2. A possible limitation of the CCA approach is the possible contamination of high SNR channels with noise after signal reconstruction as can be seen in Figure 2.8 (red line). To prevent this inconvenient, we propose an additional channel selection stage after CCA

denoising, namely selective CCA (sCCA):

$$EMG_{j,sCCA} = \begin{cases} EMG_j & \text{if } SNR_{j,CCA} < SNR_j \\ EMG_{j,CCA} & \text{otherwise} \end{cases} \quad (2.9)$$

It means that, if the obtained SNR for channel  $j$  is better after CCA denoising, we conserve the denoised vector  $EMG_{j,CCA}$  (channel  $j$ ) of the  $EMG$  matrix. We can observe on Figure 2.8 the SNR dispersion with the raw channels and the ones obtained by CCA and sCCA for one subject. This sCCA method is depicted in Figure 2.2.

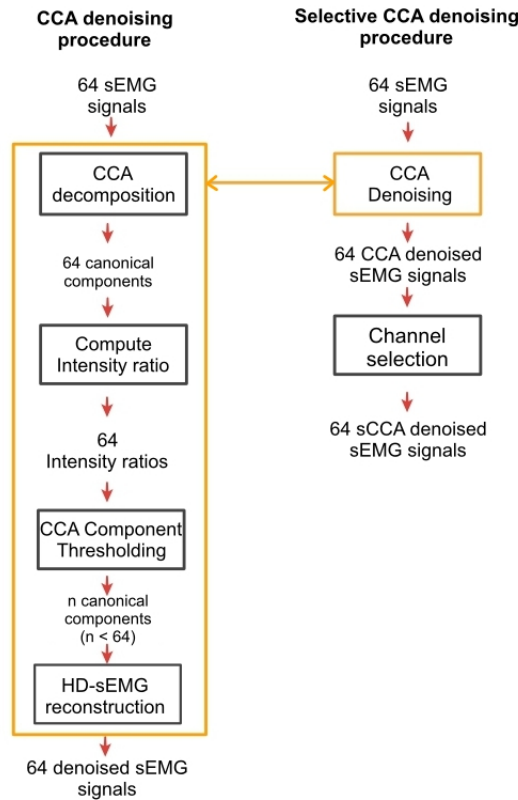


Figure 2.2: The block diagram of the CCA and the sCCA denoising techniques.

In order to evaluate the denoising procedure we used the NRMSE defined by:

$$NRMSE = \frac{1}{N_{ch}} \sum_{i=1}^{N_{ch}} \left( \sqrt{\frac{1}{N} \sum_{t=1}^N \left( \frac{EMG_{i,t} - EMG_{denoised_{i,t}}}{EMG_{i,t}} \right)^2} \right) \quad (2.10)$$

With  $N$  being the number of samples and  $N_{ch}$  the number of denoised channels after sCCA. The signals  $EMG_{i,t}$  and  $EMG_{denoised_{i,t}}$  are the simulated without any added noise and the denoised signals obtained for the channel  $i$  respectively.

All the calculations were performed by self made Matlab routine, for a HD-sEMG grid of 64 signals

of a 2048  $Hz$  sampling frequency. The time calculation was with a Dell workstation (Intel Core 2 Quad CPU 3GHz, 4Go RAM).

Now before applying our denoising method on the experimental signals, we need to find the appropriate method in order to choose and validate the threshold for the intensity component ratio. The best way to do so, is by simulation where we could compute the NRMSE between the originally simulated signals and the signals obtained after denoising. Accordingly, in the next sections we will introduce the simulation study based on a multilayered planar HD-sEMG generation model (section 4.2.2). Then we will apply our CCA and sCCA denoising algorithms (section 2.2.5).

#### 2.2.4 HD-sEMG simulation model

The model used to generate the 64 signals has been described in details in [136, 50]. This model defines a planar volume conductor with three layers: muscle, adipose and skin tissues [137] and is based on the detection of single FAPs through these three layers and the planar volume conductor. This model considers the generation of intracellular APs at the innervation zone, their propagation along the muscle fiber and their extinction at the myo-tendinous junction. It also simulates the neural drive which is represented by the MU recruitment pattern according to MU type and size as well as level of excitation. However, in our study, we used it to generate HD-sEMG signals from a grid, placed with a distance of 15 mm at the distal side from the neuromuscular junction, and by applying parallelization techniques and using a high performance computer. This model is composed of different blocks (neural drive, electrical propagation, conductor volume, instrumentation, force) using the formalism of Ayachi et al. [50]. The model setting values used for constructing our database are reported in Tables 2.1 and 2.2 for the MU and fibers characteristics and global model parameters respectively with  $S$  :Slow fatiguable,  $FR$  : fast resistant,  $FIN$  : fast intermediate,  $FF$  : fast fatiguable MU types. This model represents one biceps

Table 2.1: MU and fiber parameters (mean  $\pm$  SD) used in the simulation model.

MU Type	Number of MUs	MU diameter ( $mm$ )	Number of fibers/MU	Fiber diameter ( $\mu m$ )
S	33	$5 \pm 1$	$100 \pm 10$	$45 \pm 5$
FR	17	$5.5 \pm 1$	$150 \pm 15$	$50 \pm 5$
FIN	17	$6 \pm 1$	$200 \pm 20$	$55 \pm 5$
FF	33	$6.5 \pm 1$	$250 \pm 25$	$60 \pm 5$

muscle composed of 100 MUs disposed in a rectangular territory of 4 cm in width and 2 cm in depth. Fast MUs are preferentially disposed near the surface and slow ones deeper in the muscle tissue. For the simulation of a contraction at 20 %MVC, 36 MUs are recruited based on a Fuglevand modified law described in [138]. The firing rate of the active MUs are regulated by a linear law depending on their types based on the "oignon skin" phenomenon [50].

Table 2.2: HD-sEMG generation model parameters.

Symbol	Parameters	Value
$F_e$	Sampling frequency	2 kHz
$T$	Signal duration	5s
$L_1, L_2$	Mean fiber semi-lengths	70-65 mm
$R$	Muscle radius	20 mm
$IZ, TJ$	Innervation Zone and myo-Tendinous Junction spreads (Uniform law)	10 mm
$h$	Thickness of fat layer	3 mm
$d$	Thickness of skin layer	1 mm
$a$	Electrode diameter	1.5 mm
$IED$	Inter-Electrode Distance	4 mm
$CV$	Muscle fiber conduction velocity	$4.0 \pm 0.2 \text{ m.s}^{-1}$
$R_c$	Muscle conductivity ratio between fat and muscle layers	0.5
$R_b$	Muscle conductivity ratio between skin and fat layers	20
$R_a$	Muscle conductivity ratio between longitudinal and transversal directions	5
$VC_{IPI}$	Inter Pulse Interval Variation Coefficient	20 %
$n_{UM}$	Number of Motor Unit	100

### 2.2.5 Denoising simulated HD-sEMG signals

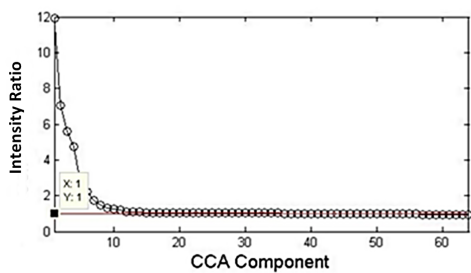
The HD-sEMG signals (64 channels) were generated using the model described in the previous section (section 2.2.4) for 100 MUs at 20 %MVC corresponding to 36 active MUs. Preliminary experimentation was performed to estimate the level of the SNR (see section 2.2.6). Then, WGN and PLI components were added so that we obtain an SNR dispersion among channels that resembles to SNR dispersion obtained for the experimental HD-sEMG recordings. In fact, the mean SNR for the five subjects was set to  $17.44 \pm 4.34$  dB. Therefore, we added first the WGN, in order to obtain an SNR dispersion over the 64 signals of the grid that follows a normal law of a  $20 \pm 3$  dB. Then, we selectively incorporated the PLI noise by creating an SNR vector with low values that follows a normal distribution of  $7 \pm 3$  dB and a random number of channels (between 15 and 20). This noise repartition has been inspired by the obtained experimental signals. We generated five noisy signal sets for the same anatomy (for precise denoising evaluation) using the procedure described above. Then, to test the limits of the proposed denoising method, we dramatically reduced, for the 5<sup>th</sup> simulation, the SNR of the channels contaminated with both WGN and PLI by using a normal distribution of  $5 \pm 2$  dB.

The SNR of all the simulated signals are presented in Table 2.3 for the denoised channels before and after denoising with the corresponding intensity ratio threshold and the NRMSE. The mean NRMSE value for the five noise simulations over the same anatomy is equal to  $7.83 \pm 2.48$  %. Figure 2.3 exposes the results for simulation 5 (see Table 2.3). Figure 2.3a represents the obtained curve by ranking the estimated canonical components according to the proposed energy ratio (see section 2.3). One can observe the high values corresponding to sources which mainly contain sEMG activity and the low values corresponding to sources dominated by the noise.

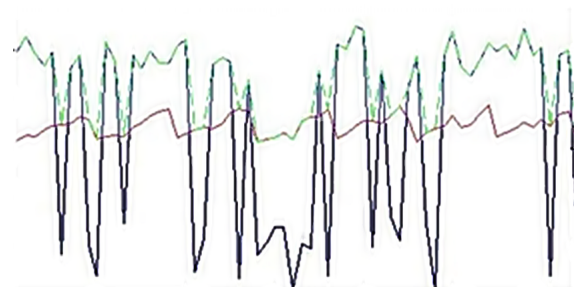
Table 2.3: The SNR of the noisy simulated HD-sEMG signals before and after denoising in dB and the corresponding SNR improvement, intensity ratio threshold and NRMSE.

Simulation number	Raw SNR (mean $\pm$ std) dB	Denoised SNR (mean $\pm$ std) dB	SNR improvement after CCA (mean $\pm$ std)dB	Number of denoised channels/Intensity ratio threshold	NRMSE (mean $\pm$ std) %
1	11.21 $\pm$ 4.52	17.98 $\pm$ 0.77	5.81 $\pm$ 2.46	29/1.4	8.34 $\pm$ 3.73
2	13.16 $\pm$ 1.85	18.59 $\pm$ 1.76	6.64 $\pm$ 2.44	34/1.8	9.28 $\pm$ 2.06
3	11.77 $\pm$ 2.91	17.32 $\pm$ 1.54	6.13 $\pm$ 2.25	33/1.3	9.83 $\pm$ 3.36
4	11.30 $\pm$ 5.12	16.78 $\pm$ 1.65	5.47 $\pm$ 2.24	32/1.5	7.40 $\pm$ 1.24
5	4.38 $\pm$ 2.23	17.11 $\pm$ 1.11	12.73 $\pm$ 2.52	21/1.0	4.34 $\pm$ 2.05

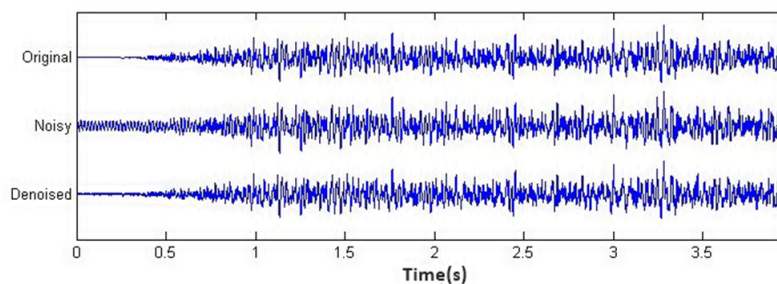
One can also observe the threshold used for the denoising procedure (equal to 1.2) which corresponds to 80 % of correlation between the obtained bipolar signals from the grid and the bipolar signals after they have been denoised by CCA approach (see section 2.2.2). The result of the denoising procedure is presented in Figures 2.3b and represents the raw SNR dispersion (blue line), the SNR dispersion after CCA (red line) and sCCA (dashed green line) among the 64 channels of the grid. In Figure 2.3c and for illustration purposes, original, noisy, and denoised signal for channel 22 are respectively presented for the studied simulation. We can clearly see the resemblance between the original and the denoised



(a) The 64 intensity ratios in descending order for simulation 5. The horizontal red line represents the corresponding threshold.



(b) The SNR dispersion of the 64 channels before (blue) and after (red) denoising with CCA and sCCA (green) presented in order for simulation 5.



(c) Top: Original sEMG signal; Middle: Noisy sEMG signal; Bottom: Denoised signal after sCCA for channel number 22 of the grid for simulation 5 in Arbitrary Units (A.U).

Figure 2.3: Obtained denoising results for the simulated HD-sEMG signals at 20 %MVC (Simulation 5).

signal. We can notice an improvement in the SNR especially for the channels with the highest noise (Figure 2.3b). The mean value of SNR of the original channels was equal to  $4.38 \pm 2.23$  dB but after denoising using CCA, this value increased to  $17.11 \pm 1.11$  dB, which means that we obtained an SNR

improvement of  $12.73 \pm 2.52$  dB after CCA denoising. Thanks to sCCA procedure, the channel with an original SNR higher than the one obtained after CCA procedure (red line) are conserved (green dashed line). Finally, in order to evaluate the accuracy of the proposed denoising method, the mean NRMSE (defined by equation 2.10) was computed for the denoised channels of this simulation and was equal to  $4.34 \pm 2.05$  %.

In the later two sections, we will apply the CCA and sCCA denoising method on experimental signals obtained from five subjects following the protocol described in section 2.2.6. This experimental study allows us to test the performance and to approve of the method on real signals through computing the SNR improvement.

## 2.2.6 Experimental protocol

In this section, we will report the details of the experimental protocol used in order to collect the HD-sEMG signals used for the experimental denoising study.

### 2.2.6.1 Subjects

Five healthy male subjects without any musculoskeletal pathology (mean  $\pm$  std, age:  $23.2 \pm 2.1$  years; stature:  $178.6 \pm 5.3$  cm; body mass:  $72.6 \pm 7.8$  kg) participated in the study respecting the declaration of Helsinki. All participants provided their written consent before participating in the study and did not relate any history of muscular or neurophysiological problem at the upper limbs.

### 2.2.6.2 Mechanical and electrophysiological recordings

The sEMG signals of the two dimensional adhesive array consisting of 64 electrodes of circular shape with an inter-electrode distance of 4 mm and an electrode diameter of 1.5 mm were recorded from the BB, during isometric voluntary contractions. The reference electrode and the ground were placed on the elbow bone and around the wrist respectively (see figure 2.5).

The monopolar sEMG signals were acquired using TMSI REFA 136 acquisition system (Twente Medical Systems International, the Netherlands) with the dedicated software (Polybench). The global force signal was measured simultaneously with the sEMG signals using a strain gauge (Celtron STC SS S-beam, Stainless Steel, IP67), and displayed in real-time on an oscilloscope as visual feedback to the subjects. The global setup is illustrated in Figure 2.4. This protocol allows us to obtain, for each subject, 64 signals of 5.5 seconds (11000 samples), wherein the first 0.5 second represent the rest period (signals recorded with no muscular activity) and the interval of 5 seconds (between 0.5 s and 5.5 s ) is the actual muscle contraction .

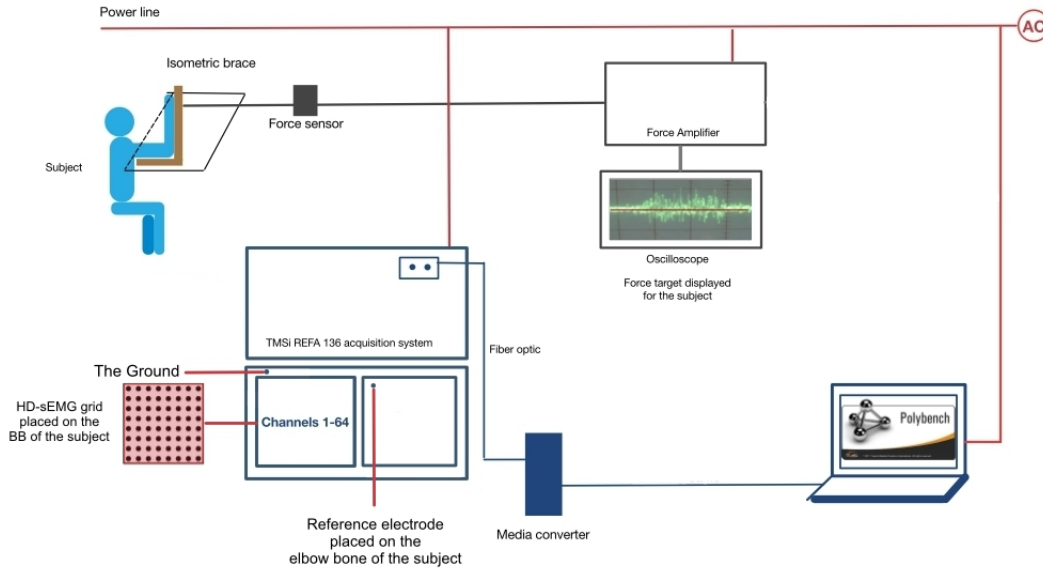


Figure 2.4: The experimental setup used for the recording of the HD-sEMG signals for isometric isotonic contractions of 20 %MVC.

### 2.2.6.3 Procedure

Subjects were seated upright in a chair with the forearm in a horizontal position, and the elbow angle fixed at  $90^\circ$ . After skin preparation (shaving, abrading and cleaning) the HD-sEMG grid of 64 electrodes was placed either proximally ( $\sim 1.5$  cm) from the middle of the BB muscle according to the SENIAM recommendations [110]. Isometric elbow flexion force was recorded synchronously with the HD-sEMG signals. The protocol started by measuring the MVC. This was done in three trials, each trial lasted 3 s with a 2 mins rest period in between in order to avoid fatigue accumulation. The MVC was chosen as reference for sub-level contractions. Three trials of isometric contractions were recorded at 20, 50 and 80 %MVC by providing a target to the subject with 1.5 mins rest in between. The target signal was displayed in real time on the oscilloscope along with the subject's instantaneous contraction level as a feedback. These force plateaus lasted 5 seconds wherein the subject was trained to keep the force as constant as possible by watching the feedback signal on the oscilloscope. The recorded signals also contained 0.5 second of rest (without any contraction) before the beginning of the contraction. This rest period is needed for SNR and intensity ratio calculations (details in sections 2.2.1 and 2.2.2).

### 2.2.7 Denoising experimental HD-sEMG signals

The CCA and sCCA algorithms were applied on the recorded HD-sEMG signals at 20 %MVC from the five subjects following the experimental protocol described in section 3.3.2.1. The first step of the proposed method is the decomposition of the 64 monopolar HD-sEMG signals into their corresponding sources.

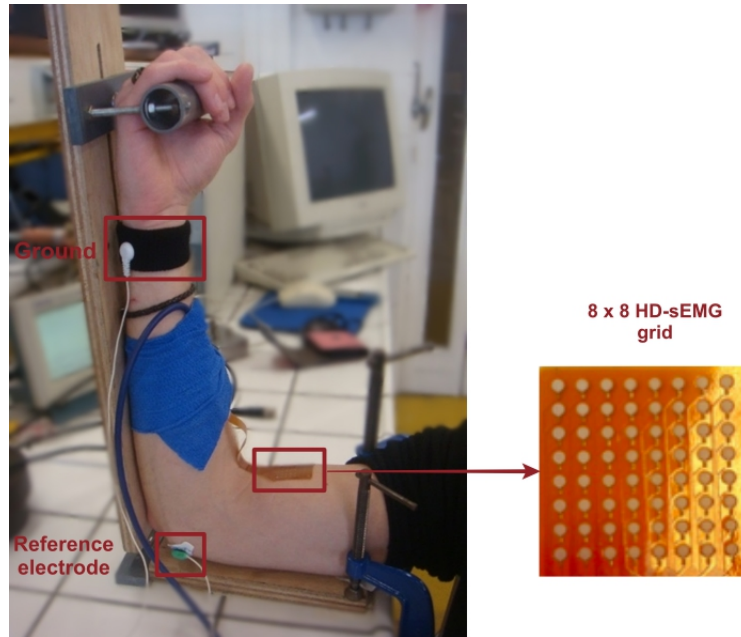


Figure 2.5: The HD-sEMG grid placement on the BB.

Figure 2.6 shows the first 32 estimated sources after decomposition with CCA for subject 1. We have chosen this subject (subject 1) as representative to all the subjects. These sources are ranked in a descending order based on the value of the autocorrelation coefficient for a unitary time delay. According to Figure 2.6, the 50 Hz PLI can clearly be localized on the first canonical component with the highest autocorrelation coefficient, as well as a MA well isolated, in this case ( $6^{th}$  canonical component). The WGN, according to visual inspection, seems to be dispersed on several components beginning from the  $23^{rd}$  component to the  $64^{th}$  component since it has low autocorrelation coefficients. The muscle activity is almost concentrated in the remained sources inside the ranking interval ( $[1 - 23]$ ). It is also interesting to observe few isolated MUAPs in the  $16^{th}$  and  $18^{th}$  source respectively. From the observation of the estimated sources, one can rapidly conclude that a single thresholding rule applied on the canonical components (as in the work of Hassan et al. [130]) will be insufficient for separating the muscle activity from the several sources of noise. Thus, it becomes necessary to construct a multi-level thresholding rule to realize, in an efficient way, the denoising operation.

Figure 2.7a, presents the dispersion of the intensity ratio  $r_j$  (see equation 2.7) ranked in a descending order for all subjects (solid line) and for subject 1 (dashed blue curve). It can be evidenced that between 0 and 2, there is a minimal  $r_j$  variance indicating intensity ratio reproducibility among subjects. These two observations indicate that the canonical components inside this intensity ratio range seem to be related to instrumental noise (WGN and PLI) and their ratio values are almost constant among subjects. In contrary, in the remaining range, an important ratio variability among subjects can be observed, indicating that this range contains muscle activity. Afterwards, in order to define the optimal threshold for each subject allowing the elimination of the sources of noise without removing the sEMG activity.

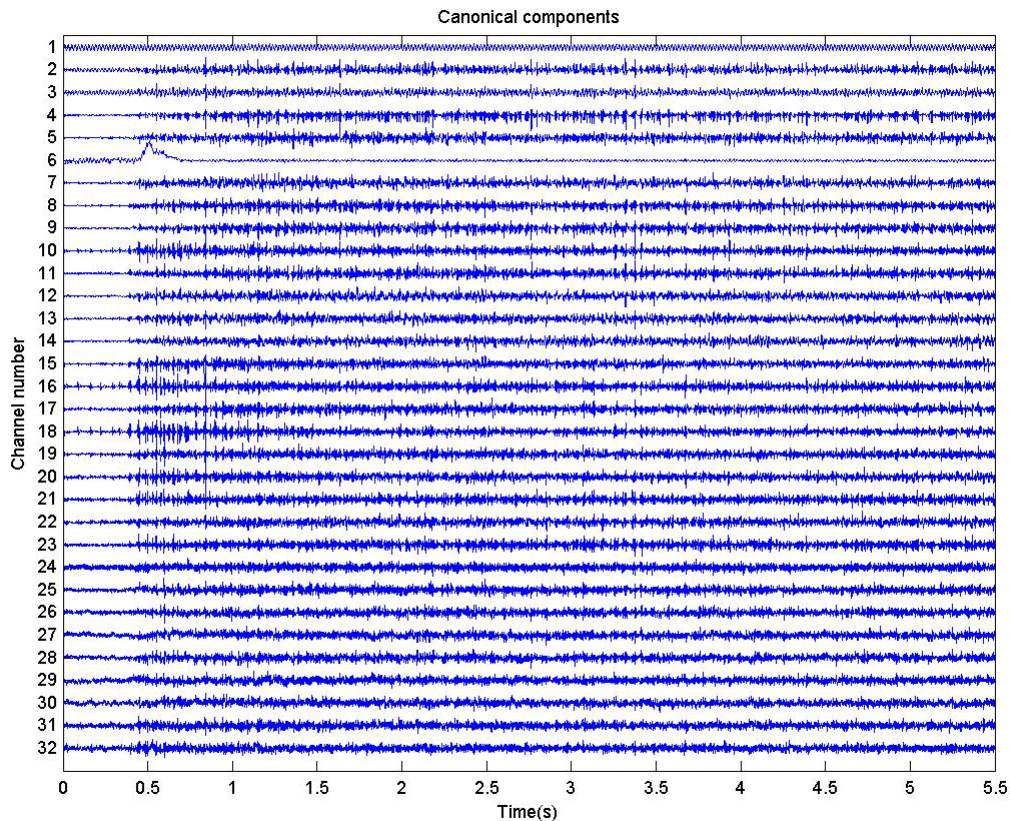
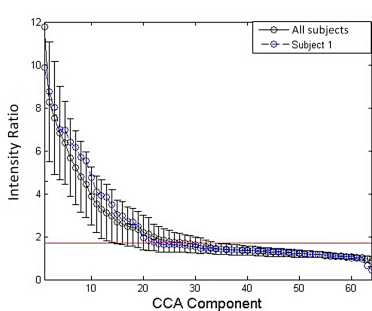


Figure 2.6: The first 32 canonical components (a.u) in descending order from top to bottom according to the value of the autocorrelation coefficient for subject 1 which we found representative of the subjects.

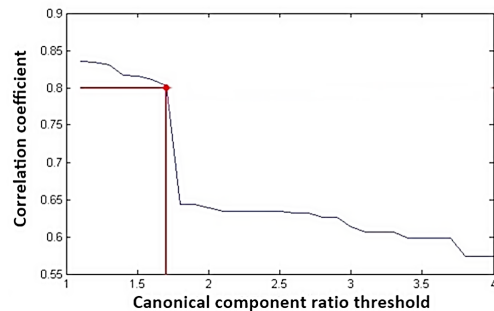
We decided to rely on the mean correlation coefficient value computed between the 32 bipolar signals obtained from vertical differentiation (muscle fiber direction) of signals from the grid before and after denoising with CCA algorithm by varying, each time, the ratio threshold (from  $r_j = 1.1$  to  $r_j = 4$ ) with a step of 0.1. This criterion justifies the rule to choose a threshold in a way that will keep the majority of sEMG sources, and removes all the sources of noise. Since our target is to eliminate the maximum of the sources with low  $r_j$  (that represent the noise) but to maintain a high correlation with the original bipolar signal, we have chosen 0.8 as an acceptable value (notice that with sCCA, a higher coefficient was obtained ( $> 0.9$ )). Since it is perfectly logical to obtain a decrease in the correlation coefficient after elimination of the noise. Meanwhile, we made sure to efficiently verify this level of correlation using simulation. Hence, the mean correlation coefficient was computed for each subject by changing the ratio threshold. An example of the thresholding procedure is presented in Figure 2.7b for subject 1. Figure 2.7c presents the eliminated canonical components in red in a descending order with respect to the correlation coefficient. In this case the chosen threshold is equal to 1.7 (see Figure 2.7b). In addition, it can be observed that this new thresholding rule, in the ranked intensity ratio curve (Figure 2.7a) can be assimilated as a multi-level thresholding rule in the ranked canonical component correlation curve

(Figure 2.7c).

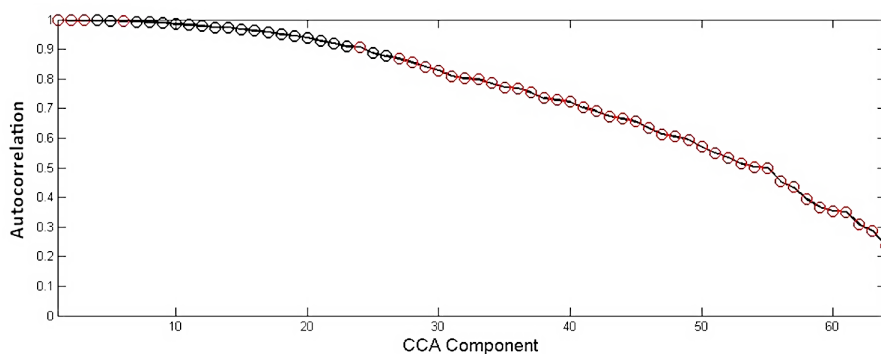
The obtained SNR dispersion curves for the five subjects before and after denoising procedures are shown in Figure 2.8. We had originally, for subject 1 (Figure 2.8), a large dispersion of the SNR throughout the grid ( $17.83 \pm 4.5$  dB) with values that goes from 23 dB (channel 33) to 4 dB (channel 62). However, after denoising via the CCA algorithm with the proposed thresholding rule, we achieved a grid SNR dispersion (red line) that is smaller (std = 0.48 dB) and, in this case, a mean SNR increase (mean = 18.4 dB). After applying sCCA (green line), one can observe, for this subject, a second mean SNR increase (18.84 dB) and a SNR dispersion increase (2.44 dB) but lower than the SNR dispersion of the raw noisy signals. These augmentations can be justified by the conservation, using the proposed method, of the original signals that have a SNR better than their denoised version. If we look at the other results, we can observe that we obtain a consistency in the denoising process. The main obtained result is the significant SNR increase of the noisiest channels that makes them acceptable for later uses. In Figure



(a) The 64 intensity ratios in descending order for the five subjects (solid curve) and for the chosen subject (dashed blue curve). The horizontal red line represents the threshold for this subject.



(b) The mean variation of the correlation coefficient between the 32 bipolar signals before and after denoising with CCA according to the intensity ratio threshold for the chosen subject.



(c) The 64 autocorrelation coefficients of the canonical components in descending order for the same subject as in 2.7b. The points in red represent the sources eliminated before reconstruction.

Figure 2.7: The CCA thresholding procedure for subject 1.

2.9 and for illustration purposes, we presented the sEMG signals (Figure 2.9a) and the corresponding PSD (Figure 2.9b) before and after denoising with CCA for the channel 62 of the same subject (subject 1). We chose this channel because it had an SNR = 4 dB (see Figure 2.8) which was the lowest SNR for

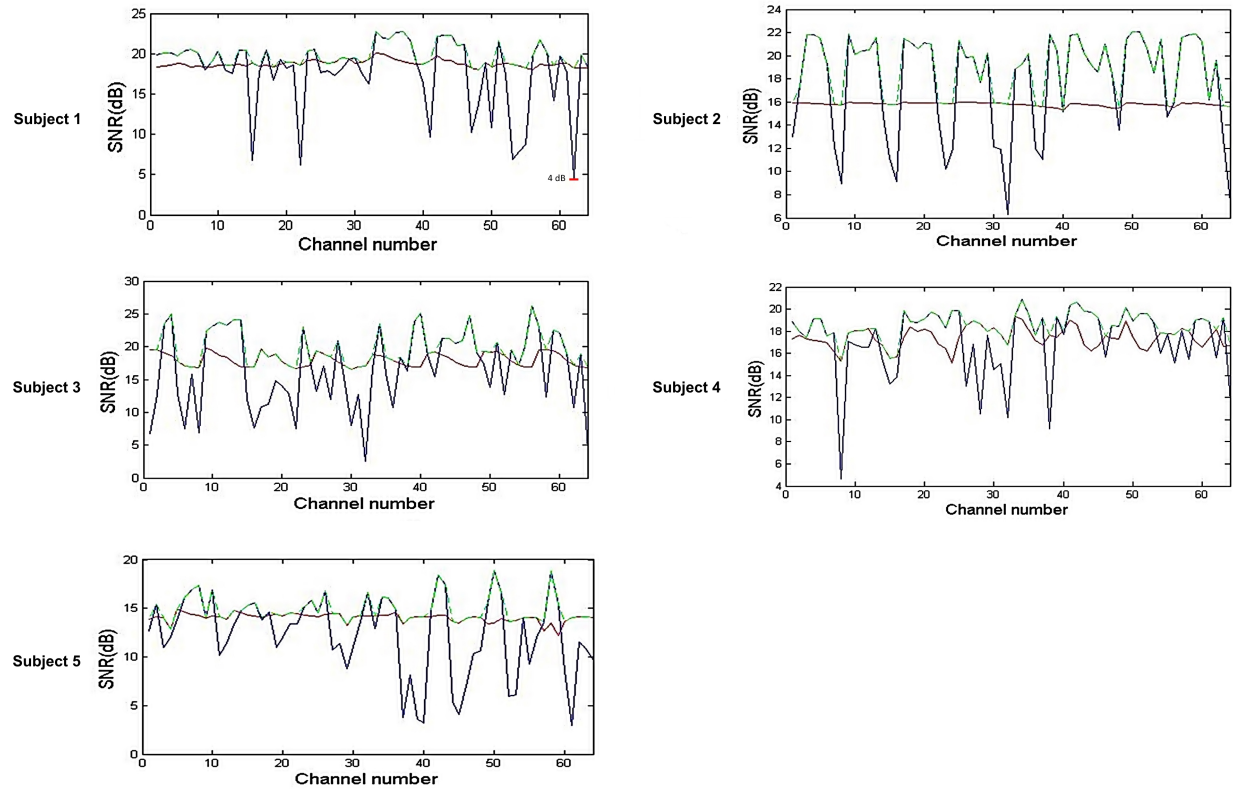


Figure 2.8: The SNR dispersion of the 64 channels before (blue) and after (red) denoising with CCA and selective CCA (green) for the five subjects.

this subject. Figure 2.9 allows us to confirm the fact that our denoising method does not alter the sEMG signals since after elimination of the 50 Hz noise the PSD of the signal is preserved with a small decrease due to the elimination of the WGN as well. It is also important to note the improvement in SNR of the channel 62 that is about 14.4 dB. Moreover, we computed the channel noise energy dispersion, for all the subjects, using signal intervals without muscle activity for the 64 monopolar signals, the 32 bipolar signals (obtained by subtracting the electrode signals along the fiber direction) and the 64 denoised signals with FastICA, CCA and sCCA respectively (see Figure 2.11a). According to this result, the CCA and especially the sCCA approach seems to be more powerful in eliminating noise than the classical FastICA and bipolar denoising methods. To evaluate the reproducibility of the denoising performances, we applied the two proposed approaches (CCA and sCCA) on signals obtained from five different subjects. Table 2.4 presents the performance of the denoising process for all the subjects. In order to clearly exhibit this performance, we chose to indicate the value of the SNR for the noisiest channels before and after denoising with CCA, as well as the global mean improvement in the SNR (in dB). We also presented the denoised channels number after sCCA and the corresponding intensity ratio threshold. It is important to note that this is a personalized method, since the number of denoised channels and the threshold value are different for each subject depending on the nature of the noise dispersion in the grid. We can clearly

Table 2.4: The SNR of the selected HD-sEMG signals before and after denoising in dB and the corresponding SNR improvement, denoised channels number, and intensity ratio threshold

Subject	Raw signal SNR (mean $\pm$ std) dB	Denoised signal SNR (mean $\pm$ std) dB	SNR improvement after CCA (mean $\pm$ std) dB	Number of denoised channels	Intensity ratio threshold
1	14.52 $\pm$ 4.66	18.70 $\pm$ 0.35	4.13 $\pm$ 4.52	25	1.7
2	12.21 $\pm$ 3.96	18.00 $\pm$ 1.06	5.79 $\pm$ 3.66	35	1.9
3	11.72 $\pm$ 2.47	15.74 $\pm$ 0.16	4.02 $\pm$ 2.51	21	2
4	15.39 $\pm$ 2.06	17.91 $\pm$ 0.19	2.32 $\pm$ 2.87	25	1.8
5	12.44 $\pm$ 4.09	14.87 $\pm$ 1.36	3.49 $\pm$ 2.24	36	2.5

see the improvement in the SNR for the denoised channels with the noteworthy decrease of the standard deviation between these channels.

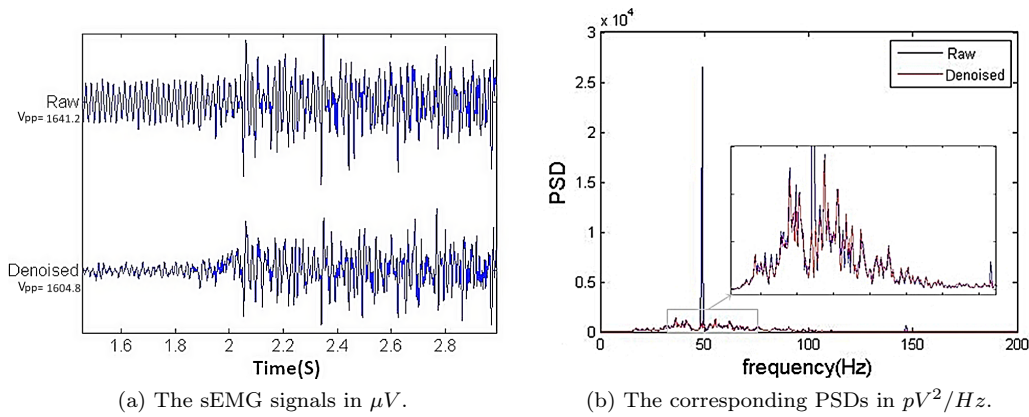


Figure 2.9: The sEMG signals and the corresponding PSDs for channel 62 before and after denoising with CCA for subject 1.

Finally, we applied our methods, CCA and sCCA denoising techniques, on the experimental signals at 50 %MVC. The obtained results are presented in Table 2.5. The first observation from these results is that we have less improvement for this level of contraction. This is explained by the fact that we have already an acceptable SNR for all the channels before denoising. Secondly, we can see that the number of the channels that have been denoised is less than that of the denoised signal at 20 %MVC. These results seem logical since the level of noise doesn't really change with force level increase, unlike the sEMG energy that increases with force level increase causing the SNR to increase as a result. As for the HD-sEMG signal recorded at 80 %MVC, we found no need to denoise them because we had an SNR  $>$  30 dB which is very acceptable.

### 2.2.8 Comparative study

The performance of the proposed denoising methods (CCA and sCCA), in term of mean SNR computed over the leads of the grid and among subjects, is evaluated and compared, using analysis of variance (ANOVA), to other methods including CCA based combinations: CCA-EMD, CCA-Wavelet (CCA-

Table 2.5: The SNR of the selected HD-sEMG signals before and after denoising in dB and the corresponding SNR improvement, denoised channels number, and intensity ratio threshold

Subject	Raw signal SNR (mean $\pm$ std) dB	Denoised signal SNR (mean $\pm$ std) dB	SNR improvement after CCA (mean $\pm$ std) dB	Number of denoised channels	Intensity ratio threshold
1	16.23 $\pm$ 3.06	19.34 $\pm$ 1.32	3.11 $\pm$ 1.96	15	2.5
2	15.88 $\pm$ 2.04	19.57 $\pm$ 2.44	4.68 $\pm$ 2.29	17	1.6
3	22.47 $\pm$ 5.07	29.56 $\pm$ 3.73	7.09 $\pm$ 5.33	26	1.8
4	25.72 $\pm$ 3.45	29.51 $\pm$ 3.91	3.79 $\pm$ 1.87	16	1.2
5	17.76 $\pm$ 2.78	21.65 $\pm$ 2.47	3.88 $\pm$ 2.90	15	1.6

WVT) and ICA (FastICA). In the next paragraphs, we will present and explain these different algorithms then we will conclude this section by the results of this study.

### 2.2.8.1 CCA-EMD

The CCA-EMD algorithm was recently developed in our team to denoise uterine sEMG recordings [130]. It uses CCA as a first step to extract the uterine bursts then uses EMD approach as a second filter stage to remove the residual noise [130]. The EMD was proposed in the late 90s to study surface wave evolution [139]. It proposes a sequential decomposition of a given signal into a sum of oscillatory modes, called intrinsic mode functions (IMF), which are amplitude and frequency modulated zero mean oscillatory signals, plus a non-zero mean low degree polynomial remainder. These IMFs are some kind of sub-bands of the signal.

This decomposition method was applied on the 64 sEMG signals after denoising with CCA. The effective steps of this procedure are presented in Algorithm 2.1.

---

#### Algorithm 2.1 Empirical Mode Decomposition (EMD)

---

1. Identify of the Extrema of  $EMG_i(t)$
  2. Interpolate along the point of  $EMG_i(t)$  identified in the first step, in order to form an upper  $e_{i_{max}}(t)$  and lower envelope  $e_{i_{min}}(t)$ .
  3. Compute the mean  $m_i(t) = (e_{i_{max}}(t) + e_{i_{min}}(t))/2$
  4. Extract of the detail  $d_i(t) = EMG_i(t) - m_i(t)$
  5. If  $d_i(t)$  does not fulfill the criteria defining an IMF (presented in [139]), repeat steps 2-4  
Else move to step 6.
  6. Compute the mean squared error between two consecutive IMFs and compare it to a stopping criterion
  7. If the stopping condition is not reached, Redo steps 1-6 on the residual  $m_i(t)$   
Else the sifting process is finalized and the final residue can be estimated as the difference between  $EMG_i(t)$  and the sum of all IMFs.
- 

The denoising of the HD-sEMG signals is divided into three steps:

1. Decomposing the signal into IMFs by following the Algorithm 2.1.

2. Thresholding the estimated IMFs.
3. Reconstructing the signal.

This denoising procedure is applied for each one of the 64 signals of the HD-sEMG grid, therefore it is much more time consuming than the other presented methods.

### 2.2.8.2 CCA-WVT

Similarly, this method uses the CCA-BSS technique at first then the wavelet packet transform as a filtering stage [127, 140]. The concept of Wavelet (WVT) filtering is defined as the cross correlation of the signal with a scaled and time shifted wavelet  $\Psi_{a,b}$  defined as:

$$\Psi_{a,b}(m) = \sqrt{|a|}\Psi((m - b)/a) \quad (2.11)$$

With  $\Psi_{a,b}$  being the mother wavelet and a, b the scale and translation parameters respectively.

This wavelet based signal decomposition is an iterative process that allows us to represent the signal as a sum of wavelets with different locations and scales. First, two symmetric filters are created from the mother wavelet. These two signals will represent the orthogonal basis for the low and high frequency signals generation in the next iterations. Figure 2.10 presents the wavelet decomposition tree of an EMG signal, where the A boxes are the low frequency components (approximations) obtained by the Low Pass Filter (LPF) and the D boxes are the high frequency components (details) obtained by the High Pass Filter (HPF).

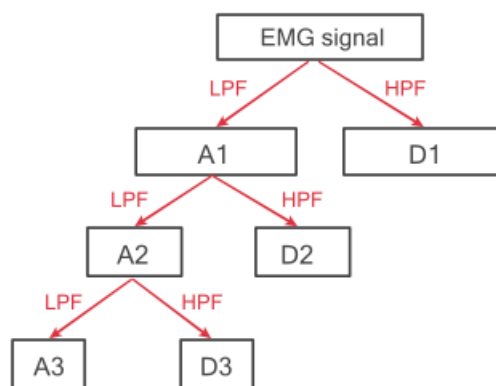


Figure 2.10: The wavelet decomposition tree.

The denoising using this method usually targets the WGN by soft thresholding. Therefore, a thresholding level obtained from the Donoho [141] estimator is used. This threshold is defined as follow:

$$T_l = \sigma \sqrt{2 \log(l)} \quad (2.12)$$

Where  $\sigma$  is the noise standard deviation and  $l$  is the signal length.

### 2.2.8.3 ICA

The ICA is a commonly used BSS method that assumes that the subcomponents are non-Gaussian signals and that they are statistically independent [131]. FastICA seeks an orthogonal rotation of pre-whitened data, through a fixed-point iteration scheme, that maximizes a measure of non-Gaussianity of the rotated components. The steps of this technique are presented in Algorithm 2.2. Afterwards, the

---

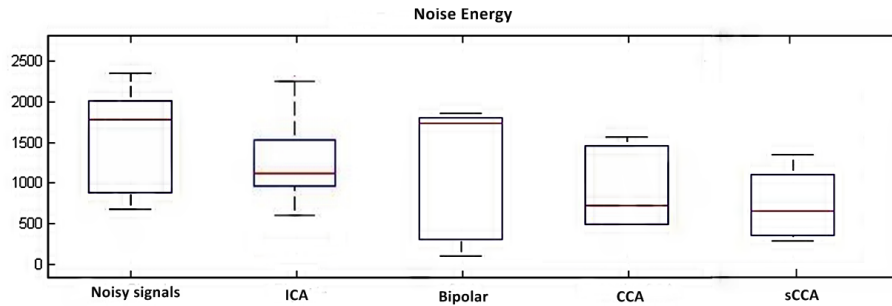
#### Algorithm 2.2 Fast ICA.

---

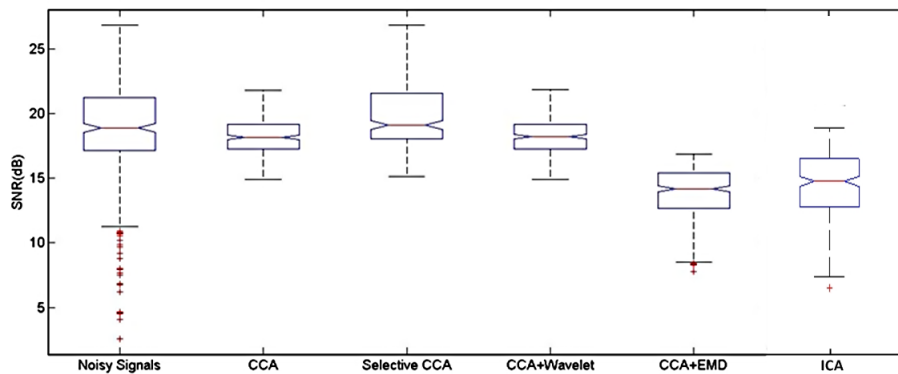
1. Pre-whitening of  $X$  (defined in Equation 2.1)
  2. Randomize the initial weight vector  $w$
  3.  $\mathbf{W}^+ = E(Xg(W^T \mathbf{X})^T) - E(g'(W^T \mathbf{X}))W$ , where  $E(X)$  is the mean over all the columns of  $X$ , and  $g$  is the first derivative of a nonquadratic nonlinearity function
  4.  $\mathbf{W} = \mathbf{W}^+ / \|\mathbf{W}^+\|$
  5. If not converged repeat all
- 

selection of ICA components accounting for the noise is based on visual inspection of the rest period and the muscle activation segments of the independent estimated sources. Then, the signals are reconstructed after zeroing the corresponding noise components [130, 131];

The performance comparison of the three proposed denoising methods with CCA-WVT, CCA-EMD and FastICA approaches is presented in Figure 2.11b. A Kruskal Wallis nonparametric one-way ANOVA revealed significant differences ( $\chi^2(dof = 3) = 647.19, p < 0.01$ ) between the five methods used for denoising the HD-sEMG signals. Then, Post-hoc tests highlighted important differences between the CCA-EMD combination (Median SNR = 14.17 dB) and the FastICA (Median SNR = 15.03 dB) with all the other methods. We also note a significant difference between the sCCA (Median SNR = 19 dB) and the other methods and no significant difference between the CCA (Median SNR = 17.87 dB) and the CCA-WVT combinations (Median SNR = 18.08 dB). Considering the computing time for eventual real-time applications, these four CCA based approaches were evaluated. And the shorter execution time was obtained for the CCA, sCCA and FastICA denoising methods with 2 seconds/subject in comparison with the CCA-EMD method, which is more computationally complex and takes about 2459 seconds/subject for each execution. The CCA-WVT combination takes about 5 seconds/subject.



(a) The averaged noise energy ( $pV^2$ ) (over electrodes) for the five subjects for the raw monopolar (64 electrodes), bipolar (32 electrodes) and denoised signals using ICA, CCA (64 electrodes) and sCCA (64 electrodes).



(b) The SNR for the Noisy signals and denoised signals using CCA, Selective CCA, CCA WVT, CCA EMD and ICA respectively (dB).

Figure 2.11: Obtained results of the comparative study for the five subjects.

## 2.2.9 Discussion and conclusion

A CCA subject specific denoising framework was presented in this study and evaluated in both simulation and experiment. This novel application of the CCA formalism was applied to denoise HD-sEMG signals during low isometric isotonic contraction levels (20 %MVC) of the BB. Numeric simulation and experimental sessions with five subjects were performed. These types of contractions are usually used for the study of the recruitment schemes of the active MUs by decomposition techniques of sEMG signals [142, 143]. Other application would be the study of shape modifications of the sEMG PDF with force variation and hence force level classification [120, 50] knowing that all processing techniques used in these studies are extremely sensitive to noise. In addition, at this contraction level, the noise contribution has stronger influence on the analysis efficiency compared to higher contraction levels. We noticed, as expected, on the recorded signals that the noise intensity spreads on the grid in a heterogeneous way linked to local disturbances as bad interfacing between the skin and the electrodes and active MU repartition. Moreover, the PLI component (50 Hz) occurred none homogeneously on sEMG channels leading to the presence of an important SNR variance among the channels of the HD-sEMG grids. Classically, if a channel is very noisy, it is suppressed or interpolated leading to a partial loss of information on the

muscle contraction activity.

In this study, by keeping all the channels of the grid, we proposed a methodology that deals with this complex problem and bears on the CCA algorithm. This methodology is based on the proposition of a thresholding paradigm linked to the noise intensity versus the muscle activity (ranked intensity ratio). Compared to previous single thresholding rule applied on the ranked canonical components [130], this thresholding on ranked intensity ratio is able to separate the muscle activity from several sources of noise (PLI and WGN). Since the noise attacks the channels in a non uniform manner, we proposed to combine raw channels having high SNR with denoised ones. We defined this procedure as sCCA. To validate the efficiency of the proposed procedure, we proposed to use a HD-sEMG generation model considering a planar multilayered volume conductor. This model allowed us to precisely assess the denoising accuracy by measuring the overall error between signals among all the denoised and the original simulated signals. This noise was incorporated in a realistic manner. The simulations also permit to check the validity of the correlation value fixed to 80 % for obtaining the energy ratio threshold. In fact, fixing this value is critical since if it is taken too high, the obtained bipolar denoised signals will fit too much to the bipolar signals leading to non efficient suppressing of the present noise. Concerning the ratio threshold, it will decrease leading to the conservation of noisy canonical component. In contrary, if the correlation value is too low, the threshold will increase leading to possible suppression of sEMG activity. To face this problem, the chosen value has to be a good compromise between suppressing maximum of noise and conserving maximum of muscle activity. According to the simulation results, the chosen value (80 %) seems to be relevant. Since we measured the mean NRMSE for the five simulated signals which was about 7 %. It clearly indicates that, in this simulation case, the proposed approaches succeeded in denoising the HD-sEMG signals. It is also important to note, that the number of denoised channels has a major effect on the efficiency of the denoising process. By observing the first four simulations (see Table 2.3), we can see that we have results that are consistent with the experimental ones. However, the last simulation demonstrated the effect of both noise dispersion in the grid and number of the denoised channels on the denoising behavior. In this case, the proposed method denoised mainly the channels with very low SNR due to the important dispersion of the grid SNR. Further studies will be done to better investigate this denoising behavior. To strengthen the validation of the proposed approaches, we applied them to denoise data from five subjects following isometric isotonic protocol on the BB as depicted on Figure 2.4. The algorithms were applied in a personalized manner since the number of denoised channels along with the intensity ratio threshold were adapted to the subject's data (see Table 2.4). In fact, the proposed ranked intensity ratio threshold is different for each subject (subject specific). Chosen based on the mean correlation maximization (among channels and subjects) between the bipolar signals from the raw recordings and the denoised bipolar signals after CCA, and threshold maximization in order to remove the maximum of noise. This operation allows us to check that muscle activity has been conserved

in the denoised signals and a maximum amount of noise has been suppressed as explained before. The level of correlation was chosen based on the fact that after denoising, the bipolar denoised signals should be different (in a small range) from the raw bipolar signals. In fact, it is supposed that the denoised bipolar signals have less noise as it can be seen in Figure 2.11a compared to classical bipolar operation. Thus, a value of 80 % for the mean correlation seems to be efficient to ensure the conservation of the sEMG sources in the proposed application. One can imagine for future work the design of optimization criterion to fix this value in a more precise manner. It can be noted on Figure 2.11b, that the noise is spread with an important SNR variance which complicates the denoising operation. Despite this strong constraint, the proposed methods were able to enhance mean SNR and reduce the SNR variance of the grid for all the subjects as presented on Figure 2.11. Concerning the assessment of the denoising efficiency, we observed that both WGN and PLI component were eliminated in an efficient way without altering neither the time or the spectral contents of the HD-sEMG recordings (see Figure 2.9). The observed MA seems also to be identified on few estimated sources and can be suppressed by the proposed procedures or by additional adequate post-processing routines as pattern matching in the temporal or the frequency domains. Finally, we operated a comparison between CCA, sCCA, ICA (FastICA) and CCA combination approaches (see Figure 2.11b). Concerning the ICA technique, we found it difficult to remove all the noise components since it does not separate the PLI in one, but in multiple components wherein we have muscle activity. It also appears from the results, that a second stage of denoising is not needed for the considered application.

To summarize the section 2.2, a method for denoising HD-sEMG signals obtained at low muscle contraction level was proposed in this study. At low contraction level, an heterogeneous spreading of the noise was commonly observed, complicating the denoising process. For this purpose, we used a CCA algorithm to decompose signals in several sources, namely canonical components, following a personalized thresholding operation based on ranked energy ratios. This threshold paradigm is motivated by its correspondence to multiple-thresholding operation in the ranked source correlation value curve classically used. This threshold was fixed according to correlation value between bipolar signals from the raw data and bipolar signals from the denoised data using CCA. Furthermore, a selective version (sCCA) was also proposed to deal with the conservation of possible high SNR channels in the grid. The efficiency of the proposed approaches was evaluated both in simulation (five realistic noise configurations) and in experiment with five subjects following an isometric isotonic protocol on the BB. The obtained results demonstrated the ability of the proposed approaches to eliminate the PLI and WGN components efficiently. Also, the CCA and sCCA outperformed bipolar filtering, previous CCA combination approaches and even other commonly used BSS denoising methods (ICA) and in less computation time. In addition, a significant increase in the mean SNR and a decrease of SNR variance were observed on all the subjects using the proposed approaches.

## 2.3 Extraction of the Brachialis's muscle activity from the HD-sEMG recorded at the surface of the Biceps Brachii

The external moment measured at the elbow joint during a pure flexion is the result of the force acting on bones by three muscles: the BB, the BR and the BRD [144]. The BR is reported to have the greatest contribution to the elbow flexion torque production and has been considered as the workhorse of the elbow joint [28]. Since BR is not a superficial muscle, its muscular activity has so far mainly been measured using intramuscular EMG signals [28, 27]. However, some studies attempted to use sEMG technique [27, 145] to measure the BR's activity. Nonetheless, these studies do not take into account the possible interference of co-contracting muscles and, do not consider the BB's impact on the obtained signal. This is legitimated by the anatomical properties of the BR where the proximal part is totally covered by the BB, and the distal part becomes increasingly superficial toward the elbow joint. But even for the distal location, we still have major influence of the BB on the obtained sEMG signal in flexion exercises. Similarly, we have also the influence of the BR on the sEMG of the BB, which is unfortunate for the muscle force estimation models based on sEMG signals not to mention the load sharing problem [145].

If we consider the geometry of the BB and the BR muscles illustrated in Figure 2.12. we can see that the BR lies below the BB and works with it as a synergist to flex the elbow. The origin of BR is in the lower half of the arm and the origin of long head and short head of BB is on the shoulder (Figure 2.12). The distal insertion of the BB (two heads) and the BR are near each other. The extraction of the BR's EMG can help decrease the error in load sharing estimation among the flexor muscles acting on the elbow since usually the BR muscle is not considered in the estimation procedure due to its deep location in the muscle. The external moment measured at the elbow is usually considered to be shared between other flexors that are BB (long and short heads) and BRD. In this study we are going to estimate the contribution of the BR by separating its sEMG signals from the BB ones.

The aim of this section is to recognize two sources of activity in the distal portion of the grid that covers the BB and BR by recording sEMG from the entire length of the BB using a HD-sEMG electrode grid. In order to do so, we attempted to extract the electrical activity of the BR using CCA decomposition and image processing techniques, during isometric isotonic non-fatiguing voluntary flexion of the elbow joints of healthy subjects.

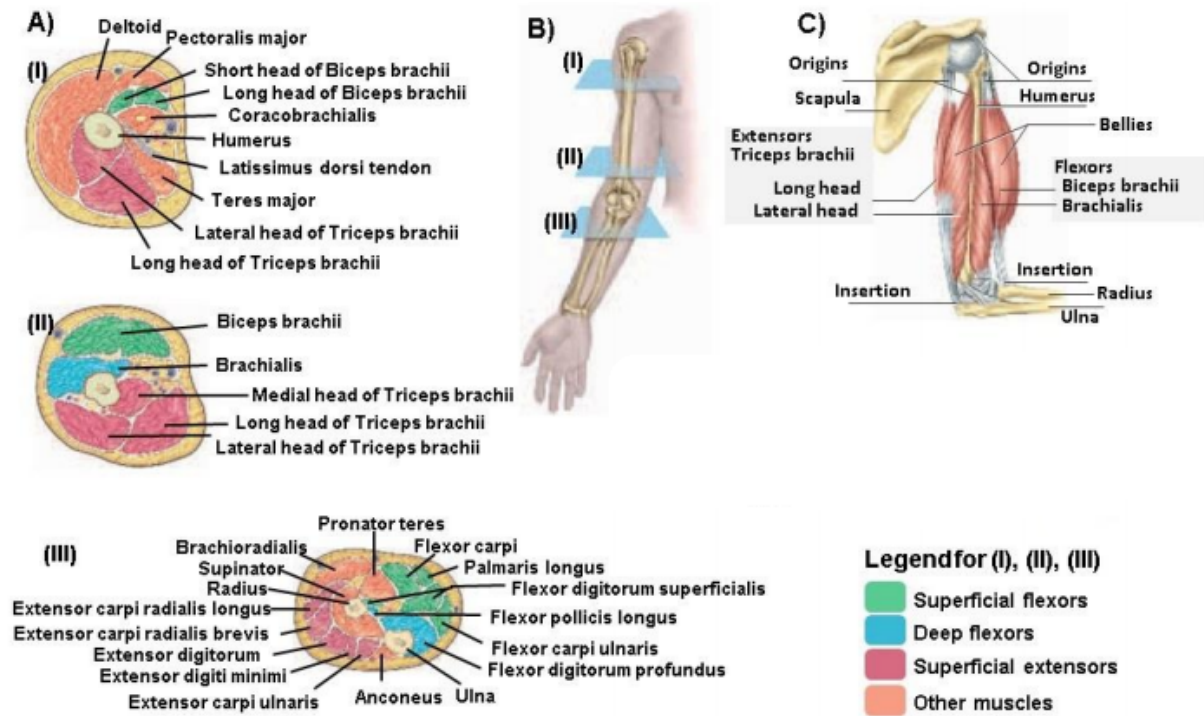


Figure 2.12: A) Serial Cross Sections Through the upper limb. Each section (I, II, and III) is taken at the corresponding labeled level in the figure at panel "B". C) Side view of the right arm showing the BB and BR muscles, which are synergists in elbow flexion. The Triceps Brachii is an antagonist of those two muscles and is the prime mover in elbow extension. Panels "A", "B" and "C" are a courtesy of Dr. Afsharipour.

## 2.3.1 Experimental protocol

### 2.3.1.1 Subjects

Seven healthy male subjects (mean  $\pm$  std, age:  $29.1 \pm 6$  years; stature:  $177 \pm 5.3$  cm; body mass:  $78.5 \pm 6.1$  Kg) participated in the study respecting the latest declaration of Helsinki. All participants provided their written consent before participating in the study and did not relate any history of muscular or neurophysiological problems at the upper limbs.

### 2.3.1.2 Procedure

Subjects were seated upright in a chair with the arm in a horizontal position, and the elbow angle fixed in an isometric brace at  $90^\circ$  (see Figure 2.13). After skin preparation, the two electrode grids were placed on the BB and the BR as shown in Figure 2.13. Elbow flexion torque was recorded synchronously with sEMG. Firstly, the MVC was measured in three trials, each trial lasted 3 s with a 2 mins rest period in between. The maximum MVC was chosen as reference for sub-level contractions. Four isometric contractions at sub-levels of MVC were recorded at 5, 10, 30 and 50 %MVC by providing a target to the subjects. These torque plateaus lasted 30 seconds wherein the subject was trained to keep the torque as

constant as possible. A rest signal of 10 seconds was recorded prior to the beginning of the contraction for denoising requirements. A rest period of 1 min between the recordings was respected in order to avoid fatigue accumulation.

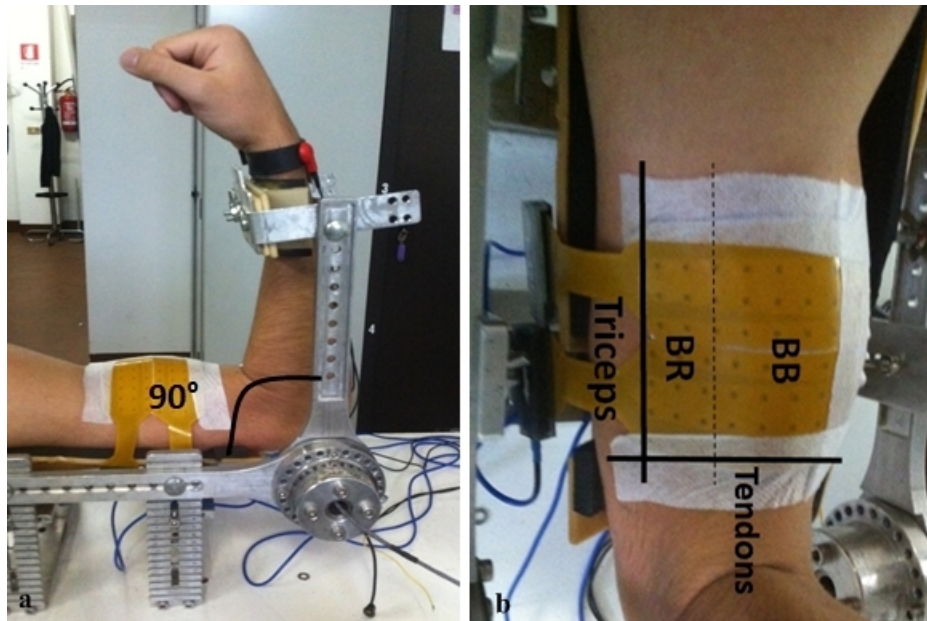


Figure 2.13: The position of the dominant arm during the isometric elbow flexion contraction (left) and the Placement of the HD-sEMG grids on the upper arm during the protocol (right). Note that the elbow was always aligned with the load cells in order to obtain a precise contraction level recording.

### 2.3.1.3 Mechanical and electrophysiological recordings

The isometric brace includes two torque transducers on the right and left side of the arm. The measured torque was displayed using a dual channel biomechanical feedback system (Force Amplifier MISO-II, LISiN, Politecnico di Torino, Italy) for the subject to keep the torque constant during the recordings. Two-dimensional adhesive arrays consisting of 32 circular electrodes ( $\varnothing=3\text{mm}$ , 4 columns and 8 rows, 10 mm inter-electrode distance, LISiN-Italy) were used to acquire 64 signals from the BB and the BR muscles. The adhesive arrays were placed as follow: electrode grid 1, was placed on the distal part of the dominant arm of the subject, where it covered the superficial portion of the BR and the long head of the BB. Electrode grid 2 was placed on the proximal part of the arm (dominant arm), where it covered the BB (see Figure 2.13 and 2.14). Electrode grid 1 and 2 were aligned vertically and horizontally. The reference electrode was placed at the wrist. Prior to the placement of the electrodes, the skin was gently abraded using abrasive paste (Meditec-Every, Parma, Italy). The sEMG signals were recorded in monopolar configuration at 2048 Hz sampling frequency with a resolution of 16 bits.

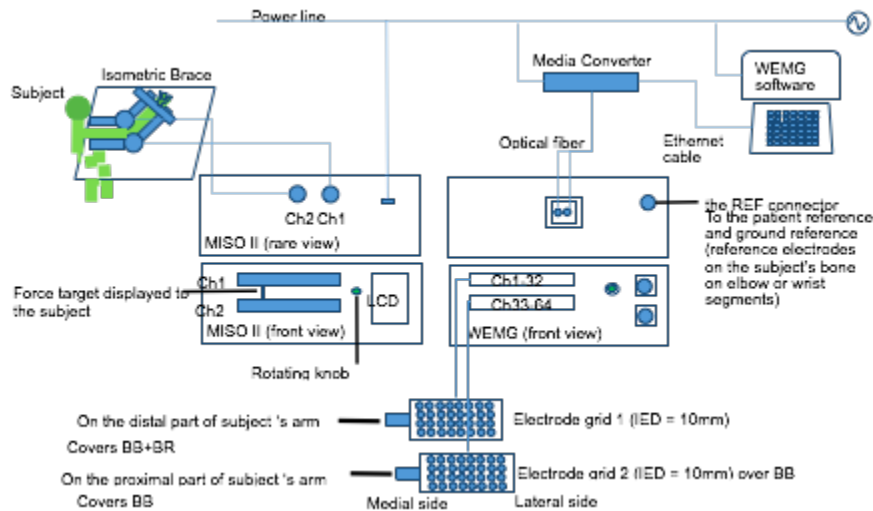


Figure 2.14: The experimental settings: A 64-channel WEMG system, a notebook PC, Isometric brace are used to record from the Brachialis and Biceps Brachii.

### 2.3.2 Data Processing

First and before applying our separation technique, all the signals were band-pass filtered (10-500 Hz; 4th order, zero lag, Butterworth) in order to remove the DC component and the additional noise. Afterwards, we applied our CCA denoising algorithm previously described in section 2.2. This algorithm is used in order to find the adequate threshold for each signal. This threshold is then used in the zeroing of the noise signals in the sources matrix.

In order to isolate the sources corresponding to the BR activity, we examined the weight vectors of each canonical component remaining after applying the thresholding criterion described in section 2.2.2. These weight vectors indicate the contribution of the corresponding source to each electrode of the grid. Therefore, we constructed the  $8 \times 8$  weight maps for each remaining source from these weight vectors. These weight matrices allow us to obtain the location of the activated region in the grid corresponding to a particular source. Then, the remaining sources were classified by applying an image segmentation method on the corresponding weight maps. The classification procedure was applied for each weight map as follow:

1. Transform the map into a grayscale image.
2. Apply the Otsu thresholding method as described in section 2.3.3
3. Classify the source based on the position of the remaining channels with respect to the BR and the BB positions.

Finally, all the sources that correspond to the BR activity were reconstructed using the following equation:

$$X_{BR} = \tilde{A} \times Z_{BR}, \tilde{A} = \tilde{W}^{-1} \quad (2.13)$$

Where the matrix  $Z_{BR}$  represents the source matrix obtained by CCA after zeroing the BB sources, and  $\tilde{A}$  is the estimated mixing matrix. Similarly, the BB sEMG signals will be obtained using eq 2.13 by zeroing, this time, the BR sources from the canonical component matrix and then multiplying it with  $\tilde{A}$ .

$$X_{BB} = \tilde{A} \times Z_{BB}, \tilde{A} = \tilde{W}^{-1} \quad (2.14)$$

With  $Z_{BB}$  the source matrix obtained by CCA after zeroing the BR sources and  $\tilde{A}$  is defined in eq 2.6.

The detailed steps of this algorithm are presented in Figure 2.15.

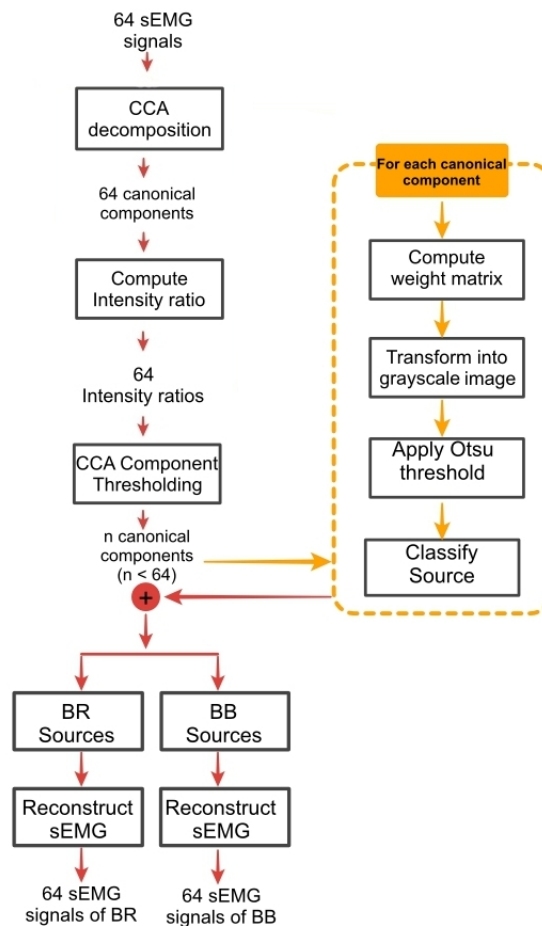


Figure 2.15: The block diagram of the CCA based muscular activity separation algorithm.

All the data were analyzed with MATLAB 7.5 (The MathWorks, Inc, Natick MA, USA).

### 2.3.3 Otsu thresholding method

The Otsu thresholding method is used to automatically perform clustering-based image thresholding. It is an unsupervised method based on finding the optimal threshold that minimizes the intra-class variance between the two classes [146]. The intra-class variance of a grayscale image is defined as:

$$\Omega_i^2(\tau) = \rho_0(\tau) \times \sigma_0(\tau) + \rho_1(\tau) \times \sigma_1(\tau) \quad (2.15)$$

Where  $\rho_{0,1}$  and  $\sigma_{0,1}$  are the probability and the variance of the two classes respectively and  $\tau$  is the threshold.

Otsu also shows that minimizing the intra-class variance is the same as maximizing inter-class variance  $\Omega_b^2(\tau)$  defined in equation (2.16)[146].

$$\Omega_b^2(\tau) = \Omega^2 - \Omega_i^2 = \rho_0(\tau) \times \rho_1(\tau) (\mu_0(\tau) - \mu_1(\tau))^2 \quad (2.16)$$

Where  $\mu_{0,1}$  are the mean values of the two classes and  $\Omega^2$  the total variance.

The algorithm of this method is presented in 2.3.

---

#### Algorithm 2.3 Otsu thresholding algorithm

---

1. Compute histogram and probabilities of each intensity level
  2. Set up initial  $\rho_i(0)$  and  $\mu_i(0)$
  3. For threshold  $\tau = 1$  to maximum intensity
    - Update  $\rho_i$  and  $\mu_i$
    - Compute  $\Omega_b^2(\tau)$
  4. Desired threshold corresponds to the maximum  $\Omega_b^2(\tau)$
- 

### 2.3.4 Application of the separation method on the experimental signals

As described in the previous section, the filtered HD-sEMG signals of each subject and each contraction level (5, 10, 30 and 50 %MVC) were decomposed into sources using the CCA algorithm. Afterwards, we extracted the  $8 \times 8$  weight matrices corresponding to each canonical component remaining after applying the denoising threshold. An example of the SNR value before and after denoising for one subject is

presented in Figure 2.16. We can see the improvement especially for the low contraction levels (5 and 10 %MVC) which were very noisy (negative SNR).

Then, a multilevel thresholding technique, the Otsu method, which classifies the values of the grids into two classes by maximizing the inter-class variance [146] was applied in order to classify the sources of the BB and the BR. This was done based on the weight matrix of each source (canonical component) and the repartition of the weights in the  $8 \times 8$  map with respect to the position of the BB and the BR muscles. Figure 2.17 presents the electrode numbering relative to their positions on the upper arm.

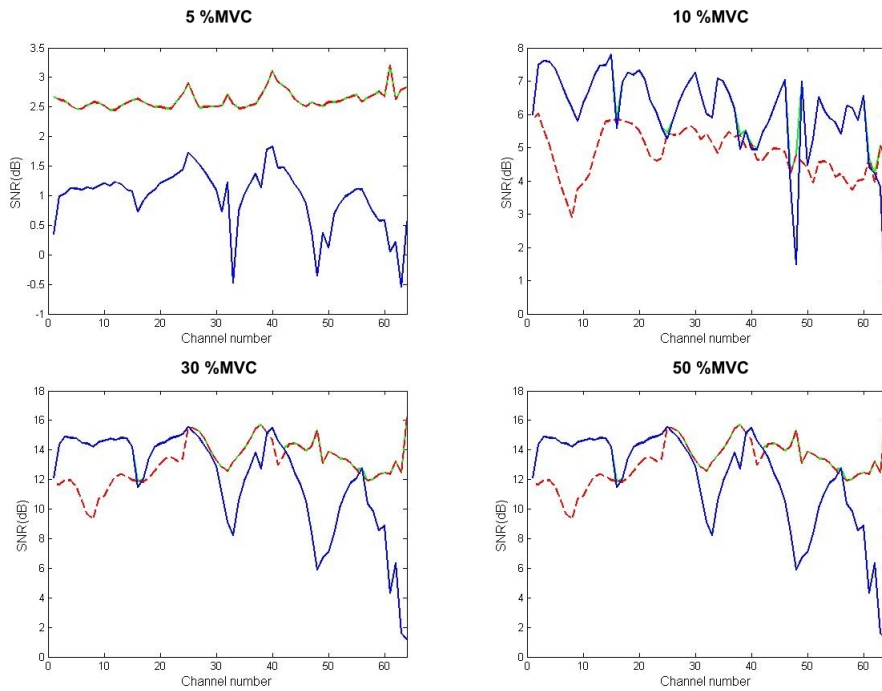


Figure 2.16: The SNR of the 64 EMG signals for one of the subjects before (blue) and after denoising with CCA (red) and sCCA (green).

Figure 2.18 displays an example of two source weight maps, one that corresponds to a BB source, and the other associated to a BR source. We noticed that the sources corresponding to the BR muscle activity are not present for low contraction levels (5% and 10% MVC). However, at 30% MVC we start to detect sources with weights concentrated near the BR region as shown in Figure 2.18. These weights increase with contraction level since new MUs are recruited. We also have new sources that appears with force increase. After classification of all the sources into two groups we reconstructed the final sEMG signals of the BB and the BR. Figures 2.19 and 2.20 present a brief segment of the single differential EMG signals (vertically computed in the fibers direction) corresponding to the BB and the BR respectively. We wanted to verify that the obtained signals show AP propagation corresponding to both muscle activities. As we can see in Figure 2.19, for the BB, we have traveling AP from the innervation zone which is located approximatively between the row 4 and 5 of the grid for this subject. We can also notice that this signal intensity increases from column 1 to column 8, due to the underlying BB muscle position. In complement,

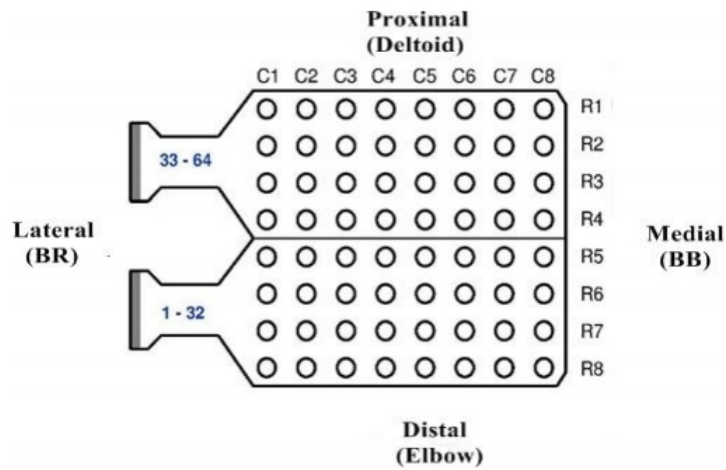


Figure 2.17: The electrode numbering of the  $8 \times 8$  kapton grid system, and the placement with respect to the geometry of the subject's arm.

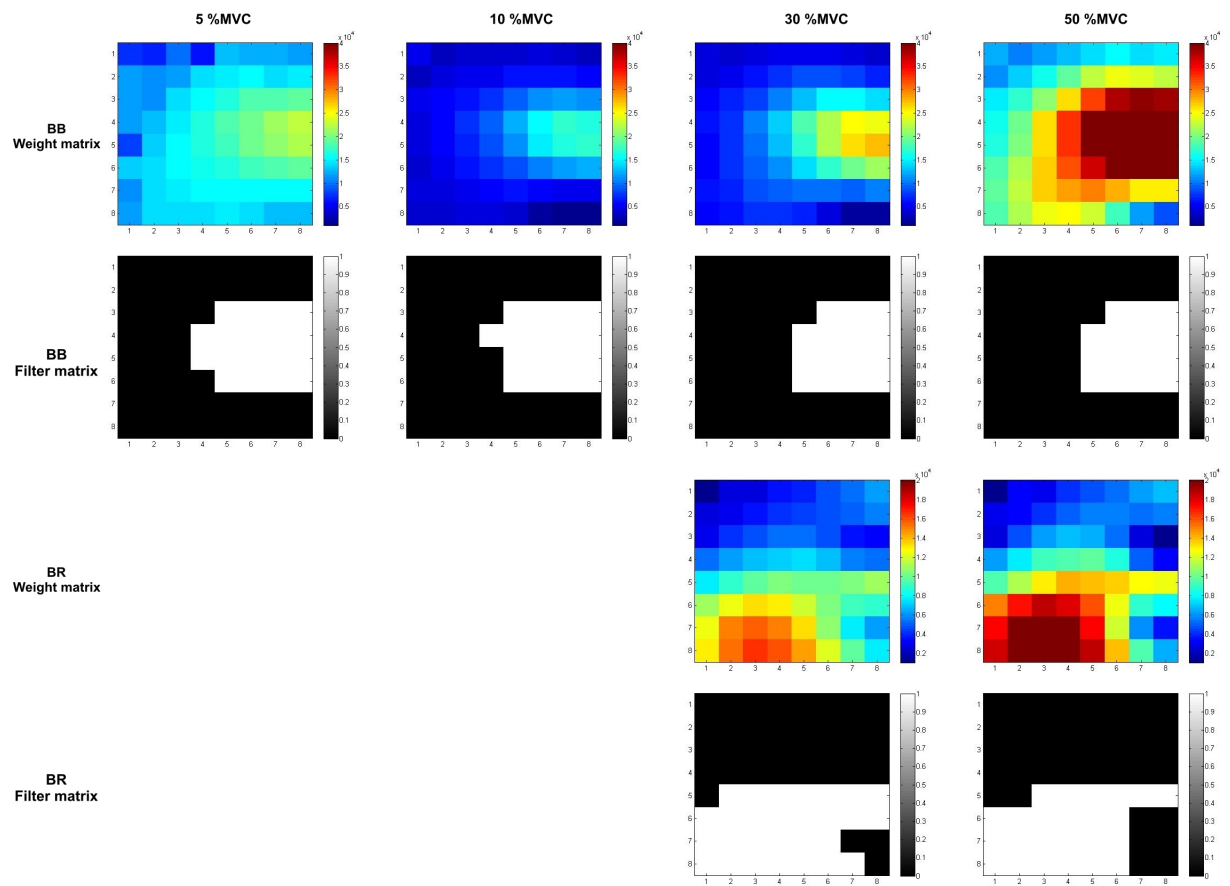


Figure 2.18: Two sources weight maps (in a.u, absolute value), one corresponding to the BB and the other for the BR according to the contraction levels: 5, 10, 30 and 50 %MVC and their corresponding filter after segmentation.

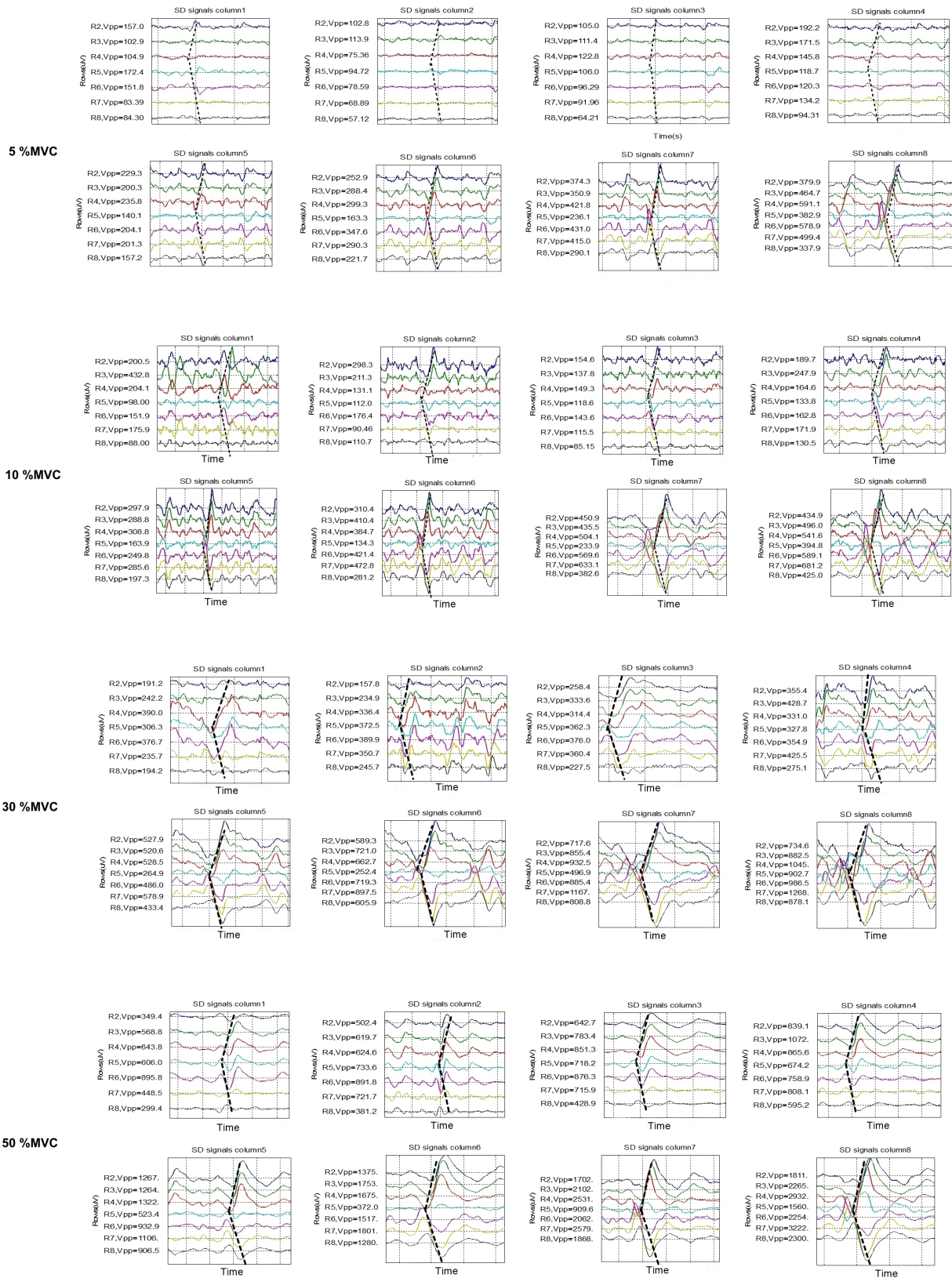


Figure 2.19: The bipolar APs corresponding to the BB for each columns of the HD-sEMG grid obtained after reconstruction for 5, 10, 30 and 50 %MVC observed for one of the subjects.

by observing the single differential AP of the BR (Figure 2.20) we can see clearly that we have one AP propagation direction which implies that the innervation zone of the BR is located more distally than of the detected NMJ of the BB outside of our electrode grid.

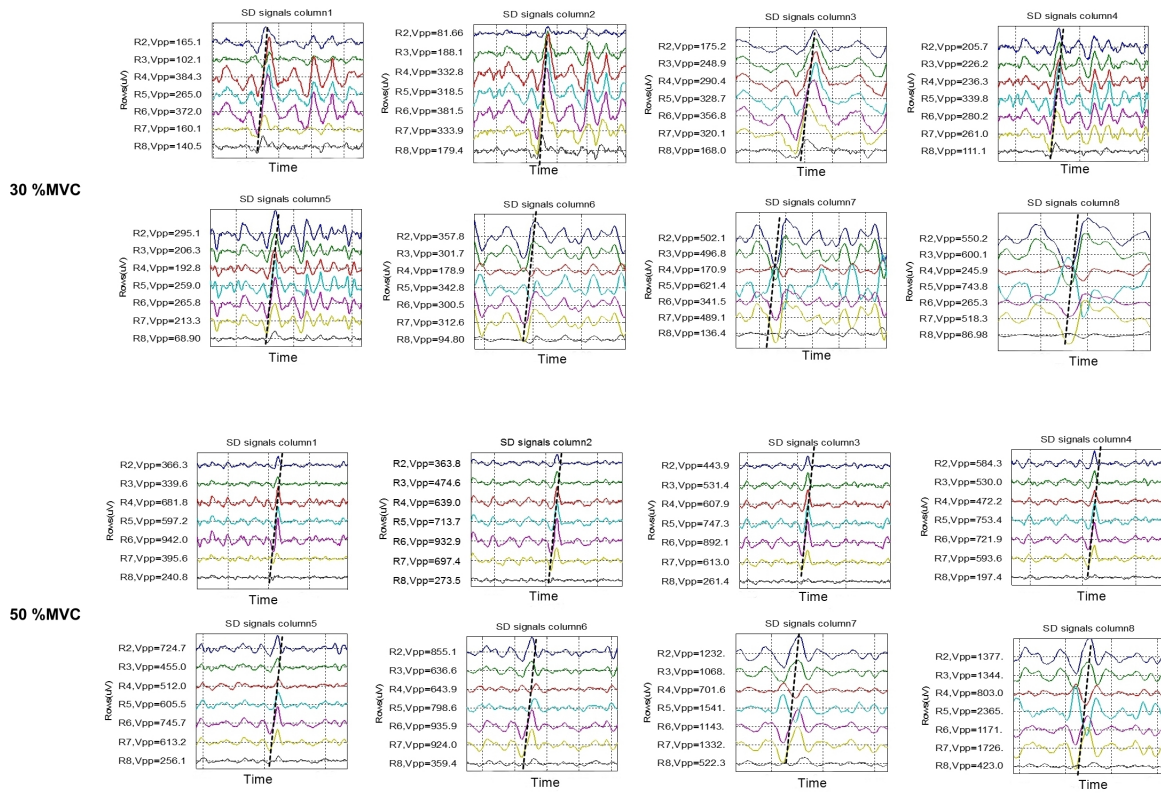


Figure 2.20: The bipolar APs corresponding to the BR for each columns of the HD-sEMG grid obtained after reconstruction for 30 and 50 %MVC observed for one of the subjects.

### 2.3.5 Analysis of the results and discussion

The BR is activated during flexion of the forearm and is the workhorse of the elbow joint [28]. In this section, our aim was to measure the BR electrical activity assuming recording a linear mixture of BR and BB over skin surface using a grid of electrode. This is motivated by the idea that we have co-contraction of the BB and the BR during elbow flexion which induce a mutual influence of each muscle on the other's sEMG due to their very close positions. Therefore, we have proposed a muscle activity separation technique based on a BSS approach the CCA. This method is based on CCA decomposition, and in particular, the source weight matrix estimation.

The main observation obtained from this study is that the BR sources radiate all over the grid. In fact, after signal reconstruction, we observed BR contributions on the electrodes positioned above the BB muscle (column 6, 7 and 8). These signals are much weaker than the BB activity but are present nonetheless. This means that the BB and the BR seem to affect each other's sEMG due to their close

positions. Hence, this points out the importance of the separation procedure not only for the extraction of the BR muscle activity but also for removing this activity from the BB signals for obtaining more accurate and solid results in many applications and especially in the muscle force estimation task, under the load sharing paradigm [42], since the BB and the BR have different biomechanical properties. The results obtained using the proposed separation technique are still preliminary and have to be validated in both experimental and simulated conditions, the possible co-activation of the triceps should also be taken into consideration.

## 2.4 Conclusion

Two preprocessing steps were presented in this chapter, these steps are judged to be very important to the later processing of the HD-sEMG signals. The first step permitted the removal of two types of noise from the HD-sEMG grid. These two types of noise are the only noise that cannot be avoided by classical skin preparation, wires fixation and other techniques. The main advantage is that it uses all the channels of the HD-sEMG acquisition system in a way to render the grid uniform from the SNR point of view. This method could possibly be further developed in order to eliminate the MAs that can occur during the signal acquisition due to wires or electrodes motion, since after decomposition, these artifact signals are usually isolated on one or several sources. Thus, adding a second thresholding rule could easily get rid of this type of noise. The second part was achieved at the LISiN laboratory in Torino, Italy. Where we applied our separation scheme on experimental signals acquired under the supervision of Prof. Merletti. This method also relied on the CCA algorithm by classifying the sources (canonical components) based on an image segmentation technique between two muscles (the BB and the BR). This method needs a validation using simulation but it can potentially contribute in a better estimation of the force.

The next chapter is dedicated to the data fusion of the information present in the grid and can contribute to the muscle activation estimation. Therefore, we will propose a map segmentation method in order to keep only the channels of interest. These channels will be used afterwards in the study of the variation of the Probability Density Function (PDF) with force level increase in isometric isotonic and non isotonic contractions in both simulation and experimental conditions.

# Chapter 3

## HD-sEMG map fusion and input parameter design

### Contents

---

<b>3.1</b>	<b>Introduction</b>	<b>113</b>
<b>3.2</b>	<b>HD-sEMG map fusion</b>	<b>113</b>
3.2.1	RMS map generation	114
3.2.2	RMS map segmentation	114
<b>3.3</b>	<b>Shape analysis of the probability density function of HD-sEMG signals</b>	<b>117</b>
3.3.1	Evaluation of High Order Statistic Trends from HD-sEMG recordings during Ramp Exercise	118
3.3.2	Monitoring of the HD-sEMG PDF shapes with varying muscle force	124
<b>3.4</b>	<b>Muscle surface deformation</b>	<b>147</b>
3.4.1	Experimental protocol	148
3.4.2	Data processing	149
3.4.3	Results and discussion	150
<b>3.5</b>	<b>Conclusion</b>	<b>154</b>

---

### 3.1 Introduction

This chapter of the thesis, is dedicated to the fusion of the information contained in the HD-sEMG grid and the choice of the parameters that can potentially define the input of the HD-sEMG/force relationship model. Accordingly, this chapter is divided into three main sections. The first section presents a data fusion method based on image segmentation algorithm. Then, the second section of this chapter presents two different studies which explore the variation of the sEMG PDF shape with different force levels during isometric isotonic and anisotonic contractions in both experimental and simulation conditions. The purpose of these investigations is to find parameters that can characterize the force level and are subject specific so that they can be added as complementary inputs to classical energetic ones that feed the HD-sEMG/force relationship model. Finally, the last section of this chapter is dedicated to finding additional parameters that can give indication about the force level. These parameters are obtained from the external BB shape deformation during different contraction levels. This study was conducted in the purpose of future combination of novel muscle deformation descriptors to the parameters obtained from the HD-sEMG signals in order to better estimate the muscle force.

### 3.2 HD-sEMG map fusion

As mentioned before, using traditional bipolar electrodes cannot permit a loyal illustration of the entire muscle activity, not to mention the positioning problem. The use of a two-dimensional electrode network can improve the efficiency of later applications [9, 2]. In fact, this bi-dimensional recording technique allows us to obtain a map of the electrical activity present on the skin surface. This map can be considered as a picture, wherein the pixels represent a certain parameter values computed over the signal of the corresponding electrode, such as an amplitude descriptor, computed for a certain time span. However, the whole picture is not always meaningful, the area of interest may change with the contraction level produced or by the subject generating this force. Accordingly, it is important to develop an effective technique to draw out the region of interest from these maps and subsequently fusion the information contained within. Such a technique is called image segmentation. Many segmentation algorithms exist in the literature. A recent work by Vieira et al. [147] presented an automatic segmentation of sEMG signals in the objective of a better estimation of the neuromuscular activity. They used a well known segmentation algorithm, the WS, and added some steps in order to enhance the segmentation results [147]. Afterwards, Afsharipour et al. [14] compared this approach with other segmentation techniques (h-dome and k-means segmentation algorithms) and found that the WS technique developed by Vieira et al. is more robust and accurate compared to the others [14, 147].

### 3.2.1 RMS map generation

The HD-sEMG signals present a grid of small electrodes where each electrode can be considered as a pixel of the EMG map or image. The RMS map was computed for the EMG signals corresponding to a constant isometric force of 5 s using equation (3.1) with an epoch of 1 ms (2000 samples).

$$RMS(i, j) = \frac{1}{N} \sum_{n=1}^N \sqrt{\left( \frac{1}{K} \sum_{k=1+(n-1)K}^{nK} (EMG(i, j, k))^2 \right)} \quad (3.1)$$

Where  $i, j$  are the row and column numbers respectively,  $K$  is the epoch length and  $N$  is the number of sample in each epoch. In this study  $K$  and  $N$  were equal to 1000 and 5 respectively. An example of the computed RMS image in grayscale is presented in figure 3.1

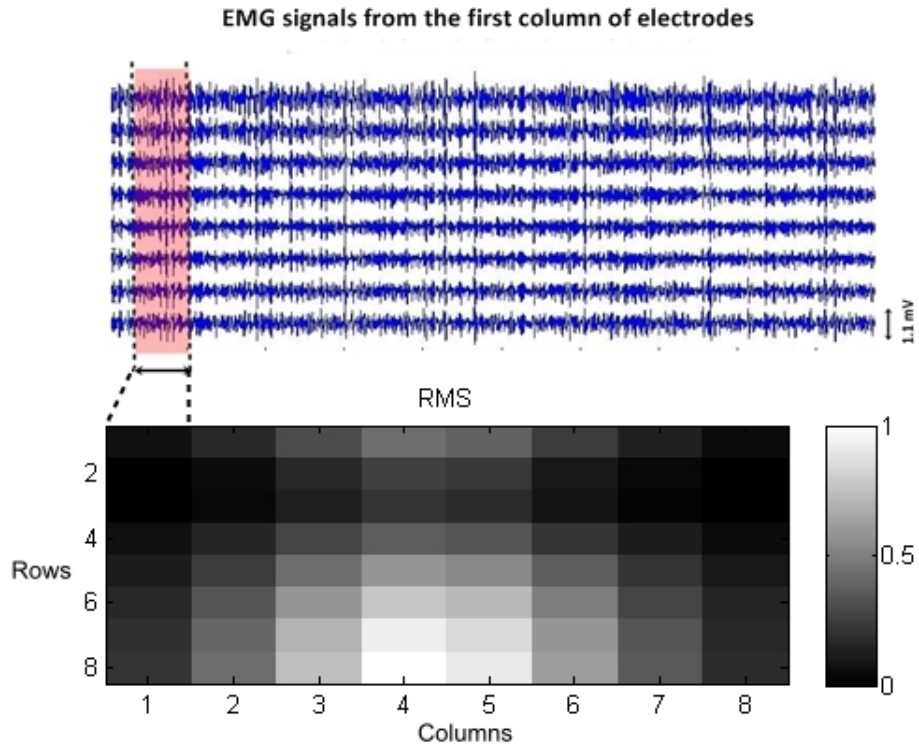


Figure 3.1: The grayscale image (bottom panel) created with the RMS values computed for an experimental EMG recorded from the BB during isometric flexion at 30 %MVC and the corresponding EMG signals for the first column (upper panel).

### 3.2.2 RMS map segmentation

By considering the RMS map as an image, we propose to use the WS transform, proposed by Beucher Lantuejoul [148] to perform the image segmentation for defining the regions of interest. The principle of this transformation is based on the idea that any grayscale image can be considered as a topographic

surface. And if this surface was flooded from its minima without the merging of waters coming from different sources, this image could therefore be divided into two different sets: the catchment basins and the WS lines [149, 148]. The algorithm consists on identifying the location of ridges (WSs) in the grayscale image and labeling the catchment basins with different numbers [149]. This algorithm is presented in 3.1.

---

**Algorithme 3.1** Watershed algorithm

---

1. A set of markers, pixels where the flooding shall start, are chosen. Each is given a different label.
  2. The neighboring pixels of each marked area are inserted into a priority queue with a priority level corresponding to the gradient magnitude of the pixel.
  3. The pixel with the lowest priority level is extracted from the priority queue. If the neighbors of the extracted pixel that have already been labeled all have the same label, then the pixel is labeled with their label. All non-marked neighbors that are not yet in the priority queue are put into the priority queue.
  4. Redo step 3 until the priority queue is empty. The non-labeled pixels are the WS lines.
- 

In our case pixels with high RMS values would be perceived as elevated surfaces. Therefore, applying the WS algorithm directly to the RMS map leads to WS line comprising of pixels representing high neuromuscular activity (high gray intensity) which is not desired (see Figure 3.2). Instead, WS algorithm will be applied on the gradient of the RMS map (G) which provides the degree of change in grayscale image [147]. The gradient map is computed as follow:

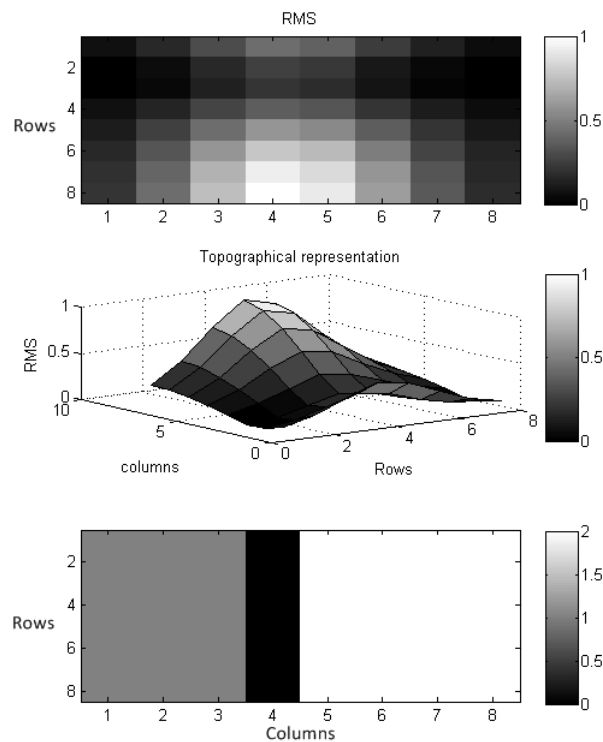


Figure 3.2: Schematic of the WS segmentation (bottom) applied to the grayscale image (Top) obtained from the RMS map of simulated EMG signals with its topographical representation (middle).

$$\begin{aligned}
G_x(m, n) &= F^{-1} \left( S^T \sum_{m=1}^N \sum_{n=1}^M RMS(m, n) e^{-j2\Pi \left( \frac{k_x m}{M} + \frac{k_y n}{N} \right)} \right) \\
G_y(m, n) &= F^{-1} \left( S \sum_{m=1}^N \sum_{n=1}^M RMS(m, n) e^{-j2\Pi \left( \frac{k_x m}{M} + \frac{k_y n}{N} \right)} \right) \\
G &= \sqrt{G_x^2 + G_y^2}
\end{aligned} \tag{3.2}$$

Where  $F^{-1}$  is the inverse Fourier transform operator,  $k_x$  and  $k_y$  are the spatial frequencies,  $M$  and  $N$  the number of rows and columns in the HD-sEMG grid and  $S$  the bi-dimensional Fourier transform of the zero-padded Sobel operator presented below:

$$S = \begin{vmatrix} +1 & +2 & +1 \\ 0 & 0 & 0 \\ -1 & -2 & -1 \end{vmatrix}$$

Since the number of clusters obtained by the WS segmentation depends on the number of regional minima in the gradient ( $G$ ), the problem of over segmentation could be confronted by smoothing sharp transitions in  $G$  using image opening and image closing operations [147]. These operations are operators from mathematical morphology derived from the fundamental operations of erosion and dilation [150]. Opening and closing  $G$  using the structural element  $v$  are defined by [150]:

$$\begin{aligned}
G \circ v &= (G \ominus v) \oplus v \\
G \bullet v &= (G \oplus v) \ominus v
\end{aligned}$$

Where the  $\circ$  and  $\bullet$  indicate the opening and closing respectively,  $\ominus$  and  $\oplus$  are the Minkowski operators for addition and difference defined by [150]:

$$\begin{aligned}
(G \oplus v)(p) &= \max_{z \in D_v} \{G(p+z)\} \\
(G \ominus v)(p) &= \min_{z \in D_v} \{G(p+z)\}
\end{aligned}$$

Where  $D_v$  is the Domain of the structuring element  $v$ , which was chosen as a square grid ( $3 \times 3$ ) of ones (i.e  $z \in [-1, 0, 1] \times [-1, 0, 1]$ ).

Figure 3.3 illustrates the clustering result of the WS algorithm applied to the gradient and the smoothed gradient of the same RMS map presented in Figure 3.2.

Also, we have to mention that we used the 4-type connectivity algorithm. This means that each pixel has four connected neighbors (top, bottom, right and left). The final step of this method is the thresholding which consists on removing further pixels or channels by applying a threshold equal to a some percentage of the maximum RMS value in the RMS map (70% in our case). The global block diagram of this segmentation method is presented in Figure 3.4.

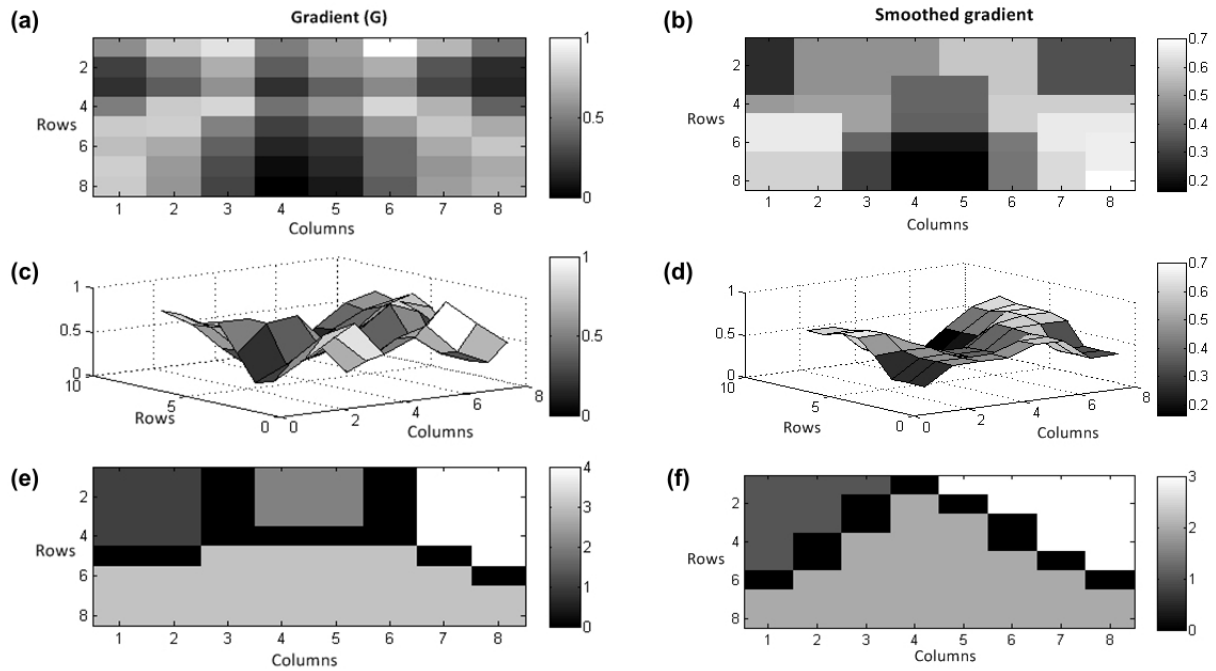


Figure 3.3: Schematic of the WS segmentation results (e) and (f) applied to: (a) the gradient (G) of the image and (b) the smoothed gradient obtained by opening and closing techniques respectively. With their corresponding topographical representation (c) and (d).

### 3.3 Shape analysis of the probability density function of HD-sEMG signals

In the literature, it has been adopted that the sEMG signal recorded during constant force, constant angle and non fatiguing contractions can be modeled as a zero mean Gaussian stationary process [151] for formalization convenience. In other studies, the PDF of the sEMG signals recorded from the BB during isometric contraction was reported to be non Gaussian for lower contraction levels [152]. Also, further studies pointed out possible variation of the PDF shape that lies between Gaussian and Laplacian shapes according to contraction levels [153].

For activation level estimation based on sEMG signals, HOS are used as distinctive features for contraction level classification or motion separation. In fact, it is supposed that the non-Gaussianity level of the sEMG signal is related to the muscular contraction level [153, 154, 50]. Indeed, recent studies using HOS (skewness and kurtosis) showed that the non Gaussianity changes with respect to the contraction level describing different tendencies [155, 136, 122]. These variation profiles seem to depend on numerous factors: anatomical (adipose and skin tissue thickness), physiological (MU number and type distribution), instrumental (electrode arrangement and location) and neurological (MUs recruitment strategy and synchronization) [156, 50]. These recent studies exhibit the ability of the PDF shape screening techniques of sEMG recordings in assessing MU recruitment schemes and muscle anatomy characteristics.

In fact, the recent study of Ayachi et al. [50] has evaluated the ability of the sEMG PDF shape screen-

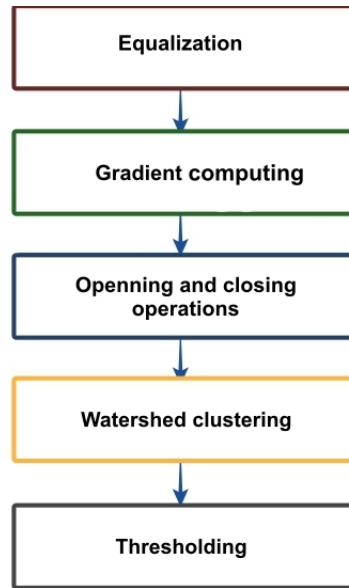


Figure 3.4: Block diagram representing the steps of the WS based segmentation method.

ing in force level classification in isometric conditions, the highest classification accuracy was obtained for Laplacian electrode configuration and the lowest using classical bipolar one. The authors supposed that the PDF shape classification accuracy according to contraction level should be strongly dependent on many tested parameters. These PDF shape differences were assessed using HOS and Shape Distance (SD) derived from the Core Shape Model (CSM) formalism [157]. It was also observed, using sensitivity analysis, that some parameters (electrode arrangement type and position, fat thickness, sampling frequency, etc..) are critical and can potentially reduce the PDF shape classification accuracy. All these observations pointed out abilities of PDF shape screening for muscle system assessment but also strong limitations linked to the employed protocol.

In this section, we will present an evaluation of the PDF shape variation trends relative to contraction level. Therefore, two different studies were conducted. The first study, which was an experimental study, was a continuous tracking of the PDF shape modification, also using HOS parameters, with force increase following an isometric anisotonic contraction. The second study concerns a global investigation combining simulation and experimentation in order to provide a solid analysis that explain the lack of a general consensus in the literature concerning the non-Gaussianity of sEMG signals according to force level.

### 3.3.1 Evaluation of High Order Statistic Trends from HD-sEMG recordings during Ramp Exercise

In this section, we present a robust screening approach of HD-sEMG PDF shape evolution in experimental conditions following a ramp exercise from 0% to 50% of the MVC during 25 s of isometric contractions of the BB from six healthy subjects. This study describes a subject-specific method, includ-

ing both Laplacian channel selection and Principal Component Analysis (PCA) decomposition (described below), for the evaluation of the HOS/force relationship on an experimental database using the kurtosis and the skewness for PDF shape screening examined on selectively positioned Laplacian sEMG channels obtained on an  $8 \times 8$  HD-sEMG grid.

### 3.3.1.1 High Order Statistics (HOS)

The HOS parameters, the skewness (asymmetry) and the kurtosis (flatness), track indirectly the PDF shape modifications of the sEMG signal as in Ayachi et al. [50]. We recall briefly the definitions of both normalized parameters in the following equations for the sEMG amplitude:

$$Skew(sEMG) = \frac{E[(sEMG - \mu)^3]}{\left(E[(sEMG - \mu)^2]\right)^{\frac{3}{2}}} \quad (3.3)$$

$$Kur(sEMG) = \frac{E[(sEMG - \mu)^4]}{\left(E[(sEMG - \mu)^2]\right)^2} - 3 \quad (3.4)$$

Where  $E(\cdot)$  is defined as the expectation operator, and  $\mu$  is the mean value of the sEMG signal amplitude. It is important to note, that these high moments are invariant to the mean value and variance variability. These parameters were computed for 5s of constant force plateaus by averaging the values obtained over ten epochs of 0.5s (sampling frequency,  $f_s$ , fixed at 2048 Hz) in order to minimize the bias of the used HOS estimators that employ empirical formula.

### 3.3.1.2 Principal Component Analysis (PCA)

The PCA is a transformation method which converts a set of observations of possibly correlated variables into a set of values of linearly uncorrelated variables called principal components. In our study and after obtaining the four different Laplacian matrices we applied PCA as a data fusion method. The steps of PCA are as follow: Let's consider  $X$  the observation matrix,  $\alpha$  the Eigen Value (EV) and  $V$  the corresponding Eigen vector;

$$R_x = X \times X^T \quad (3.5)$$

The eigenvalues of the matrix  $R_x$  can be determined by finding the roots of the characteristic polynomial  $\det(R_x - \alpha I) = 0$ . Then the corresponding eigenvectors can be found by finding non-zero solutions of the eigenvalue equation. The final step is taking the transpose of the vector  $V$  of the highest EV and

multiplying it on the left of the original data set (after checking that the other EVs are beyond a low level).

$$X_{new} = V^T \times X \quad (3.6)$$

Where  $X_{new}$  is the new data vector and  $V^T$  is the transposed vector of  $V$ .

### 3.3.1.3 Experimental protocol

The experimental signals were obtained by applying the same setup described previously (see section 2.2.6) for the recording of isometric isotonic contraction but this time we recorded isometric anisotonic contractions. The six subjects (mean  $\pm$  std, age: 22.2  $\pm$  1.3 years; stature: 176.7  $\pm$  5.5 cm; body mass: 71.1  $\pm$  5.8 kg), that participated in the study respecting the declaration of Helsinki, were requested to perform series of isometric force ramps from 0%MVC to 50%MVC lasting 25 s by following the reference force ramp on the oscilloscope screen. Few ramps were performed before the beginning of the protocol to train the subjects to track the ramp target. For the processing algorithm, signals of 25.5s in duration were used wherein we took the first part of the recordings (0.5s) where there is no contraction as an estimation of the observed noise in order to calculate the SNR (see Equation 2.8). As for the kurtosis and the skewness they were computed on a 2.5 s moving window (5000 samples) covering the 25 s force ramp without overlapping to obtain acceptable estimation accuracy.

### 3.3.1.4 Laplacian selection procedure

The selection of the Laplacian matrices for each subject was done automatically after channel selection. Since not all the channels of the grid have the same SNR, we find some channels with high level of noise superposition (PLI, WGN). Thus, we computed the SNR of all the channels of the grid. Then, we eliminated the channels with an SNR lower than a threshold defined as:

$$Thres = \frac{1}{64} \sum_{i=1}^{64} SNR(i) - \sigma_{SNR} \quad (3.7)$$

Where  $SNR(i)$  is the SNR of the  $i^{th}$  channel of the grid and  $\sigma_{SNR}$  is the standard deviation of the SNR throughout the grid. Then, the Laplacian matrices were automatically placed so that we obtain independent channels localized in areas with maximum muscle activation (areas with maximum SNR). This approach is presented in Figure 3.5 for one of the six subjects (subject 1).

Afterwards, we used the PCA in order to obtain the principal trend of the kurtosis and the skewness computed from the selected Laplacian signals according to force level variation. This was accomplished

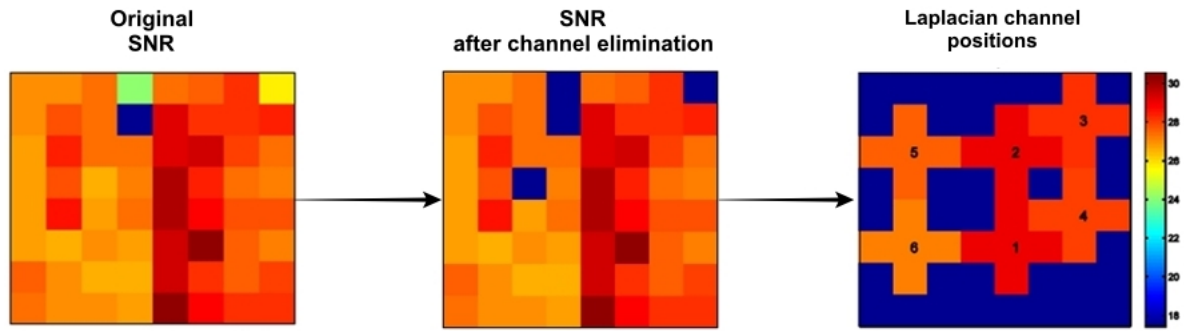


Figure 3.5: Laplacian channel positions according to higher muscle activation areas for subject 1.

by keeping only the first principal component obtained by PCA as representative of both HOS trends, since it had the majority of the weight (mean Eigen value  $> 80\%$ ). The block diagram of this parameter fusion technique described above is illustrated in Figure 3.6.

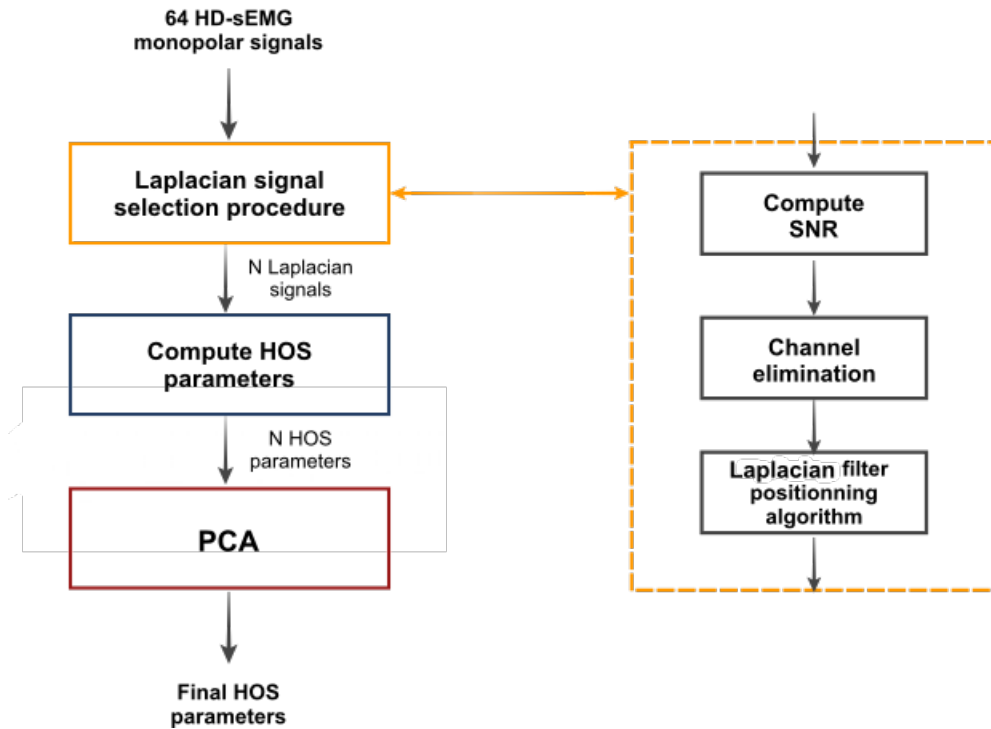


Figure 3.6: Schematic of the steps employed in order to obtain the final HOS parameters.

### 3.3.1.5 Results and discussion

For each subject, Laplacian channel position selection procedure was applied as previously described. Afterwards, we computed the classical amplitude estimators, the ARV and the RMS, along with the HOS parameters, the skewness and the kurtosis, for each Laplacian signal obtained after finding its optimal position that reflects the highest muscle activation. An example of the resultant variation of the HOS parameters trends with force increase from 0% to 50% MVC for subject 1 are presented in Figure 3.7. For this subject, the Laplacian channel positions corresponding to the different trends are presented in

Figure 3.5. As we can clearly see in Figure 3.7, we have different trends for the kurtosis and skewness with a strong sensitivity to the position of the Laplacian channel in the grid. However, for the ARV and the RMS we have almost the same profile for all the Laplacian signals but with different variation dynamic that depends on the amount of activity for the corresponding Laplacian channel position (MU recruitment). According to ARV and RMS values, we obtained the biggest dynamics for Laplacian 2, 3 and 4. Then, the PCA algorithm previously described is performed to obtain the dominant trend for both HOS parameters. The trends of the skewness and the kurtosis after reconstruction from their respective principal modes having Eigen value weights above 5% are also depicted in Figure 3.5. We can clearly observe that we have a dominant shape variation profile (an increase with force intensity increase) for both HOS parameters (principal mode).

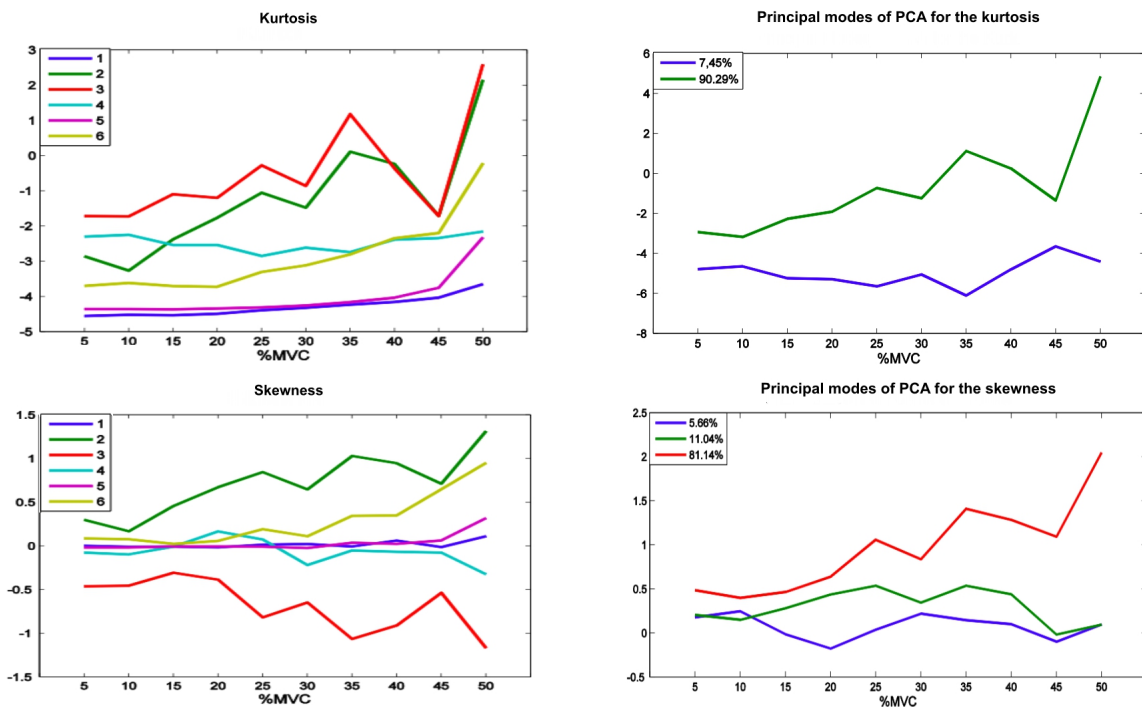


Figure 3.7: The kurtosis and skewness variations for the six Laplacian signals obtained for subject 1 (see Figure 3.5) and the corresponding PCA modes according to force level increase from 0% to 50%MVC.

Eventually, this procedure was applied to all six ramps collected from six different subjects with different anatomical (MU number, type and position), physiological (conduction velocity), neural (MU recruitment pattern) and instrumental (grid position according to IZ) properties. The results are presented in Figure 3.8 where the trends of the principal mode for the skewness and the kurtosis for the six subjects according to continuous force intensity increase (ramp exercise) after PCA are illustrated. By observing Figure 3.8, we can observe that we retrieved the increasing trend observed previously for both HOS parameters. However, although we have a global trend, we can clearly observe an important variability in the shape of these trends among subjects.

The objective of this study was the evaluation of possible trends of the HOS parameters, indicating

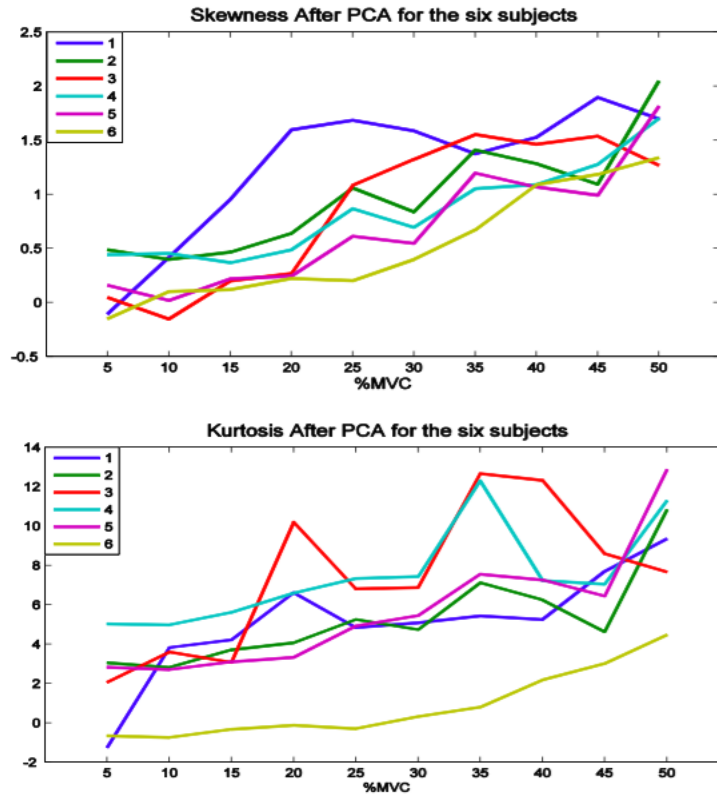


Figure 3.8: Trends of the Skewness (up) and the Kurtosis (bottom) for the six subjects with force intensity increase from 0% to 50% MVC.

reproducible shape modifications of the sEMG PDF, according to isometric anisotonic contractions for different subjects. This interest is motivated by recent studies that pointed out, with no consensus on its nature, a possible non-Gaussianity behavior of the sEMG signal amplitude according to force increase [156, 153]. However, this behavior is difficult to observe in presence of several sources of variability. For this purpose, we developed a subject-specific procedure that allows the extraction of HOS trends from a grid of 64 monopolar channels by combining channel selection, Laplacian arrangement, and PCA algorithm. The main obtained result of the proposed study is the estimation of a common trend for both HOS parameters despite the presence of the described variability. This trend represents an increase in non-Gaussianity when the measured force increases from 0% to 50% MVC. This trend has been observed in recent studies in simulation and experimentation but not systematically for all subjects as in this study [63]. An attempt to physiologically explain this trend should be linked to the MU recruitment strategies. In fact, with force increase, more FFMU, localized closer to the surface for the Biceps Brachii, are recruited [51], which results in relative high amplitude MUAP trains. And since the Laplacian arrangement generates highly asymmetric MUAPs with important positive wave, the direct consequence should be the apparition of PDF shape deformation toward positive amplitude sEMG values explaining the positive skewness and kurtosis according to force increase. This proposed hypothesis should be clearly demonstrated in future works. Another application of this study should be a better definition

of the HD-sEMG/force relationship including robust functional PDF shape parameters related to sEMG signal amplitude [157] (see section 3.3.2.2).

### 3.3.2 Monitoring of the HD-sEMG PDF shapes with varying muscle force

The proposed study aims at exploiting the advantage of combining the HD-sEMG technique and PDF shape screening, using HOS and recent robust functional statistics [157] in order to evaluate PDF shape variation trends during several isometric contraction levels. For this purpose, this study also includes a sensitivity analysis of used PDF shape descriptors according to the identified parameters variation using a fast cylindrical HD-sEMG generation model [158]. In addition, these trends will be also investigated using experimentation and confronted to the simulated data in order to explain the principal causes of the experimentally observed trends.

The main motivation of the proposed work is to provide a solid analysis that explains the lack of a general consensus in the literature concerning the non-Gaussianity of sEMG signals according to force level. For this purpose, the presented study will bear on a focused sensitivity analysis, by simulation, of PDF shape descriptors toward selected anatomical, instrumental and neural parameters and by experimental investigation on several healthy subjects. Therefore, this work is divided into two parts: a simulation study with realistic HD-sEMG signal database (simulated  $8 \times 8$  electrode grid) at three contraction levels ((30,50, and 80% MVC) using morphological parameters (adipose tissue thickness, skin tissue thickness, muscle length, arm radius and bone radius), neural parameters (two MU spatial recruitment laws and three MU type distributions) and instrumental parameters (electrode arrangement type). The second part concerns an experimental study with a database collected from six subjects, during isometric constant force contractions same as the simulated ones, using an  $8 \times 8$  electrode grid disposed on the BB. For both studies, the evaluation of the non-Gaussianity of HD-sEMG signals according to force level is assessed using HOS and functional statistics after data fusion procedure with a subject specific image segmentation method applied on the obtained maps as in [147]. Since PDF shape screening is very sensitive to different sources of noise, a preprocessing step is added, for the experimental study, and concerns the grid channel denoising using a recent approach that bears on CCA and specific thresholding paradigm as in [159]. After, both simulated and experimental PDF shape descriptor trends according to force level are constructed and deeply scrutinized. Finally, the obtained results are discussed and possible benefits and limitations of HD-sEMG PDF shape screening methods, for assessing muscle function and architecture at different contraction levels, are highlighted.

### 3.3.2.1 Experimental protocol

Six healthy male subjects (mean  $\pm$  std, age:  $27.2 \pm 1.3$  years; stature:  $176.8 \pm 5.1$  cm; body mass:  $73.8 \pm 7.3$  kg; Body Mass Index (BMI):  $22.6 \pm 1.6$ ) participated in the study respecting the declaration of Helsinki. All participants provided their written consent and did not relate any history of muscular or neurophysiological problem at the upper limbs. First, an electrostimulation device (Compex Sprt-P, Medicompex SA, Ecullens, Switzerland) was used to locate the NMJ of the BB [160]. This parameter is then used to measure the physiological parameters with ultrasound, by placing the probe at 1cm below the NMJ with elbow angle fixed at  $90^\circ$ . Then, an ultrasound device (Siemens ACUSON Antares 5.0 Ultrasound System) with a 7.5 MHz probe was used to scan the specified site of the BB. For each subject, a cross sectional ultrasound image was taken at 1 cm below the NMJ (position of the HD-sEMG grid) in order to measure the skin and adipose tissue thickness. Then, a longitudinal image along the BB was taken by sliding the probe starting from the deltoid insertion to the elbow tracing a straight line outlined at the middle of the muscle. Finally, a panoramic image for the illustration of the muscle section was taken by sliding the probe around the muscle at 1 cm below the NMJ (see Figure 3.9). These three images were taken at rest position (no muscular contraction) for all subjects. This protocol was repeated twice, and the average value was considered for further analysis. All measurements were performed by a skilled experimenter with elbow angle fixed at  $90^\circ$ . We computed the intra-class correlation (ICC) for one of the subject for which we repeated the measurements three times. We obtained an ICC  $> 0.95$  which indicates the reproducibility of the ultrasound measurements. We also repeated these measurements at approximately 50 %MVC for several subjects in order to determine the BB diameter increase percentage. We found it equal to +30% of the original value (at rest position). The measured parameters are presented



Figure 3.9: The three ultrasound images: a: Longitudinal, b: Panoramic and c: Cross section, taken for the extraction of morphological parameters for one of the subjects.

in Table 3.1 for the six subjects.

The sEMG signals are obtained from a two dimensional adhesive array consisting of 64 electrodes of circular shape with an inter-electrode distance of 4 mm and an electrode diameter of 1.5 mm, recorded from the BB, during isometric voluntary contractions with the elbow flexed at  $90^\circ$ . The adhesive HD-sEMG grid was placed at 1 cm below the NMJ according to the SENIAM recommendations [110]. The

Table 3.1: Morphological parameters obtained from ultrasound measurements for six subjects.

Subject	Muscle length $L(cm)$	Adipose tissue thickness $\rho_b(mm)$	Skin tissue thickness $\rho_c(mm)$
1	8.98	2.33	1.45
2	12.61	3.40	1.20
3	9.74	2.70	1.30
4	9.56	3.58	1.55
5	9.33	1.68	1.55
6	9.84	2.30	1.13

reference electrode and the ground electrode were placed on the lateral epicondyle (elbow bone) and around the wrist respectively. The monopolar sEMG signals were acquired using TMSi REFA 136 acquisition system (Twente Medical Systems International, the Netherlands) with the corresponding software (Polybench). The global force signal was measured simultaneously with the sEMG signals using a strain gauge (Celtron STC SS S-beam, Stainless Steel, IP67), and displayed in real-time on an oscilloscope as visual feedback for the subjects. The protocol began by measuring the MVC (Maximum Voluntary Contraction) of the subjects. Then the subjects were requested to perform a series of constant isometric force at 30%, 50% and 70% MVC lasting about 5 seconds by following the reference on the oscilloscope. A resting time of 1.5 ~ 2 mins was respected between measurements in order to avoid muscle fatigue. This protocol allows us to obtain for each subject 64 signals of 5 seconds at 2048 Hz of sampling frequency.

### 3.3.2.2 HD-sEMG signal processing

#### Denoising

For the denoising of the HD-sEMG signal obtained using the experimental protocol described above (Section 3.3.2.1), we used the CCA based technique recently detailed in section 2.2. This denoising technique is an automatic and specific algorithm that targets two types of noise, the PLI and the WGN, using canonical component selection, noise ratio thresholding and channel selection procedures. In this work we applied this denoising technique in order to remove mainly the 50 Hz noise. This noise type is always present in HD-sEMG experimental signals in an heterogeneous manner along the electrodes of the grid due to various reasons, which can alter substantially the PDF shape descriptors by causing bimodal PDF shape appearance. This multichannel denoising method is described in details in section 2.2.

#### Channel selection by image processing

The HD-sEMG technique can be considered as an imaging tool [117] in complement to sonography and Magnetic Resonance Imaging (MRI) for assessing muscle systems. Therefore, we propose to use an automatic and personalized channel selection method based on image segmentation for both monopolar and

bipolar configurations. This method is obtained using a previously validated HD-sEMG image segmentation method, the WS algorithm [147]. This approach is a non parametric unsupervised segmentation method that selects an optimal threshold based on discriminant analysis to maximize the separability of the classes in gray levels [161, 146].

For monopolar signals, the thresholding was done on monopolar RMS value maps for the three studied contraction levels (30%, 50% and 70% MVC). We chose the RMS value instead of the ARV based on its robustness to spatial aliasing [162]. This procedure is exhibited in Figure 3.10 for the monopolar configuration. One can see the RMS value maps with the corresponding filters obtained by the thresholding technique for the experimental signals described by Vieira et al. [147]. As we can see, we have different filters for each contraction level. Thusly, the final chosen filter is the intersection of all three filters (multiplication of the three binary matrices). This filter is then applied to the RMS value maps in order to remove the unneeded channels. Lastly and after channel selection via image segmentation, the parameter profiles (HOS and SDs) are obtained by averaging the monopolar trends of the remaining channels. We applied the exact same technique on the bipolar RMS value maps computed from the bipolar signal obtained by subtraction of monopolar channels along the fiber direction. These bipolar maps consists on an  $7 \times 8$  matrices (56 bipolar channels). An example is shown in Figure 3.11

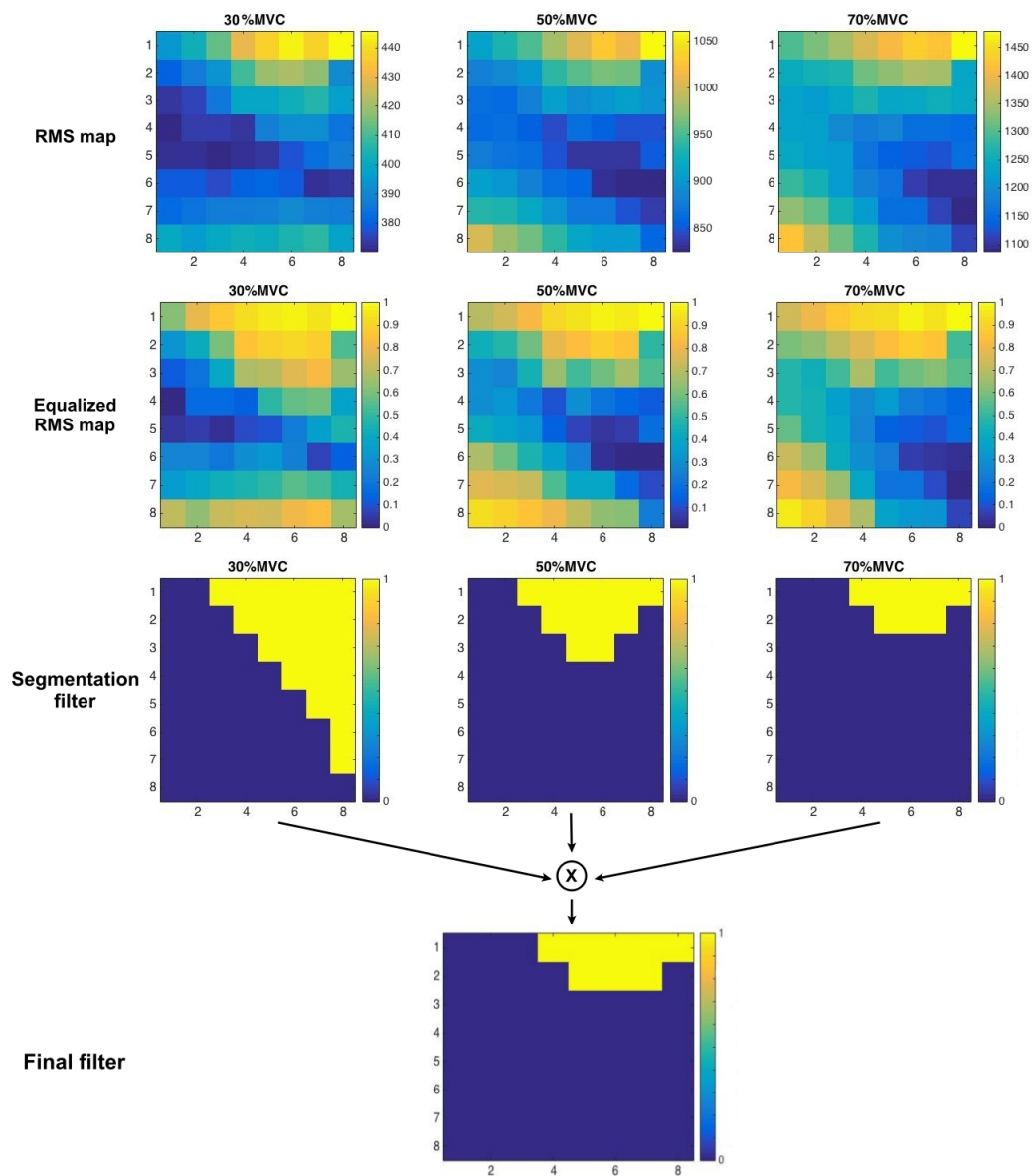


Figure 3.10: The steps of the monopolar channels selection procedure for subject 1. Starting from the RMS maps (top), then the equalized RMS maps (middle) the segmentation filter is computed by WS segmentation (bottom) for the three contraction levels (30, 50 and 70% MVC) and the final filter is the intersection of all three filters.

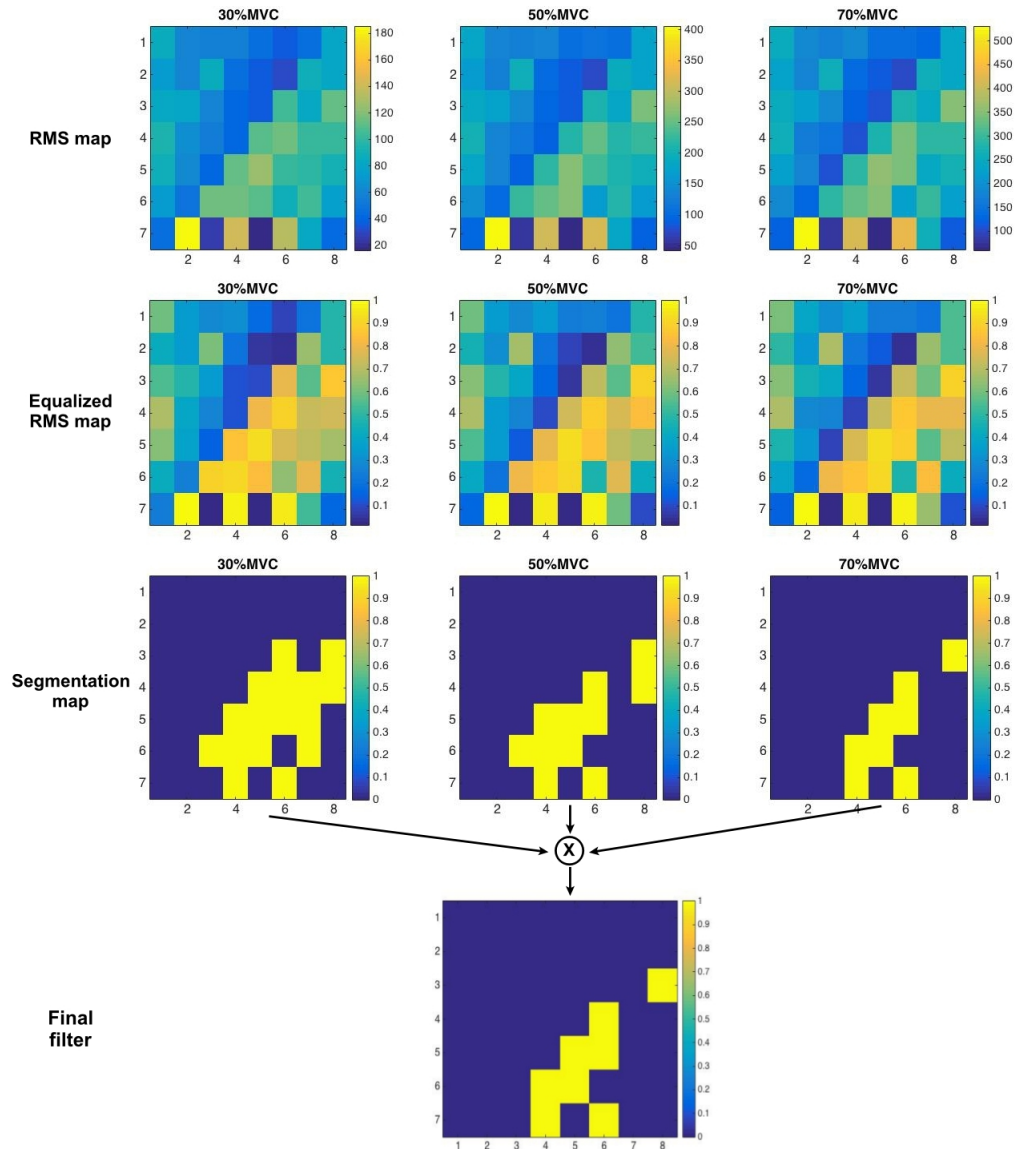


Figure 3.11: The steps of the bipolar channels selection procedure for subject 1. Starting from the RMS maps (top), then the equalized RMS maps (middle) the segmentation filter is computed by WS segmentation (bottom) for the three contraction levels (30, 50 and 70% MVC) and the final filter is the intersection of all three filters.

For the Laplacian configuration since it is already the result of a filtering stage consisting of five channels, we proceeded with a different approach. We applied also a personalized and automatic channel selection procedure that involves a specific Laplacian filter placement algorithm. This algorithm places the filters in an independent manner (no superposition of Laplacian filters) on the grid in order to obtain the maximum of RMS dynamic between 30% and 70%MVC contraction levels. An example of this Laplacian channel selection technique is shown in Figure 3.12 for one of the subjects (subject 1). The final trend, similarly to the monopolar and the bipolar approaches, is obtained by averaging the parameters profiles of the obtained Laplacian channels. One can note that both channel selection and data fusion methods allow us to obtain the optimal position of the signals based on the maximum energy i.e the maximum MUs activities superposition.

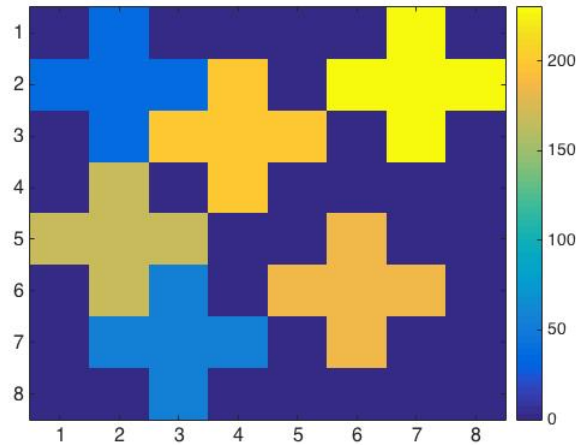


Figure 3.12: The obtained Laplacian filter after Laplacian selection for the same subject presented in Figure 3.10

### PDF shape descriptors

In addition to the HOS parameters, recent robust functional statistics are used to evaluate precisely the departure from Gaussianity of the studied PDF. These amplitude statistics are derived from the CSM formalism and are easy to compute [157]. They measure localized SDs between a reference Normal PDF and the observed PDF curved estimated using kernel density estimation [163]. Thus, these metrics measure the distance of a PDF from Gaussianity including asymmetry and flatness measures as for the HOS parameters. They assume that there are two PDFs  $p(x)$  and  $g(x)$  that represent a random sEMG signal PDF and a normal PDF respectively defined on  $[-l, l]$ . The Normal PDF  $g(x)$  is obtained using its analytic definition. The sEMG PDF  $p(x)$  is obtained using a kernel estimation procedure [163] to obtain a smooth continuous (better abscissa resolution) curve less noisy than the classical histogram. Their normalized integrals (distribution function in  $\mathcal{F}$ ) can be defined as:

$$\begin{aligned} P(x) &= \frac{\int_{a_p}^x p(u) du}{\int_{a_p}^{b_p} p(u) du} \\ G(x) &= \frac{\int_{a_g}^x g(u) du}{\int_{a_g}^{b_g} g(u) du} \end{aligned} \quad (3.8)$$

Where  $[a_p, b_p] \in [-l, l]$  and  $[a_g, b_g] \in [-l, l]$  are the nonzero supports of  $P(x)$  and  $G(x)$  respectively. The obtained distribution functions  $P(x)$  and  $G(x)$  can typically be linked through a warping function expressed as  $\phi$  or  $\psi$ . Specifically, we can write:

$$\begin{aligned} P &= G \circ \phi \\ G &= P \circ \psi \end{aligned} \quad (3.9)$$

where  $P = G \circ \varphi$  is a shorthand notation for the composition function  $P(x) = G(\varphi(x))$ . The time warping function  $\psi = \varphi^{-1}$  links  $P(x)$  to  $G(x)$  and represents the fluctuations in both shape and abscissa support. The PDF shape analysis, aims at separating intrinsic shape variation from those caused by first and second moment variability. To reach this objective, we propose a representation of  $\varphi$ :

$$\begin{aligned}\varphi &= v \circ A, \quad v = w^{-1} \\ \psi &= A^{-1} \circ w\end{aligned}\tag{3.10}$$

where  $A(x) = ax + b$ ,  $a \in \mathbb{R}^+$ ,  $b \in \mathbb{R}$  is an affine function (polynomial function of order 1) that accounts for mean and variance variability of  $p(x)$ . The second element  $w$  is a monotonically increasing nonlinear function that represents shape fluctuations on a constant support. Therefore, we can rewrite (3.8) as follows in  $\mathcal{F}$  and  $\mathcal{F}^{-1}$  respectively:

$$\begin{aligned}P &= G \circ v \circ A, & G &= P \circ A^{-1} \circ w \\ P^{-1} &= A^{-1} \circ w \circ G^{-1}, & A \circ P^{-1} &= w \circ G^{-1}\end{aligned}\tag{3.11}$$

Where  $w(y) = y + n(y)$ ,  $y \in [0, 1]$  and  $n(y)$  is a function that accounts for small intrinsic shape modification and modeling the departure from linearity of  $w$ . By replacing this last equation in (3.9), we obtain:

$$\alpha P^{-1} + \beta = G^{-1}(y) + n(G^{-1}(y)), \quad y \in [0, 1]\tag{3.12}$$

where the term  $n(G^{-1}(y))$  represents the shape difference between the realigned function  $\hat{A}(P^{-1}(y))$  and  $G^{-1}(y)$ . The parameters  $\alpha$  and  $\beta$  are estimated by constrained linear regression between  $P^{-1}(y)$  and  $G^{-1}(y)$ . Then, we propose three distances, namely, the Center Shape Distance (CSD), the Left Shape Distance (LSD) and the Right Shape Distance (RSD) that measure shape differences between realigned  $\hat{A}(P^{-1}(y))$  and  $G^{-1}(y)$  in the center, the left and the right regions respectively. These distances are defined as follows:

$$\begin{aligned}CSD(x, g) &= \sqrt{\int_{0.4}^{0.6} \left( \hat{\alpha} X^{-1}(y) + \hat{\beta} - G^{-1}(y) \right)^2 dy}, \\ LSD(x, g) &= \sqrt{\int_0^{0.25} \left( \hat{\alpha} X^{-1}(y) + \hat{\beta} - G^{-1}(y) \right)^2 dy}, \\ RSD(x, g) &= \sqrt{\int_{0.75}^1 \left( \hat{\alpha} X^{-1}(y) + \hat{\beta} - G^{-1}(y) \right)^2 dy},\end{aligned}\tag{3.13}$$

From these definitions, one can observe that the CSD distance is a metric that is sensitive to the flatness

or peakedness (as the kurtosis) of  $p(x)$  and observed in the middle region of its inverse distribution function  $p^{-1}(y)$ . The LSD and RSD distances scrutinize the departure from gaussianity in the left tail and right tail region of  $p(x)$ . These two distances if they are not equal can inform us about possible asymmetry of  $p(x)$  as for the skewness parameter by subtracting LSD to RSD value. One can note that the three proposed distances are positive if  $p(x)$  is not a Gaussian PDF and equal to zero if  $p(x)$  is a Gaussian PDF. These functional statistics have demonstrated robustness to the sample size effect in simulation [157]. In this study, they will be used to obtain PDF shape profiles according to force level and compared to those obtained using classical HOS parameters.

### 3.3.2.3 HD-sEMG simulation

For the generation of the 64 HD-sEMG signals, we used a fast multilayered cylindrical model [158] with the geometry illustrated in Figure 3.13a. This model is characterized by generating a high resolution potential map over the skin related to active MUs [158]. The conductor volume, is described as a three layered cylinder (muscle, adipose and skin tissues) in which the sources are located longitudinally within the muscle layer. The sources are depicted by a spatiotemporal function which describes the generation, propagation and extinction of the intracellular AP at the end plate, along the fiber and at the myotendinous area, respectively. Electrodes are modeled as a surface integration operation under the electrode area of the generated potential map allowing a variety of electrode shapes and grids [158]. The HD-sEMG analytical calculus is fully performed in the frequency domains and parallel computing is used in order to achieve optimal speed. To perform a realistic personalized simulations with authentic parameters, we conducted an experimental study using ultrasound imaging in order to measure the morphological parameters of six healthy subjects. this protocol is described in details below.

All the parameter values used for the simulation are presented in Table 3.2. We used the average values from the six subjects for the morphological parameters obtained from sonography (see Table 3.1).

We should add that the bone radius as well as the BR region are taken into account for the placement of the MUs in the muscle layer as exhibited in Figure 3.13b. The value of the bone and BR thickness is the mean value measured using ultrasound. Mitchell's best-candidate algorithm was used for the placement of the MUs [164] in order to fulfill the muscle area and better mimic the BB rather than using unconstrained uniform laws for MU placement [165]. In this study three force levels: 30, 50 and 70 % MVC were generated for five different anatomies of 300 MUs and three adipose tissue thicknesses ( $\rho_b$ ). The muscle radius was fixed at the average value obtained by sonography for the six subjects.

The morphological parameters were obtained using ultrasound imaging as described in section 3.3.2.1. With the values presented in Table 3.1. Three different MU distributions were chosen in order to study the influence of the repartition of Slow and Fast MUs percentages on the PDF shape descriptors. These

Table 3.2: Description of the parameters used to simulate the HD-sEMG signals.

Parameter	Value (unit)
Number of MU ( $n_{MU}$ )	300
Time frequency sample ( $f_t$ )	2048 ( $Hz$ )
Muscle radius ( $\rho_a$ )	46.48 ( $mm$ )
Bone + BR thickness ( $\rho_d$ )	18.23( $mm$ )
Skin tissue thickness ( $\rho_c$ )	1.42 ( $mm$ )
Radial muscle conductivity ( $\sigma_{mp}$ )	0.1 ( $S.m^{-1}$ )
Angular muscle conductivity ( $\sigma_{m\theta}$ )	0.1 ( $S.m^{-1}$ )
Muscle Length ( $L$ )	101.0 ( $mm$ )
Longitudinal muscle conductivity ( $\sigma_{mz}$ )	0.5 ( $S.m^{-1}$ )
Adipose tissue conductivity ( $\sigma_f$ )	0.05 ( $S.m^{-1}$ )
Skin conductivity ( $\sigma_s$ )	1 ( $S.m^{-1}$ )
Center of electrode grid ( $\theta, z$ )	(0, 30) ( $^\circ, mm$ )
Number of electrodes	8×8
Electrode radius ( $r_e$ )	1 ( $mm$ )
Inter-electrode distance ( $d_\theta, d_z$ )	(4, 4) ( $mm, mm$ )
Simulation time ( $T$ )	5 ( $s$ )
Angular discretization ( $k_\theta$ )	101

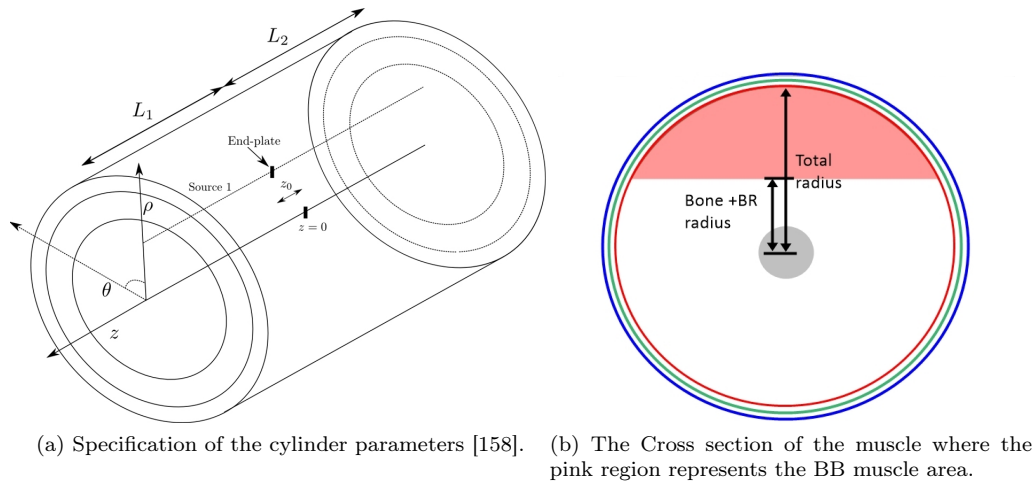


Figure 3.13: Schematic of the cylindrical simulation model.

distributions are presented in Table 3.3. These percentages are realistic distributions of MUs types in the muscle that respect the total percentage of slow ( $\sim 40\%$ ) and fast ( $\sim 60\%$ ) MUs within the BB [166].

Table 3.3: MUs percentage for each distribution

MUs Distribution	SMU(%)	FRMU(%)	FIMU(%)	FFMU(%)
1	33	17	17	33
2	43	15	15	27
3	37	10	10	43

Moreover, we generated two different recruitment strategies for each configuration of parameters. These two recruitment strategies follow a modified Flugveland recruitment law [167]. They are called Low Recruitment Strategy (LRS) and High Recruitment Strategy (HRS). The LRS does not start to recruit FFMU before 50% MVC, as for the HRS it does have active FFMUs before 50% MVC. The general

recruitment law for these two strategies is represented by the following equation:

$$RTE(i) = \left(\frac{Ki}{N}\right) e^{ai}; \quad a = \frac{\ln\left(\frac{RR}{K}\right)}{N} \quad (3.14)$$

Where  $N$  is the total number of MUs,  $K$  is a constant,  $RR$  is the contraction level at which all MUs are recruited and  $i$  is the MU number. The two recruitment strategies are illustrated in Figure 3.14.

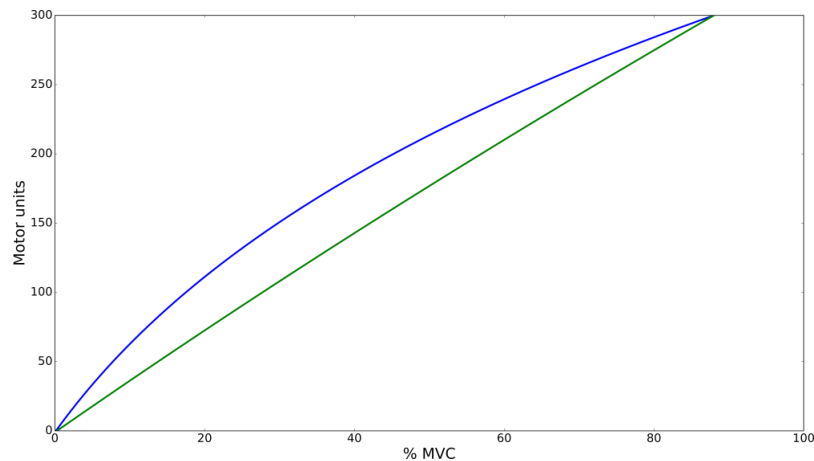


Figure 3.14: The two recruitment strategies LRS (green) and HRS (blue) used in the simulation model.

For the first MU type distribution (see Table 3.3) 6 simulations were conducted by changing each time one of the three morphological parameters ( $\rho_b(mm)$ ,  $\rho_c(mm)$  and  $L(cm)$ ) between the maximum and the minimum values presented in Table 3.1. As for the second and the third MU type distributions (see table 3.3) only the  $\rho_b$  was changed (extremum values).

Thus, 24 simulations in total were conducted for the sensitivity analysis of HOS parameters: 1 MU type distributions  $\times$  3 parameters  $\times$  2 values  $\times$  2 recruitment strategies + 2 MU type distributions  $\times$  1 parameter  $\times$  2 values  $\times$  2 recruitment strategies + 2 nonlinear recruitment strategies  $\times$  1 parameter  $\times$  2 values. These simulations with the corresponding parameters values are presented in Table 3.4. We added WGN for the simulated signals in order to obtain the same range of SNR dispersion over the grid as the one observed on the experimental signals.

#### 3.3.2.4 HOS and SD variations with force level increase for the simulated signals

For the simulation study, we chose to investigate the impact of the morphological parameters (adipose tissue thickness  $\rho_b$ , skin tissue thickness  $\rho_c$  and muscle length  $L$ ), the spatial recruitment strategy (HRS or LRS) and the MU type percentage distribution (D1, D2 and D3) on the profile variation of the amplitude PDF shape descriptors (HOS and SD). The morphological parameters values are taken from the minimum, maximum and average values obtained from the six subjects using ultrasound imaging technique (see section 3.3.2.1 and Table 3.1).

Table 3.4: The morphological parameters values corresponding to the different simulations.

Simulation	MUs Distribution	$\rho_b$ (mm)	$\rho_c$ (mm)	$L$ (mm)
$D1min\rho_b$	1	1.68	1.42	101.0
$D1max\rho_b$	1	3.58	1.42	101.0
$D1min\rho_c$	1	2.74	1.13	101.0
$D1max\rho_c$	1	2.74	1.75	101.0
$D1minL$	1	2.74	1.42	89.8
$D1maxL$	1	2.74	1.42	126.1
$D2min\rho_b$	2	1.68	1.42	101.0
$D2max\rho_b$	2	3.58	1.42	101.0
$D3min\rho_b$	3	1.68	1.42	101.0
$D3max\rho_b$	3	3.58	1.42	101.0

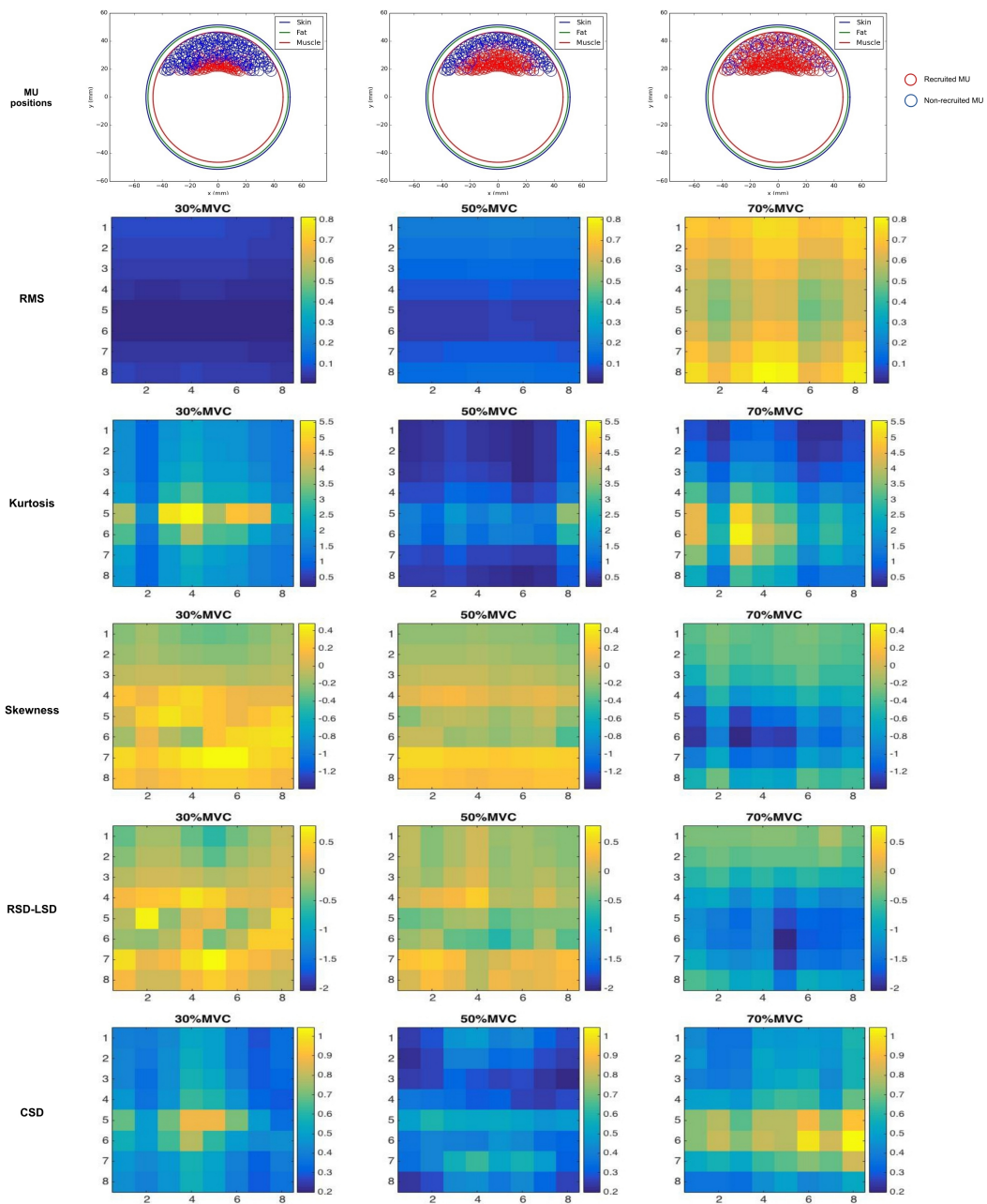


Figure 3.15: The muscle anatomy, the corresponding kurtosis, skewness and the three SDs (LSD, RSD and CSD) maps of the 64 HD-sEMG signals according to contraction level (30, 50 and 70% MVC) for the LRS strategy.

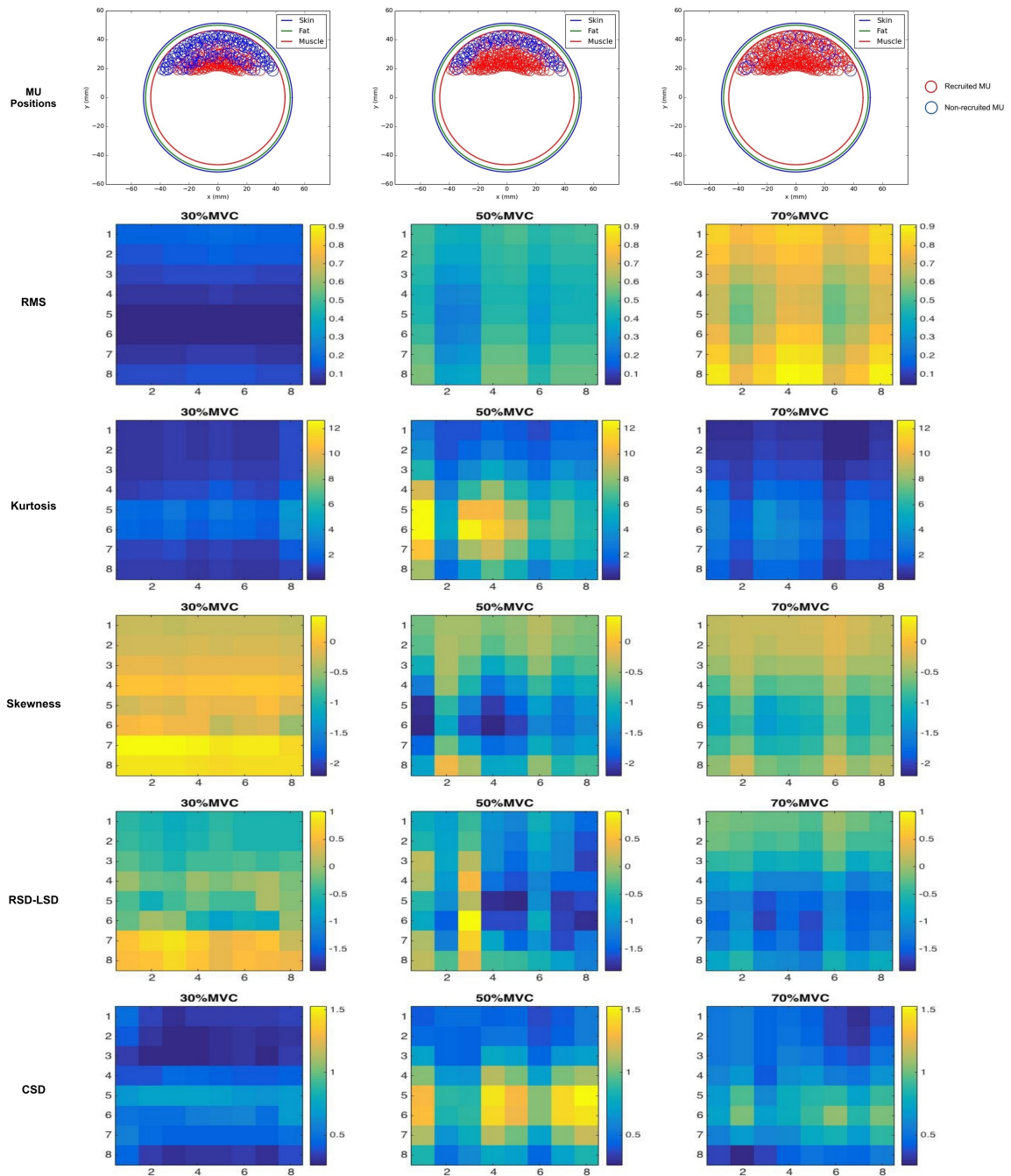


Figure 3.16: The muscle anatomy, the corresponding kurtosis, skewness and the three SDs (LSD, RSD and CSD) maps of the 64 HD-sEMG signals according to contraction level (30, 50 and 70% MVC) for the HRS strategy.

All these simulations are presented in Table 3.4. We started with the first MU type percentage distribution D1 (see Table 3.3) where we have the same percentage of SMUs and FFMUs. The first six simulations in Table 3.4 present a focused sensitivity analysis between the maximum and the minimum values of the three chosen morphological parameter ( $\rho_b$ ,  $\rho_c$  and  $L$ ) at a time. Figure 3.15 and 3.16 illustrate the  $8 \times 8$  RMS, kurtosis, skewness, RSD-LSD and CSD grids respectively for the first simulation ( $D1min\rho_b$ ) for the LRS and HRS respectively (see Table 3.4). The main observation from Figure 3.15 is

that these parameter maps are heterogeneous as expected following the underlying MU distribution. This presses upon the importance of the segmentation or the channel selection method. A simple comparison between Figures 3.15 and 3.16 allows us to see the major influence of the recruitment strategy on the HOS and the SD variation profiles. We can see that for the HRS, we have an increase (decrease) in the values of the kurtosis from 30% MVC to 50% MVC then a decrease (increase) from 50% to 70% MVC for the kurtosis (skewness) contrary to the first case (low recruitment strategy) where we had continuous increase (decrease) of the kurtosis (skewness) grid values.

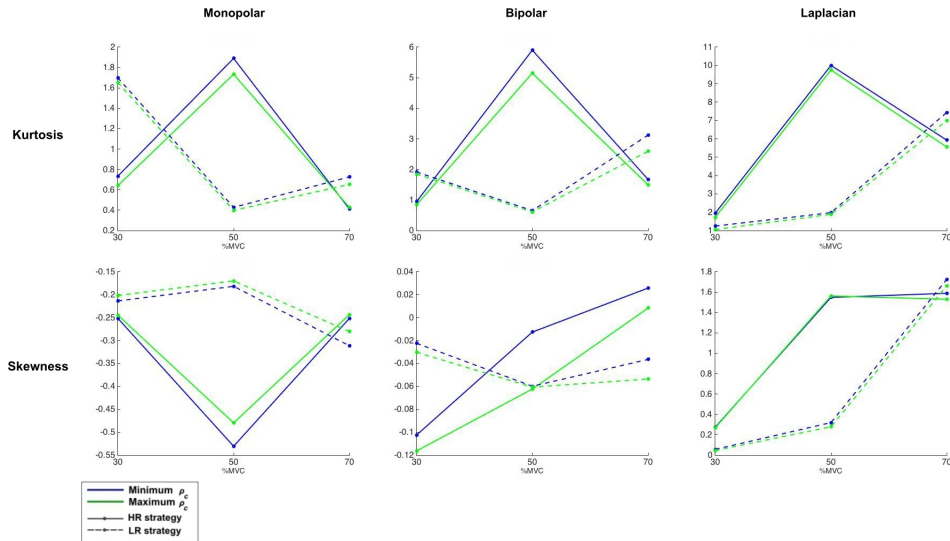


Figure 3.17: The profile variation for the kurtosis, skewness for the monopolar (left), bipolar (middle) and Laplacian (right) signals according to the contraction level (30, 50 and 70 %MVC) for the maximum and the minimum skin tissue thickness.

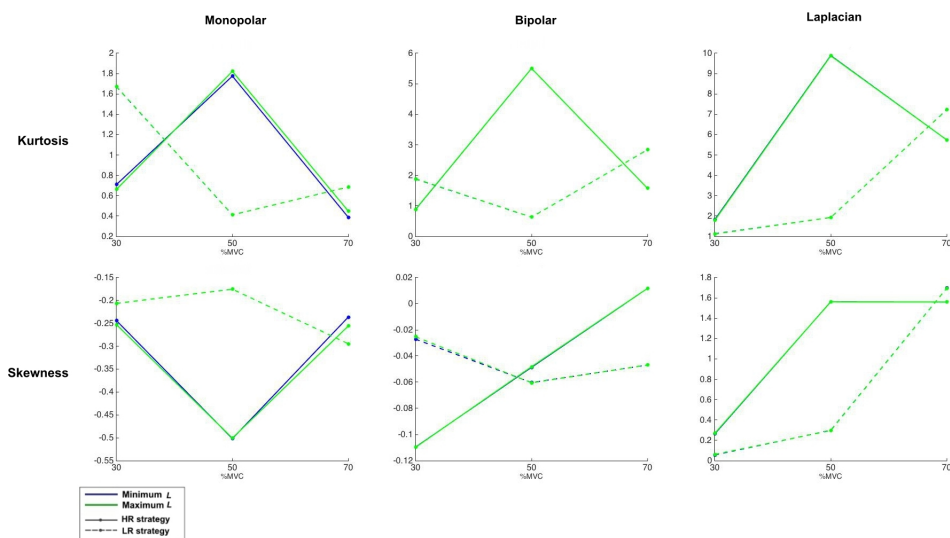


Figure 3.18: The profile variation for the kurtosis, skewness for the monopolar (left), bipolar (middle) and Laplacian (right) signals according to the contraction level (30, 50 and 70 %MVC) for the maximum and the minimum muscle length.

In order to explore more precisely the impact of skin tissue thickness ( $\rho_c$ ) and muscle length ( $L$ ) variations, we computed the dominant profile variation for simulations  $D1min\rho_c$  &  $D1max\rho_c$  and  $D1minL$  &

$D1_{max}L$  that exhibit the minimum and the maximum values of  $\rho_c$  and  $L$ . The profiles were obtained for monopolar, bipolar and Laplacian arrangements after the channel selection procedures and data fusion as described in section 3.3.2.2. The results for the kurtosis and the skewness are exposed in Figures 3.17 and 3.18 for  $\rho_c$  and  $L$  variation respectively each for the two recruitment strategies HRS and LRS. As we can see in Figure 3.17, we have an impact of the skin tissue thickness ( $\rho_c$ ) on the dynamic of the profile variations that is more pronounced for the HRS than the LRS. When changing the skin tissue thickness from min to max value, we have a decrease in the dynamic of the trends due to the filtering effect of the skin. In addition, we can also acknowledge that the dynamic variation due to  $\rho_c$  variation is more significant for the bipolar configuration. Contrastingly, no noticeable change of the HOS profiles with the muscle length variation was observed between minimum and maximum values; in spite of the notable length variation (2.63 cm) there is no clear influence on the HOS or the SD parameters computed for the monopolar, bipolar or Laplacian arrangements. These results are presented in Figure 3.18 for the kurtosis and the skewness. One can also notice the important PDF asymmetry obtained using monopolar and Laplacian arrangement (inverse) and the small one for the bipolar arrangement. Same results were observed for the SDs.

In order to compare the variation profiles for the two recruitment strategies by varying the adipose tissue thickness ( $\rho_b$ ) and the MUs type percentage distributions, we applied the same procedure described above on the monopolar, bipolar and Laplacian profiles obtained for the HOS and the SD parameters. The results are presented in Figures 3.19 and 3.20 for the three distributions D1, D2 and D3 for the minimum and the maximum  $\rho_b$  values ( $D1_{min\rho_b}$  &  $D1_{max\rho_b}$ ,  $D2_{min\rho_b}$  &  $D2_{max\rho_b}$  and  $D3_{min\rho_b}$  &  $D3_{max\rho_b}$ ) each for the two recruitment strategies, LRS and HRS, respectively.

By observing the variation profile of the parameters for the HRS, we can see that we have a similar variation profile; a departure from Gaussianity from 30 to 50% MVC and a convergence toward Gaussianity from 50 to 70% MVC for the three distributions D1, D2 and D3 for the kurtosis, skewness and CSD parameters in the monopolar and the Laplacian curves. It is important to recall that the 0% MVC corresponds to Gaussian observed signals. In fact, we have checked that all the PDF parameters are near to zero. The remaining parameter the RSD-LSD for these two configurations, monopolar and Laplacian, seems to have different trends. In the monopolar case, for D1 and D2, we have the same profile for the RSD-LSD as the other parameters but a profile that is continuously decreasing for the D3. For the Laplacian case, the RSD-LSD seems to have different profiles for each MU type percentage distribution. On the other hand, in the bipolar case we can see a common trend between D1, D2 and D3 for the kurtosis and the CSD. For the skewness however we have two different profiles; an increase then a decrease for D2 and D3 and a continuous increase for the D1.

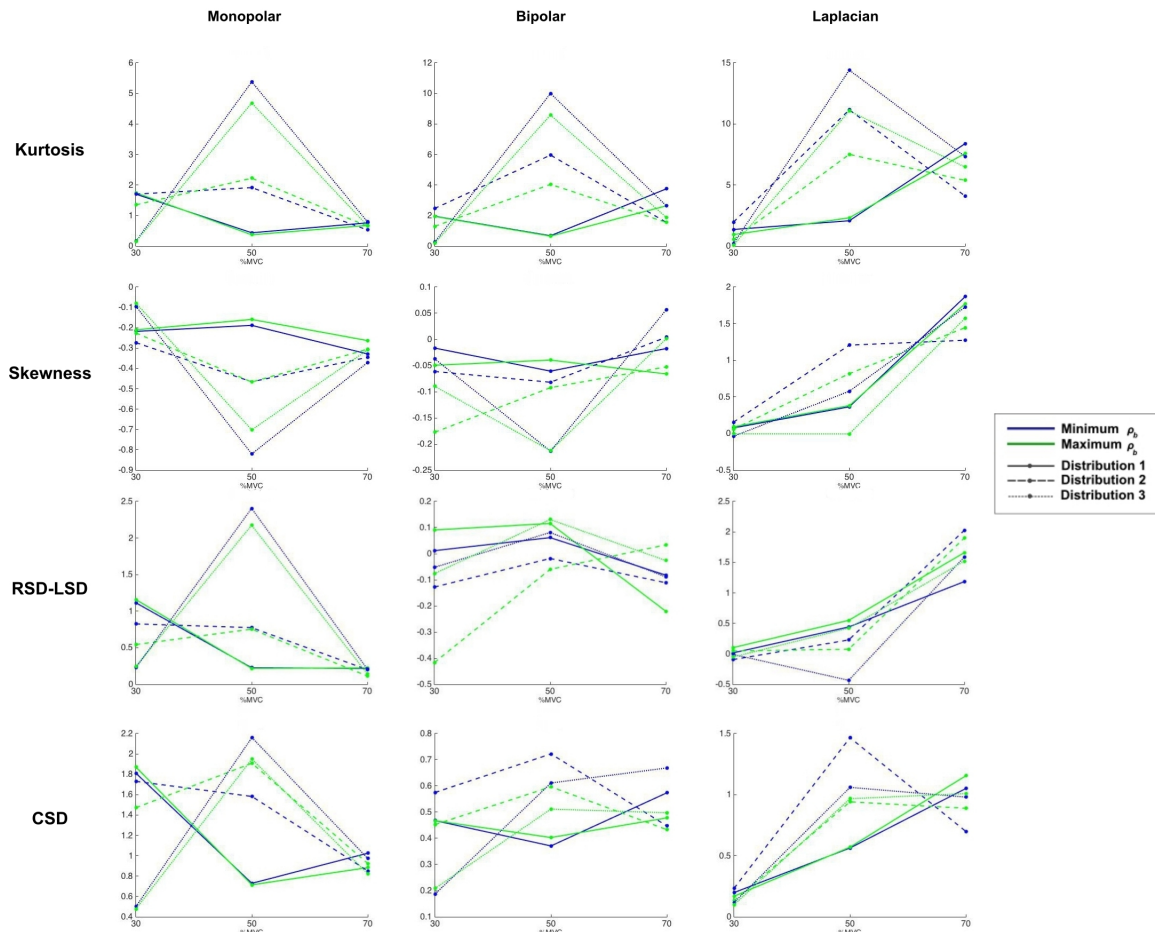


Figure 3.19: The obtained profile variation for kurtosis, the skewness, RSD-LSD and CSD according to contraction level (30, 50 and 70 %MVC) for the LRS for monopolar, bipolar and Laplacian arrangements.

If we examine now these same parameter trends for the LRS (Figure 3.19), we can see that we have a different variation profile for the HOS and the SD parameters. the profile seems to vary according to the MU type percentage distribution. For the monopolar configuration, we can see three groups of curves for all the parameters corresponding to D1, D2 and D3 but only two types of variations; an decrease then an increase which we called a V-shape variation for the D1 and an inverse V-shape variation (an increase then a decrease) for D2 and D3. These dynamics are much more pronounced in the D3 case. In the Laplacian configuration case, we have a continuous increase for all the parameters corresponding to D1. But for D2 and D3 we have a continuous departure from Gaussianity from 30 to 70 %MVC for both skewness and RSD-LSD parameters that describe the asymmetry of the PDF shape and an inverse V-shape profile for both kurtosis and CSD that describe the flatness of the PDF shape. Lastly for the bipolar configuration, we have similar profiles for the kurtosis and the CSD as the monopolar ones. Differently, the CSD parameter produces three different trends for D1, D2 and D3. The RSD-LSD parameter however does not have consistent results. Now by comparing between the HRS and LRS we can see different profiles for the same MU type percentage distribution. For example, in the monopolar configuration for D1 we have a V-shape profile for the LRS and an inverse V-shape profile for the HRS

according to all the parameters. We have to notice here the influence of the adipose tissue thickness ( $\rho_b$ ) on the parameters profile variation, that seems to have more pronounced effect than the skin tissue thickness ( $\rho_c$ ). This effect on the trend dynamics is, similarly to the  $\rho_c$ , more noticeable in the bipolar configuration type than the monopolar and the Laplacian. We can also observe that the monopolar arrangement is the more sensitive to the MU type distribution comparing to the others.

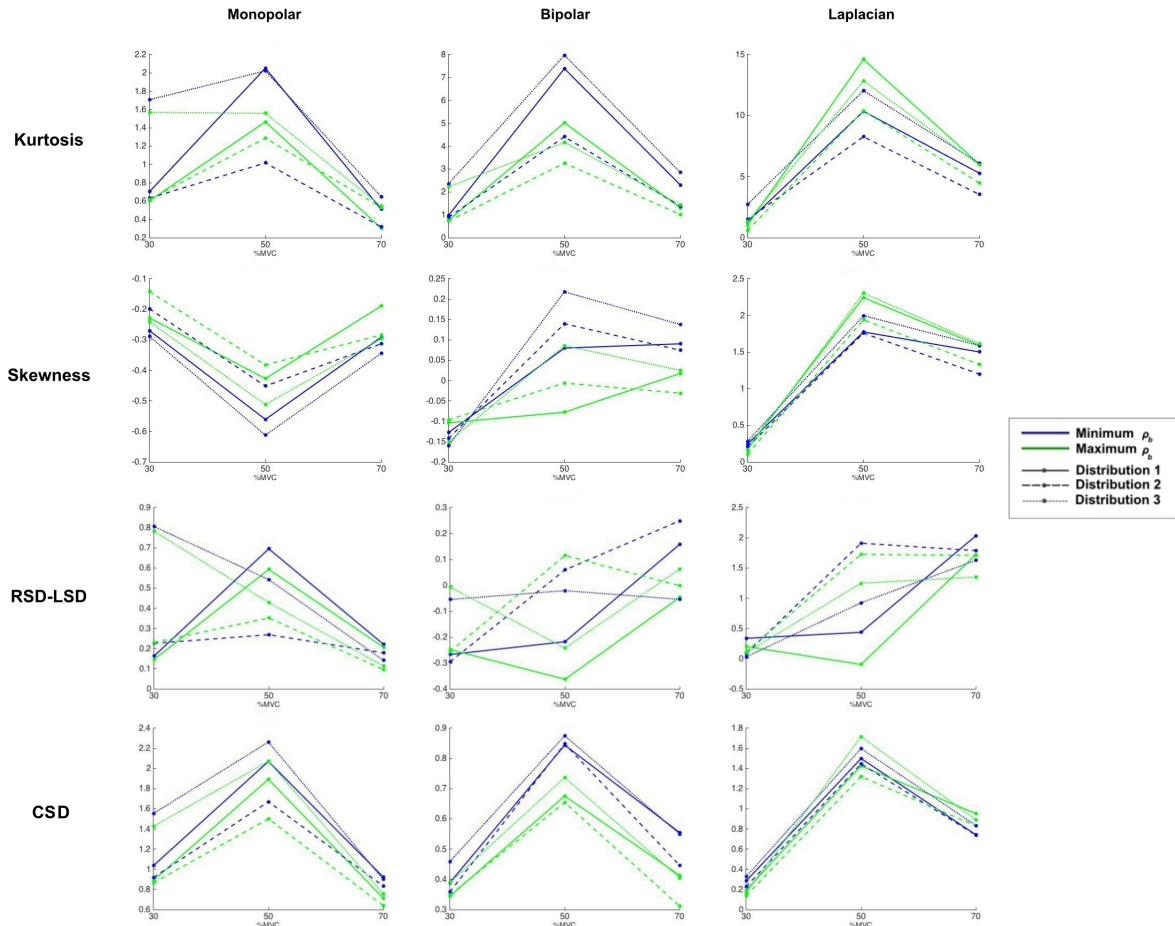


Figure 3.20: The obtained profile variation for kurtosis, the skewness, RSD-LSD and CSD according to contraction level (30, 50 and 70 %MVC) for the HRS for monopolar, bipolar and Laplacian arrangements..

Furthermore, we generated new signals of the first two simulations using nonlinear discharge frequencies (rate coding) in low and high recruitment forms (same principle as the ones for the linear rate coding case) [50]. The main observation from the monopolar, bipolar and Laplacian results is that we found the same global trends as the ones for the linear case. Figure 3.21 presents an example of the PDF shape variation with force level increase for both monopolar, bipolar and Laplacian configurations after extraction of the dominant profile for simulation  $D1min\rho_b$ .

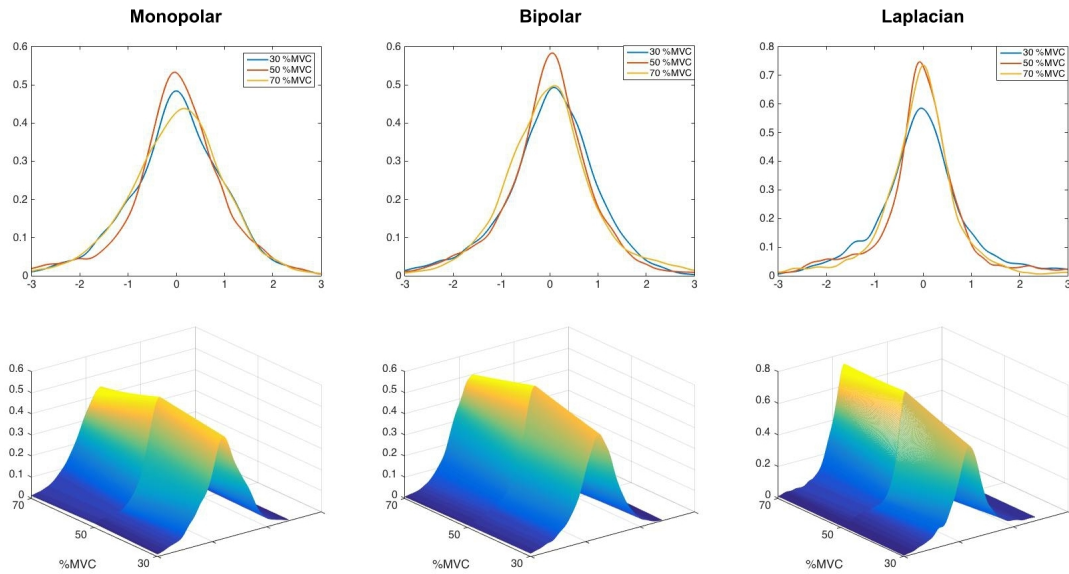


Figure 3.21: The PDF corresponding to the dominant profiles according to force intensity (30, 50 and 70 %MVC) for anatomy 1 with high recruitment strategy.

### 3.3.2.5 HOS and SDs variations with force level increase for the experimental signals

For the experimental signals, after denoising using the CCA approach, we started by computing the PDF shape descriptors for the 64 monopolar HD-sEMG signals of the grid according to the three levels of muscle force 30, 50 and 70%MVC. Figure 3.22 illustrates these matrices for one of the six subjects (subject 1) that was chosen for illustration purposes. The main observation is that all parameter matrices are heterogeneous which is common for all subjects indicating the important impact of the MU distribution within the muscle similarly to the simulation case. We chose in this case to show the LSD instead of the RSD-LSD since we have very little dynamic for both RSD and LSD parameters.

Afterwards, the parameters trends were computed for the signals obtained after channel selection and data fusion (see section 3.3.2.2) identically to the simulation study. This dominant profiles were computed for three subjects for the monopolar, bipolar and Laplacian configurations after removing subjects 4, 5 and 6 from this part of the study since they were not capable of maintaining a constant force for 5s and had important force variation along the supposed constant force plateau. The obtained results for all parameters are presented in Figure 3.23. These results corresponding to subjects with different anatomical properties present different variation profiles as expected.

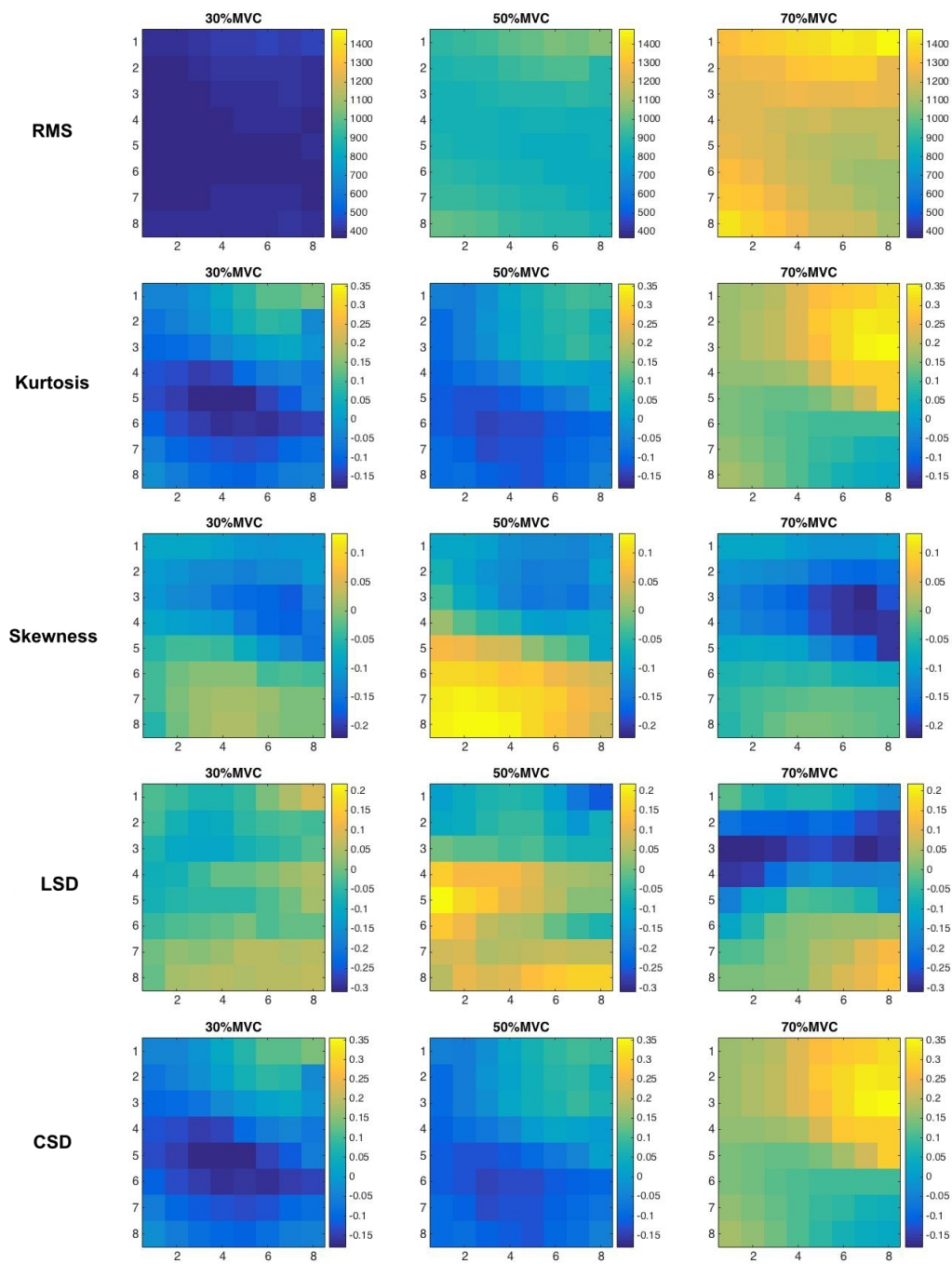


Figure 3.22: The RMS, kurtosis, skewness, LSD and CSD variations for the  $8 \times 8$  HD-sEMG grid according to force intensity (30, 50 and 70% MVC) for subject 1.

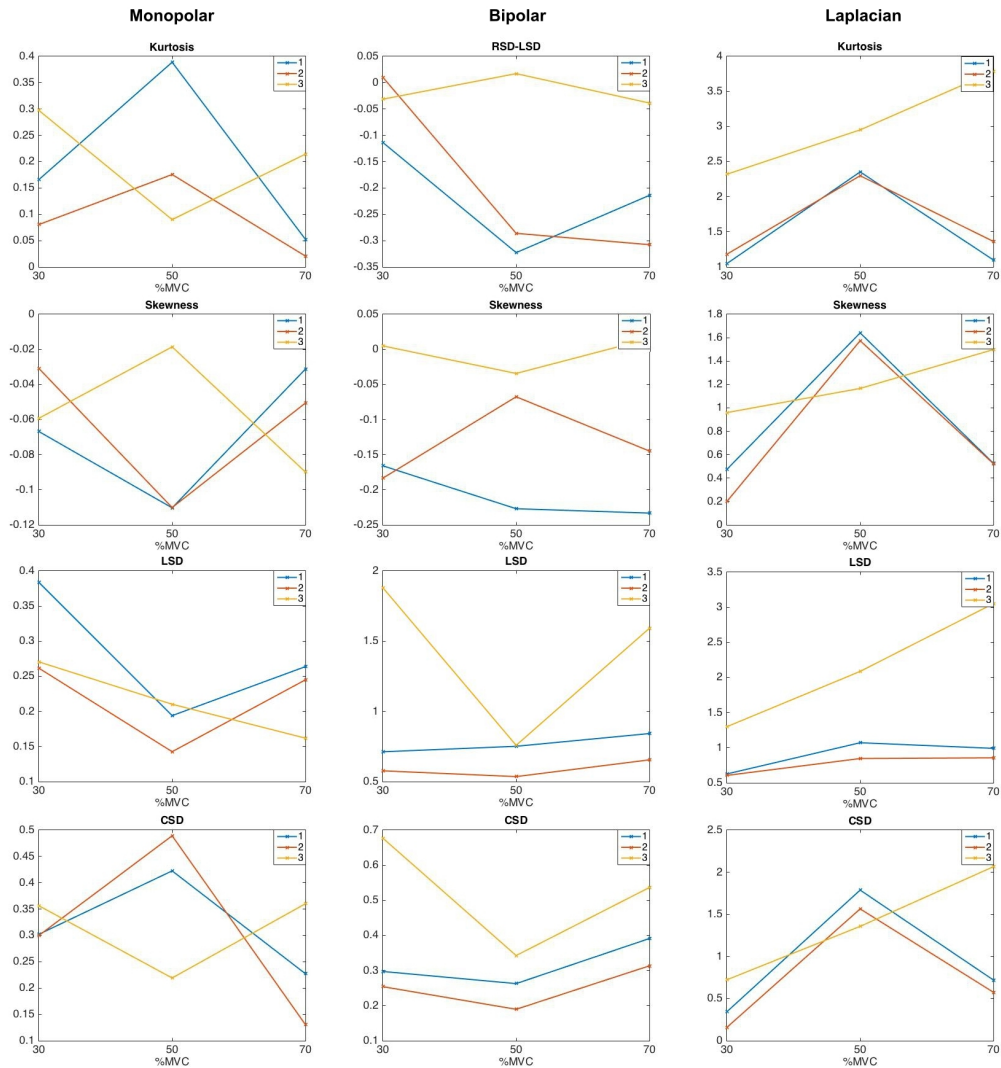


Figure 3.23: The variation of the kurtosis, skewness and LSD and CSD) for the monopolar, bipolar and Laplacian arrangements according to force intensity (30, 50 and 70 %MVC) for subjects 1, 2 and 3.

If we start by the monopolar signals, we can find two global trends that were also observed in simulation which are the V-shape and inverse V-shape trends. The first type of trend was observed for subjects 1 and 2 where we have a departure from it from 30 to 50 %MVC then a convergence toward Gaussianity from 50 to 70 %MVC. This profile was obtained by both HOS and SD parameters computed for the monopolar signals after image segmentation as previously explained. The other type was obtained for subject 3 where we have the inverse profile of subjects 1 and 2. In this case, we have a convergence toward Gaussianity from 30 to 50 %MVC then a departure from it between 50 and 70 %MVC.

In the Laplacian case, we can uncover a consistency between the parameters. In fact, subjects 1 and 2 have profiles that increases from 30 to 50 %MVC then decreases from 50 to 70 %MVC for the kurtosis, skewness, LSD and CSD. Further, subject 3 has profiles that increase for all the parameters which resembles the results obtained in simulation.

Finally, for the bipolar configuration, we cannot really find any consistency in the trends except for

subject 5 where we have a convergence toward Gaussianity detected by all the parameters. An example of the PDF shape variations with force level increase for both monopolar, bipolar and Laplacian configurations after extraction of the dominant profile is shown in Figure 3.24 for subject 1.

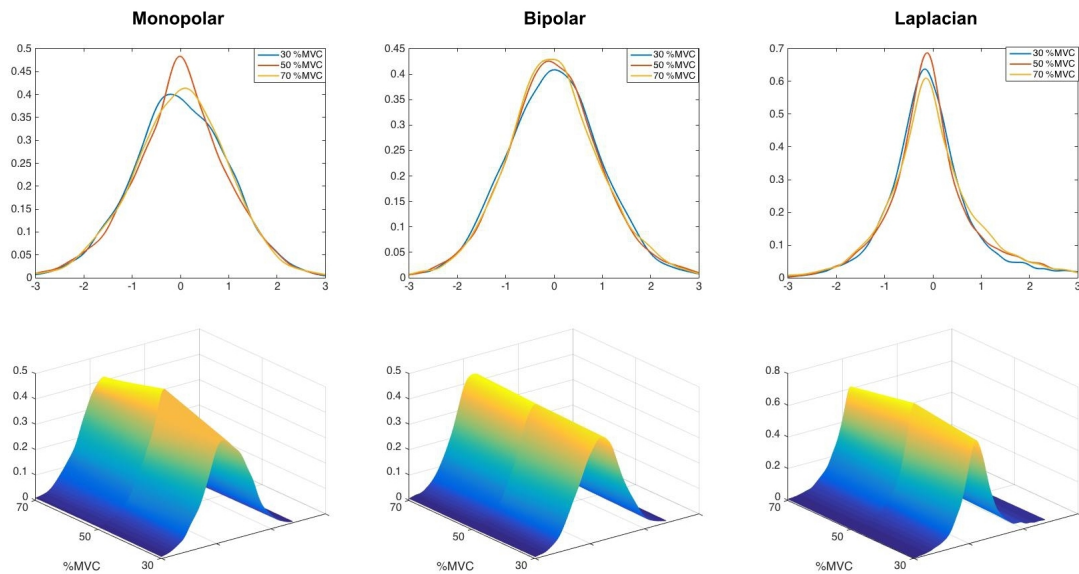


Figure 3.24: The PDF corresponding to the dominant profiles according to force intensity (30, 50 and 70 %MVC) for subjects 1.

### 3.3.2.6 Discussion and conclusion

This study focused on the shape variation monitoring of the PDF of the sEMG signal with force increase in isometric conditions, which is justified by the link existing between the amplitude variation of the sEMG signal and the recruitment of MUs. Three electrode arrangements (monopolar, bipolar and Laplacian) were investigated based on a recent simulation study [50] on the evaluation of the ability of shape descriptors in classifying muscle contraction levels solely based on sEMG PDF shape modifications.

Following this last study, the main objective of the proposed simulation study is to possibly explain the results obtained in experimental conditions, by performing a focused sensitivity analysis toward specific parameters that can influence the variation profile of the HOS and the SDs. Therefore, we started by studying the influence of the morphological parameters: the adipose tissue thickness  $\rho_b$ , the skin tissue thickness  $\rho_c$  and the muscle length  $L$ . The results for the monopolar, bipolar and Laplacian signals indicated that muscle length basically has no influence on the HOS profiles (Figure 3.18). Contrarily, the skin tissue thickness has an important influence on the dynamic of the parameters (Figure 3.17) particularly for the bipolar signals. This dynamic variation appears to decrease with skin tissue thickness increase which is normal due to its filtering effect even for a limited variation of 0.09 mm. For the  $\rho_b$ , if we look closely at Figures 3.19 and 3.20 and compare between the anatomies that have the same MU repartitions but different  $\rho_b$ , we can clearly see the effect of  $\rho_b$  on the variation dynamics of all parameters. On that account, the first main result obtained through the simulation study is that morphological

parameters and predominately the skin and adipose tissue thicknesses have an effect only on the dynamic of the parameter profile variations. Needless to remind here the important spatial filtering effect of the adipose tissue on the sEMG signals [168]. It is also important to recall that the observed signals are almost Gaussian in the absence of muscle contraction (0% MVC) in both simulation and experimental studies.

Then, we turned our focus on the effect of the MU recruitment strategy on the variation profiles. Therefore, we tested two different recruitment strategies that we named LRS and HRS (see section 3.3.2.3). Figures 3.19 and 3.20 exhibit the variation profiles for the LRS and HRS respectively according to the three MU type distributions (see Table 3.3) and the  $\rho_b$  extrema values. The main observation is that the recruitment strategy has a major effect on the global profile variation of the HOS and SD parameters. If we start by analyzing this effect on the monopolar signals, we can see that for the HRS (Figure 3.20) we have the same profile for all three MU type percentage distributions, except for the RSD-LSD that presents two different profiles, which can be explained physiologically by the fact that at 50%MVC Fast MUs start to be recruited. Therefore for the monopolar and Laplacian arrangements, the PDF becomes more peaked and negatively (positively) asymmetric which leads to an important skewness (toward negative values and positive ones for the Laplacian arrangement) and CSD and kurtosis increase. Then, at 70% MVC, we have a profile that reach toward a Gaussian distribution, when most MUs are recruited for all parameters and MU type distributions indicating possible influence of the number of the underlying random variables according to the central limit theorem. Differently, in the LRS case (Figure 3.19), we can clearly detect three groups of curves corresponding to D1, D2 and D3 wherein we can find the same profile for D2 and D3 in both LRS and HRS. This profile is an increase in the non Gaussianity from 0 to 50 %MVC. This increase is more significant for D3 since we have less SMUs and more FFMUS (see Table 3.3). Therefore, we have less SMUs superposition and signals with asymmetric and peaked PDFs. Then a return to Gaussianity from 50 to 70 %MVC due to the recruitment of important number of FFMUs that causes the PDF to become more flat and symmetric. The profiles relative to D1, however, adopts opposite trends for the LRS and the HRS. This fact can be explained by taking in consideration the Gaussianity of the signal before the beginning of the contraction (at 0 %MVC). Thus, for the HRS since we have already FFMU that are recruited before 50 %MVC we have a departure from Gaussianity from 0 to 50 %MVC then we start to converge toward Gaussianity at 50 %MVC when we have enough MUs that are recruited. As for the LRS, the PDF start almost Gaussian at 0%MVC then, as MUs are recruited, we have a departure from Gaussianity until we reach 30%MVC where we have a certain number of MUs without any recruited FFMUs then we start to lean back toward Gaussianity from 30 to 50%MVC. But at 50 %MVC, we have a recruitment of FFMUs that causes a departure from Gaussianity once again from 50 to 70%MVC. We have similar trends for the Laplacian configuration except for a continuous departure from Gaussianity for the D1 in LRS case instead of a decrease then an increase like in the monopolar configuration. This

continuous departure from Gaussianity for all parameters (HOS and SD) can be explained by considering the shape of Laplacian PDFs of sEMG signals that are less flat than the monopolar ones. Thus, with force level increase from 0 to 30 %MVC, the PDF becomes more peaked and positively asymmetrical. This departure from Gaussianity becomes more decisive when FFMUs, closer to the surface, are recruited from 50 to 70 %MVC. This should be explained by the generation and superposition of asymmetrical MUAPs from the rapid (FF) MUs closer to the surface. Lastly for the bipolar configuration, we have the same trends as the monopolar ones for the kurtosis and the CSD that describes the flatness of the PDF. No consistency is obtained with the bipolar arrangement concerning both skewness and RSD-LSD measure indicating clear irrelevance of PDF asymmetry checking for this arrangement. This should be explained by the recorded symmetrical MUAPs generating symmetrical PDFs. These same profiles were also obtained for the nonlinear discharge frequency in HRS and LRS. In order to make sure that these trends are not the result of a particular anatomy we regenerated all the results for different anatomies (placement of MUs) and found the same trends. To finish with the simulation results, we found the monopolar and the Laplacian configuration to be more relevant in the monitoring of the PDF shape trends than the bipolar one. In fact, monopolar arrangement has the greater detection volume that possibly justifies its sensitivity to varying MU distribution and neural control paradigm. For the Laplacian arrangement, its spatial selectivity should explain its sensitivity to modification related to a muscle region closer to the surface and related to FFMU modification (type and recruitment). We also found that the kurtosis and the CSD have consistent trends among all configurations. In fact, the proposed SDs seems to be relevant, in complement to classical HOS parameters, in PDF shape analysis.

The second part of this study was dedicated to the experimental signals obtained from the five subjects after removing the three other subjects because they were not able to follow the target force (std > 20%). The study of the sEMG shape variation using HOS and SD parameters gave us interesting profile variations. Globally, by observing the obtained trends in Figure 3.23 for all the signals, we can see that we have different trends between the subjects.

As previously described, for subjects 1 and 2 we have profiles for the monopolar signals that resembles the ones obtained by simulation (see Figure 3.19). This is also confirmed by the profiles depicted for the Laplacian configuration. In addition, if we observe the profiles dynamics we can say that they have comparable dynamics which is confirmed by the adipose and skin tissue thicknesses values for these two subjects (see Table 3.1). Now if we look at the trends computed for subject 3, we can see that they fit the LRS trends obtained for first MU type distribution D2 (see Table 3.3). This is verified by the same trend for all the monopolar and Laplacian results corresponding to the kurtosis, skewness, LSD and CSD. The bipolar profiles are less clear to explain, which is normal due to the symmetrical shape of the corresponding MUs PDFs that can prevaricate the results (see Figure 3.21).

In conclusion, we investigated by simulation and by experimental studies the variation of the PDF of

HD-sEMG with isometric contraction level variation. For this purpose, we tested the influence of different parameters on the profile variation of HOS (kurtosis and skewness) and the SD (CSD and RSD-LSD) parameters. These parameters were chosen as an adequate shape screening approach based on a recent study [50]. Three electrode arrangements were analyzed; monopolar, bipolar and Laplacian. We chose the WS segmentation method [147] in order to extract the dominant profile for both experimental and simulated signals. The main obtained result from this study is that the profile variation of the PDF shape with force level increase seems to be subject specific. Indeed, it depends on many variables, starting from the recruitment strategy and the MU distribution in the muscle that were proven to have the prominent influence in comparison to the architectural parameters. It is important to note here the limitations of this study in the cases of aging people, and even people with a very high BMI. Because there is a lack of realistic skin and adipose tissue conductivity information for these cases that can be incorporated in the proposed HD-sEMG simulation model. Even in our case, where we had healthy people with  $BMI < 25$ , the used conductivities were obtained from [169] where there is no physiological validation for the proposed values. This can explain why we had higher PDF shape parameter ranges in simulation in comparison with experimental signals. Another explanation could be that in the case of LRS the number MUs is not sufficient to faithfully portrait the reality. Finally, this study is the first global analysis that tries to present a simulation explanation to the observed experimental profiles, and enables a sort of electronic biopsy. In fact, from the analysis of HOS and the SD profile variations, one can figure out the recruitment strategy type or the MU type distribution for this particular subject as for the analysis of the MUAP amplitude in [170]. We can also compare the adipose tissue thickness between two subjects based on their corresponding profile variation dynamics. In the next chapter, we will use these information to separate subjects according to there MU type distribution to ease the force estimation process.

### 3.4 Muscle surface deformation

Muscle's architectural parameters were proven to provide complementary information for muscle functionality assessment [79]. In recent years, the architectural parameters of the BB (muscle thickness, dimension and cross-sectional area) were measured using sonography [79] as a noninvasive method for musculoskeletal assessment and control [77, 171]. However, the external shape of the BB obviously changes with contraction level. It could potentially provide a noninvasive information about muscle activation, without the complications of the load sharing problem and the cross-talk phenomena that should be present using sEMG technique [79]. In parallel, Motion Capture (MoCap) is often used in entertainment fields (movies, animation games...), sports for improving performances and clinical analysis for diagnostics and treatment [172, 173]. The most common technique for human MoCap uses markers placed on the skin surface, and are tracked in real-time by an appropriate system [174]. Recent developments on the

camera resolution and motion capture post-processing allowed the 3D tracking of anatomical segments positions or motion [175]. Thus, the aim of this study is to demonstrate the feasibility of monitoring the 3D curvature change of the BB under isometric contractions using MoCap technique. Therefore, a Mo-Cap system was used to study the variation of the curvature of the BB with contraction level. Then, the 3D positions of the reflective markers relative to four contraction levels: 20, 40, 60 and 80% MVC were recorded for five subjects. The obtained 3D data are used to reconstruct simulated ellipsoidal volume that provides parameters for curvature monitoring. Afterwards, relationship between these parameters and muscle contraction level are assessed.

### 3.4.1 Experimental protocol

Five healthy male subjects (mean  $\pm$  std, age:  $27.2 \pm 2$  years; stature:  $176.8 \pm 4.7$  cm; body mass:  $73.8 \pm 2.3$  kg; Body Mass Index BMI:  $23.2 \pm 1.7$ ) participated in the study respecting the declaration of Helsinki. All participants provided their written consent and did not relate any history of muscular or neurophysiological problem at the upper limbs. Their dominant hands were selected for the investigation.

In this study, an ultrasound device (Siemens ACUSON Antares 5.0 Ultrasound System) with a 7.5 MHz probe was used in order to mark the BB boundaries for each subject before the placement of the reflective markers. In order to track the surface deformation of the BB muscle, we placed 41 small reflective markers (4 mm diameter). These lightweight markers are made of polystyrene hemispheres and covered in special retro-reflective tape. These markers were placed as shown in Figure 3.28, following a lozenge shape with diagonals equal to the length (L) and the width (l) of the BB obtained with ultrasound imaging for each subject. The inter-markers distance is equal to  $L/8$  longitudinally and  $l/8$  transversally. Additional markers were placed in order to verify the elbow angle (fixed at  $90^\circ$ ) and the displacement vector of the exercised force. These markers were placed as follow: C7, acromion, medial and lateral epicondyle, clavicle, radius, ulna and four markers on the force sensor cord. The markers 3D positions were captured by a motion analysis system Vicon T160 (Vicon Motion Systems Ltd., Oxford, UK) with the Nexus 1.7.1 software, through 18 synchronized infrared cameras T160 of 16 Megapixel ( $4704 \times 3456$ ) and a frame rate of 100 frames per second. The block diagram of the experimental setup is presented in Figure 3.25. The global force signal was measured simultaneously with the muscle deformation using a strain gauge (S-Beam SB2500) (Figure 3.26) with a Biometrics K800 Amplifier and an Analog to Digital Converter. The force was displayed in real-time using a LabVIEW customized interface as visual feedback for the subjects as shown in Figure 3.27. The subjects were seated in a customized ergometer using a preacher curl bench with the dominant arm placed on the bench (Figure 3.26). A flexible backing and rigid protection were placed around the wrist to block its movement and protect it. Then, the strap attached to the force sensor was placed on top of the wrist protective elastic. Before beginning the experiment, the position

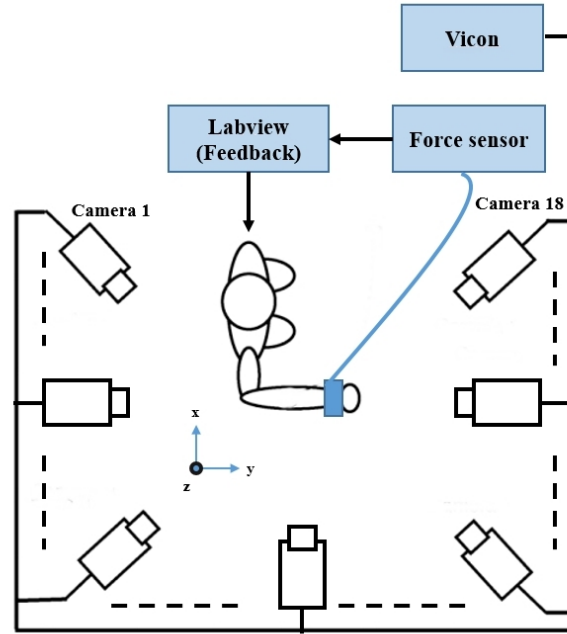


Figure 3.25: Setup for the simultaneous collection of the muscle force and the motion data.

of the bench is adjusted such as the elbow angle is equal to  $90^\circ$  in isometric condition with continuous monitoring (see Figure 3.29). After the MVC values were measured; the subjects were asked to perform a series of constant isometric forces at 20, 40, 60 and 80% of the MVC lasting about 5 seconds each with a resting time of 1.5 ~ 2 min between the contractions, by following the reference on the screen (Figure 3.26). Three trials were conducted for each force level and additional relaxation recording was conducted for each subject to calibrate the markers during the rest condition.

### 3.4.2 Data processing

All the motion capture data (3D positions of the markers) were imported into MATLAB<sup>TM</sup> (MathWorks, R2013b) where a customized algorithm was developed for the processing and the analysis of the skin marker's displacement. The protocol described above allows us to obtain for each subject: 4 contraction levels  $\times$  3 trials  $\times$  41 markers  $\times$  500 samples. Thus, for each force level we averaged the coordinates along the 5 seconds plateau of constant force. Afterwards, the positions were normalized for each subject since the positioning of the markers was subject-specific (with respect to the corresponding muscle length and width). Then, the normalized 3D data points were fitted first, in a freely manner, into a surface of the form  $z(x, y)$  using a surface modeling tool (MATLAB, gridfit.m) in order to visualize the 3D surface deformation. Secondly, the 3D data were employed for constrained ellipsoidal fitting using linear least square minimization and Singular Value Decomposition (SVD) in order to determine the 9 parameters describing the ellipsoid algebraic equation:

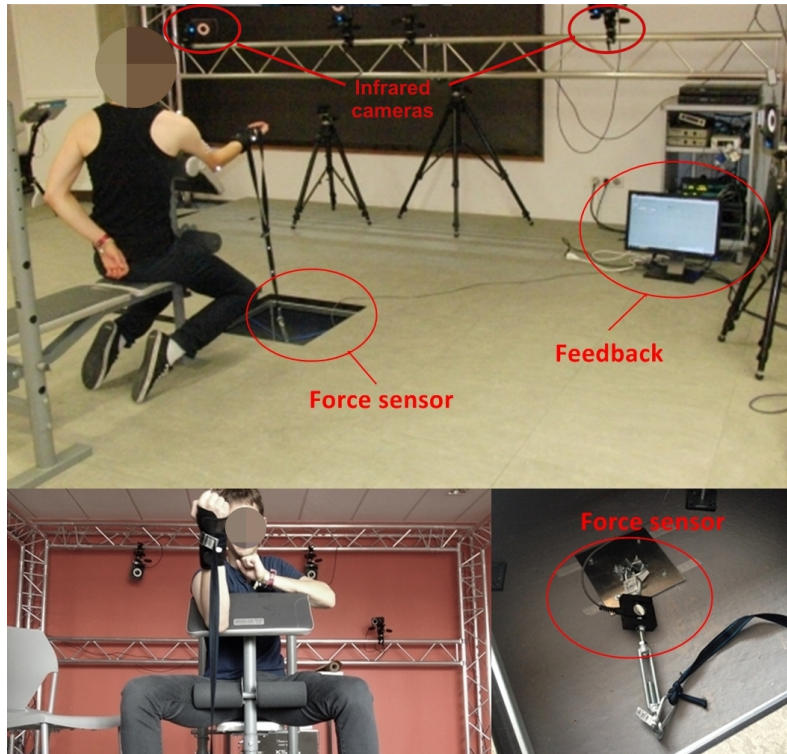


Figure 3.26: The experimental protocol setup with the force sensor.

$$Ax^2 + By^2 + Cz^2 + 2Dxy + 2Exz + 2Fyz + 2Gx + 2Hy + 2Iz = 1 \quad (3.15)$$

Where  $x$ ,  $y$  and  $z$  present the Cartesian coordinates and  $A$ ,  $B$ ,  $C$ ,  $D$ ,  $E$ ,  $F$ ,  $G$ ,  $H$  and  $I$  are real constant parameters.

This ellipsoidal fitting was chosen as suitable for the 3D volume deformation of the BB, since the NRMSE of the fitting obtained for all normalized experimental data was small ( $<10\%$ ). The elbow angle was also computed for each force level by tracking the positions of the 5 markers placed on the acromion, the medial and lateral epicondyle, the radius and the ulna as shown in Figure 3.29 to verify that its value is fixed at  $90^\circ$ .

### 3.4.3 Results and discussion

As mentioned previously, we started by fitting the 3D positions of the markers into a surface on a 2D grid of the form  $z(x, y)$ . This fitting extrapolates smoothly the surface beyond the convex hull of the data. The result of this fitting is presented in Figure 3.31 for 0% MVC (relaxed muscle) and for 80% MVC. As we can see in Figure 3.31, the deformation of the muscle surface can be clearly observed. Since with muscle activation increase, we have a shortening of the muscle resulting in curvature increase.

Afterwards, we fit the data into an ellipsoidal volume. The result for one of the subjects is presented

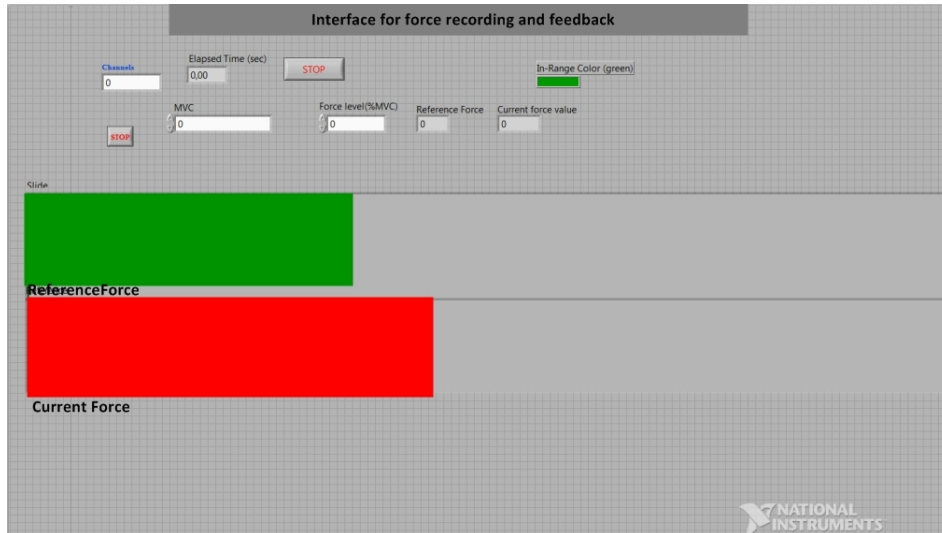


Figure 3.27: The LabVIEW force monitoring interface used as feedback for the subjects.

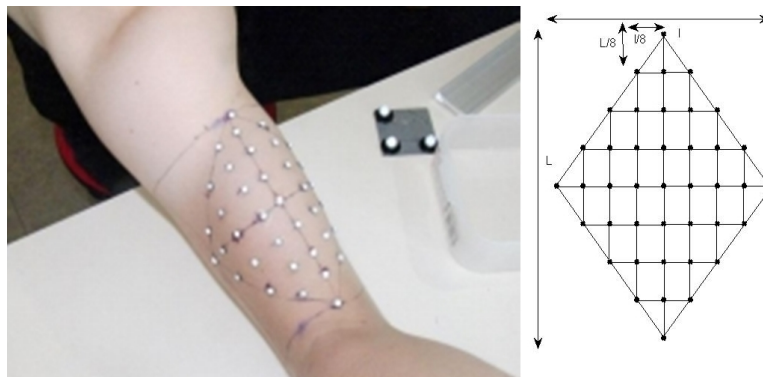


Figure 3.28: The placement of the 41 markers in a lozenge shape on the BB .

in Figure 3.30 for two levels: 20% and 80% MVC. One can clearly observe that the ellipsoid cross-section becomes larger and its length decreases with contraction increase (Figure 3.30).

Then, we took the middle row of the marker lozenge, since it has the maximum deformation and we computed the parameters in 2D of the corresponding ellipses for the four contraction levels 20, 40, 60 and 80% MVC. Figure 3.32 shows the positions of the nine markers for the four levels of force initially (Figure 3.32a) then the result of the fitting to an ellipse (Figure 3.32b). The obtained relationships of the two used parameters ( $a$  and  $b$ ) for all the subjects with contraction level increase are shown in Figure 3.33. These relationships seem to be monotonic for both studied parameters with a smaller observed variance for the parameter  $b$ .

We proposed, in this study, an instrumental and processing protocol for the estimation of BB muscle deformation during isometric contractions. The proposed methodology bears on MoCap technique and a force sensor. For this purpose, in an attempt to model the BB volume deformation, we proposed an ellipsoid fitting method using the 3D positions of small 41 markers attached to the surface of the BB muscle using specific surface mesh. This ellipsoidal hypothesis seems to be relevant for monitoring



Figure 3.29: Elbow angle computing from the positions of the 5 markers placed on the acromion, the medial and lateral epicondyle, the radius and the ulna.

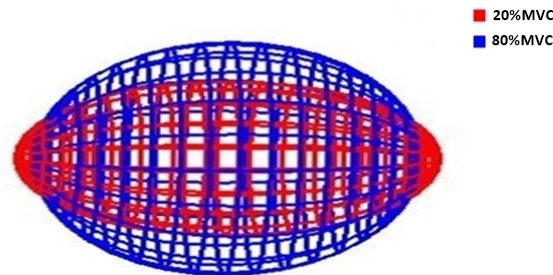
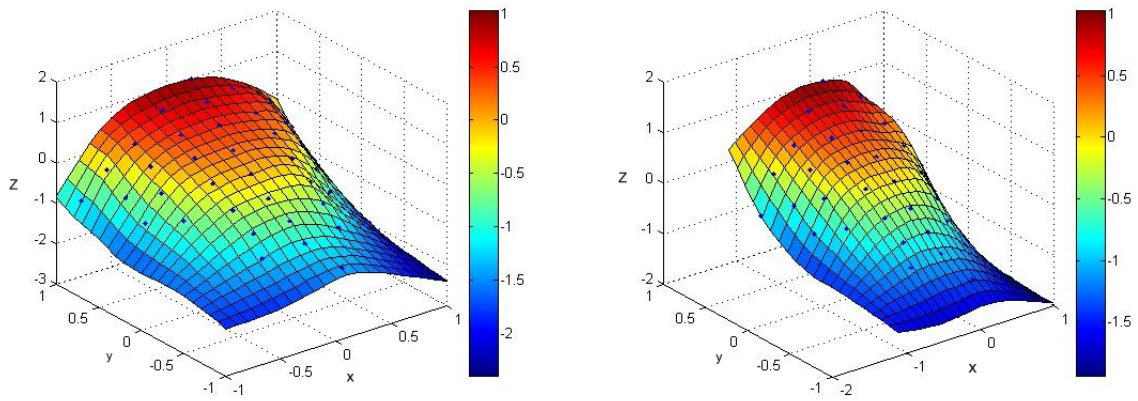


Figure 3.30: The ellipsoid fitting of the 3D marker positions for two contraction levels: 20 and 80%MVC for one studied subject.

BB volume deformation since usually the BB volume is either modeled using 3D finite elements or finite volume models [176, 177] or analytically using a fixed volume cylinder [158]. Thus, the ellipsoid hypothesis was chosen over the cylinder fitting based on the fitting NRMSE which was important in the second case.

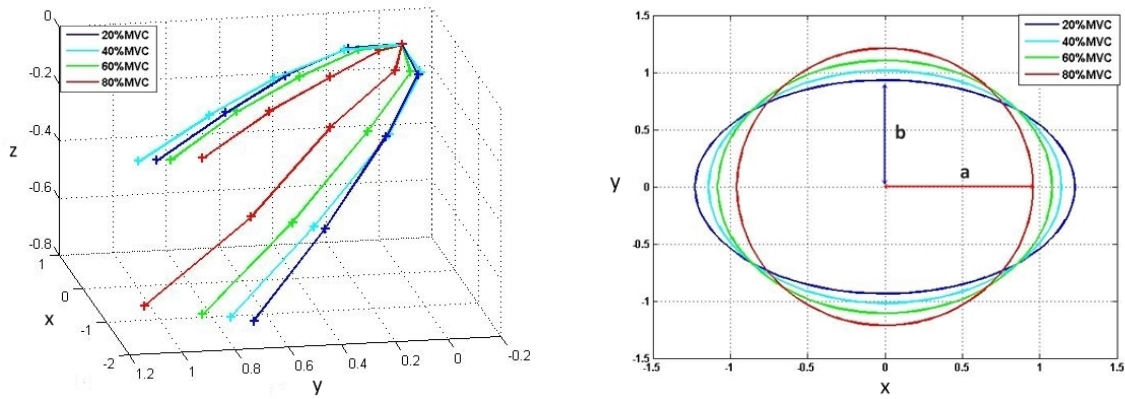
We had not included the relaxation data in the ellipsoid fitting since it did not give coherent results. It seems that ellipsoidal hypothesis doesn't hold in rest state. We have also proposed to monitor BB surface deformation in a freely manner. For the 2D cross-sectional ellipse fitting, we chose the middle row since it has the maximum of points (9 points) and the maximum deformation in comparison to the other lines of the marker mesh. Further investigations with more markers at the belly of the BB should be performed to demonstrate if it could provide more accurate information on the 3D external surface of the muscle.

The relationship between muscle architecture and its functionalities is useful for providing valuable and complementary information [171] to the classical tools and instrumental modalities. Thus, it should be interesting to combine the information obtained from the muscle external shape deformation in order to estimate the muscular activation and force in complement with sEMG-driven force estimators [120] that suffer from the load sharing problem [42] for their validation. Another important application of the proposed work is providing realistic muscle deformation models for simulation purposes [50] of both electrical and mechanical phenomenon that occurs during muscle contraction. It is important to add that there is a strong limitation related to the adipose layer thickness of the subject. Since the access to the



(a) The 3D surface fitting of the surface of the BB for 0% MVC (b) The 3D surface fitting of the surface of the biceps for 80% MVC

Figure 3.31: 3D surface fitting of the surface of the BB



(a) The 3D positions of the 9 markers of the middle line. (b) The four ellipses corresponding to the fitting of the 9 markers 3D positions for four contraction levels: 20, 40, 60 and 80 %MVC.

Figure 3.32: Ellipsoid fitting for the 9 markers at the center of the diamond.

actual muscle deformation is limited by the layer of adipose tissue. In our study we had only subjects with a healthy BMI (small adipose tissue thickness).

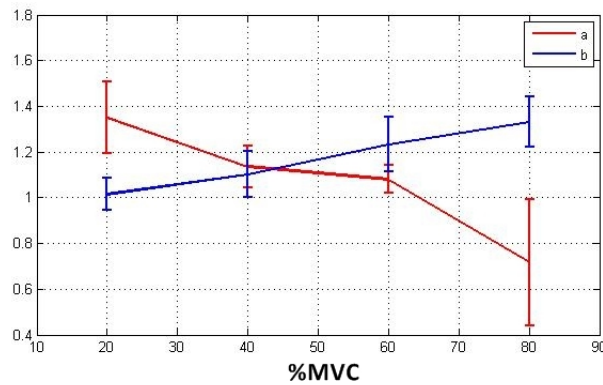


Figure 3.33: The corresponding parameters (a and b) for all subjects.

In fact, the present study demonstrated that it seems to exist a monotonic relationship between the curvature of the BB and the contraction level which is consistent with previous work on the morphological deformation of the BB, that demonstrated that the architectural changes during muscle contraction are more related to the mechanical output (torque) [79]. However, further studies are needed to ameliorate the proposed methodology for multimodal analysis dedicated to functional evaluation of skeletal striated muscles.

### 3.5 Conclusion

In this chapter of the thesis, our aim was to design the input parameters of the HD-sEMG/force relationship model from the HD-sEMG map that best describes the muscle activation. Accordingly, in the first section we presented a recently used image segmentation method, the WS, for localization of the region of interest in a HD-sEMG electrode map of ARV values [147]. This method serves as a dimension reduction procedure to decrease the number of channels in the  $8 \times 8$  map. However, in our study, we chose to use the RMS value instead of the AVR since it was proven more robust to spacial aliasing [162]. This segmentation method on the RMS maps allows us to obtain, after averaging, one value of the RMS parameters for each contraction level. Afterwards, the next section is a global study of the PDF shape variation with contraction level increase. Thus, we started by an experimental study of parameters profile variations in isometric anisotonic contractions. Then, we evaluated the variations of parameters for isometric isotonic contractions in simulation and experimental conditions. The purpose of this study was to test the sensibility of HOS and SD parameters to different morphological, anatomical and neural parameters in order to find out if they can be used as additional input parameters in the HD-sEMG/force relationship. The obtained results, for both presented studies, were promising in the sense that they can undoubtedly provide information about the different parameters mentioned earlier. In addition, we have to mention that the poor experimental results are due to the difficulty of following the

target force value in isometric isotonic contractions. Nevertheless, these profiles can help to improve force estimation by providing information that can characterize each muscle (subject specific). The final section of this chapter aimed at testing additional parameters that can quantify the muscle activation. These parameters are obtained from the muscle external surface deformation using MoCap technique. However, this recording technique need heavy materials and special equipment and location unlike the HD-sEMG acquisition system that is portable and easily used. In the last chapter of the thesis we will investigate the HD-sEMG/force relationship modeling and propose a new relation type model based primarily on the RMS parameter and secondly on morphological parameters complemented by anatomical parameters discovered by analysis of the HOS profiles.

# Chapter 4

## HD-sEMG/Force relationship modeling

### Contents

---

<b>4.1</b>	<b>Introduction</b>	<b>157</b>
<b>4.2</b>	<b>HD-sEMG/Force relationship modeling</b>	<b>158</b>
4.2.1	Muscle force generation model	159
4.2.2	HD-sEMG simulation	160
4.2.3	Study of the parameters influencing the shape of the HD-sEMG/Force relationship	162
4.2.4	HD-sEMG/force relationship fitting	166
4.2.5	Improving polynomial fitting using optimization	169
4.2.6	Sensitivity analysis of the polynomial fitting	170
4.2.7	Discussion and conclusion	176
<b>4.3</b>	<b>HD-sEMG driven muscle force estimation model</b>	<b>177</b>
4.3.1	Supervised regression approach	177
4.3.2	Analytical approach	185
<b>4.4</b>	<b>Conclusion</b>	<b>188</b>

---

## 4.1 Introduction

This chapter is dedicated to the HD-sEMG/force relationship modeling. In order to model this relationship, we need a realistic HD-sEMG and force simulation models that are fed with the same muscle configuration and MU discharge pattern as shown in Figure 4.1. This Figure depicts the proposed approach used in simulation for the estimation of the HD-sEMG/force relationship for an individual simulated muscle; the BB. Accordingly, we will be using the multilayered cylindrical model [158], described in chapter 3, for the HD-sEMG signals generation and a twitch based model for the force simulation [178].

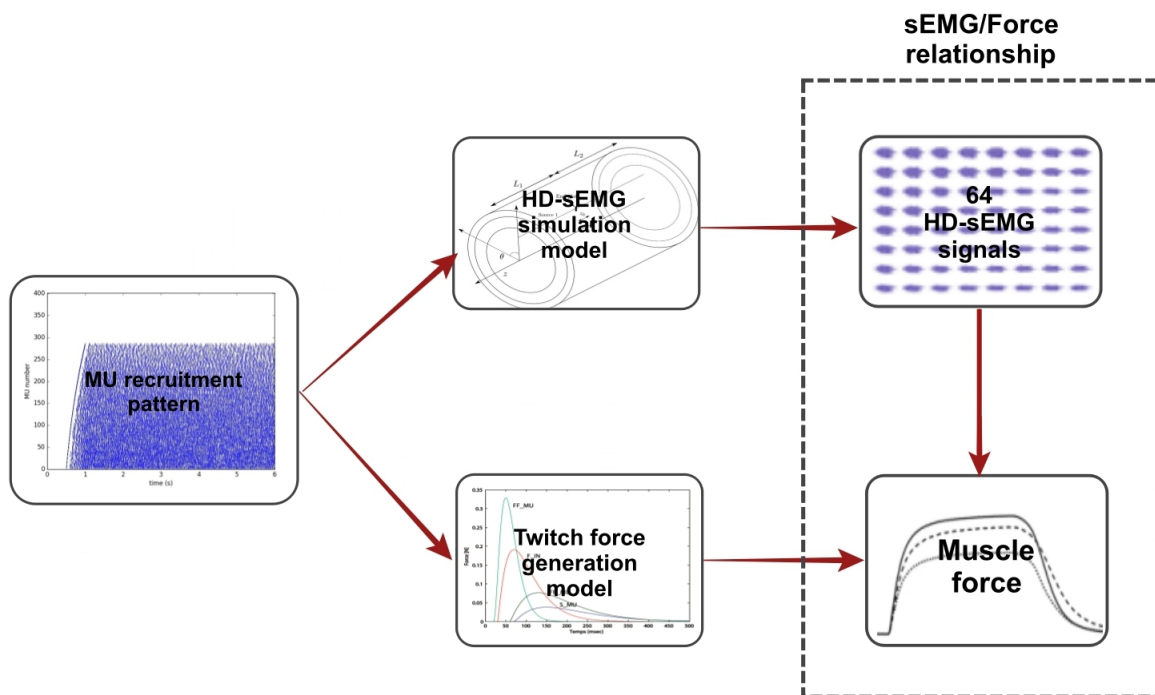


Figure 4.1: Schematic of the HD-sEMG and Force simulation models used in the modeling of the sEMG/Force relationship.

This chapter is divided into two parts that are interconnected. The first part will be a survey of the HD-sEMG/force relationship shape and the parameters that influence it. It aims at discovering the parameters that affect the most this relation and how, as well as proposing an equation that best describes it from a panel of existing relations used in the literature. The second part will therefore be the estimation of the force levels using the equation type acquired from the first study. Two methods will be used in order to compute the HD-sEMG/force relationship. The first approach bears on machine learning paradigm using ANN to evaluate possible benefits of including additional parameters to the amplitude ones in order to enhance de force estimation accuracy. In addition, a combination of input parameters will be tested in order to accomplish our objective. Then, a second analytical approach will be proposed,

where polynomial coefficients will be estimated after adding some constraints. Lastly we will conclude the chapter by comparing the two approaches.

## 4.2 HD-sEMG/Force relationship modeling

The study of the relationship between the sEMG signal and the muscle force in isometric non fatiguing voluntary contractions, and understanding the factors and mechanisms that affect it, are essential to the modeling and estimation steps. Few studies in the literature explore the shape of the relationship between sEMG signal recorded from an individual muscle and the corresponding force due to the high complexity of the experimental evaluation. However, we will present a review of the studies that attempt to analyze the shape of this relationship. Starting by the Milner-Brown and Stein work in 1975 [83], that described the relationship between a single MUAP amplitude and corresponding force of the first dorsal interosseous muscle using needle electrode technique. They found that the ARV of the MUAP varies approximately linearly with the corresponding force [83]. Afterwards, Moritani and deVries [179] confirmed the linear theory by exploring the relationship between the iEMG and the global force of the elbow joint using unipolar recording electrodes. They also found a curvilinear relation between bipolar sEMG signals and force. However, this study does not address a single muscle but rather a group of muscles (elbow joint muscles). Then, Lawrence and De Luca in 1983 [84], attempted to assess the shape of this relation for three different muscles in experimental conditions. They also found that for the first dorsal interosseous muscle, the relationship between the normalized sEMG signal and the corresponding normalized force was quasi-linear. For the other two muscles (BB and Deltoid) the relationship was found to be nonlinear. We have to insist here on the fact that the muscle force measured experimentally for the BB or the Deltoid are not the individual muscle forces but the summation of forces produced by the group of muscles that cocontract with these muscles. Thus, aside from small muscles like the interosseous muscles of the hand, it is complex to launch a faithful investigation of an individual muscle sEMG/Force relationship using experimental studies. Consequently, we need to use simulation in order to have a truthful analysis of the form variation of this relationship since we have a direct access to the force and corresponding sEMG signals generated by the same MU recruitment pattern. However, the efficiency of this methodology in assessing more precisely the HD-sEMG/force relationship is strongly related to the physiological realism of the employed generation models. Thus, Zhou and Rymer [13], presented a simulation study that tests the effect of different parameters on the shape of the obtained normalized sEMG/Force relationship [13]. They used the motoneuron pool and force models developed by Fuglevand et al. [180] and adapted them to fit the first dorsal interosseous muscle. To model the the sEMG signal, they used Hermite Rodriguez functions [13]. They tested different recruitment and firing rate strategies and two different types of MUAP-twitch relations as well as the effect of MU firing synchrony that is

supposed to occur during fatigue [13]. They found that the firing rate had an influence on the shape of the relationship but the MUAP-twitch relation had the major influence. The synchrony did not have an impact of the HD-sEMG/force relation form [13]. Even though this study proposed to test the factors governing the HD-sEMG/force relationship shape, it lacks realism in the sEMG signal simulation model as well as MU firing rate strategies and force generation.

In this section, we will use the cylindrical HD-sEMG simulation model as well as the twitch force model depicted in the previous chapter, in order to study the variation of the HD-sEMG/force relationship form following morphological (skin tissue thickness, adipose tissue thickness and muscle length), neural (recruitment strategy and rate coding) and anatomical parameters (MU type distribution and placement) through a focused sensitivity analysis. The main purpose of this study is to present a solid and realistic ground for the HD-sEMG/force relationship modeling that we will bare on to propose, in the later section, a specific approach. The simulated signals will be adapted to represent the BB muscle electrical and mechanical activity in a non fatiguing voluntary isometric isotonic context and in a patient specific manner.

### 4.2.1 Muscle force generation model

As described in Chapter 1 (section 1.2.3), each MU responds to an impulse from the CNS by producing a twitch. The twitch characteristics depend on the MU type generating it [178]. Thus, in order to simulate the force produced by an individual muscle, we need to model the summation of particular twitches for the different types of MUs according to their shapes. Raikova et al. [20] proposed an analytical model of the twitches that takes into account four twitch parameters: contraction time, maximal force amplitude, half relaxation time and lead time. They also defined a model for the summation of twitches [178]. Consequently, in this work we will be using their model in order to simulate the force produced by the BB. We recall the twitch parameters and their values for the different MU types in Table 4.1.

Table 4.1: The twitch parameters corresponding to the four MU types [20].

	$T_{EM}(ms)$	$T_c(ms)$	$T_{hr}(ms)$	$T_{tot}(ms)$	$F_{max}(N)$
S	70	80	200	480	0.382
FR	20	30	60	120	3.288
Fint	60	70	175	420	0.764
FF	30	40	100	240	1.910

with  $T_{EM}$  as the electromechanical delay between the time the stimulus is sent and the start of the contraction,  $F_{max}$  the twitch maximum value,  $T_c$  the contraction time between the start of the contraction and when it reaches  $F_{max}$ ,  $T_{hr}$  the duration between the start of the contractile response and the moment the force decreases to half the maximum value and  $T_{tot}$  the total duration of the contraction.

The analytical function describing the MU twitch response to a neural stimulus is described by [20]:

$$F_{MU}(t) = pt^m e^{-kt} \quad (4.1)$$

with  $p$ ,  $m$  and  $k$  are constants defined as:

$$k = \frac{\ln 2}{-T_c \ln(T_{hr}/T_c) + T_{hr} - T_c}$$

$$m = kT_c$$

$$p = F_{max} e^{-kT_c(\ln T_c - 1)}$$

Accordingly, the total force  $F(t)$  developed by a muscle is obtained after convolution operation as follow:

$$F(t) = \sum_{i=1}^{Nb} (F_{MU_i}(t) * \sum_{k=1}^{P_i} \delta(t_k)) \quad (4.2)$$

Where  $\delta$  is the Dirac function,  $t_k$  is the discharge instant,  $P_i$  the number of impulses in the  $i^{th}$  MU discharge impulses train and  $Nb$  is the total number of active MUs in the muscle for a specific contraction level.

## 4.2.2 HD-sEMG simulation

The model used for the simulation of the HD-sEMG signals was presented in details in the previous chapter (see section 3.3.2.3). In this study, we used the exact same description for the parameters of the model, except for the the MU number where we simulated 400 MUs, to increase physiological realism, in order to generate 64 HD-sEMG signals of isometric isotonic contractions of 10, 20, 30, 40, 50, 60, 70, 80, 90 and 100 %MVC. We also used the same morphological parameters described in Table 3.1 and obtained from the sonography experimental protocol (see section 3.3.2.1) as well as the three MU type distribution described in Table 3.3. Concerning the neural parameters, we tested two rate coding profiles: linear and nonlinear and the two recruitment strategies LRS and HRS previously described. Figure 4.3 illustrates the diagram of the simulation parameters where the five “sim” represent different values of morphological parameters obtained from the experimental study described in section 3.3.2.1. These values are presented in Table 4.2.

Table 4.2: The physiological parameters used in the simulations.

	Adipose tissue thickness(mm)	Skin thickness(mm)	Muscle length (mm)
Sim 1	2.74	1.42	101.0
Sim 2	1.768	1.42	101.0
Sim 3	3.58	1.42	101.0
Sim 4	2.74	1.75	101.0
Sim 5	2.74	1.42	126.1

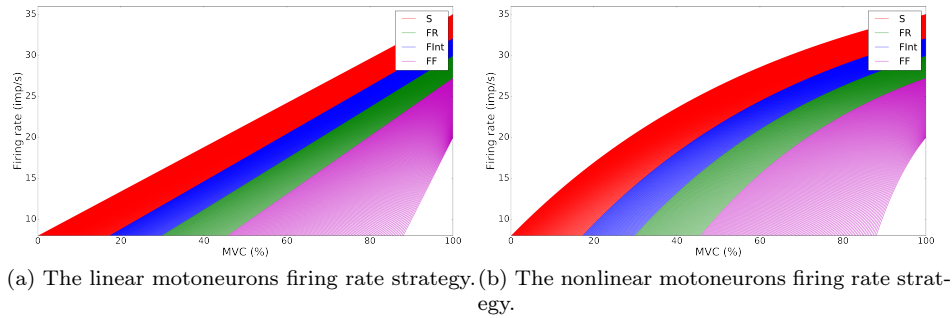


Figure 4.2: The two rate coding strategies used in simulation.

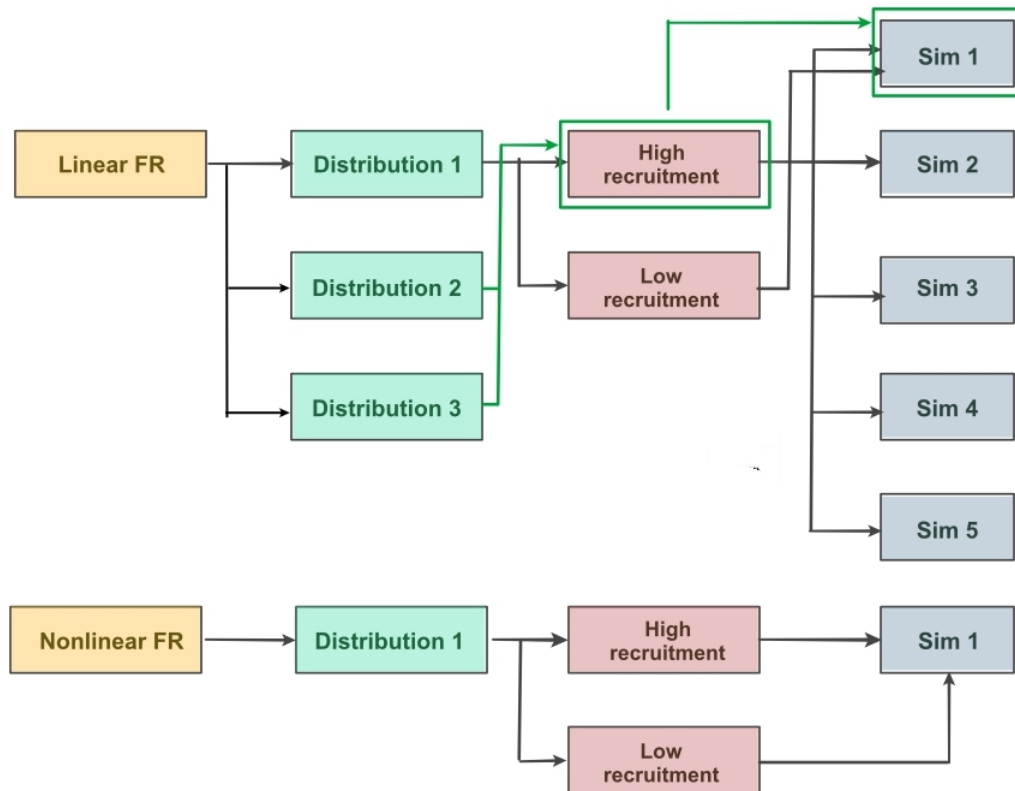


Figure 4.3: Schematic diagram presenting the different configurations used for the simulation.

Furthermore, for each configuration of parameters, we generated five different anatomies of MUs in order to test the effect of the MU positions on the HD-sEMG/force relationship. Subsequently, we have in total 10 different configuration of parameters  $\times$  5 anatomies  $\times$  10 levels of muscle contractions which make up 500 different simulations. For both HD-sEMG and force signals, we simulated a plateau of a constant force that lasted 5 s at each contraction level (2048 Hz sampling frequency).

We chose to use the RMS parameter as an amplitude descriptor since it has shown robustness to spatial aliasing in comparison with the ARV which is usually used in similar studies [162]. The value of the RMS was extracted from the  $8 \times 8$  RMS map by applying the same methodology as in the previous chapter (see section 3.2.2). Thus, for each simulation, we applied the WS segmentation algorithm for all 10 contraction levels, then we computed the final map filter by a logical addition of the 10 filters (maps

of 0's and 1's). Afterwards, the final RMS value for each force level was obtained by averaging the RMS values of the channels remaining after filtering of the RMS maps with the obtained filter.

### 4.2.3 Study of the parameters influencing the shape of the HD-sEMG/Force relationship

The two simulation models along with the processing stage allowed us to obtain the sEMG RMS in  $mV$  and the corresponding force value in Newton ( $N$ ) at a given excitation level. After plotting the HD-sEMG/force relationship for all five anatomies at the same time, we found important variability in the form of the relationship with different MU anatomies. Therefore, we decided to plot these relationships per MU anatomy in order to visualize the variation of the relation shape with the chosen parameters. We also have to mention, that we tested the effect of different simulations of the recruitment patterns for the same MU anatomy and muscle configuration. However, we did not find a variation in the relationship between five different recruitment patterns with the same spatial recruitment law and rate coding ( $\text{std}=0.0768 N$ ). Thus, in this part, we will present the different relations per anatomies for the parameters previously discussed.

#### 4.2.3.1 Morphological parameters

As explained in the previous section of this chapter, we tested three morphological parameters that are suspected to affect the HD-sEMG/force relationship. These parameters are the adipose tissue thickness, skin tissue thickness and muscle length. Figure 4.4 illustrates the HD-sEMG/force relationships corresponding to different values of these parameters for the linear rate coding, HRS recruitment strategy and first MU type distribution D1. For the adipose tissue thickness we compared between the minimum, average and maximum values obtained from the experimental study. As for the skin tissue thickness and the muscle length, we only compared between the average and the maximum values (see table 3.1). If we look at the variation of the relations for different adipose and skin tissue thicknesses, we can clearly state that these parameters have a direct effect on the HD-sEMG/force relationship. We can also notice that this effect is mainly present between 40 and 100 %MVC of force values. However, between 10 and 40% MVC we did not find a consequential influence. Furthermore, the variation of these two parameters have the same effect on the relation curve. This effect manifests by shifting the curve toward smaller RMS values increasing their thickness values. The muscle length, on the other hand, did not have a noticeable impact.

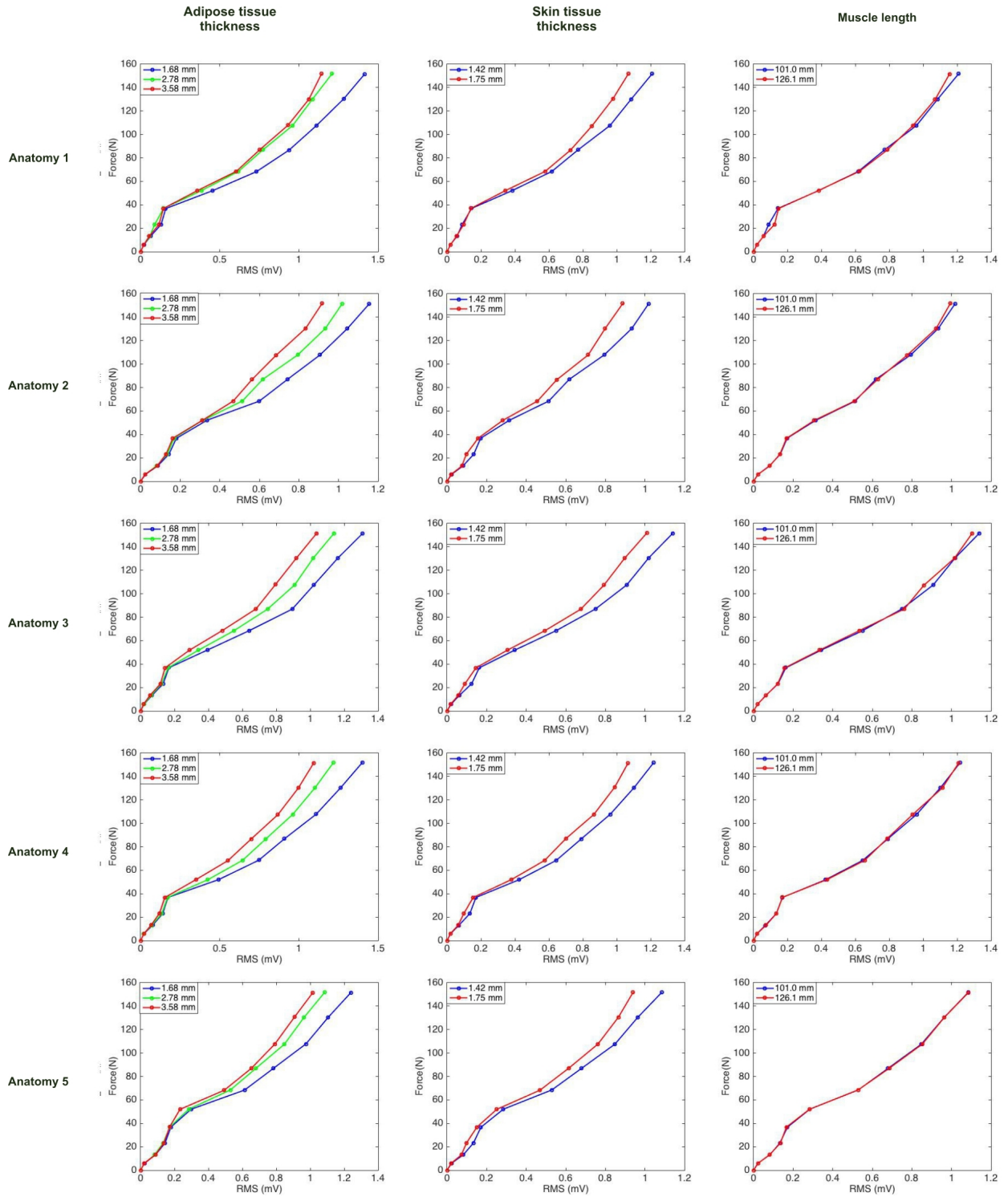


Figure 4.4: The HD-sEMG/force relations for the five anatomies relative to different morphological parameters and values (see Table 4.2).

#### 4.2.3.2 Anatomical and neural parameters

In this paragraph, we will study the effect of both anatomical and neural parameters on the HD-sEMG/force relationship. Figure 4.5 presents the relations relative to different types of these parameters. First, we presented the relations for the three considered MU type distribution percentages D1, D2 and D3 (see table 3.3) illustrated for the five different anatomies for the linear rate coding, HRS recruitment strategy and average values of the morphological parameters. Then, we considered the two different rate coding types: linear and nonlinear as well as the two recruitment strategies: LRS and HRS. For the MU type distribution, we can see a significant impact on the shape of the relationship, especially for the D3. The main effect is the change of the curve inflection point position, where it is located at 40 %MVC for the D1, 50 %MVC for the D2 and 30 %MVC for the D3 (see Figure 4.5). These variations can be easily explained according to the MU distribution type. For example, for D3, we have more FFMUs, therefore it is expected for the relationship to change shape earlier than in the D1 case where we have equal number of SMUs and FFMUs which means FFMUs are recruited later on, even moreso for the D2 where we have more SMUs than FFMUs which explains the inflection point at 50 %MVC. One can also observe that the D1 strategy reaches the higher force value at 100% followed by D3 and D2 strategies respectively. This important observation put a focus on the role of both SMUs and FFMUs in building the force output.

If we consider now the neural parameters influence, we can notice little variation between the relations for LRS and HRS especially for the linear rate coding strategy. However, there is also a shift in the position of the inflection point where for the LRS it is present at 50 %MVC and for the HRS at 40 %MVC. This can be explained by the fact that for the HRS strategy, we have FFMUs that are recruited before 50 %MVC which is not the case for the LRS strategy. For the rate coding scheme effect, we found important difference between the relations for the linear and nonlinear strategies as shown in Figure 4.5. If we look closer, we can notice that for the same RMS values, we have more produced force for the nonlinear rate coding in comparison with the linear which is expected since the discharge frequency per MU is higher in the nonlinear case than the linear one for the same excitation level.

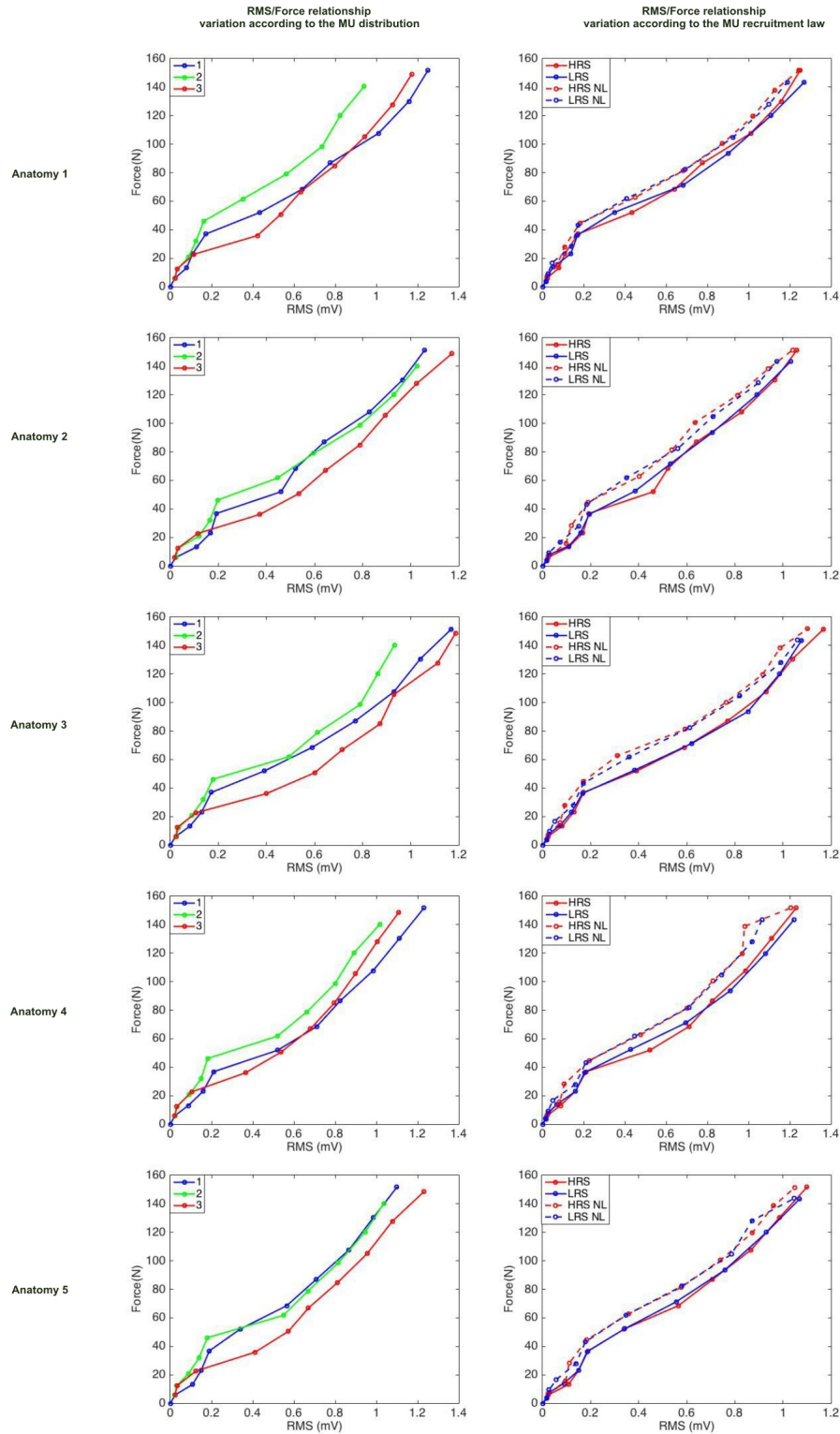


Figure 4.5: The HD-sEMG/force relations for the five anatomies relative to different MU type distributions, recruitment strategies and firing rates (see Table 3.3).

#### 4.2.4 HD-sEMG/force relationship fitting

Based on the literature, there are different types of proposed HD-sEMG/force relationships between linear [85], polynomial [108, 181], nonlinear [42] or exponential [182]. Thus in this section, we propose to test these hypothesis on our database of 500 couples of signals (HD-sEMG, force) in order to find the best fit. The fitting will be done by least square minimization. Which means that based on a predefined parametric model (polynomial, exponential,...), the outcome of the fitting is an estimate of the model coefficients. In order to do so, the difference between the simulated and estimated force by the model is minimized by the least square algorithm. Thus, the difference between the simulated and the estimated force response at a certain level  $i$  is called the residual  $r_i$  at this value. Thus  $r_i$  is defined as:

$$r_i = F_i - F_{e_i} \quad (4.3)$$

Where  $F_i$  is the simulated force at the  $i^{th}$  contraction level,  $F_{e_i}$  is the estimated force by fitting at the  $i^{th}$  contraction level.

The Sum of the Squared Residuals is thus given by:

$$SSR = \sum_{i=1}^{N_c} r_i^2 \quad (4.4)$$

Where  $N_c$  is the total number of contraction levels.

Thence, the model coefficients are determined by minimizing the SSR with respect to each coefficient . In the case where we have only two coefficients a and b, the minimization problem will be solved by setting the derivative of the  $SSR$  with respect to each of the coefficients equal to zero as follow:

$$\begin{aligned} \frac{\partial SSR}{\partial a} &= 0 \\ \frac{\partial SSR}{\partial b} &= 0 \end{aligned} \quad (4.5)$$

In order to evaluate the fitting models, we will compute the NRMSE between the simulated force and the estimated force by fitting for each one of the ten simulations (parameter configurations discussed in the previous section) and five anatomies. This NRMSE is defined by:

$$NRMSE = \frac{1}{\bar{F}} \sqrt{\frac{1}{N_c} \sum_{i=1}^{N_c} (F_i - F_{e_i})^2} \quad (4.6)$$

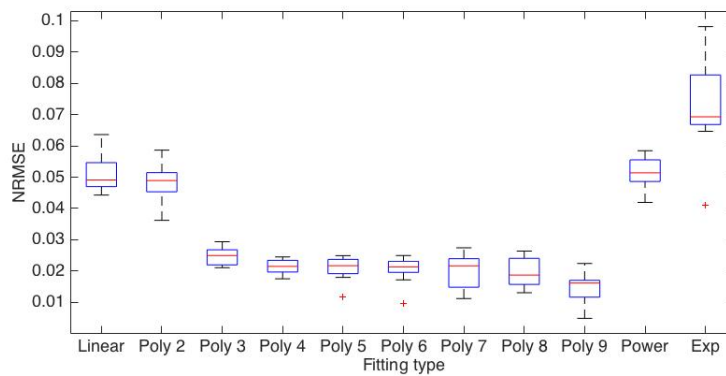
Where  $N_c$  is the total number of contraction levels,  $F_i$  is the simulated force at the  $i^{th}$  contraction level,  $F_{e_i}$  is the estimated force by fitting at the  $i^{th}$  contraction level and  $\bar{F}$  is the deviation between the maximum and the minimum value of  $F$  ( $F(max) - F(0)$ ).

And the R-square value expressed by:

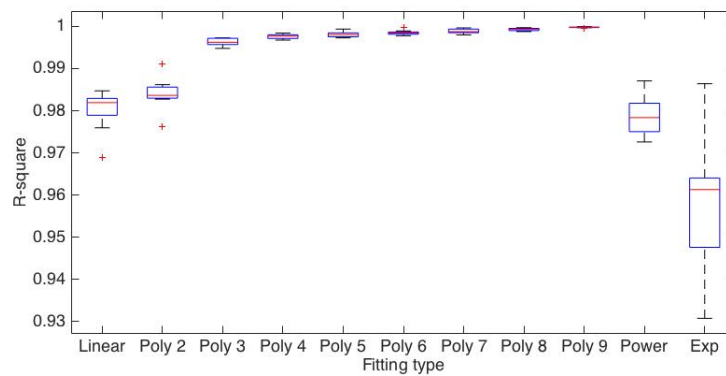
$$R - square = \frac{SS}{SST} - 1 \tag{4.7}$$

with  $SS = \sum_{i=1}^{N_c} (F_i - \bar{F})^2$  and  $SST = \sum_{i=1}^{N_c} (F_{e_i} - \bar{F})^2$

R-square can take on any value between 0 and 1, with a value closer to 1 indicating that a greater proportion of variance is accounted for by the model. It indicates how successful the fitting is in explaining the variation of the data.



(a) The variation of the NRMSE relative to the fitting method for the different simulations.



(b) The variation of the R-square value relative to the fitting method for the different simulations.

Figure 4.6: The variation of the fitting parameters with respect to the fitting type.

As mentioned above, we decided to compare between ten different fitting models: linear fitting ( $F = aRMS + b$ ), Polynomial fittings with order that changes from 2 to 9 of the form:  $F = p_nRMS^n + p_{n-1}RMS^{n-1} + \dots + p_0$ , power fitting ( $F = aRMS^b$ ) and exponential fitting ( $F = a \exp^{bRMS}$ ). The mean and std values of  $RMSE$  and the  $R - square$  computed for the ten simulations are presented in Figure 4.3. By observing the box plot for the  $NRMSE$  (Figure 4.6a) and the  $R - square$  value (Figure 4.6b), we can see that we have the worst fitting results for the exponential type fitting. We also have similar results for the power type as well as linear fittings. However, we have the minimal error and

maximal correlation between the simulated force values and the predicted force values for the polynomial fittings (from order 3 to order 9).

Afterwards, we performed a Kruskal Wallis nonparametric one-way ANOVA on both *NRMSE* and *R-square* value. This test revealed significant differences for the *NRMSE* ( $\chi^2(\text{df}=10) = 86.32, p < 0.000001$ ) as well as for the *R-square* value ( $\chi^2(\text{df}=10) = 101.56, p < 0.000001$ ) between the ten methods used to describe the shape of the HD-sEMG/force relationship. Then, Post-hoc tests revealed maximal difference between the linear, exponential and power type fittings with 3<sup>rd</sup> to 9<sup>th</sup> order polynomial fittings. These tests allow us to choose the best way to characterize the variation of the individual force with the RMS value. Whereof, we found the best regression type model to be the polynomial fitting (from order 3 to order 9). Now if we focus only on the polynomial fitting errors, we can notice that with increasing polynomial order, we have decreasing *NRMSE* and increasing *R-square* value. These values decrease significantly from the second to the third order polynomial, where it attains a minimal value of 0.024, then it remains near this value as far as the 9<sup>th</sup> order polynomial where it decreases to 0.016.

Based on the study presented above, the polynomial fitting seems to be the most adequate for the studied relationship. The choice of the polynomial degree should be a compromise between minimal error and complexity (number of coefficients to estimate). Thus, we decided to use the 3<sup>rd</sup> order polynomial fitting by judging that it is a good compromise from the point of view of the number of unknown parameters to find. Since we have to consider the direct application of this polynomial in the force model where the aim will be to find the parameters of the polynomial. The corresponding equation is given by:

$$F = P_3RMS^3 + P_2RMS^2 + P_1RMS + P_0 \quad (4.8)$$

Where  $P_3, P_2, P_1$  are the polynomial coefficients obtained by the least square algorithm, since  $P_0$  is supposed to be equal to 0 indicating the absence of force generation where there is no electrical activation.

Based on the choice of the 3<sup>rd</sup> order polynomial, we computed the error in %MVC between the force value obtained through the polynomial and the simulated value. The results are depicted in Tables 4.3 for the morphological (Table 4.3a), anatomical (Table 4.3b) and neural (Table 4.3c) parameters for each of the five MU anatomies. By observing these Tables, we can see that the fitting error varies between 0.99 and 2.35% with a  $mean \pm std = 1.64 \pm 0.17\%$ .

Table 4.3: The error computed for the 3<sup>rd</sup> degree polynomial fitting for all the parameter types discussed above.

(a) The error computed for the 3<sup>rd</sup> degree polynomial fitting for the morphological parameters (see Table 4.2) in %MVC.

Anatomy	Sim 1	Sim 2	Sim 3	Sim 4	Sim 5
1	2.04	1.78	1.47	1.53	1.42
2	1.54	1.65	1.57	1.40	1.71
3	1.25	1.92	1.69	1.58	1.34
4	1.59	1.89	1.32	1.55	1.78
5	1.74	2.06	2.35	1.12	1.84

(b) The error computed for the 3<sup>rd</sup> degree polynomial fitting for the three MU type distributions (see Table 3.3) in %MVC.

Anatomy	D 1	D 2	D 3
1	2.04	1.82	1.44
2	1.54	1.63	1.76
3	1.25	1.86	1.48
4	1.59	2.14	1.49
5	1.74	2.13	1.55

(c) The error computed for the 3<sup>rd</sup> degree polynomial fitting for the neural parameters in %MVC.

Anatomy	Linear		Nonlinear	
	LRS	HRS	LRS	HRS
1	2.03	2.04	1.98	2.30
2	1.37	1.54	1.33	1.73
3	0.99	1.25	1.25	1.68
4	1.23	1.59	1.28	2.01
5	1.58	1.74	1.77	1.61

#### 4.2.5 Improving polynomial fitting using optimization

In presence of residual muscle activity and noise, the force level is considered to be equal to 0 for an almost 0 RMS value, thus the  $P_0$  coefficient of the 3<sup>rd</sup> degree polynomial fitting is supposed to be equal to zero in this study for calculus simplification. Therefore, the fitting procedure should be adapted in order to take into account the first point of the relationship (0 mV, 0 N). In this section, we propose to use an adapted version of the least square algorithm presented above, where we will force the curve to pass by the origin point. This will be done through the use of a linear constraint with the linear least square algorithm. This new system can be illustrated by the equation presented below:

$$\text{Min}(\sqrt{\|P \cdot EMG - F\|^2})_P \quad \text{such that} \quad \begin{cases} A_{eq} \cdot P = B_{eq} \end{cases} \quad (4.9)$$

With  $F$  the force vector,  $EMG$  the RMS vector,  $P$  the vector of polynomial coefficients ( $P_3$ ,  $P_2$  and  $P_1$ ),  $A_{eq}$  is the Vandermonde matrix for  $RMS = 0$  and  $B_{eq}$  is the value the curve should take at that point.

The new error results are depicted in Tables 4.4 for the morphological (Table 4.4a), anatomical (Table 4.4b) and neural (Table 4.4c) parameters for each of the five MU anatomies. The new mean error is equal to  $1.80 \pm 0.26\%$  which means that we have an increase of  $0.15\%$  of fitting error in comparison with the original fitting algorithm with not constraints.

Table 4.4: The error computed for the  $3^{rd}$  degree polynomial fitting by optimization for the different morphological, anatomical and neural parameter values.

(a) The error computed for the 3rd degree polynomial fitting for the morphological parameters (see Table 4.2) in %MVC.

Anatomy	Sim 1	Sim 2	Sim 3	Sim 4	Sim 5
1	2.20	2.31	1.61	1.65	1.54
2	1.65	1.54	1.57	1.39	1.71
3	1.94	1.34	1.75	1.70	1.38
4	2.15	1.77	1.42	1.71	1.93
5	1.90	1.73	2.29	1.10	1.83

(b) The error computed for the  $3^{rd}$  degree polynomial fitting for the three MU type distributions (see Table 3.3) in %MVC.

Anatomy	D 1	D 2	D 3
1	2.31	1.82	1.23
2	1.54	1.66	1.51
3	1.34	1.89	1.65
4	1.77	2.19	2.31
5	1.73	2.21	2.35

(c) The error computed for the  $3^{rd}$  degree polynomial fitting for the neural parameters in %MVC.

Anatomy	Linear		Nonlinear	
	LRS	HRS	LRS	HRS
1	2.34	2.31	2.21	2.48
2	1.38	1.54	1.33	1.78
3	0.99	1.34	1.37	1.70
4	1.30	1.77	1.241	2.14
5	1.61	1.73	1.77	1.55

#### 4.2.6 Sensitivity analysis of the polynomial fitting

In this section, we will use the relationship type obtained from the fitting study above, in order to perform a focused sensitivity analysis of the variation of the polynomial with the previously discussed parameters. Therefore, the same data obtained from the models described previously, will be exploited to study each parameter effect on the polynomial coefficients. Firstly, for the morphological parameters, skin tissue thickness, adipose tissue thickness and muscle length, we plotted both polynomial fitting and simulated data. These plots are illustrated in Figure 4.7 for the skin and adipose tissues. We decided not to include the muscle length parameter in this study since it did not have any effect on the relationship (see section 4.2.3).

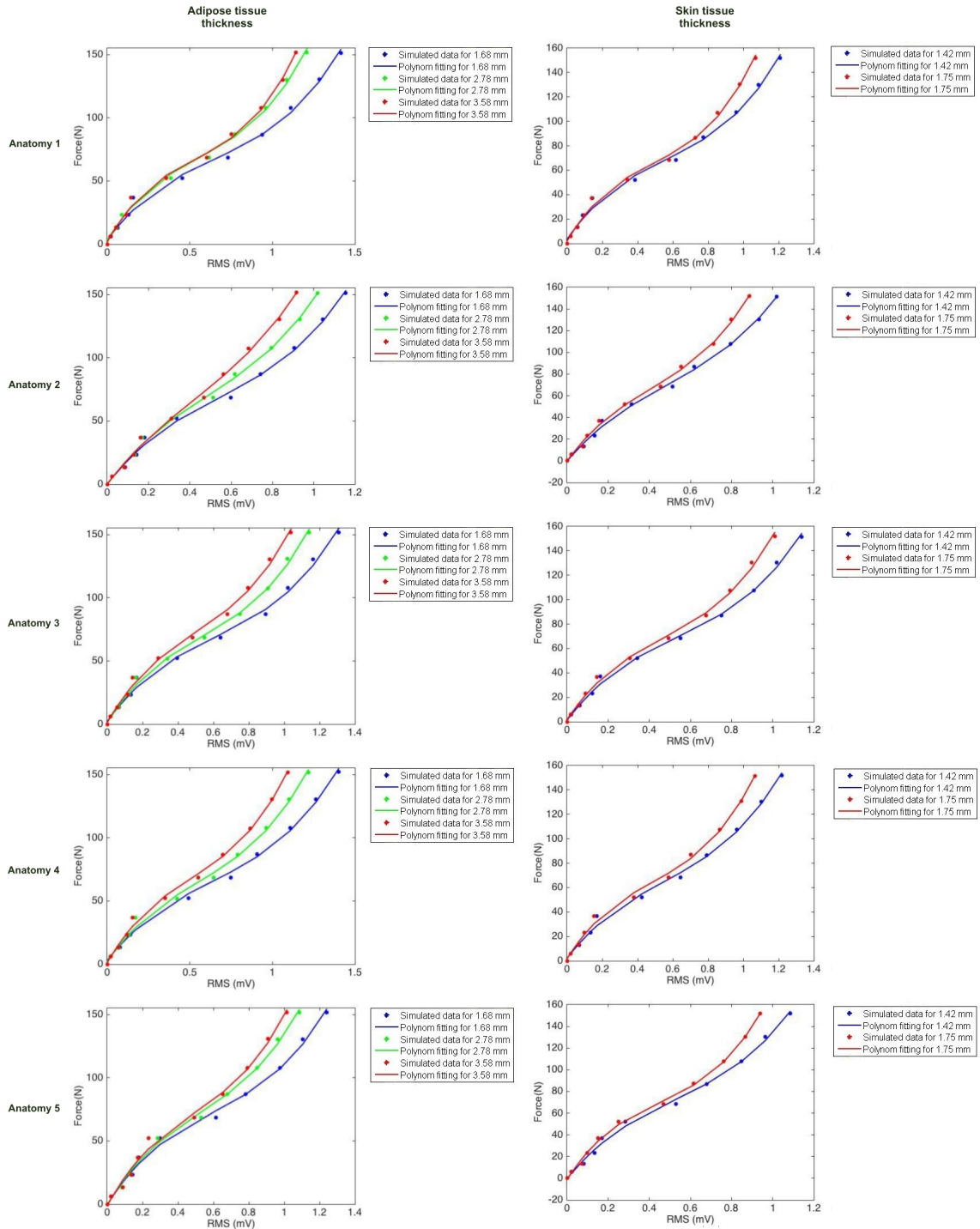


Figure 4.7: The RMS/Force relationships for the simulated data and the polynomial fitting using different skin and adipose tissue thickness for each one of the five anatomies.

Figure 4.7 indicates the variation of the polynom defined by:

$$F = P_3RMS^3 + P_2RMS^2 + P_1RMS \quad (4.10)$$

Where  $P_3$ ,  $P_2$  and  $P_1$  are the polynom coefficients obtained by the optimization method described in

the previous section.

It is obvious from Figure 4.7, that the skin and adipose tissue thickness have the same influence on all the parameters of the polynomial since they do not change the form of the relationship. Figures 4.8 and 4.9 illustrate the variation of the coefficients  $P_3$ ,  $P_2$  and  $P_1$  with adipose and skin tissue thickness variation respectively. These results confirms our previous observation that all the coefficients change in the same manner. By inspecting further the plots in Figures 4.8 and 4.9, we can notice that we have the same sign for the coefficients,  $P_3$  and  $P_1$  are always positive in contrast to  $P_2$  which is always negative.

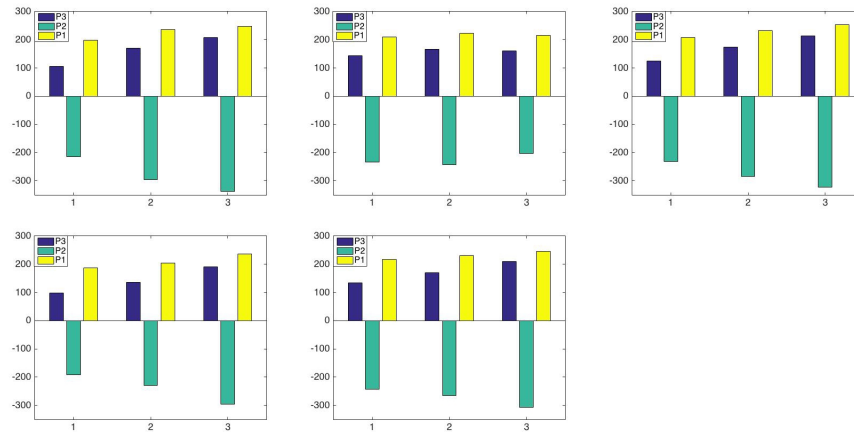


Figure 4.8: The three coefficients of the polynomial fitting using different adipose tissue thickness for the five anatomies.

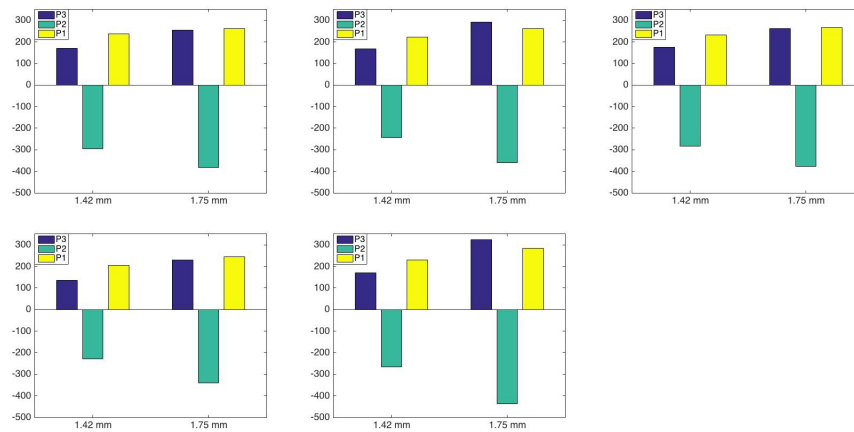


Figure 4.9: The three coefficients of the polynomial fitting using different adipose tissue thickness for the five anatomies.

Also, we can perceive that the parameters values increase in absolute value with increasing skin and adipose tissue thickness, with the maximum increase for the coefficient  $P_2$ . This effect was also observed in figure 4.7. This means that when the skin or adipose tissue increases, we obtain the same force for less RMS value due the spatial filtering of the sEMG signals caused by these tissue conductivities.

Considering now the MU type distribution, the plots of the polynomial relationship variations for the three MU type percentages D1, D2 and D3 are illustrated in Figure 4.10.

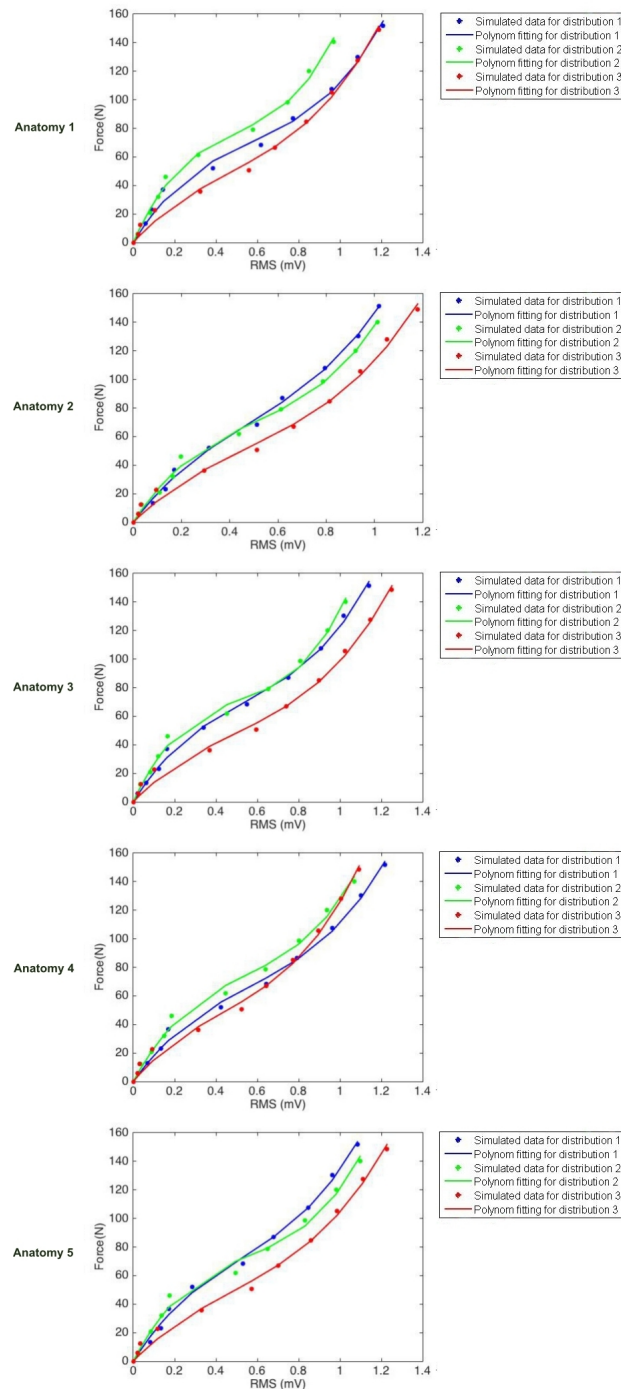


Figure 4.10: The RMS/Force relationships for the simulated data and the polynomial fitting using different MU type distributions for each one of the five anatomies.

As depicted in Figure 4.10, the MU type distribution in the muscle has the major effect of the shape of the relationship and the polynomial fitting coefficients. In order to thoroughly analyze this effect on the polynomial form, we plotted the corresponding coefficients. The variation of the polynomial coefficients with

respect to the MU type percentages in the muscle are presented in Figure 4.11. The first observation from Figure 4.11 is that we have the same signs for the different MU type distributions. If we compare between D1 and D2, we can see that we have an increase in the polynomial coefficients for D2, where we have more SMUs than FFMUs, in comparison with D1 where we have the equal numbers of SMUs and FFMUs. On the contrary, if we compare between D1 and D3, where we have more FFMUs than SMUs, we can see a decrease in all parameters. Thus, we have the minimal coefficients for the D3 which is logical since we have maximum number of FFMUs, which mean that we have larger muscle fibers that produce more force [83]. However, these large fibers conduct faster and ergo their amplitude will be reduced [83] which explains that we have less force for same values of RMS. The same explanation could be made toward the D2 distribution in order to justify the high coefficient values.

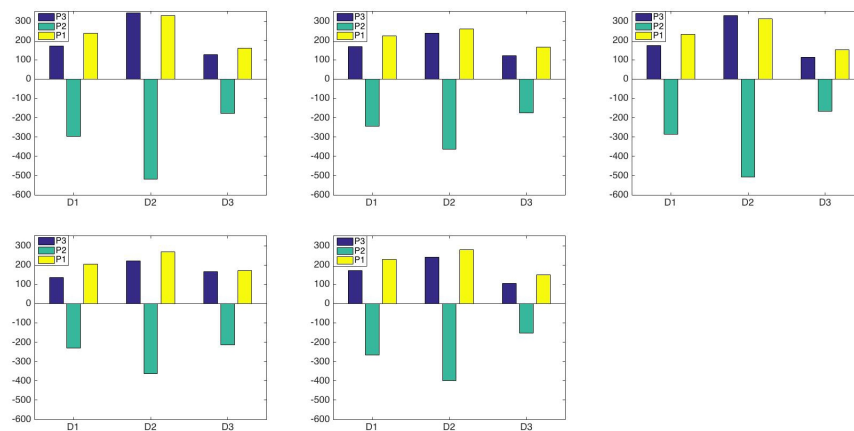


Figure 4.11: The three coefficients of the polynomial fitting using different MU type distributions for the five anatomies.

Finally, for the neural parameters evaluation, we performed the same examination process by plotting the polynomial relationship variations for the LRS and HRS for both linear and non linear rate coding. Figure 4.12 presents these relations for the five MU anatomies. The main observation from these plots, is that we do not have a major influence of the spatial recruitment strategy on the HD-sEMG/force relationship. However, it seems that we have an influence of the rate coding scheme. If we look at the polynomial coefficients presented in Figure 4.13, we can see a little influence of the recruitment strategy where the coefficients corresponding to the LRS are greater than the HRS ones. This is true in both linear and nonlinear rate coding cases. Differently, if we compare between the polynomial coefficient for the linear and the nonlinear rate coding, we can see that the influence on the coefficients is highly dependent on the MU anatomy. It was shown by Lawrence and De Luca that the BB relies essentially on the spatial recruitment to increase its force not on the rate coding scheme [84].

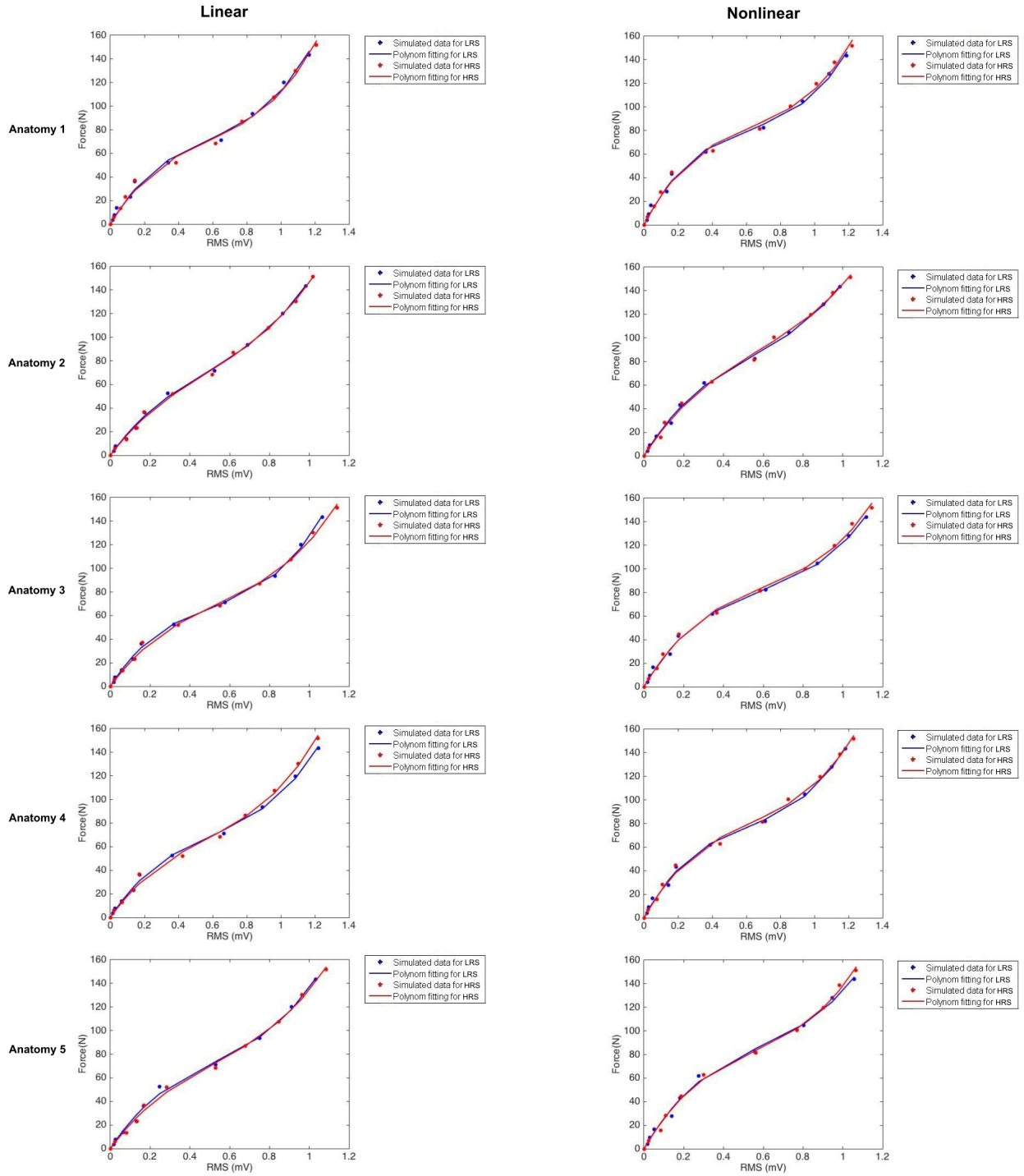


Figure 4.12: The RMS/Force relationships for the simulated data and the polynomial fitting using different spatial recruitment strategies and firing rates for the five anatomies.

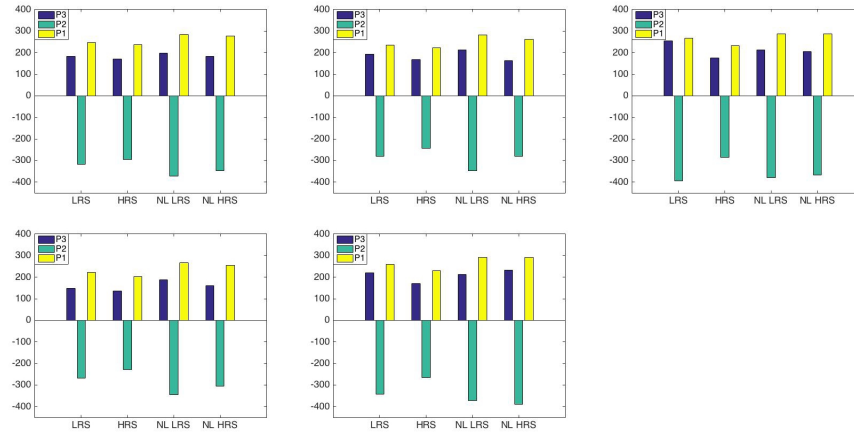


Figure 4.13: The three coefficients of the polynomial fitting using different spatial recruitment strategies (LRS vs HRS) and firing rates (linear vs nonlinear) for the five anatomies.

#### 4.2.7 Discussion and conclusion

The proposed simulation study allowed us to explore the different parameters that affect the HD-sEMG/force relationship dynamic and pattern. We also tested different fitting algorithms in order to find the best equation that describes the HD-sEMG/force relationship. We found the  $3^{rd}$  order polynomial to be the best to describe the observed relations. Then, we used this relation type (polynomial of order 3) in order to study in depth the impact of morphological, anatomical and neural parameters on the shape of the relationship. Among the tested morphological parameters, we found an important impact of the adipose and skin tissue thickness. This impact revealed a monotonic variation of the polynomial coefficients with the thicknesses values. For the neural parameters, we observed that the major influence was due to the rate coding scheme. The spatial recruitment strategy however had a slight influence on the polynomial coefficients. The last type of parameters that we tested was the MU type distribution in the muscle where we found it has a significant effect of the relationship shape and thence the coefficients of the  $3^{rd}$  degree polynomial. We also found that the positioning of the MU in the muscle have an influence on the relation even when all other parameters are fixed to certain values. This was clearly demonstrated when we generated five different anatomies of muscle (different MU placement) for each configuration of parameters and we found that we have an important standard deviation among the observed polynomial coefficients set. This means that the HD-sEMG/force relationship is subject specific and should be adapted to each subject's personal morphological, neural and anatomical properties.

In the next section of this chapter, we will present different approaches of HD-sEMG/force relationship estimation by using the model type obtained by this study. Therefore, the aim of this next section is to find the coefficients of this model using as input three values of RMS corresponding to three force levels in order to find the relationship parameters that allows us to estimate any force level knowing the

polynomial coefficients.

## 4.3 HD-sEMG driven muscle force estimation model

### 4.3.1 Supervised regression approach

In this section, we will use one classical machine learning method namely, the ANN, in order to estimate the polynom coefficients by training and testing the network on all the data and providing different RMS inputs corresponding to three force levels possibly completed with morphological parameters (tissue thicknesses). Then, the accuracy of the approach will be assessed by computing the NRMSE between estimated and simulated forces from a validation set that is different from the training set. In fact, the objective of this section is to evaluate possible benefits of including additional inputs to the amplitude ones (RMS values) for a better estimation of the force.

#### 4.3.1.1 Artificial Neural Network (ANN)

An ANN is a general mathematical computing model that mimic the behavior of the central nervous system. It was first elaborated by MacCulloch and Pitts in 1943 [183], then Frank Rosenblatt published the first neural network generation in 1958 [184]. Throughout the last 50 years, the concept and architectures of ANNs have greatly progressed. This was predominately due to its application in the signal processing and data mining domains [185]. The ANNs are networks of interconnected computational units called neurons. They are characterized by the ability of learning, which means that they are able to adjust their parameters based on the employed learning strategy. From the point of view network architecture, the ANNs can be broken down into three main categories [186]:

- Feed-forward: this type of network is the simplest. It presents only one direction of propagation which is forward from the input to the output nodes with not loops or cycles.
- Feed-back or recurrent: in this type the connections between the nodes of the networks make up cycles.
- Self-organizing: which have an unsupervised learning process and have a sheet like architecture.

In this thesis, we will be using a feed-forward ANN type in order to solve the force estimation problem. These ANNs have one or several layers of nonlinear neurons. The neurons of a specific layer are related to others by weight values. The first feed forward ANNs were called perceptrons [186, 184]. These

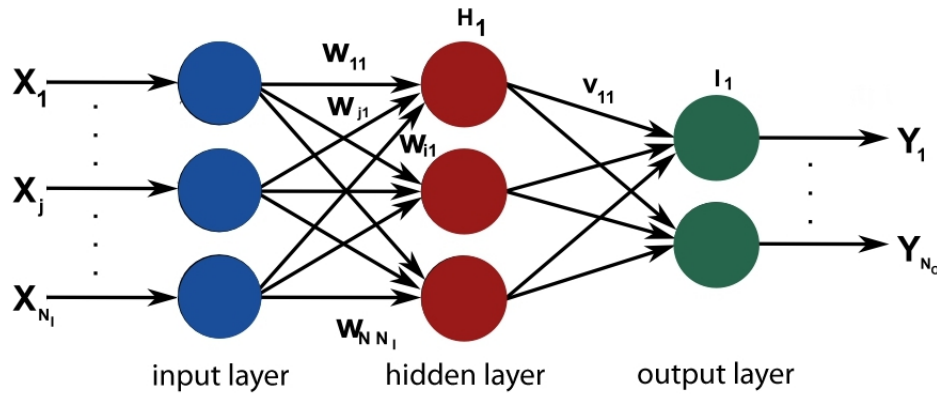


Figure 4.14: The feedforward neural network basic architecture.

perceptrons have simple architecture composed of only input and output layers. Afterwards, the multilayered feed forward ANN was introduced in the late 80s [186]. The basic architecture of a multilayered feedforward perceptron is presented in Figure 4.14, where we have only one hidden layer.

Each node of the network represent an artificial neuron. These neurons have the task of responding to a stimuli and adapting its weights according to the situation. The architecture of a single artificial neurons is illustrated in Figure 4.15. As depicted, a neuron includes two components: the net and the activation functions. The net function is a linear combinations of the neuron's inputs expressed by:

$$u = \sum_{i=1}^N w_i x_i + \theta \quad (4.11)$$

Where  $x_i$  and  $w_i$  are input number  $i$  and corresponding weight,  $N$  is the total number of inputs and  $\theta$  is the threshold of the neuron. The activation function is a linear or nonlinear function that transforms  $u$  into the output  $y$  such as:

$$y = F(u) \quad (4.12)$$

There are different types of activation functions. The commonly used activation function are mentioned in Table 4.5.

Now if we consider the ANN illustrated above with one hidden layer (see Figure 4.14), The output  $Y_k$  can be expressed by:

$$Y_k = F(I_k) = F\left(\sum_{i=1}^N v_{ki} F(H_i)\right) = F\left(\sum_{i=1}^N v_{ki} F\left(\sum_{j=1}^{N_I} w_{ji} X_j\right)\right) \quad (4.13)$$

Where  $w_{ji}$  are the synaptic weights of the neuron  $H_i$  from the input  $X_j$ ,  $v_{ki}$  is the synaptic weight of the neuron  $I_k$  from the neuron  $H_i$ ,  $N_I$  is the total number of inputs,  $N$  is the number of neurons  $H$  and

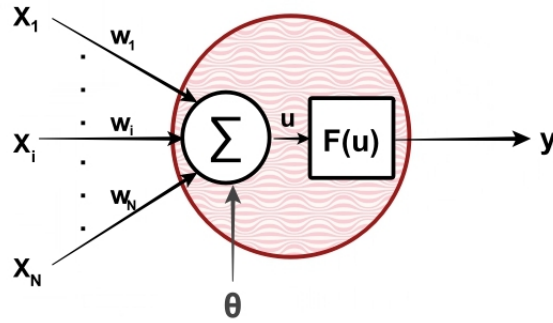


Figure 4.15: A simple artificial neuron.

Sigmoid	Hyperbolic tangent	Linear	Step
$F(u) = \frac{1}{1+e^{-\frac{u}{T}}}$	$F(u) = \tanh(u)$	$F(u) = au + b$	$f(u) = \begin{cases} 1 & u > 0 \\ 0 & u < 0 \end{cases}$

Table 4.5: Commonly used activation functions and their corresponding equations.

$N_o$  is the number of neurons  $I$ .

The ANN is a machine learning algorithm that have three phases:

- Training phase: the network is trained by a series of input and output values by using a learning method to adapt its synaptic weights in order to minimize the error between the target values (provided outputs) and the produced outputs.
- Testing phase: this phase is a part of the training phase where the network generalization ability is measured in order to halt the training where it stops improving.
- validation phase: this is an independent measurement of the system performance by using data that were not used in the training in order to compute the estimation error.

It is obvious that the training phase is very important in a neural network based estimation. There are many learning algorithms that are used for training supervised neural networks like bayesian regularization [187], scaled conjugate gradient [188] and Levenberg-Marquardt [189] algorithms.

#### 4.3.1.2 Levenberg-Marquardt algorithm

The Levenberg-Marquardt (LM) approach is an optimization algorithm that is primarily employed to solve nonlinear least squares problems where the aim is to find parameters that minimize the sum of squared errors between the target and the output values [190]. This algorithm combines two minimization techniques:

- The gradient descent: which is an optimization algorithm that aims at finding the local minimum of a function by updating parameters toward the negative of the gradient for maximum reduction of the least square residuals.
- The Gauss-Newton: which is also dedicated to minimizing the sum of squared function values. It assumes that the squared errors are locally quadratic and then searches for its minimum.

The LM algorithm uses the Gauss-Newton method when the parameters tend to their optimal values and the gradient descent method at the beginning when they are farther away from the end values. The detailed LM steps are detailed in Algorithm 4.1. The reason we chose the LM algorithm is that it proved efficiency over the others in terms of convergence in less computing time [189].

---

**Algorithm 4.1** The Levenberg-Marquardt algorithm.

---

1. Compute the output from the inputs and the corresponding error vector  $e$ ;
  2. Compute the Jacobian matrix  $J$ ;
  3. Compute  $\Delta x$  by solving the equation:  $\Delta x = (J^T \cdot J + \mu \cdot I)^{-1} J^T \cdot e$ ;
  4. Update the error vector corresponding to  $x + \Delta x$ ;
  5. Compute the new error vector
    - (a) If the sum of squared errors has decreased, set  $\mu = \mu - \beta^-$  and go back to step 1;
    - (b) else set  $\mu = \mu + \beta^+$  and go back to step 3;
  6. Continue while:
    - (a) maximum number of epochs has not been reached
    - (b) and goal performance has not been reached
    - (c) and the performance gradient is  $> G_{min}$
    - (d) and  $\mu < \mu_{max}$
    - (e) and maximum number of fails has not been reached
    - (f) and maximum time has not been exceeded
- 

#### 4.3.1.3 Force estimation

As explained before, the aim of this section is to find the 3<sup>rd</sup> order polynomial coefficients from the knowledge of three RMS values corresponding to three isometric contraction levels. The global

schematic of the estimation problem is visualized in Figure 4.16, where the inputs are the three RMS values corresponding to three different contraction levels in addition to other subject specific parameters (morphological, anatomical,...) and the outputs are the three coefficients that describe the relationship between the RMS and the force values (see Equation 4.10).

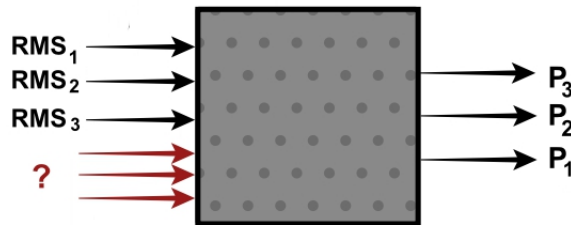


Figure 4.16: Schematic of the input/output system.

In consequence, we need to define an appropriate feed forward ANN network that is able to find the polynomial coefficient with minimal error possible. Accordingly, there are different steps to follow in order to achieve this goal. The first step is the determination of the optimal three force levels that can allow us to estimate the coefficients  $P_3$ ,  $P_2$  and  $P_1$  with the slightest *NRMSE*. Thus, first off we only used the RMS values as inputs to the ANN. We tested all the possible combinations of three force levels among seven (10 to 70 %MVC). This means that we have  $C_7^3 = 35$  different combinations of contraction levels (see Table B.1). We chose not to use the high contraction values (80, 90 and 100 %MVC) since it would be very difficult to obtain in experimental conditions. We need to remind here, that the database we used for this study is the same as the one described in section 4.2.2. For this investigation, we defined a neural network of three layers: 1 input layer, 1 hidden layer of 10 neurons and 1 output layer of three neurons. For the training function, we used the LM algorithm described above. The corresponding parameters were detailed in Table 4.6.

Parameter	Value
Performance goal	0
Maximum number of epochs to train	1000
Minimum performance gradient ( $G_{min}$ )	$10^{-7}$
Maximum time to train in seconds	$\infty$
Maximum validation failures	6
Percentage of training samples	70%
Percentage of validation samples	15%
Percentage of testing samples	15%
Initial $\mu$ value	0.001
$\mu$ decrease factor	0.1
$\mu$ increase factor	10
Maximum value of $\mu(\mu_{max})$	$10^{10}$

Table 4.6: ANN training parameters.

We performed 1000 trials of training for each combination of force contractions. The mean  $\pm$  std values of the NRMSE for each combination are illustrated in Figure 4.17. We obtained the minimum mean value for the combination number 30 which is composed of the three force levels: 30, 50 and 70 %MVC. The corresponding NRMSE was equal to  $0.084 \pm 0.035$ . Thus, for the following processing we will be using only these three contraction levels to determine the polynomial coefficients  $P_3$ ,  $P_2$  and  $P_1$ .

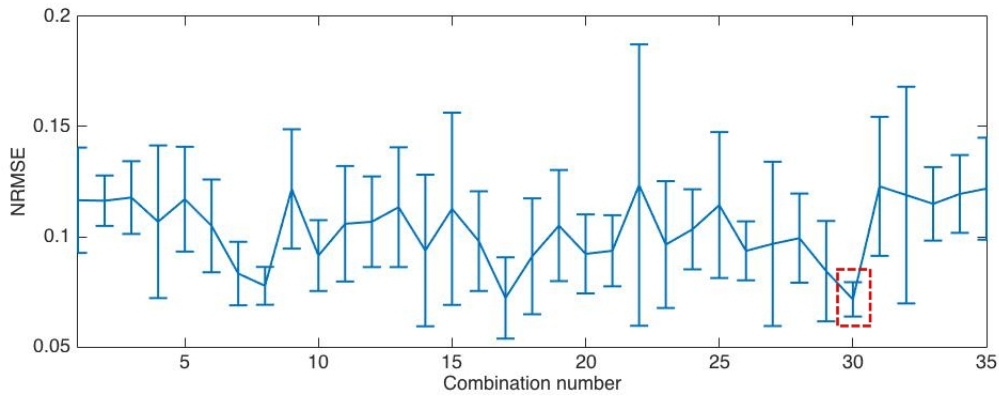


Figure 4.17: The NRMSE between the target and the estimated coefficients using ANN approach for the 35 different contraction level combinations.

Using these three contraction levels, we tested different numbers of neurons in the hidden layer in order to fix the optimal ANN configuration. Therefore we computed the mean  $\pm$  std values of NRMSE computed for the force levels of 10, 20, 40, 60, 80, 90 and 100 %MVC for the signals that were not used in the training phase as well as the NRMSE on the polynomial coefficients for different hidden neurons number. The results are presented in Table 4.7. We can see that the NRMSE decreases with the number of neurons with the minimal error for only three hidden neurons. However, we have the minimal error on the force estimation for 10 hidden neurons.

Table 4.7: The mean  $\pm$  std values of NRMSE computed for the force levels 10, 20, 40, 60, 80, 90 and 100 %MVC for the signals that were not used in the training phase for different configurations of ANN parameters.

Hidden neurons number	NRMSE for coefficients	NRMSE for the force
3	$0.0777 \pm 0.0413$	$0.0562 \pm 0.0385$
4	$0.0806 \pm 0.0411$	$0.0419 \pm 0.0198$
5	$0.0824 \pm 0.0417$	$0.0380 \pm 0.0224$
10	$0.0939 \pm 0.0352$	$0.0370 \pm 0.0165$
20	$0.1295 \pm 0.0516$	$0.0576 \pm 0.0383$
30	$0.1738 \pm 0.0691$	$0.0544 \pm 0.0329$
40	$0.1836 \pm 0.0745$	$0.0567 \pm 0.0451$

The study described earlier allowed us to fix the RMS input levels of the model (see Figure 4.16). The other parameters that can help in the estimation of the coefficients are the morphological parameters: skin and adipose tissue thickness values and conceivably the anatomical parameters: MU type distribution percentages since we saw the important effect they had on the polynom coefficients (see section 4.2.6).

For the morphological parameters, the inputs that can be added are clear and can be measured from the subjects (in the experimental case). However, for the MU type distribution which have a significant impact on the coefficients of the polynom, as depicted in a previous study (section 4.2.6), it is not clear what input can we choose to represent the different distributions. But before, we increased the number of simulations in our data base to obtain more samples of the D2 and the D3 distributions. Thus, we added three different configurations for each distribution as follow: linear LRS, nonlinear LRS and HRS with Sim1 morphological parameters (see Table 4.2). This allows us to have 80 samples instead of 50 wherein we have 40 samples for D1, 20 samples for D2 and 20 samples for D3.

Table 4.8: The mean  $\pm$  std values of NRMSE computed for the force levels 10, 20, 40, 60, 80, 90 and 100 %MVC for the signals that were not used in the training phase and the NRMSE for the polynom coefficient estimation for different input parameters.

	NRMSE for coefficients	NRMSE for the force
RMS	0.1018 $\pm$ 0.0512	0.0431 $\pm$ 0.0290
RMS+ $\rho_b$	0.1026 $\pm$ 0.0343	0.0354 $\pm$ 0.0251
RMS+ $\rho_c$	0.0959 $\pm$ 0.0289	0.0375 $\pm$ 0.0201
RMS+ $\rho_c + \rho_b$	0.0985 $\pm$ 0.0312	0.0332 $\pm$ 0.0185

For the first type of subject specific parameters (the morphological parameters) we investigated the effect of adding the skin tissue thickness, the adipose tissue thickness and both thickness values to the three RMS input values on the NRMSE. These results are depicted in Table 4.8. We can notice that we have a decrease in the NRMSE value for the polynom coefficients when we add the skin and adipose tissue thicknesses as input to the ANN. The next step is to investigate adding informations about the anatomical properties (MU type distribution) of the muscle to the ANN system.

#### 4.3.1.4 Improving force estimation using HOS

Following the sensitivity analysis of the polynom coefficients in section 4.2.6, we found a significant influence of the MU type distribution on the polynom shape. On that account, it could be beneficial to use HOS statistics in order to classify our data base according the the MU type distribution (D1, D2 or D3). Since as demonstrated in the previous chapter (see section 3.3.2.4), the HOS parameters allows us to differentiate between the different MU type distributions based on the obtained profile for the kurtosis and the skewness. This classification approach aims at dividing the database into three groups in order to train three different ANNs according to the MU type distribution. The general block diagram of this approach is illustrated in Figure 4.18.

Based on this procedure, the first step is to compute the HOS profiles. Thus we computed the kurtosis and the skewness for the three distributions D1, D2 and D3, the results are shown in Figure 4.19. Following these results, it is clear that we can easily classify the input/output data based on their MU

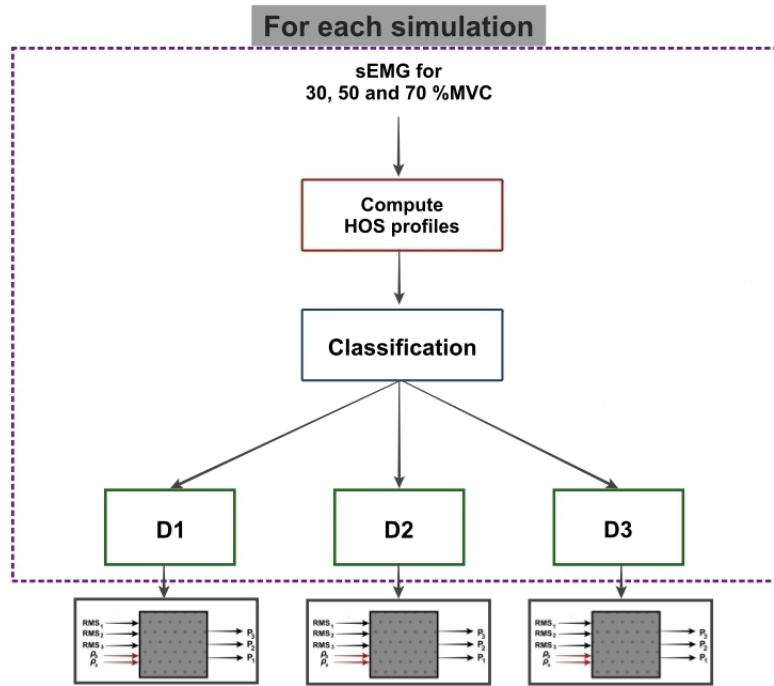


Figure 4.18: The block diagram of the polynomial coefficients estimation after classification into three groups according to the MU type distribution.

type distribution. Which can be automatized using a clustering algorithm.

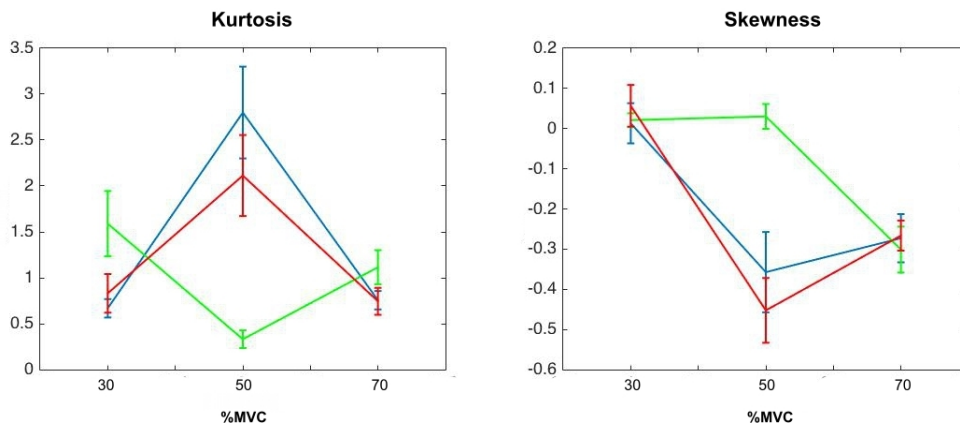


Figure 4.19: The mean and std variation of the HOS parameters the kurtosis and the skewness according to the force levels 30, 50 and 70 %MVC.

On that account, we tested this new approach on the force estimation after classification algorithm using machine learning and pattern recognition (neural pattern recognition and classification toolbox in MATLAB R2015a). For ANN based classification, we used 100 hidden neurons after multiple trials. The results gave a 91.7% of correct classification using the skewness, 91.1% correct classification using the kurtosis and 92.2 % of correct classification using both HOS parameters. Table 4.9 presents the new obtained NRMSE for each class of MU type distribution after classification, where we have only the three RMS values as inputs in order to test the influence of homogenizing the data base relative to the MU type distribution on the polynomial coefficients and force estimation NRMSE respectively. Thus, we notice that

by breaking down the database, following the MU type distribution, we obtain less force and polynomial coefficient estimation errors as expected.

Table 4.9: The mean  $\pm$  std values of NRMSE computed for the force levels 10, 20, 40, 60, 80, 90 and 100 %MVC (not used in the training phase) and the NRMSE for the polynom coefficient estimation for different input parameters.

	NRMSE for coefficients	NRMSE for the force
D1	0.0771 $\pm$ 0.0330	0.0265 $\pm$ 0.0120
D2	0.0919 $\pm$ 0.0320	0.0233 $\pm$ 0.0104
D3	0.0954 $\pm$ 0.0319	0.0239 $\pm$ 0.0199

To conclude, the main result of this study is that the HD-sEMG/force relationship has to be treated as a subject specific relation. As a result, for accurate force estimation using HD-sEMG data it is primordial to add morphological and anatomical information. However, in experimental conditions, where we will be obligated to switch to a multi-muscle context, using an ANN approach and training would be inconceivable since we will have only one output; the global moment or force. Therefore, we need an analytical approach that can be used later on in load sharing problem resolution.

### 4.3.2 Analytical approach

The objective of this section is to provide us with a resolution method with minimum complexity for a future attempt of solving the load sharing problem. In this study, since we are facing three unknowns ( $P_3$ ,  $P_2$  and  $P_1$ ), in order to find the solution we need at least three equations, hence three contraction levels. Let us write the HD-sEMG/force relationship model of the 3<sup>rd</sup> order polynomial for three different contraction levels  $F_1$ ,  $F_2$  and  $F_3$  as follow:

$$F_1 = P_3 RMS_1^3 + P_2 RMS_1^2 + P_1 RMS_1 \quad (4.14)$$

$$F_2 = P_3 RMS_2^3 + P_2 RMS_2^2 + P_1 RMS_2 \quad (4.15)$$

$$F_3 = P_3 RMS_3^3 + P_2 RMS_3^2 + P_1 RMS_3 \quad (4.16)$$

With  $F_i$  and  $RMS_i$  the force and RMS values at contraction level  $i$  respectively.

Following the equations above, we can now compute the polynomial coefficients relative to each simulation of parameters (see section 4.2.2) using optimization technique by least square minimization and gradient algorithm. Accordingly, we used the linear least squares solver in the optimization toolbox of

MATLAB 2015a (lsqlin.m) that solves curve fitting problems with boundaries or linear constraints. Thus, since we found in a previous study that  $P_3$  and  $P_1$  are always positive and  $P_2$  is always negative (see section 4.2.6), we can add constraints on the signs of the coefficients of the polynomial.

Using the approach described above, we computed the NRMSE between the estimated and the simulated force levels, that were not used in the coefficient estimation process, on all the possible combinations of three force levels among seven similar to the previous study (see Table B.1). The minimum averaged NRMSE value for all the simulation was also that of levels: 30, 50 and 70%MVC as illustrated in Figure 4.20. The values of the NRMSE for each simulation relative to this combination of contraction levels are presented in Figure 4.21.

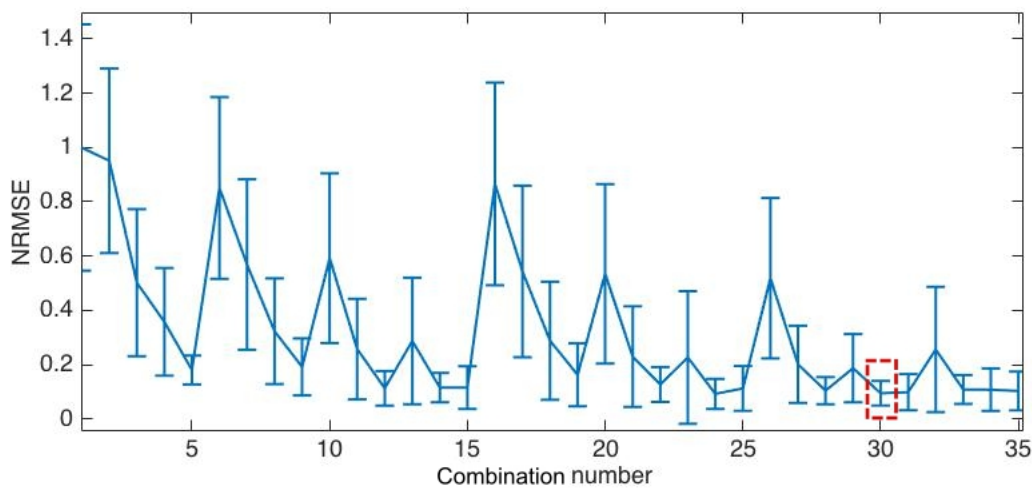


Figure 4.20: The NRMSE between the target and the estimated coefficients using optimization approach for the 35 different contraction level combinations.

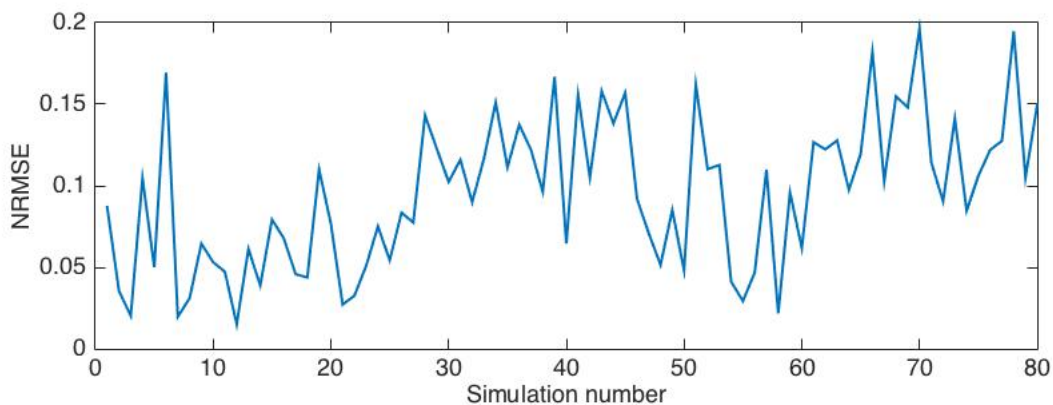


Figure 4.21: The NRMSE values obtained for all the different HD-sEMG/force simulations.

It is obvious that we have a big dispersion of the NRMSE among the different simulations (mean  $\pm$  std=  $0.0954 \pm 0.0454$ ). This is expected due the variation of the shape of the relationship with different configurations of morphological, neural and anatomical parameters (see section 4.2.6). Therefore, in order to properly and efficiently estimate the coefficients of the HD-sEMG/force relationship, we need

to personalize our model by adding boundaries on the optimization procedure following the different morphological and anatomical parameters.

Based on the sensitivity study presented in the previous section, we can add boundaries on the polynomial coefficients values with respect to the MU type distribution. If we suppose that we classified the simulations into D1, D2 and D3 using the same HOS based procedure as in section 4.3.1.4, we can add the boundaries that were found in the sensitivity analysis study (section 4.2.6) for each MU type distribution. The new obtained NRMSE is illustrated in Figure 4.22. In this case, we have a NRMSE of  $0.0594 \pm 0.025$  which means that we have  $\sim 4\%$  decrease in the estimation error compared to the previous estimation. As for the morphological parameters, we need to test more values in order to incorporate their effect on the HD-sEMG/force relationship. A larger database will be adequate for this kind of future study with additional constraints.

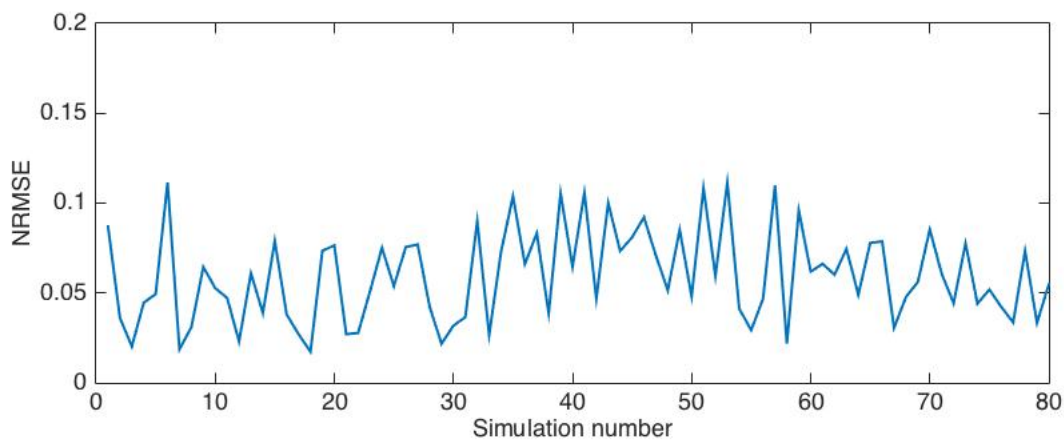


Figure 4.22: The NRMSE values obtained for all the different HD-sEMG/force simulations.

To conclude this section of the chapter, it seems that the HD-sEMG/force relationship model is a subject specific model. Subsequently, adding personalized parameters to the energetic ones is a must for efficient force estimation process as demonstrated by simulation. In this section, we introduced two exploratory studies concerning the estimation of the polynomial coefficients of the HD-sEMG/force relation in simulation using realistic HD-sEMG and force generation models. The aim of this investigation was, firstly, to test the influence of adding morphological and anatomical parameters on the polynomial coefficients estimation and hence force estimation. Secondly, to test how we could incorporate these additional information in the mono-muscle context in the prospect of employing it also in a multi-muscle context in a perspective work. Thus, for the ANN approach we found that adding morphological parameters improved the estimation of both polynomial coefficients and resultant force. Also, we found that homogenizing the database based on HOS profiles permits additional improvement in the results. However, the ANN approach cannot be employed eventually in experimental conditions (multi-muscle context) since we will have one output; the global force of all the muscles acting on the same joint ( elbow

joint). On the other hand, the analytical approach seems promising and employing it in a load sharing problem appears feasible.

## 4.4 Conclusion

In this chapter, a new HD-sEMG/force relationship has been proposed after a thorough investigation and comparison between different equation types used in the literature. This new relationship was found based on simulations from a realistic multilayered cylindrical HD-sEMG simulation model and a twitch force generation model. The RMS value was chosen as representative of the sEMG signal map after data fusion method by applying the image segmentation method described in chapter 3 (see section 3.2.2). Then, we employed the 3<sup>rd</sup> order polynomial equation, found the most suitable to describe the observed relationship, in a focused sensitivity analysis study that aimed at finding the parameters that mostly influence the relationship shape and thence on the polynomial coefficients. This simulation study demonstrated that morphological parameters (tissue thicknesses) seem to have a monotonic influence on the polynomial coefficients. The anatomical parameters however had the major impact on the coefficient values.

Afterwards, in a more prospective work, we tested both supervised regressive and analytical approaches for the estimation of the polynomial coefficients. The ANN approach gave acceptable results for sEMG based force estimation, especially after adding the skin and adipose tissue thicknesses as additional inputs. Finally, we proposed an amelioration of the force estimation model by homogenizing the data based for the neural network training. Thus, we introduced an additional classification step to our model where we classified the data into three groups based on their MU distribution type. Then, we trained the neural network on the data from the same group which decreased the force estimation error. For the analytical approach, we used optimization procedure with constraints in order to estimate the polynomial coefficients. This approach also gave acceptable estimation error but more importantly a promising performance that need to be further improved in a larger and more heterogeneous database to be employed in experimental conditions.

# General conclusion and perspectives

In this general conclusion, we will run through the essential points that were addressed and developed within this thesis. Then, we will mention some of the limitations of the methods proposed. And we will finish by elaborating the perspective of future works.

As previously explained, this thesis aims at proposing a new sEMG/force relationship model by using HD-sEMG recording technique. For this purpose, we are faced with several steps of signal processing and preparation to finally model the sEMG/force relationship. The first task is to preprocess the 64 HD-sEMG signals in order to prepare them for the data fusion stage. This preprocessing includes primarily denoising the sEMG signals. However, in the literature, there is no multichannel denoising algorithm that takes into account the heterogeneity of the noise spread throughout the HD-sEMG grid. Thus, the first contribution of the thesis was the development of a denoising algorithm based on a second order BSS method, the CCA. This method, called sCCA, combines channel selection procedure and source elimination and thresholding in order to denoise the HD-sEMG signals in the most efficient way possible. This algorithm was also compared to the commonly used denoising methods and showed better performance and robustness than the others. The second step of the preprocessing, was aimed at the separation of the electrical activity of the BB and the BR. Actually, due to the position of the BR alongside the BB and the fact that it is a deep muscle whose sEMG cannot easily be measured using classical bipolar electrodes, we have a superposition of its electrical signal to that of the BB. For this reason it is of great interest to extract the sEMG of the Brachialis from that of the BB for a valid sEMG force estimation. Accordingly, the second contribution of this work is the proposition of a muscle activities separation procedure, in collaboration with the LiSIN Lab (Prof. R. Merletti), that is also based on CCA in addition to an image segmentation algorithm. This method allows us to remove the BR sEMG that overlaps with the total sEMG measured from the skin surface above the BB muscle.

After preprocessing of the signals, the next stage of the work was dedicated to the data fusion and the model input vector selection. For the data fusion step, we compared two image segmentation algorithms that address the data fusion by treating the HD-sEMG parameter map as an image and reducing the number of channel through localizing the region of interest and thence the channels of significance.

Afterwards, our third contribution was the analysis of sensitivity of HOS with force increase in simulation where we compared the PCA technique, used in dimension reduction problems for different Laplacian filtering techniques, to simple averaging of the HOS parameters. Complementary, the fourth contribution was studying the variations of the HOS parameters in experimental conditions during isometric anisotonic contractions by proposing a data fusion method based on channel selection procedure, optimum Laplacian positioning algorithm and PCA. In this work we succeeded at finding the same profile variation for the two studied HOS parameters, the skewness and the kurtosis, for all the subjects despite the substantial variability between subjects. Another contribution in this stage was to accomplish a simulation and an experimental monitoring of HOS and SD parameters with contraction level variation by personalizing a cylindrical HD-sEMG model using physiological parameters obtained by using ultrasound imaging technique. Then, we performed a sensitivity analysis of anatomical, neural and morphological parameters on the HOS and SD profiles variations with increasing force which allows us to associate PDF shape descriptor profiles to specific physiological parameter values. This can be of great interest in experimental conditions where we can collect subject specific information and parameters and perform a kind of non-invasive biopsy. The last contribution of this stage was the proposition of a new experimental protocol that allows us to study the deformation of the external BB surface deformation with force increase. The objective of this investigation was to find additional information that can characterize the force level in complement to the sEMG signal that are subject specific and particular to each muscle. These additional parameters can assist in solving the load sharing problem by introducing boundaries for the coefficients of the polynoms that describes the HD-sEMG/force relationship.

The last stage of this thesis was devoted to the HD-sEMG/force relationship modeling. First, we carried out a focused sensitivity analysis using the cylindrical HD-sEMG generation model for the 64 simulated sEMG signals and a twitch based force model for the simulation of the corresponding muscle force where we established the major parameters that affect the HD-sEMG/force relationship and their impact. Following, we compared between different fitting type equations proposed in the literature and we found the best type that describe the HD-sEMG/force relation. Accordingly, another contribution was to propose and validate, using realistic simulations, a relevant model for the HD-sEMG/force relationship. Subsequently, using this new found equation, we tested the effect of neural, morphological and anatomical parameters on its coefficients in the aim of quantifying this impact for a better force estimation in later work. Finally, the last contribution was to propose a machine learning type model to estimate the coefficients of the HD-sEMG/force relationship after training on the dataset from the simulations described earlier, in addition to an analytical approach based on optimization technique with constraints. The supervised regressive approach showed satisfactory results for force estimation with an error of 3%. Nevertheless, the analytical approach showed promising results that can be incorporated in a multi-muscle experimental context.

The HD-sEMG/force relationship modeling developed in this thesis is mainly based on simulation models of the HD-sEMG signals and their corresponding force profiles. The next step would be to employ this new found relationship in an experimental multi-muscle context. Moving to the multi-muscle scale of the elbow joint in isometric isotonic contractions means tackling the challenging “load sharing” paradigm. Solving this load sharing problem, which has been the concern of many researchers in the last decade, implies finding the contributions of each of the three muscles, the BB, the BR and the BRD, in the global moment applied on the elbow joint during isometric flexion. Thus, by using our sEMG/force relationship and by considering the three muscles involves in the elbow flexion, we can write the individual force equations of the the three muscles as follow:

$$F_1 = P_1^3 RMS_1^3 + P_1^2 RMS_1^2 + P_1^1 RMS_1 \quad (4.17)$$

$$F_2 = P_2^3 RMS_2^3 + P_2^2 RMS_2^2 + P_2^1 RMS_2$$

$$F_3 = P_3^3 RMS_3^3 + P_3^2 RMS_3^2 + P_3^1 RMS_3$$

Where  $P_i^j$  is the  $j^{th}$  polynomial coefficient of the  $i^{th}$  muscle and the  $RMS_i$  and  $F_i$  are the RMS and force values of the  $i^{th}$  muscle respectively. If we switch from the force to the muscle moments, given that the moment is equal to to force times the lever arm, we can rewrite the previous equation as follow:

$$M_1 = Q_1^3 RMS_1^3 + Q_1^2 RMS_1^2 + Q_1^1 RMS_1 \quad (4.18)$$

$$M_2 = Q_2^3 RMS_2^3 + Q_2^2 RMS_2^2 + Q_2^1 RMS_2$$

$$M_3 = Q_3^3 RMS_3^3 + Q_3^2 RMS_3^2 + Q_3^1 RMS_3$$

Where  $Q_i^j$  is the  $j^{th}$  polynomial coefficient of the  $i^{th}$  muscle and the  $RMS_i$  and  $M_i$  are the RMS and moment values of the  $i^{th}$  muscle respectively.

Thus, we can obtain the total moment, for one contraction level, by a simple summation of the three equations above such as:

$$M = \sum_{i=1}^3 M_i \quad (4.19)$$

$$M = \sum_{i=1}^3 (Q_i^3 RMS_i^3 + Q_i^2 RMS_i^2 + Q_i^1 RMS_i)$$

As we can see, using this equation, we will have nine different unknown coefficient to estimate in order to compute the three sEMG/force relationship for the three flexor muscles at several flexion intensities. If we try to solve this relationship in simulation we need a HD-sEMG generation model that can simulate the three muscles of the elbow joint at the same time. However, the main near future objective is to solve the expressed load sharing problem in an experimental context. Thus, we implemented a multi-muscle experimental protocol that uses three HD-sEMG grids in order to record the sEMG signals of the three muscle in parallel with the total force/moment. Using this protocol, our next work will be oriented toward solving the load sharing problem by using the Equation 4.19 as well as optimization algorithm for estimating the nine polynomial coefficients.

Finally, the approaches presented in this work have applications in many fields; starting by the denoising method that can be applied to the denoising of other biomedical signals just by simple adaptation of the thresholding rule. The source separation algorithm that can be applied in order to separate the electrical activity of other muscles in the musculoskeletal system that have the same vicinity and co-contraction problem. Furthermore, the tested PDF shape approaches should be used for extracting useful physiological informations, in a non-invasive manner, from the recorded HD-sEMG data. In addition, the proposed sEMG/force relationship model could potentially be used in a later period, when experimentally validated, in prosthesis control, fatigue evaluation, neuromuscular disorder detection or rehabilitation.

# Bibliography

- [1] K. E. Barrett and W. F. Ganong, *Ganong's Review of medical physiology*. New York: McGraw-Hill Medical, 2012.
- [2] R. Merletti and P. A. Parker, *Electromyography: Physiology, Engineering, and Non-Invasive Applications*. Piscataway: IEEE Press, Hoboken : Wiley-Interscience, 2004.
- [3] C. A. Oatis, "The mechanics and pathomechanics of human movement," 2003.
- [4] K. Bouillard, A. Nordez, and F. Hug, "Estimation of individual muscle force using elastography," *PLoS One*, vol. 6, no. 12, 2011.
- [5] J. V. Basmajian, *Muscles alive, their functions revealed by electromyography*. Baltimore: Williams & Wilkins, 1979.
- [6] C. J. De Luca, "The use of surface electromyography in biomechanics," *Journal of Applied Biomechanics*, vol. 13, pp. 135–163, 1997.
- [7] C. Disselhorst-Klug, T. Schmitz-Rode, and G. Rau, "Surface electromyography and muscle force: limits in sEMG–force relationship and new approaches for applications," *Clinical Biomechanics*, vol. 24, no. 3, pp. 225–235, 2009.
- [8] D. Staudenmann, K. Roeleveld, D. F. Stegeman, and J. H. van Dieen, "Methodological aspects of SEMG recordings for force estimation—a tutorial and review," *Journal of Electromyography and Kinesiology*, vol. 20, no. 3, pp. 375–387, 2010.
- [9] D. Staudenmann, I. Kingma, A. Daffertshofer, D. F. Stegeman, and J. H. van Dieen, "Improving EMG-based muscle force estimation by using a high-density EMG grid and principal component analysis," *IEEE Transactions on BioMedical Engineering*, vol. 53, no. 4, pp. 712–719, 2006.
- [10] D. Farina, C. Cescon, and R. Merletti, "Influence of anatomical, physical, and detection-system parameters on surface EMG," *Biological Cybernetics*, vol. 86, no. 6, pp. 445–456, 2002.

- [11] M. W. Berchtold, H. Brinkmeier, and M. Müntener, “Calcium ion in skeletal muscle: its crucial role for muscle function, plasticity, and disease,” *Physiological Reviews*, vol. 80, no. 3, pp. 1215–1265, 2000.
- [12] K. L. Rowley, C. B. Mantilla, and G. C. Sieck, “Respiratory muscle plasticity,” *Respiratory Physiology & Neurobiology*, vol. 147, no. 2, pp. 235–251, 2005.
- [13] P. Zhou and W. Z. Rymer, “Factors governing the form of the relation between muscle force and the EMG: A simulation study,” *Journal of Neurophysiology*, vol. 92, no. 5, pp. 2878–2886, 2004.
- [14] B. Afsharipour, *Estimation of load sharing among muscles acting on the same joint and Applications of surface electromyography*. Phd, Politecnico di Torino, 2014.
- [15] K. Manal and T. S. Buchanan, “A one-parameter neural activation to muscle activation model: estimating isometric joint moments from electromyograms,” *Journal of Biomechanics*, vol. 36, no. 8, pp. 1197–1202, 2003.
- [16] T. S. Buchanan, D. G. Lloyd, K. Manal, and T. F. Besier, “Neuromusculoskeletal modeling: Estimation of muscle forces and joint moments and movements from measurements of neural command,” *Journal of Applied Biomechanics*, vol. 20, no. 4, pp. 367–395, 2004.
- [17] M. Hayashibe and D. Guiraud, “Voluntary EMG-to-force estimation with a multi-scale physiological muscle model,” *Biomedical Engineering Online*, vol. 12, no. 1, 2013.
- [18] Y. Na, C. Choi, H. D. Lee, and J. Kim, “A study on estimation of joint force through isometric index finger abduction with the help of semg peaks for biomedical applications,” *IEEE Transactions on Cybernetics*, vol. 46, no. 1, pp. 2–8, 2016.
- [19] J. Honeybourne, M. Hill, and H. Moors, *Advanced Physical Education and Sport for AS-level*. Nelson Thornes, 2000.
- [20] R. T. Raikova and H. Aladjov, “Hierarchical genetic algorithm versus static optimization investigation of elbow flexion and extension movements,” *Journal of Biomechanics*, vol. 35, no. 8, pp. 1123–1135, 2002.
- [21] G.-B. Duchenne, *Physiologie des mouvements: demontree a l’aide de l’experimentation electrique et de l’observation clinique et applicable a l’etude des paralysies et des deformations*. Paris: J.-B. Bailliere, 1867.
- [22] H. U. Kuriki, F. M. de Azevedo, L. S. O. Takahashi, E. M. Mello, R. de Faria Negrão Filho, and N. Alves, *The Relationship Between Electromyography and Muscle Force, EMG Methods for Evaluating Muscle and Nerve Function*. InTech Open Access Publisher, 2012.

- [23] E. N. Marieb and K. Hoehn, *Human Anatomy & Physiology*. San Francisco: Pearson Benjamin Cummings, 2007.
- [24] L. S. Lippert, *Clinical Kinesiology and Anatomy*. Philadelphia: F. A. Davis, 2011.
- [25] R. Drake, A. W. Vogl, and A. W. M. Mitchell, *Gray's anatomy for students*. Philadelphia: Churchill Livingstone/Elsevier, 2014.
- [26] F. E. Zajac, "Muscle and tendon: properties, models, scaling, and application to biomechanics and motor control," *Critical Reviews in Biomedical Engineering*, vol. 17, no. 4, pp. 359–411, 1989.
- [27] D. Staudenmann and W. Taube, "Brachialis muscle activity can be assessed with surface electromyography," *Journal of Electromyography and Kinesiology*, vol. 25, no. 2, pp. 199–204, 2015.
- [28] J. V. Basmajian and A. Latif, "Integrated Actions and Functions of the Chief Flexors of the Elbow," *The Journal of Bone & Joint Surgery*, vol. 39, no. 5, pp. 1106–1118, 1957.
- [29] B. R. MacIntosh, P. F. Gardiner, and A. J. McComas, *Skeletal Muscle: Form and Function*. Champaign: Human Kinetics, 2006.
- [30] G. J. Tortora, N. P. Anagnostakos, S. R. Grabowski, and P. Mathieu, *Principes d'anatomie et de physiologie*. De Boeck, 1994.
- [31] S. Bouisset and B. Maton, *Principes d'anatomie et de physiologie*. Paris: Hermann, 1995.
- [32] M. K. Floeter, *Structure and function of muscle fibers and motor units*. In: *Disorders of Voluntary Muscle*. Cambridge: Cambridge University Press, 2010.
- [33] R. E. Burke, *Comprehensive Physiology*, ch. Motor Units: Anatomy, Physiology, and Functional Organization, pp. 345–422. John Wiley & Sons, 2011.
- [34] A. F. Huxley, "Muscle structure and theories of contraction," *Progress in Biophysics and Biophysical Chemistry*, vol. 7, pp. 255–318, 1957.
- [35] H. E. Huxley and J. Hanson, "The structural basis of the contraction mechanism in striated muscle," *Annals of the New York Academy of Sciences*, vol. 81, no. 2, pp. 403–408, 1959.
- [36] R. F. Schmidt, *En bref... Physiologie*. De Boeck, 1999.
- [37] A. J. Vander, J. H. Sherman, D. S. Luciano, and R. Brière, *Physiologie humaine*. Chenelière/McGraw-Hill, 1995.
- [38] A. F. Huxley, "Muscle structure and theories of contraction," *Progress in Biophysics and Biophysical Chemistry*, vol. 7, pp. 255–318, 1957.

- [39] E. P. Widmaier, H. Raff, and K. T. Strang, *Vander's Human Physiology: The Mechanism of Body Function*. New York: McGraw-Hill, 2010.
- [40] E. D. Adrian and D. W. Bronk, "The discharge of impulses in motor nerve fibres: Part II. the frequency of discharge in reflex and voluntary contractions," *The Journal of Physiology*, vol. 67, no. 2, pp. 9–151, 1929.
- [41] C. D. Hardyck, L. F. Petrinovich, and D. W. Ellsworth, "Feedback of speech muscle activity during silent reading: rapid extinction," *Science*, vol. 154, no. 3755, pp. 1467–1468, 1966.
- [42] A. Botter, H. R. Marateb, B. Afsharipour, and R. Merletti, "Solving EMG-force relationship using Particle Swarm Optimization," in *2011 Annual International Conference of the IEEE Engineering in Medicine and Biology Society*, pp. 3861–3864, 2011.
- [43] D. Farina, N. Jiang, H. Rehbaum, A. Holobar, B. Graimann, H. Dietl, and O. C. Aszmann, "The extraction of neural information from the surface EMG for the control of upper-limb prostheses: emerging avenues and challenges," *IEEE Transactions on Neural Systems and Rehabilitation Engineering*, vol. 22, no. 4, pp. 797–809, 2014.
- [44] R. V. J. Miller, "Electromyography: Uses and limitations," *California Medicine*, vol. 89, no. 4, pp. 250–252, 1958.
- [45] C. J. De Luca and E. C. Hostage, "Relationship between firing rate and recruitment threshold of motoneurons in voluntary isometric contractions," *Journal of Neurophysiology*, vol. 104, no. 2, pp. 1034–1046, 2010.
- [46] E. Henneman, G. Somjen, and D. O. Carpenter, "Functional significance of cell size in spinal motoneurons," *Journal of Neurophysiology*, vol. 28, pp. 560–580, 1965.
- [47] C. J. De Luca, R. S. LeFever, M. P. McCue, and A. P. Xenakis, "Behaviour of human motor units in different muscles during linearly varying contractions," *The Journal of Physiology*, vol. 329, no. 1, pp. 113–128, 1982.
- [48] C. J. Heckman and M. D. Binder, "Computer simulations of the effects of different synaptic input systems on motor unit recruitment," *Journal of Neurophysiology*, vol. 70, no. 5, pp. 1827–1840, 1993.
- [49] A. J. Fuglevand, D. A. Winter, and A. E. Patla, "Models of recruitment and rate coding organization in motor-unit pools," *Journal of Neurophysiology*, vol. 70, no. 6, pp. 2470–2488, 1993.
- [50] F. S. Ayachi and S. Boudaoud, "Evaluation of muscle force classification using shape analysis of the sEMG probability density function: A simulation study," *Medical & Biological Engineering & Computing*, vol. 52, no. 8, pp. 673–684, 2014.

- [51] H. Cao, S. Boudaoud, F. Marin, and C. Marque, "Surface EMG-force modelling for the biceps brachii and its experimental evaluation during isometric isotonic contractions," *Computer Methods in Biomechanics and Biomedical Engineering*, vol. 18, no. 9, pp. 1014–1023, 2014.
- [52] C. A. Sinderby, A. S. Comtois, R. G. Thomson, and A. E. Grassino, "Influence of the bipolar electrode transfer function on the electromyogram power spectrum," *Muscle & Nerve*, vol. 19, no. 3, pp. 290–301, 1996.
- [53] D. Farina and A. Rainoldi, "Compensation of the effect of sub-cutaneous tissue layers on surface EMG: a simulation study," *Medical Engineering & Physics*, vol. 21, no. 6, pp. 487–497, 1999.
- [54] M. Nielsen, T. Graven-Nielsen, and D. Farina, "Effect of innervation-zone distribution on estimates of average muscle-fiber conduction velocity," *Muscle & Nerve*, vol. 37, no. 1, pp. 68–78, 2008.
- [55] V. Carriou, M. Al Harrach, J. Laforet, and S. Boudaoud, "Sensitivity analysis of HD-sEMG amplitude descriptors relative," in *XIV Mediterranean Conference on Medical and Biological Engineering and Computing 2016*, vol. 57, p. 119, 2016.
- [56] T. Masuda, H. Miyano, and T. Sadoyama, "The position of innervation zones in the biceps brachii investigated by surface electromyography," *IEEE Transactions on BioMedical Engineering*, vol. 32, no. 1, pp. 36–42, 1985.
- [57] H. Piitulainen, T. Rantalainen, V. Linnamo, P. Komi, and J. Avela, "Innervation zone shift at different levels of isometric contraction in the biceps brachii muscle," *Journal of Electromyography and Kinesiology*, vol. 19, no. 4, pp. 667–675, 2009.
- [58] R. Merletti and L. R. Lo Conte, "Surface emg signal processing during isometric contractions," *Journal of Electromyography and Kinesiology*, vol. 7, no. 4, pp. 241–250, 1997.
- [59] E. A. Clancy, E. L. Morin, and R. Merletti, "Sampling, noise-reduction and amplitude estimation issues in surface electromyography," *Journal of Electromyography and Kinesiology*, vol. 12, no. 1, pp. 1–16, 2002.
- [60] B. Bigland-Ritchie, "EMG/force relations and fatigue of human voluntary contractions," *Exercise and Sport Sciences Reviews*, vol. 9, pp. 75–117, 1981.
- [61] H.-P. Huang and C.-Y. Chen, "Development of a myoelectric discrimination system for a multi-degree prosthetic hand," in *1999 IEEE International Conference on Robotics and Automation*, vol. 3, pp. 2392–2397, 1999.
- [62] F. Romero, F. J. Alonso, J. Cubero, and G. Galan-Marín, "An automatic SSA-based de-noising and smoothing technique for surface electromyography signals," *Biomedical Signal Processing and Control*, vol. 18, pp. 317–324, Apr. 2015.

- [63] K. Nazarpour, A. H. Al-Timemy, G. Bugmann, and A. Jackson, "A note on the probability distribution function of the surface electromyogram signal," *Brain Research Bulletin*, vol. 90, pp. 88–91, 2013.
- [64] A. Holobar, D. Farina, M. Gazzoni, R. Merletti, and D. Zazula, "Estimating motor unit discharge patterns from high-density surface electromyogram," *Clinical Neurophysiology*, vol. 120, no. 3, pp. 551–562, 2009.
- [65] D. Staudenmann, I. Kingma, D. F. Stegeman, and J. H. van Dieen, "Towards optimal multi-channel EMG electrode configurations in muscle force estimation: a high density EMG study," *Journal of Electromyography and Kinesiology*, vol. 15, no. 1, pp. 1–11, 2005.
- [66] D. F. Stegeman, B. U. Kleine, B. G. Lapatki, and J. P. Van Dijk, "High-density Surface EMG: Techniques and Applications at a Motor Unit Level," *Biocybernetics and Biomedical Engineering*, vol. 32, no. 3, pp. 3–27, 2012.
- [67] V. Glaser, A. Holobar, and D. Zazula, "Real-Time Motor Unit Identification From High-Density Surface EMG," *IEEE Transactions on Neural Systems and Rehabilitation Engineering*, vol. 21, pp. 949–958, Nov. 2013.
- [68] A. Phinyomark, C. Limsakul, H. Hu, P. Phukpattaranont, and S. Thongpanja, *The usefulness of mean and median frequencies in electromyography analysis*. InTech Open Access Publisher, 2012.
- [69] R. D. Herbert and S. C. Gandevia, "Twitch interpolation in human muscles: mechanisms and implications for measurement of voluntary activation," *Journal of Neurophysiology*, vol. 82, no. 5, pp. 2271–2283, 1999.
- [70] R. Raikova and H. Aladjov, "The influence of the way the muscle force is modeled on the predicted results obtained by solving indeterminate problems for a fast elbow flexion," *Computer Methods in Biomechanics and Biomedical Engineering*, vol. 6, no. 3, pp. 181–196, 2003.
- [71] L. Wang and T. S. Buchanan, "Prediction of joint moments using a neural network model of muscle activations from emg signals," *IEEE Transactions on Neural Systems and Rehabilitation Engineering*, vol. 10, no. 1, pp. 30–37, 2002.
- [72] Y. Huang, K. B. Englehart, B. Hudgins, and A. D. Chan, "A Gaussian mixture model based classification scheme for myoelectric control of powered upper limb prostheses," *IEEE Transactions on BioMedical Engineering*, vol. 52, no. 11, pp. 1801–1811, 2005.
- [73] D. Graupe and W. K. Cline, "Functional separation of EMG signals via ARMA identification methods for prosthesis control purposes," *IEEE Transactions on Systems Man and Cybernetics*, vol. 5, no. 2, pp. 252–259, 1975.

- [74] P. Madeleine, P. Bajaj, K. Sogaard, and L. Arendt-Nielsen, "Mechanomyography and electromyography force relationships during concentric, isometric and eccentric contractions," *Journal of Electromyography and Kinesiology*, vol. 11, no. 2, pp. 113–121, 2001.
- [75] W. Youn and J. Kim, "Estimation of elbow flexion force during isometric muscle contraction from mechanomyography and electromyography," *Medical & Biological Engineering & Computing*, vol. 48, no. 11, pp. 1149–1157, 2010.
- [76] J. T. Cramer, T. J. Housh, T. K. Evetovich, G. O. Johnson, K. T. Ebersole, S. R. Perry, and A. J. Bull, "The relationships among peak torque, mean power output, mechanomyography, and electromyography in men and women during maximal, eccentric isokinetic muscle actions," *European Journal of Applied Physiology*, vol. 86, no. 3, pp. 226–232, 2002.
- [77] Y.-P. Zheng, M. M. Chan, J. Shi, X. Chen, and Q.-H. Huang, "Sonomyography: Monitoring morphological changes of forearm muscles in actions with the feasibility for the control of powered prosthesis," *Medical Engineering & Physics*, vol. 28, no. 5, pp. 405–415, 2006.
- [78] J.-Y. Guo, Y.-P. Zheng, H.-B. Xie, and X. Chen, "Continuous monitoring of electromyography (EMG), mechanomyography (MMG), sonomyography (SMG) and torque output during ramp and step isometric contractions," *Medical Engineering & Physics*, vol. 32, no. 9, pp. 1032–1042, 2010.
- [79] J. Shi, Y. P. Zheng, Q. H. Huang, and X. Chen, "Continuous Monitoring of Sonomyography, Electromyography and Torque Generated by Normal Upper Arm Muscles During Isometric Contraction: Sonomyography Assessment for Arm Muscles," *IEEE Transactions on BioMedical Engineering*, vol. 55, no. 3, pp. 1191–1198, 2008.
- [80] M. A. Dresner, G. H. Rose, P. J. Rossman, R. Muthupillai, A. Manduca, and R. L. Ehman, "Magnetic resonance elastography of skeletal muscle," *Journal of Magnetic Resonance Imaging*, vol. 13, no. 2, pp. 269–276, 2001.
- [81] A. Nordez and F. Hug, "Muscle shear elastic modulus measured using supersonic shear imaging is highly related to muscle activity level," *Journal of Applied Physiology*, vol. 108, no. 5, pp. 1389–1394, 1985.
- [82] M. Al Harrach, S. Boudaoud, K. Ben Mansour, J.-F. Grosset, and F. Marin, "Estimation of the relationship between external biceps brachii deformation and isometric contraction level using motion capture technique," in *XIV Mediterranean Conference on Medical and Biological Engineering and Computing*, pp. 37–41, 2016.
- [83] H. S. Milner-Brown and R. B. Stein, "The relation between the surface electromyogram and muscular force," *The Journal of Physiology*, vol. 246, no. 3, pp. 549–569, 1975.

- [84] J. H. Lawrence and C. J. De Luca, "Myoelectric signal versus force relationship in different human muscles," *Journal of Applied Physiology: Respiratory, Environmental and Exercise Physiology*, vol. 54, no. 6, pp. 1653–1659, 1983.
- [85] M. Solomonow, R. V. Baratta, and R. D'Ambrosia, "EMG-force relations of a single skeletal muscle acting across a joint: Dependence on joint angle," *Journal of Electromyography and Kinesiology*, vol. 1, no. 1, pp. 58–67, 1991.
- [86] A. V. Hill, "The Heat of Shortening and the Dynamic Constants of Muscle," *Proceedings of the Royal Society of London. Series B: Biological Sciences*, vol. 126, no. 843, pp. 136–195, 1938.
- [87] V. T. Inman, H. J. Ralston, J. B. Saunders, B. Feinstein, and E. W. J. Wright, "Relation of human electromyogram to muscular tension," *Electroencephalography and Clinical Neurophysiology*, vol. 4, no. 2, pp. 187–194, 1952.
- [88] B. Bigland and O. C. Lippold, "The relation between force, velocity and integrated electrical activity in human muscles," *The Journal of Physiology*, vol. 123, no. 1, pp. 214–224, 1954.
- [89] L. L. Menegaldo and L. F. de Oliveira, "Effect of muscle model parameter scaling for isometric plantar flexion torque prediction," *Journal of Biomechanics*, vol. 42, no. 15, pp. 2597–2601, 2009.
- [90] M. Sartori, M. Reggiani, D. Farina, and D. G. Lloyd, "EMG-driven forward-dynamic estimation of muscle force and joint moment about multiple degrees of freedom in the human lower extremity," *PLoS One*, vol. 7, no. 12, 2012.
- [91] J. J. Woods and B. Bigland-Ritchie, "Linear and non-linear surface EMG/force relationships in human muscles. An anatomical/functional argument for the existence of both," *American Journal of Physical Medicine*, vol. 62, no. 6, pp. 287–299, 1983.
- [92] H. S. Milner-Brown, R. B. Stein, and R. Yemm, "Changes in firing rate of human motor units during linearly changing voluntary contractions," *The Journal of Physiology*, vol. 230, no. 2, pp. 371–390, 1973.
- [93] D. G. Lloyd and T. F. Besier, "An EMG-driven musculoskeletal model to estimate muscle forces and knee joint moments in vivo," *Journal of Biomechanics*, vol. 36, no. 6, pp. 765–776, 2003.
- [94] F. Goubel, "Muscle mechanics," in *Muscular Function in Exercise and Training*, pp. 24–35, Karger Publishers, 1987.
- [95] A. M. Gordon, A. F. Huxley, and F. J. Julian, "The variation in isometric tension with sarcomere length in vertebrate muscle fibres," *The Journal of Physiology*, vol. 184, no. 1, pp. 170–192, 1966.

- [96] E. J. Perreault, C. J. Heckman, and T. G. Sandercock, "Hill muscle model errors during movement are greatest within the physiologically relevant range of motor unit firing rates," *Journal of Biomechanics*, vol. 36, no. 2, pp. 211–218, 2003.
- [97] G. I. Zahalak, "A distribution-moment approximation for kinetic theories of muscular contraction," *Mathematical Biosciences*, vol. 55, no. 1, pp. 89–114, 1981.
- [98] J. Bestel, F. Clement, and M. Sorine, "A Biomechanical Model of Muscle Contraction," in *Medical Image Computing and Computer-Assisted Intervention*, no. 2208, pp. 1159–1161, Berlin: Springer Heidelberg, 2001.
- [99] M. J. Hoozemans and J. H. van Dieen, "Prediction of handgrip forces using surface EMG of forearm muscles," *Journal of Electromyography and Kinesiology*, vol. 15, no. 4, pp. 358–366, 2005.
- [100] M. M. Liu, W. Herzog, and H. H. Savelberg, "Dynamic muscle force predictions from EMG: an artificial neural network approach," *Journal of Electromyography and Kinesiology*, vol. 9, no. 6, pp. 391–400, 1999.
- [101] J. J. Luh, G. C. Chang, C. K. Cheng, J. S. Lai, and T. S. Kuo, "Isokinetic elbow joint torques estimation from surface emg and joint kinematic data: using an artificial neural network model," *Journal of Electromyography and Kinesiology*, vol. 9, no. 3, pp. 173–183, 1999.
- [102] W. H. de Vries, H. E. Veeger, C. T. Baten, and F. C. van der Helm, "Can shoulder joint reaction forces be estimated by neural networks?," *Journal of Biomechanics*, vol. 49, no. 1, pp. 73–79, 2016.
- [103] J. M. Eklund, F. Mobasser, and K. Hashtrudi-Zaad, "Hand force estimation using fast orthogonal search," in *26th Annual International Conference of the IEEE Engineering in Medicine and Biology Society*, pp. 695–698, 2004.
- [104] F. Mobasser, J. M. Eklund, and K. Hashtrudi Zaad, "Estimation of elbow induced wrist force with emg signals using fast orthogonal search," *IEEE Transactions on BioMedical Engineering*, vol. 54, no. 4, pp. 683–693, 2007.
- [105] G. Johns, E. Morin, and K. Hashtrudi-Zaad, "Force modelling of upper limb biomechanics using ensemble fast orthogonal search on high-density electromyography," *IEEE Transactions on Neural Systems and Rehabilitation Engineering*, vol. PP, no. 99, 2016.
- [106] J. Hashemi, E. Morin, P. Mousavi, K. Mountjoy, and K. Hashtrudi-Zaad, "EMG force modeling using parallel cascade identification," *Journal of Electromyography and Kinesiology*, vol. 22, no. 3, pp. 469–477, 2012.

- [107] J. Hashemi, E. Morin, P. Mousavi, and K. Hashtrudi-Zaad, “Enhanced dynamic emg-force estimation through calibration and pci modeling,” *IEEE Transactions on Neural Systems and Rehabilitation Engineering*, vol. 23, no. 1, pp. 41–50, 2015.
- [108] E. A. Clancy and N. Hogan, “Relating agonist-antagonist electromyograms to joint torque during isometric, quasi-isotonic, nonfatiguing contractions,” *IEEE Transactions on BioMedical Engineering*, vol. 44, no. 10, pp. 1024–1028, 1997.
- [109] T. S. Buchanan, M. J. Moniz, J. P. Dewald, and W. Z. Rymer, “Estimation of muscle forces about the wrist joint during isometric tasks using an emg coefficient method,” *Journal of Biomechanics*, vol. 26, no. 4, pp. 547–560, 1993.
- [110] H. J. Hermens, B. Freriks, C. Disselhorst-Klug, and G. Rau, “Development of recommendations for SEMG sensors and sensor placement procedures,” *Journal of Electromyography and Kinesiology*, vol. 10, no. 5, pp. 361–374, 2000.
- [111] R. Merletti, B. Afsharipour, and G. Piervirgili, “High Density Surface EMG Technology,” in *Converging Clinical and Engineering Research on Neurorehabilitation*, no. 1 in Biosystems & Biorobotics, pp. 1205–1209, Berlin: Springer Heidelberg.
- [112] M. Rojas-Martinez, M. A. Mananas, and J. F. Alonso, “High-density surface EMG maps from upper-arm and forearm muscles,” *Journal of NeuroEngineering and Rehabilitation*, vol. 9, 2012.
- [113] P. Zhou, M. Lowery, J. A. Dewald, and T. Kuiken, “Towards Improved Myoelectric Prosthesis Control: High Density Surface EMG Recording After Targeted Muscle Reinnervation,” in *2005 Annual International Conference of the IEEE Engineering in Medicine and Biology Society*, vol. 4, pp. 4064–4067, 2005.
- [114] H. Daley, K. Englehart, L. Hargrove, and U. Kuruganti, “High density electromyography data of normally limbed and transradial amputee subjects for multifunction prosthetic control,” *Journal of Electromyography and Kinesiology*, vol. 22, no. 3, pp. 478–484, 2012.
- [115] J. P. van Dijk, J. H. Blok, B. G. Lapatki, I. N. van Schaik, M. J. Zwartz, and D. F. Stegeman, “Motor unit number estimation using high-density surface electromyography,” *Clinical Neurophysiology*, vol. 119, no. 1, pp. 33–42, 2008.
- [116] M. J. Zwartz and D. F. Stegeman, “Multichannel surface EMG: basic aspects and clinical utility,” *Muscle & Nerve*, vol. 28, no. 1, pp. 1–17, 2003.
- [117] R. Merletti, A. Holobar, and D. Farina, “Analysis of motor units with high-density surface electromyography,” *Journal of Electromyography and Kinesiology*, vol. 18, no. 6, pp. 879–890, 2008.

- [118] B. U. Kleine, J. P. van Dijk, B. G. Lapatki, M. J. Zwarts, and D. F. Stegeman, "Using two-dimensional spatial information in decomposition of surface EMG signals," *Journal of Electromyography and Kinesiology*, vol. 17, no. 5, pp. 535–548, 2007.
- [119] G. Drost, D. F. Stegeman, B. G. van Engelen, and M. J. Zwarts, "Clinical applications of high-density surface emg: a systematic review," *Journal of Electromyography and Kinesiology*, vol. 16, no. 6, pp. 586–602, 2006.
- [120] S. Allouch, M. Al Harrach, S. Boudaoud, J. Laforet, F. Ayachi, and R. Younes, "Muscle force estimation using data fusion from high-density SEMG grid," in *2nd International Conference on Advances in Biomedical Engineering*, pp. 195–198, IEEE, 2013.
- [121] Euljoon Park and S. Meek, "Adaptive filtering of the electromyographic signal for prosthetic control and force estimation," *IEEE Transactions on BioMedical Engineering*, vol. 42, pp. 1048–1052, 1995.
- [122] M. Al Harrach, S. Boudaoud, D. Gamet, J. F. Grosset, and F. Marin, "Evaluation of HD-sEMG Probability Density Function deformations in ramp exercise," *2014 Annual International Conference of the IEEE Engineering in Medicine and Biology Society*, vol. 2014, pp. 2209–2212, 2014.
- [123] R. V. Baratta, M. Solomonow, B. H. Zhou, and M. Zhu, "Methods to reduce the variability of EMG power spectrum estimates," *Journal of Electromyography and Kinesiology*, vol. 8, no. 5, pp. 279–285, 1998.
- [124] R. G. T. Mello, L. F. Oliveira, and J. Nadal, "Digital Butterworth filter for subtracting noise from low magnitude surface electromyogram," *Computer Methods and Programs in Biomedicine*, vol. 87, pp. 28–35, 2007.
- [125] R. G. T. Mello, L. F. Oliveira, and J. Nadal, "EMG signal filtering based on Empirical Mode Decomposition," *Biomedical Signal Processing and Control*, vol. 1, pp. 44–55, 2006.
- [126] X. Zhang and P. Zhou, "Filtering of surface EMG using ensemble empirical mode decomposition," *Medical Engineering & Physics*, vol. 35, no. 4, pp. 537–542, 2013.
- [127] P. M. Agante and J. de Sa, "ECG noise filtering using wavelets with soft-thresholding methods," in *Computers in Cardiology*, pp. 353–358, 1999.
- [128] A. Phinyomark, C. Limsakul, and P. Phukpattaranont, "A Comparative Study of Wavelet Denoising for Multifunction Myoelectric Control," in *International Conference on Computer and Automation Engineering, 2009. ICCAE '09*, pp. 21–25, 2009.
- [129] G. Aschero and P. Gizdulich, "Denoising of surface EMG with a modified Wiener filtering approach," *Journal of Electromyography and Kinesiology*, vol. 20, no. 2, pp. 366–373, 2010.

- [130] M. Hassan, S. Boudaoud, J. Terrien, B. Karlsson, and C. Marque, "Combination of canonical correlation analysis and empirical mode decomposition applied to denoising the labor electrohysterogram," *IEEE Transactions on BioMedical Engineering*, vol. 58, no. 9, pp. 2441–2447, 2011.
- [131] D. Safieddine, A. Kachenoura, L. Albera, G. Birot, F. Wendling, L. Senhadji, and I. Merlet, "ICA versus CCA pour le debruitage de signaux epileptiques intercritiques : une etude comparative de performances basee sur la localisation de la zone epileptogene," *IRBM*, vol. 32, pp. 298–301, 2011.
- [132] K. Sweeney, S. McLoone, and T. Ward, "The Use of Ensemble Empirical Mode Decomposition With Canonical Correlation Analysis as a Novel Artifact Removal Technique," *IEEE Transactions on BioMedical Engineering*, vol. 60, no. 1, pp. 97–105, 2013.
- [133] W. De Clercq, A. Vergult, B. Vanrumste, W. Van Paesschen, and S. Van Huffel, "Canonical Correlation Analysis Applied to Remove Muscle Artifacts From the Electroencephalogram," *IEEE Transactions on BioMedical Engineering*, vol. 53, pp. 2583–2587, 2006.
- [134] A. Vergult, W. De Clercq, A. Palmmini, B. Vanrumste, P. Dupont, S. Van Huffel, and W. Van Paesschen, "Improving the interpretation of ictal scalp EEG: BSS-CCA algorithm for muscle artifact removal," *Epilepsia*, vol. 48, no. 5, pp. 950–958, 2007.
- [135] M. Rakibul Mowla, N. Siew-Cheok, M. S. A. Zilany, and R. Paramesran, "Artifacts-matched blind source separation and wavelet transform for multichannel EEG denoising," *Biomedical Signal Processing and Control*, vol. 22, pp. 111–118, 2015.
- [136] M. Al Harrach, F. S. Ayachi, S. Boudaoud, J. Laforet, and F. Marin, "Sensitivity evaluation of HOS parameters by data fusion from HD-sEMG grid," in *2013 2nd International Conference on Advances in Biomedical Engineering*, pp. 97–100, 2013.
- [137] D. Farina and R. Merletti, "A novel approach for precise simulation of the EMG signal detected by surface electrodes," *IEEE Transactions on BioMedical Engineering*, vol. 48, pp. 637–646, 2001.
- [138] C. J. De Luca and P. Contessa, "Hierarchical control of motor units in voluntary contractions," *Journal of Neurophysiology*, vol. 107, no. 1, pp. 178–195, 2012.
- [139] N. E. Huang, Z. Shen, S. R. Long, M. C. Wu, H. H. Shih, Q. Zheng, N.-C. Yen, C. C. Tung, and H. H. Liu, "The empirical mode decomposition and the hilbert spectrum for nonlinear and non-stationary time series analysis," in *Proceedings of the Royal Society of London A: Mathematical, Physical and Engineering Sciences*, vol. 454, pp. 903–995, 1998.
- [140] D. Safieddine, A. Kachenoura, L. Albera, G. Birot, A. Karfoul, A. Pasnicu, A. Biraben, F. Wendling, L. Senhadji, and I. Merlet, "Removal of muscle artifact from EEG data: comparison between

- stochastic (ICA and CCA) and deterministic (EMD and wavelet-based) approaches,” *EURASIP Journal on Advances in Signal Processing*, vol. 2012, no. 1, pp. 1–15, 2012.
- [141] D. L. Donoho, “De-noising by soft-thresholding,” *IEEE Transactions on Information Theory*, vol. 41, no. 3, pp. 613–627, 1995.
- [142] S. A. Murphy, R. Berrios, P. A. Nelson, F. Negro, D. Farina, B. Schmit, and A. Hynstrom, “Impaired regulation post-stroke of motor unit firing behavior during volitional relaxation of knee extensor torque assessed using high density surface emg decomposition,” in *2015 37th Annual International Conference of the IEEE Engineering in Medicine and Biology Society*, pp. 4606–4609, 2015.
- [143] U. Yavuz, F. Negro, O. Sebik, A. Holobar, C. Frommel, K. S. Turker, and D. Farina, “Estimating reflex responses in large populations of motor units by decomposition of the high-density surface electromyogram,” *The Journal of Physiology*, vol. 593, no. 19, pp. 4305–4318, 2015.
- [144] Y. Kawakami, K. Nakazawa, T. Fujimoto, D. Nozaki, M. Miyashita, and T. Fukunaga, “Specific tension of elbow flexor and extensor muscles based on magnetic resonance imaging,” *European Journal of Applied Physiology and Occupational Physiology*, vol. 68, no. 2, pp. 139–147, 1994.
- [145] M. Praagman, E. K. J. Chadwick, F. C. T. van der Helm, and H. E. J. Veeger, “The effect of elbow angle and external moment on load sharing of elbow muscles,” *Journal of Electromyography and Kinesiology*, vol. 20, no. 5, pp. 912–922, 2010.
- [146] N. Otsu, “A Threshold Selection Method from Gray-Level Histograms,” *IEEE Transactions on Systems, Man and Cybernetics*, vol. 9, no. 1, pp. 62–66, 1979.
- [147] T. M. Vieira, R. Merletti, and L. Mesin, “Automatic segmentation of surface EMG images: Improving the estimation of neuromuscular activity,” *Journal of Biomechanics*, vol. 43, no. 11, pp. 2149–2158, 2010.
- [148] S. Beucher and C. Lantuejoul, “Use of Watersheds in Contour Detection,” in *International workshop on image processing, real-time edge and motion detection*, 1979.
- [149] L. Vincent and P. Soille, “Watersheds in digital spaces: an efficient algorithm based on immersion simulations,” *IEEE Transactions on Pattern Analysis and Machine Intelligence*, vol. 13, no. 6, pp. 583–598, 1991.
- [150] H. J. A. M. Heijmans, “Mathematical Morphology: A Modern Approach in Image Processing Based on Algebra and Geometry,” *SIAM Review*, vol. 37, no. 1, pp. 1–36, 1995.

- [151] E. A. Clancy and N. Hogan, "Probability density of the surface electromyogram and its relation to amplitude detectors," *IEEE Transactions on BioMedical Engineering*, vol. 46, no. 6, pp. 730–739, 1999.
- [152] M. Bilodeau, M. Cincera, A. B. Arsenault, and D. Gravel, "Normality and stationarity of EMG signals of elbow flexor muscles during ramp and step isometric contractions," *Journal of Electromyography and Kinesiology*, vol. 7, no. 2, pp. 87–96, 1997.
- [153] K. Nazarpour, A. R. Sharafat, and S. M. Firoozabadi, "Application of higher order statistics to surface electromyogram signal classification," *IEEE Transactions on BioMedical Engineering*, vol. 54, no. 10, pp. 1762–1769, 2007.
- [154] M. S. Hussain, M. B. I. Reaz, F. Mohd-Yasin, and M. I. Ibrahimy, "Electromyography signal analysis using wavelet transform and higher order statistics to determine muscle contraction," *Expert Systems*, vol. 26, no. 1, pp. 35–48, 2009.
- [155] K. C. Chua, V. Chandran, U. R. Acharya, and C. M. Lim, "Application of higher order statistics/spectra in biomedical signals—a review," *Medical Engineering & Physics*, vol. 32, no. 7, pp. 679–689, 2010.
- [156] F. Ayachi, S. Boudaoud, J. F. Grosset, and C. Marque, "Study of the Muscular Force/HOS Parameters Relationship from the Surface Electromyogram," in *15th Nordic-Baltic Conference on Biomedical Engineering and Medical Physics*, no. 34, pp. 187–190, 2011.
- [157] S. Boudaoud, H. Rix, M. Al Harrach, and F. Marin, "Robust functional statistics applied to probability density function shape screening of sEMG data," in *36th Annual International Conference of the IEEE Engineering in Medicine and Biology Society*, pp. 2213–2216, 2014.
- [158] V. Carriou, S. Boudaoud, J. Laforet, and F. S. Ayachi, "Fast generation model of high density surface EMG signals in a cylindrical conductor volume," *Computers in Biology and Medicine*, vol. 74, pp. 54–68, 2016.
- [159] M. Al Harrach, S. Boudaoud, M. Hassan, F. S. Ayachi, D. Gamet, J. F. Grosset, and F. Marin, "Denosing of HD-sEMG signals using canonical correlation analysis," *Medical & Biological Engineering & Computing*, pp. 1–14, 2016.
- [160] M. Gobbo, P. Gaffurini, L. Bissolotti, F. Esposito, and C. Orizio, "Transcutaneous neuromuscular electrical stimulation: influence of electrode positioning and stimulus amplitude settings on muscle response," *European Journal of Applied Physiology*, vol. 111, no. 10, pp. 2451–2459, 2011.
- [161] P. K. Sahoo, S. Soltani, and A. K. C. Wong, "A survey of thresholding techniques," *Computer Vision, Graphics, and Image Processing*, vol. 41, pp. 233–260, 1988.

- [162] B. Afsharipour, U. Khalil, and R. Merletti, “Amplitude indicators and spatial aliasing in high density surface electromyography recordings,” *Biomedical Signal Processing and Control*, vol. 22, pp. 170–179, 2015.
- [163] A. Bowman and A. Adelchi, *Applied Smoothing Techniques for Data Analysis: The Kernel Approach with S-PLUS Illustrations*. Oxford Statistical Science Series, 1997.
- [164] D. P. Mitchell, “Spectrally optimal sampling for distribution ray tracing,” in *18th Annual Conference on Computer Graphics and Interactive Techniques*, vol. 25, pp. 157–164, 1991.
- [165] V. Carriou, J. Laforet, S. Boudaoud, and M. Al Harrach, “Realistic motor unit placement in a cylindrical hd semg generation model,” 2016.
- [166] C. S. Klein, G. D. Marsh, R. J. Petrella, and C. L. Rice, “Muscle fiber number in the biceps brachii muscle of young and old men,” *Muscle & Nerve*, vol. 28, no. 1, pp. 62–68, 2003.
- [167] C. J. De Luca and P. Contessa, “Hierarchical control of motor units in voluntary contractions,” *Journal of Neurophysiology*, vol. 107, no. 1, pp. 178–195, 2012.
- [168] C. Nordander, J. Willner, G. A. Hansson, B. Larsson, J. Unge, L. Granquist, and S. Skerfving, “Influence of the subcutaneous fat layer, as measured by ultrasound, skinfold calipers and bmi, on the emg amplitude,” *European Journal of Applied Physiology*, vol. 89, no. 6, pp. 514–519, 2003.
- [169] D. Farina, L. Mesin, S. Martina, and R. Merletti, “A surface emg generation model with multilayer cylindrical description of the volume conductor,” *Biomedical Engineering, IEEE Transactions on*, vol. 51, no. 3, pp. 415–426, 2004.
- [170] E. Zalewska and I. Hausmanowa-Petrusewicz, “Approximation of motor unit structure from the analysis of motor unit potential,” *Clinical Neurophysiology*, vol. 119, no. 11, pp. 2501–2506, 2008.
- [171] B. J. van der Linden, H. F. Koopman, H. J. Grootenboer, and P. A. Huijing, “Modelling functional effects of muscle geometry,” *Journal of Electromyography and Kinesiology*, vol. 8, no. 2, pp. 101–109, 1998.
- [172] K. Ben Mansour, F. R. Sarhan, C. Neiva, C. Godard, B. Devauchelle, F. Marin, and S. DakpÃ©, “Analysis of mimic facial movements based on motion capture,” *Computer Methods in Biomechanics and Biomedical Engineering*, vol. 17, pp. 78–79, 2014.
- [173] G. Bleser, D. Steffen, M. Weber, G. Hendeby, D. Stricker, L. Fradet, F. Marin, N. Ville, and F. CarrÃ©, “A personalized exercise trainer for the elderly,” *Journal of Ambient Intelligence and Smart Environments*, vol. 5, no. 6, pp. 547–562, 2013.

- [174] I. Zelman, M. Galun, A. Akselrod-Ballin, Y. Yekutieli, B. Hochner, and T. Flash, “Nearly automatic motion capture system for tracking octopus arm movements in 3D space,” *Journal of Neuroscience Methods*, vol. 182, no. 1, pp. 97–109, 2009.
- [175] L. Edward, S. Dakpe, P. Feissel, B. Devauchelle, and F. Marin, “Quantification of facial movements by motion capture,” *Computer Methods in Biomechanics and Biomedical Engineering*, vol. 15, pp. 259–260, 2012.
- [176] S. S. Blemker, P. M. Pinsky, and S. L. Delp, “A 3d model of muscle reveals the causes of nonuniform strains in the biceps brachii,” *Journal of Biomechanics*, vol. 38, no. 4, pp. 657–665, 2005.
- [177] J. Teran, S. Blemker, V. Ng Thow Hing, and R. Fedkiw, “Finite Volume Methods for the Simulation of Skeletal Muscle,” in *Proceedings of the 2003 ACM SIGGRAPH/Eurographics Symposium on Computer Animation*, pp. 68–74, 2003.
- [178] R. Raikova, J. Celichowski, M. Pogrzebna, H. Aladjov, and P. Krutki, “Modeling of summation of individual twitches into unfused tetanus for various types of rat motor units,” *Journal of Electromyography and Kinesiology*, vol. 17, no. 2, pp. 121–130, 2007.
- [179] T. Moritani and H. A. DeVries, “Reexamination of the relationship between the surface integrated electromyogram (iemg) and force of isometric contraction.,” *American Journal of Physical Medicine & Rehabilitation*, vol. 57, no. 6, pp. 263–277, 1978.
- [180] A. J. Fuglevand, D. A. Winter, and A. E. Patla, “Models of recruitment and rate coding organization in motor-unit pools,” *Journal of neurophysiology*, vol. 70, no. 6, pp. 2470–2488, 1993.
- [181] X. Chen, H. Wen, Q. Li, T. Wang, S. Chen, Y.-P. Zheng, and Z. Zhang, “Identifying transient patterns of in vivo muscle behaviors during isometric contraction by local polynomial regression,” *Biomedical Signal Processing and Control*, vol. 24, pp. 93–102, 2016.
- [182] J. Vredenburg and G. Rau, “Surface electromyography in relation to force, muscle length and endurance,” *New Developments in Electromyography and Clinical Neurophysiology*, vol. 1, pp. 607–622, 1973.
- [183] W. S. McCulloch and W. Pitts, “A logical calculus of the ideas immanent in nervous activity,” *The Bulletin of Mathematical Biophysics*, vol. 5, no. 4, pp. 115–133, 1943.
- [184] F. Rosenblatt, “The perceptron: a probabilistic model for information storage and organization in the brain,” *Psychological Review*, vol. 65, no. 6, p. 386, 1958.
- [185] Y. H. Hu and J.-N. Hwang, *Handbook of Neural Network Signal Processing*. CRC Press, 2001.

- [186] N. Karayiannis and A. N. Venetsanopoulos, *Artificial Neural Networks: Learning Algorithms, Performance Evaluation, and Applications*. Springer Science & Business Media, 2013.
- [187] D. J. C. MacKay, "Bayesian interpolation," *Neural Computation*, vol. 4, no. 3, pp. 415–447, 1992.
- [188] M. F. Moller, "A scaled conjugate gradient algorithm for fast supervised learning," *Neural networks*, vol. 6, no. 4, pp. 525–533, 1993.
- [189] M. T. Hagan and M. B. Menhaj, "Training feedforward networks with the marquardt algorithm," *IEEE Transactions on Neural Networks*, vol. 5, no. 6, pp. 989–993, 1994.
- [190] K. Levenberg, "A method for the solution of certain non-linear problems in least squares," *Quarterly of Applied Mathematics*, vol. 2, no. 2, pp. 164–168, 1944.

# Appendix A

## Image segmentation study

In this appendix, we present a comparative study between this WS algorithm and the classic Otsu thresholding algorithm in simulation using a fast cylindrical HD-sEMG generation model for three different contraction levels: 30, 50 and 70 %MVC. This study aims at finding the best segmentation algorithm, which is robust to the noise level and adipose tissue thickness, as well as the corresponding optimal threshold that enables the definition of the active region accurately. The anatomical repartition of the MUs in the muscle for one of the anatomies as well as the position of the electrodes are illustrated in Figure A.1.

### A.1 Implementation and accuracy computing

The accuracy of the two proposed algorithms, the watershed segmentation and the Otsu thresholding method, from the standpoint of muscle activity segmentation were evaluated by computing false positive and false negative pixels. Pixels are considered false positive when they are located above inactive portion of the muscle but considered as an part of the active cluster after segmentation. Similar, pixels are considered false negative if they are located above active region of the muscle but not classified with the active cluster. Therefore, in order to compute the accuracy in percentage of the segmentation method we applied the following equation:

$$A_{cc} = 100 \times \left( \frac{N_{ch} - (F_{pos} + F_{neg})}{N_{ch}} \right) \quad (\text{A.1})$$

where  $F_{pos}$ ,  $F_{neg}$  and  $N_{ch}$  are the numbers of false positives, false negatives and the total number of channels in the grid respectively.

The final segmentation matrix (an image of 1s and 0s where 1s represent the active regions and 0s the inactive regions of the simulated muscle. This matrix is then compared to the original matrix obtained

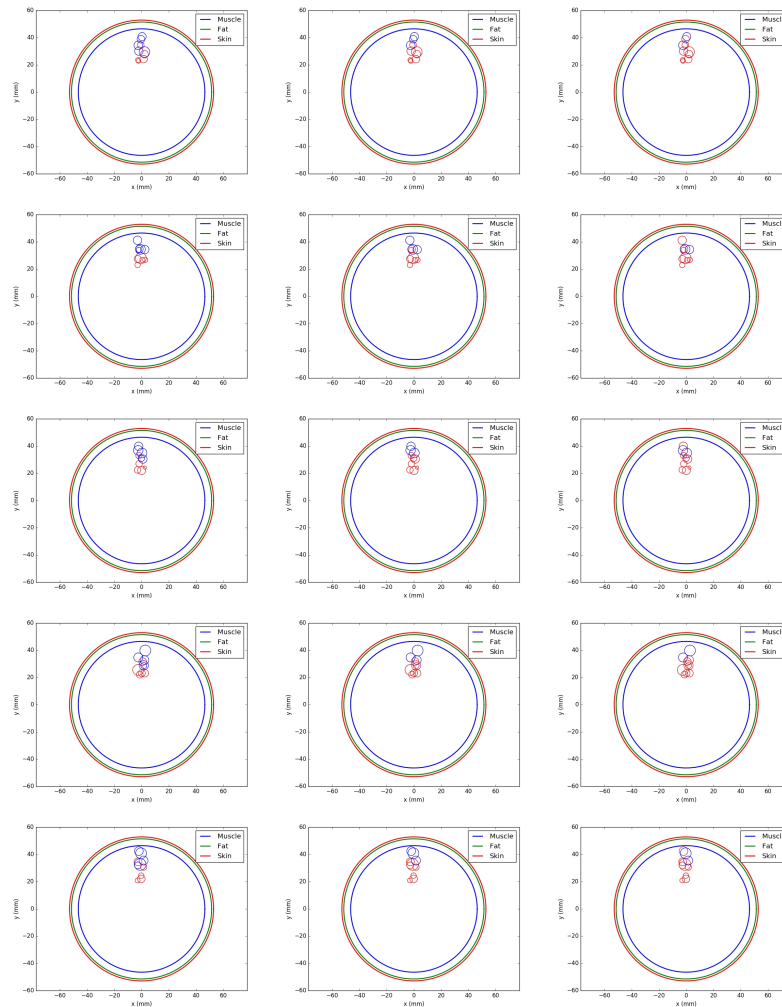


Figure A.1: The repartition of the MUs in the muscle for the five anatomies relative to three contraction level: 30, 50 and 80 %MVC. The red MUs are the active (recruited) MUs and the blue MUs are the inactive (non recruited) MUs.

based on the actual position of MUs in the muscle (see Figure A.1) in order to compute the percentage of accuracy. this will be done by changing for each method the SNR, the adipose tissue thickness, the thresholding level and the force level. We have to note that we performed the equalization and the thresholding step for the Otsu method similarly to the WS method in order to perform more accurate comparison between the two algorithms.

## A.2 Results and Discussion

An example of the segmentation results using the two segmentation algorithms: the WS (section 3.2.2) and the Otsu algorithm (section chap2 ref) for one of the simulations (anatomy 1, 50 %MVC, adipose tissue thickness= 1 mm, SNR=30 dB) is presented in Figure A.2. Where Figure A.2a and A.2b represent the RMS and the Equalized RMS maps respectively. The histogram equalization of an image induces an increases in its global contrast which leads to a better dispersion of pixel energies over the map. The

filters obtained after segmentation using both segmentation algorithms discussed above are illustrated in Figures A.2c and A.2d. We can see clearly the competence of each technique in extracting the region of interest from the equalized RMS map (Figure A.2b).

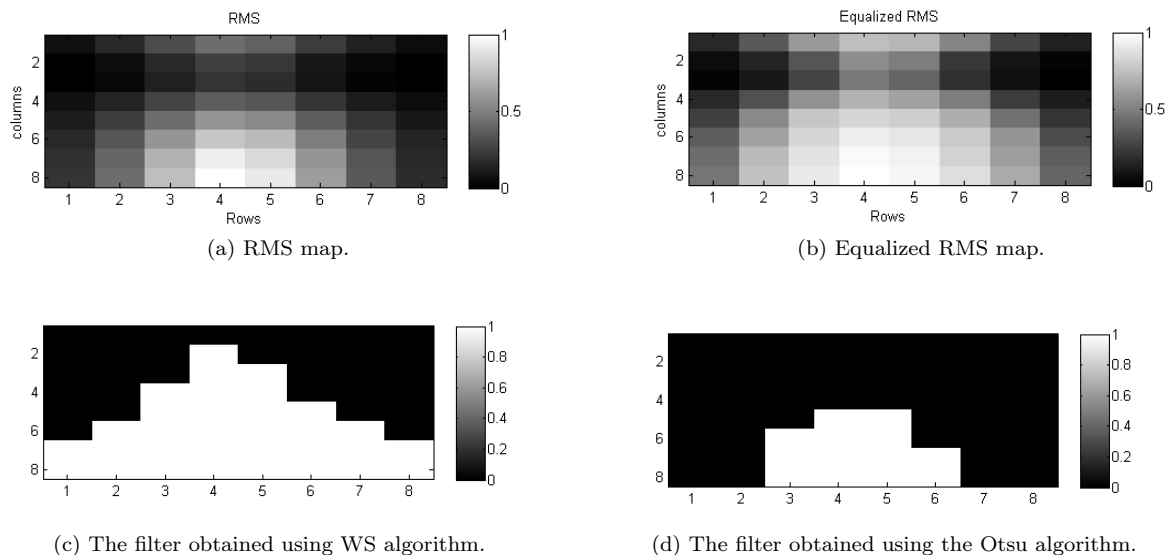
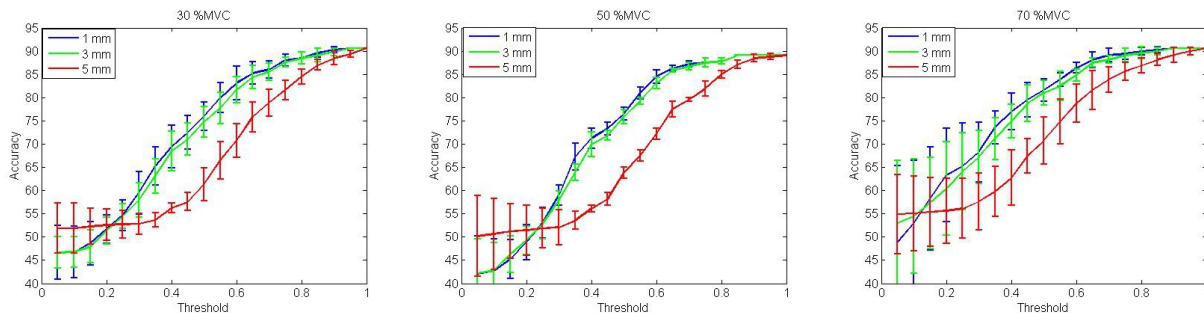


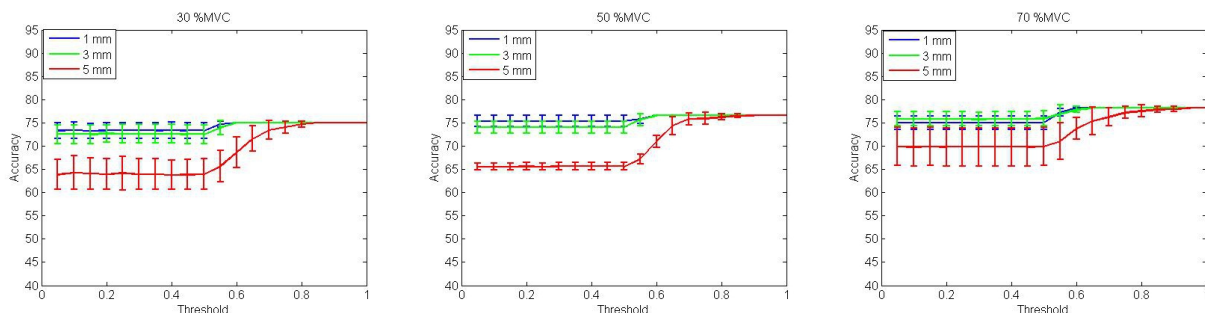
Figure A.2: An example that shows the ability of watershed and Otsu algorithms in detecting the active portion of a simulated RMS map (a), after equalization (b) using the watershed (c) and the Otsu (d) algorithms.

In order to test the accuracy of each method with respect to the threshold value variation as well as the adipose tissue thickness, we computed the accuracy percentage mean  $\pm$  std values as defined in A.1 for the five anatomies each for three adipose tissue thicknesses: 1, 3 and 5 *mm* and three contraction levels: 30, 50 and 80 %MVC by changing the threshold between 5 and 100% of the maximum RMS value (with a step of 5%). The results for the WS and the Otsu algorithms are displayed in Figure A.3. The SNR values used for each force levels were obtained from experimental values and are equal to 20, 30 and 45 *dB* for 30, 50 and 70 %MVC respectively.

Starting by the WS algorithm (Figure A.3a), we can see an important influence of the threshold value on the segmentation accuracy. the accuracy percentage increases with the threshold until we obtain an accuracy  $>88\%$  at a threshold value equal to 70% of the maximum RMS value. This is true for the three adipose value thicknesses but nevertheless we have to note the effect of the adipose tissue thickness of the accuracy percentage values for low thresholds. Thus, for this method we can say that we have a very good segmentation accuracy for a threshold  $>70\%$  of the maximum RMS value. And this accuracy is robust to the adipose tissue thickness as well as the contraction level. As for the Otsu method (Figure A.3b), we also have an increase of the accuracy with the threshold value increase but no more than 15%. We can see that for an adipose tissue thickness equal to 1 or 3 *mm* we have almost the save accuracy results. However for the 5 *mm* adipose tissue thickness we have a greater dynamic. We can also divide these curves into three parts: for a threshold between 5 to  $\sim 50\%$  we have somewhat constant accuracy



(a) Percentage accuracy values of HD-sEMG map segmentation for 20 threshold levels (from 5% to 100% of the maximum of the simulated RMS) and three adipose tissue thickness values using watershed algorithm.



(b) Percentage accuracy values of HD-sEMG map segmentation for 20 threshold levels (from 5% to 100% of the maximum of the simulated RMS) and three adipose tissue thickness values using Otsu thresholding algorithm.

Figure A.3: Percentage accuracy values of EMG segmentation for 20 threshold levels (from 5% to 100% of the maximum of the simulated RMS) and three adipose tissue thickness values using both watershed and Otsu algorithms and three contraction levels: 30, 50 and 70 %MVC. The SNR values were obtained from realistic experimental signals.

percentage values, then from a threshold between  $\sim 50$  %MVC to  $\sim 80$  %MVC we have an slight increase of the accuracy. Finally, for the rest (threshold  $\gtrsim 80$  %MVC we have a constant accuracy for all adipose tissue values but different for each contraction level. By comparing the two methods accuracy results (Figure A.3) we can say that the WS algorithm delivered better results that the Otsu algorithm (All the curves have an accuracy  $< 78\%$ ).

Finally, we tested the stability of WS and Otsu segmentation algorithms with different levels of noise (WGN). Therefore we added different WGN values in order to obtain realistic SNR values (compared to experimental signals). The mean values for the five different SNR values for the three adipose tissue thicknesses and contraction levels are presented in the Tables A.1a, A.1b and A.1c. We can see that the two segmentation methods are robust toward noise, but we can observe the minor effect of the adipose tissue thickness especially for the Otsu algorithm.

In conclusion, it seems that the WS segmentation algorithm proposed by Vieira et al. [147] and adapted to our HD-sEMG generation model is a solid and robust segmentation algorithm for extracting the active region of the RMS map. This method would be of great interest for the model input parameters determination and fusion from the HD-sEMG map as well as the study of the probability density function shape variation of HD-sEMG signals using amplitude descriptors.

Table A.1: Percentage accuracy values of EMG segmentation for three adipose tissue thickness values using both watershed and Otsu algorithms and three contraction levels: 30, 50 and 70 %MVC. The threshold was fixed at 70%.

(a) Percentage accuracy values of EMG segmentation for three adipose tissue thickness values using both watershed and Otsu algorithms for 30 %MVC contraction level.

	WS segmentation method			Otsu segmentation method		
	Fat layer			Fat layer		
SNR	1 mm	3 mm	5 mm	1 mm	3 mm	5 mm
5	82.81	82.81	79.68	81.25	79.68	74.21
10	82.81	82.81	79.68	80.46	80.46	75.00
15	82.81	82.81	79.68	80.46	80.46	75.00
20	82.81	82.81	79.68	80.46	80.46	75.00
25	82.81	82.81	79.68	80.46	80.46	75.00

(b) Percentage accuracy values of EMG segmentation for three adipose tissue thickness values using both watershed and Otsu algorithms for 50 %MVC contraction level.

	WS segmentation method			Otsu segmentation method		
	Fat layer			Fat layer		
SNR	1 mm	3 mm	5 mm	1 mm	3 mm	5 mm
15	86.93	86.71	85.46	85.93	85.72	79.68
20	86.93	86.71	85.46	85.93	85.72	79.46
25	86.93	86.71	85.46	85.93	85.72	79.68
30	86.93	86.71	85.46	85.93	85.72	79.68
35	86.93	86.71	85.46	85.93	85.72	79.68

(c) Percentage accuracy values of EMG segmentation for three adipose tissue thickness values using both watershed and Otsu algorithms for 70 %MVC contraction level.

	WS segmentation method			Otsu segmentation method		
	Fat layer			Fat layer		
SNR	1 mm	3 mm	5 mm	1 mm	3 mm	5 mm
25	87.34	87.34	85.43	74.21	74.21	63.28
30	87.34	87.34	85.43	74.21	74.21	63.28
35	87.34	87.34	85.43	74.21	74.21	63.28
40	87.34	87.34	85.43	74.21	74.21	63.28
45	87.34	87.34	85.43	74.21	74.21	63.28

## Appendix B

# The anatomies and force combinations used in chapter 4

- B.1 An example of the MU positions for LRS and HRS for one muscle anatomy

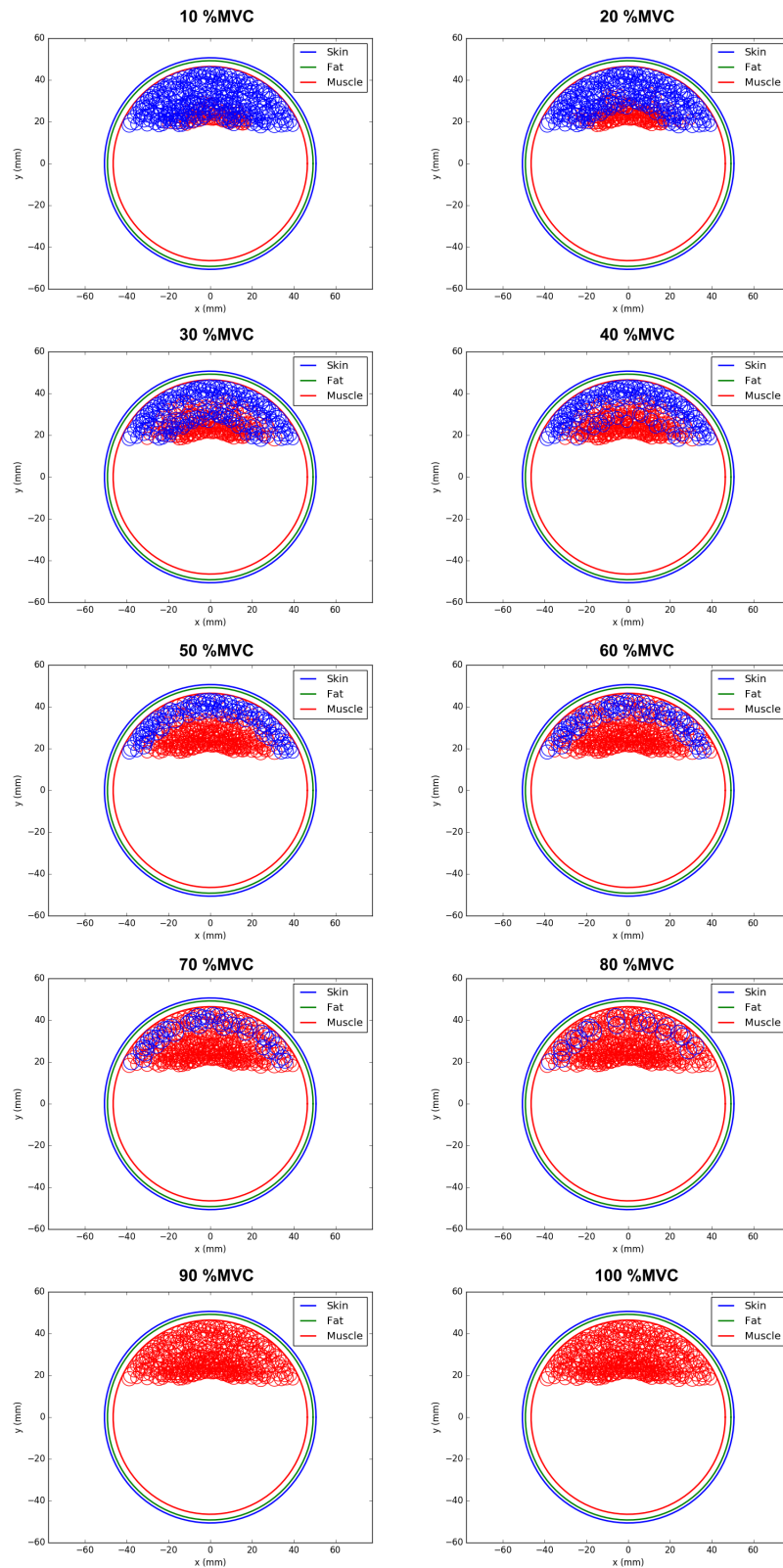


Figure B.1: The MU placement in the muscle for anatomy 1, D1, HRS for the ten force levels 10, 20, 30, 40, 50, 60, 70, 80, 90 and 100 %MVC. With the recruited MUs are illustrated in red and the non recruited MUs in blue.

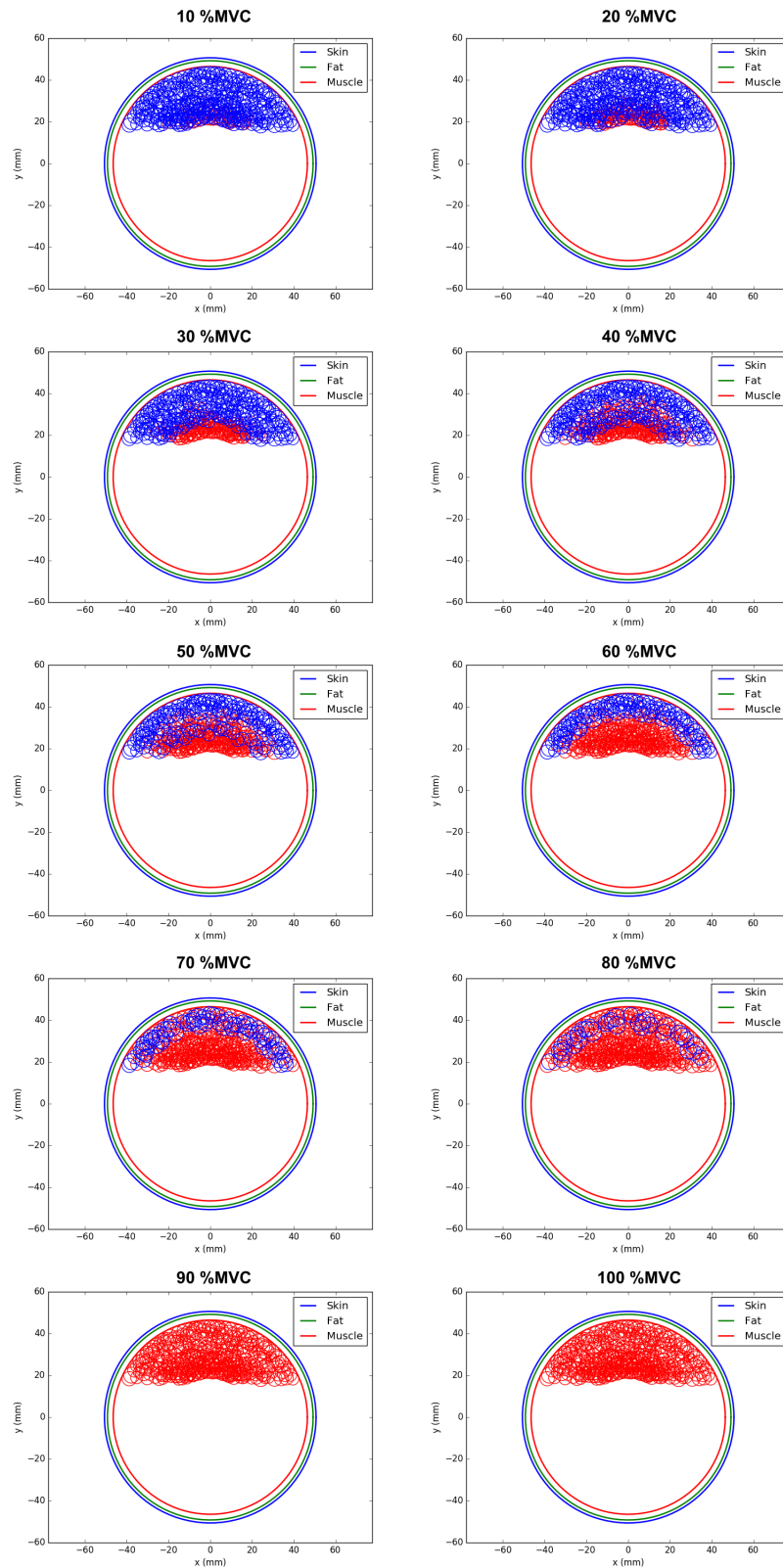


Figure B.2: The MU placement in the muscle for anatomy 1, D1, LRS for the ten force levels 10, 20, 30, 40, 50, 60, 70, 80, 90 and 100 %MVC. With the recruited MUs are illustrated in red and the non recruited MUs in blue.

## B.2 The different force level combinations tested for force estimation by ANN

Table B.1: Different combinations of contraction levels tested for the polynomial coefficients estimation.

Combination number	Force level 1	Force level 2	Force level 3	Combination number	Force level 1	Force level 2	Force level 3
1	10	20	30	19	20	30	70
2	10	20	40	20	20	40	50
3	10	20	50	21	20	40	60
4	10	20	60	22	20	40	70
5	10	20	70	23	20	50	60
6	10	30	40	24	20	50	70
7	10	30	50	25	20	60	70
8	10	30	60	26	30	40	50
9	10	30	70	27	30	40	60
10	10	40	50	28	30	40	70
11	10	40	60	29	30	50	60
12	10	40	70	30	30	50	70
13	10	50	60	31	30	60	70
14	10	50	70	32	40	50	60
15	10	60	70	33	40	50	70
16	20	30	40	34	40	60	70
17	20	30	50	35	50	60	70
18	20	30	60				

